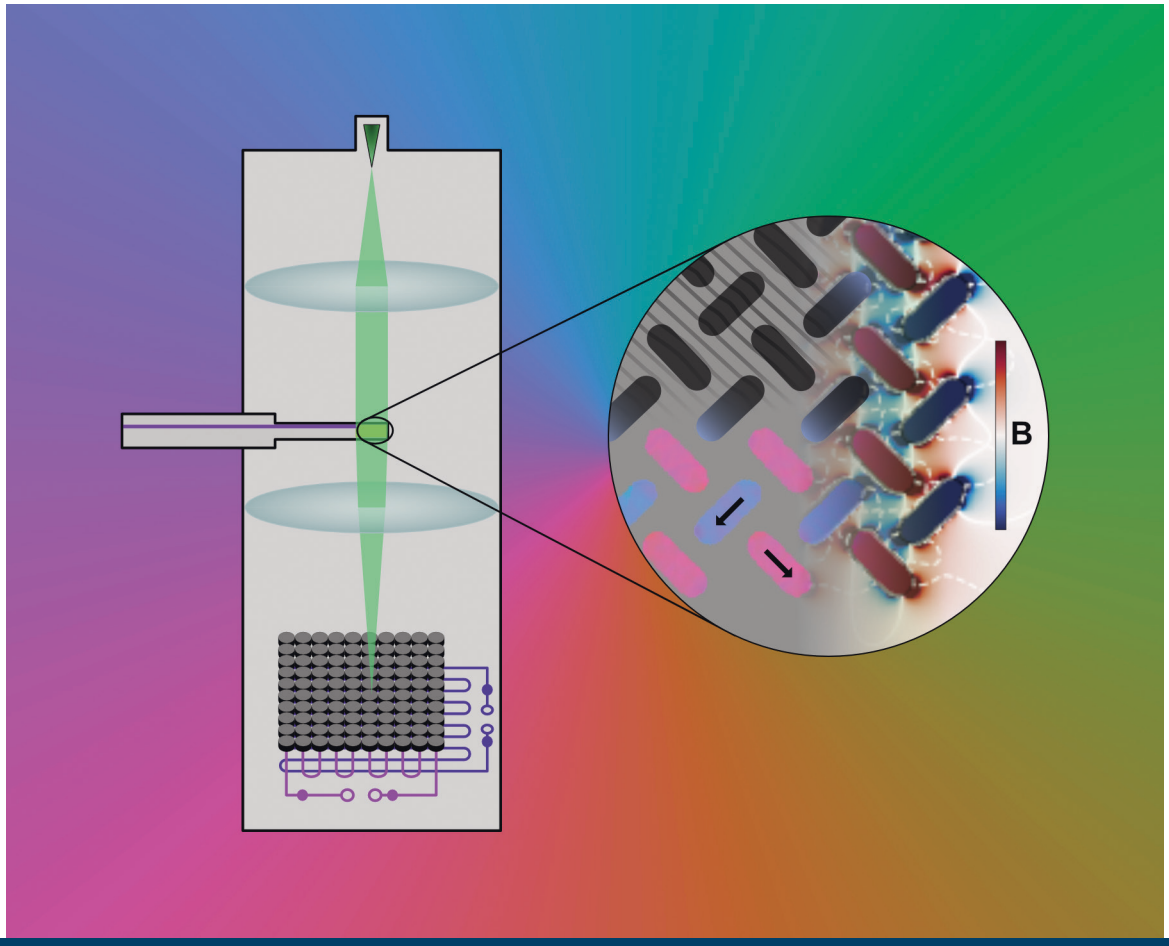

Time-resolved and three-dimensional characterisation of magnetic states in nanoscale materials in the transmission electron microscope

Teresa Weßels

Schlüsseltechnologien / Key Technologies
Band / Volume 265
ISBN 978-3-95806-685-4

Mitglied der Helmholtz-Gemeinschaft

JÜLICH
Forschungszentrum

Schriften des Forschungszentrums Jülich
Reihe Schlüsseltechnologien / Key Technologies Band / Volume 265

Forschungszentrum Jülich GmbH
Ernst Ruska-Centrum für Mikroskopie und Spektroskopie mit Elektronen (ER-C)
Physik Nanoskaliger Systeme (ER-C-1 / PGI-5)

Time-resolved and three-dimensional characterisation of magnetic states in nanoscale materials in the transmission electron microscope

Teresa Weßels

Schriften des Forschungszentrums Jülich
Reihe Schlüsseltechnologien / Key Technologies Band / Volume 265

ISSN 1866-1807 ISBN 978-3-95806-685-4

Bibliografische Information der Deutschen Nationalbibliothek.
Die Deutsche Nationalbibliothek verzeichnet diese Publikation in der
Deutschen Nationalbibliografie; detaillierte Bibliografische Daten
sind im Internet über http://dnb.d-nb.de abrufbar.

Herausgeber und Vertrieb:	Forschungszentrum Jülich GmbH Zentralbibliothek, Verlag 52425 Jülich Tel.: +49 2461 61-5368 Fax: +49 2461 61-6103 zb-publikation@fz-juelich.de www.fz-juelich.de/zb
Umschlaggestaltung:	Grafische Medien, Forschungszentrum Jülich GmbH
Druck:	Grafische Medien, Forschungszentrum Jülich GmbH
Copyright:	Forschungszentrum Jülich 2023

Schriften des Forschungszentrums Jülich
Reihe Schlüsseltechnologien / Key Technologies, Band / Volume 265

D 82 (Diss. RWTH Aachen University, 2022)

ISSN 1866-1807
ISBN 978-3-95806-685-4

Vollständig frei verfügbar über das Publikationsportal des Forschungszentrums Jülich (JuSER)
unter www.fz-juelich.de/zb/openaccess.

Acknowledgements

I would like to express my deep gratitude to all members of the PGI-5 and ER-C and also to all other colleagues who contributed to this work. They were always supportive wherever they could and I really enjoyed working with them. Here, I can only name a few of those who helped me along my journey:

- My supervisor Prof. Dr. Rafal E. Dunin-Borkowski, who gave me the opportunity for doing my PhD. He was always there to give guidance for critical and non-critical questions, took time for my submissions and never failed to supply me with enthusiastic encouragement.
- Prof. Dr. Joachim Mayer for kindly accepting the role as co-assessor of this work and ensuring a pleasant working atmosphere in the institute.
- Dr. András Kovács, who was my first point of contact whenever I left the office with any kind of question and helped me throughout my thesis with his patient guidance. He also made sure that scientific discussion took place in a relaxed and pleasant atmosphere in the formal and informal meetings.
- Dr. Vadim Migunov without whom I could not have carried out the time-resolved experiments. Together with other collagues, we set up the experiments, solving any issue which we faced along the way.
- Dr. Yoshie Murooka, who shared his time, knowledge and enthusiasm so generously with me.
- Patrick Diehle for essentially teaching me everything I needed to know when I started my PhD, from operating a microscope to whom to ask without losing his patience once.
- Dr. Jan Caron, whose Python package I set out using. He helped me through any issue and had an open ear for any of my ideas.
- Maximilian Kruth for preparing and transferring my samples even when it was not a standard preparation and others would have told me that it is simply not possible.
- All my colleagues from the institute who contributed to this work in so many different ways. I experienced very helpful scientific discussion, ideas, experimental support in a great working environment. Special thanks goes to Dr. Juri Barthel, Alexander Clausen, Dr. Thibaud Denneulin, Dr. Janghyun Jo, Tim Lienig, Dr. Marta Lipinska-Chwalek, Peng-Han Lu, Alexander Müller, Dr. Paul Paciok, Dr. Michael Schnedler.

- All my colleagues who helped me with the sample fabrication in the HNF cleanroom, including Rainer Benczek, Dr. Thomas Grap, Dr. Marvin Kaminski, Dr. Florian Lentz, Dr. Jürgen Moers, Dr. Stefan Trellenkamp, Janine Worbs, as well as Prof. Dr. Beata Kardynal from PGI-9.
- Working in a scientific institute would not be possible without the people who kept the institute running in the background. Therefore, I would like to thank René Borowski, Marie Göcking, Gaby Mertzbach, Werner Pieper, Ingrid Ritsche-Radloff and Dr. Karsten Tillmann.
- My cooperation partners from other research centres and universities: Dr. Sebastian Gliga, Dr. Simone Finizio, Sina Mayr, Dr. Sebatian Wintz and Dr. Jörg Raabe from the Paul Scherrer Institute, Dr. Simon Däster and Dr. Yves Acreman from the ETH Zurich and Dr. Benjamin Zingsem from the University of Duisburg-Essen. None of my projects would have been possible without the help of those.
- Dr. András Kovács, Dr. Juri Barthel, Dr. Jan Caron, Dr. Simon Däster, Dr. Thibaud Denneulin, Dr. Thomas Feggeler, Franziska Knuth, Jonas Krehl, Dr. Matti Partanen, who took a lot of time and effort to improve this thesis.
- My friends and my family who kept me running through the good and the challenging times of my PhD. Especially, I would like to thank Arne Bayer for making sure that my blood sugar level was always high enough to encounter any mood I might be in.

Abstract

Magnetism of nanoscale systems offers promising novel pathways in the quest for smaller, faster and more efficient devices. Understanding the interaction of multiple nanomagnets and their dynamics is essential for these developments and requires a high-resolution probe of magnetic states and characterisation of field distributions quantitatively on the picosecond time regime. In this thesis, magnetic imaging techniques in the transmission electron microscopy (TEM) were employed to study the magnetic properties of nanomagnets and improve the temporal resolution of magnetisation dynamics studies in TEM.

Chiral ice is a specific type of artificial spin ice (ASI) where a unidirectional rotation of the net magnetisation has been observed during thermal relaxation. According to micromagnetic simulation, the process is driven by the stray field distribution. In this thesis, the quantitative stray field distribution was verified experimentally for a regular pattern of permalloy (Py) nanomagnets. First, the reversal mechanism and effects of composition and sample oxidation were described. Second, the projected in-plane magnetic induction was mapped using off-axis electron holography. Third, the projected in-plane magnetisation was determined by applying a model-based iterative reconstruction. The average magnetic polarisation was measured to be 0.7 T which is lower than the expected value, most likely due to a combination of microstructure, composition and possible oxidation of the sample. Forth, the three-dimensional stray field distribution of chiral ice was calculated using experimental measurements.

Magnetic vortices are of particular interest in the context of magnetisation dynamics due to their stability and reproducibility. Combing TEM with a fast delay line detector allows imaging of the gyration of the vortex core while maintaining the excellent imaging properties of TEM. The vortex core motion in a Py disk was excited using a microwave magnetic specimen holder and measured using Fresnel defocus imaging. The vortex core resonance was found to be at ~417 MHz and an intrinsic temporal resolution of ~122 ps was achieved in a frequency range from 0.1 to 2.3 GHz. Conventional Fresnel imaging revealed a breathing-like behaviour of the vortex core motion, possibly due to sample heating or vortex core polarity switching. A shape distortion of the Py disk, originating from the sample preparation, was observed. However, the analysis showed that this had no effect on the vortex core gyration in the studied regime.

The presented work on ASI pushes the limits of quantitative analysis of weak magnetic stray fields and presents a methodology to reconstruct the fields in three dimensions. Moreover, an easy-to-implement approach is presented to achieve picosecond temporal and nanometre spatial resolution. In the future, both techniques can be combined giving nearly unique access to stray field dynamics.

Kurzfassung

Der Magnetismus von nanoskaligen Systemen bietet Impulse für kleinere, schnellere und effizientere Geräte. Das Verständnis der Wechselwirkung mehrerer Nanomagnete und ihrer Dynamik erfordert eine hochauflösende Untersuchung der magnetischen Zustände im Pikosekundenbereich. In dieser Arbeit wurde Transmissionselektronenmikroskopie (TEM) genutzt, um die Eigenschaften von Nanomagneten zu untersuchen und die zeitliche Auflösung der TEM verbessert. Chirales Eis (eine Untergruppe des künstlichem Spineises(ASI)) zeigt eine unidirektionale Rotation der Nettomagnetisierung während der thermischen Relaxation. Diese ist laut mikromagnetischen Simulationen auf die Streufeldverteilung zurückzuführen. Für entsprechende Anordnung von Permalloy (Py)-Nanomagneten wurden zunächst der Umpolungsmechanismus und die Auswirkungen der Probenzusammensetzung und -oxidation untersucht. Danach wurde die projizierte magnetische Induktion in der Ebene mit Hilfe der Off-Axis-Elektronenholographie gemessen und die entsprechende Magnetisierung mit einer modellbasierten iterativen Rekonstruktion bestimmt. Die durchschnittliche magnetische Polarisation war mit 0,7 T wahrscheinlich auf Grund einer Kombination aus Mikrostruktur, Zusammensetzung und möglicher Oxidation der Probe niedriger als der erwartete Wert. Schließlich wurde die dreidimensionale Streufeldverteilung von chiralem Eis anhand experimenteller Messungen bestimmt und die Simulationen bestätigt.
Magnetische Vortexe sind für dynamische Messungen aufgrund ihrer Stabilität und Reproduzierbarkeit besonders interessant. Die Kombination von TEM mit einem Verzögerungsliniendetektor ermöglicht es, die Gyration des Vortexkerns abzubilden und die Abbildungseigenschaften der TEM zu erhalten. Die Bewegung des Vortexkerns in einer Py-Scheibe wurde mit mikrowellen Magnetfeldern angeregt und mit dem Fresnel-Defokus-Abbildungverfahren gemessen. Die Resonanz lag bei ~417 MHz und eine intrinsische zeitliche Auflösung von ~122 ps wurde in einem Frequenzbereich von 0,1 bis 2,3 GHz erreicht. Die konventionelle Fresnel-Abbildung zeigte ein atmungsähnliches Verhalten der Gyration, das möglicherweise auf eine Probenerwärmung oder Polaritätsänderung des Kernes zurückzuführen ist. Die Probenherstellung führt zu einer Verformung der Py-Scheibe, die jedoch keinen Einfluss auf die Gyration im untersuchten Bereich hat. Diese Promotionsarbeit über ASI stellt die quantitativen Analyse schwacher magnetischer Streufelder und ihre Rekonstruktion in drei Dimensionen vor. Darüber hinaus wurde ein einfacher Aufbau entwickelt, mit dem zeitliche und räumliche Auflösungen im Pikosekunden-, beziehungsweise Nanometerbereich erreicht wurden. In Zukunft können beide Techniken kombiniert werden, was einen nahezu einzigartigen Zugang zur Dynamik von Streufeldern ermöglicht.

Contents

List of Figures **xi**

List of Tables **xv**

Nomenclature **xvii**

1. Introduction **1**

2. Magnetism of nanoscale objects **5**
2.1. General magnetic concepts 5
2.2. Basis of micromagnetism 7
2.3. Artificial spin ice 10
2.4. Magnetic vortex state 13
2.4.1. Description of a static magnetic vortex state 14
2.4.2. Magnetic vortex core dynamics 15
2.5. Measurement magnetisation dynamics employing X-rays 18
2.6. Summary 21

3. Conventional and magnetic imaging in transmission electron microscopy **23**
3.1. Conventional transmission electron microscopy 23
3.1.1. Electron-specimen interactions 23
3.1.2. The transmission electron microscope 25
3.2. Off-axis electron holography 30
3.2.1. Scattering of electrons by electromagnetic fields 30
3.2.2. Reconstruction of phase information 33
3.2.3. Experimental setup 36
3.2.4. Separation of electrostatic and magnetic contributions to the phase 39
3.2.5. Model-based iterative reconstruction of magnetisation . . 40
3.3. Lorentz microscopy 44
3.4. Time-resolved microscopy 46

3.5. Summary 49

4. Quantitative measurement of virtual antivortices in artificial spin ice 51
4.1. Theoretical background of chiral ice 51
4.2. Sample fabrication 53
4.3. Data analysis 56
4.3.1. Automated detection of particles 58
4.3.2. Removal of a phase ramp in the presence of magnetic stray fields 60
4.3.3. Image distortions and warping of phase images 62
4.3.4. Stitching of multiple phase images 64
4.3.5. Computation of magnetic induction from a known magnetisation distribution 67
4.4. Initial magnetic state of chiral ice 70
4.5. Effect of external magnetic field on chiral ice 74
4.5.1. Magnetic fields required for switching of artificial spin ice pattern 74
4.5.2. Driving mechanism of magnetic reversal of nanomagnets 77
4.6. Detection of virtual antivortices 81
4.6.1. Magnetic state of saturated artificial spin ice 81
4.6.2. Reconstruction of the magnetisation 87
4.6.3. Determination of the three-dimensional magnetic induction from the reconstructed magnetisation 95
4.6.4. Determination of virtual antivortex positions 98
4.6.5. Effect of missing stray fields on the positions of virtual antivortices 102
4.7. Summary 104

5. Magnetic vortices in Py disks 105
5.1. Sample preparation and structure 105
5.2. Reconstruction of the projected in-plane magnetic induction and magnetisation of magnetic vortices 108
5.2.1. Influence of the reference hologram on phase reconstruction 108
5.2.2. Off-axis electron holography of magnetic vortices and reconstruction of the projected in-plane magnetisation . . . 109
5.2.3. Comparison of reconstructed magnetisation with micromagnetic simulations 115
5.2.4. Dependence of core shape on the thickness and diameter of the disk 117

5.3. Effect of the three-dimensional shape of the disks 119
5.3.1. Shape variations of the Py disks 119
5.3.2. Movement of vortex core with sample tilt 121
5.3.3. Magnetic state of a cross-section 128
5.4. Summary 130

6. Dynamic imaging using a fast readout detector in a transmission electron microscope 131
6.1. Fabrication and expected features of the sample 132
6.2. Experimental setup for time-resolved microscopy 135
6.2.1. Overview of general setup 136
6.2.2. Experimental characterisation of the magnetising holder . 139
6.2.3. Simulations of electromagnetic fields induced by the RF magnetising holder 145
6.3. Basics of data analysis: Principal component analysis 148
6.4. Breathing-like behaviour of the vortex core during its gyration . . 150
6.4.1. Experimental details 150
6.4.2. Data analysis 152
6.4.3. Characteristics and consequences of the breathing-like behaviour 155
6.5. Resonance frequency of magnetic vortex cores 159
6.5.1. Vortex motion studied by scanning tunnelling X-ray microscopy 160
6.5.2. Vortex core motion studied by conventional Lorentz microscopy 163
6.5.3. Time-resolved electron microscopy using a delay line detector 165
6.5.4. Comparison of the methods 170
6.6. Limitations of time-resolved microscopy with a delay line detector 172
6.6.1. Temporal resolution and applicable frequency range . . . 172
6.6.2. Comparison of different approaches to achieve sub-ns temporal resolution 175
6.7. Summary 176

7. Summary and outlook 177

A. Sample fabrication 183

B. Data analysis 185
B.1. Finding unique solutions in model-based iterative reconstruction 185
B.2. Principal component analysis for noise reduction 187

B.3. Data analysis for STXM 188
B.4. Energy filter status during DLD experiments 188
B.5. Calibration of DLD images 190

Bibliography **193**

List of Figures

2.1. Magnetic fields 7
2.2. Formation of magnetic domains 10
2.3. Square and kagome ice 13
2.4. Magnetic vortex in a disk 14
2.5. Visualisation of magnetic vortex core motion described by the LLG equation 16
2.6. Spiral trajectory of a magnetic vortex core under short pulse excitation 17
2.7. Principle and practise of XMCD 20

3.1. Schematic image for TEM 26
3.2. Reconstruction process for off-axis electron holography 35
3.3. Setup for off-axis electron holography 38
3.4. Two approaches for of the electrostatic and magnetic contributions to the phase shift 41
3.5. Model-based iterative reconstruction 43
3.6. Schematic diagram for Fresnel imaging 45
3.7. Basic setups for time-resolved microscopy 48

4.1. Chiral ice - schematic diagram and magnetic induction 52
4.2. Overview images of the spin ice samples 55
4.3. Cross-section view of a 10-nm-thick nanomagnet 57
4.4. Cross section view of a 18-nm-thick nanomagnet 57
4.5. Automated detection of masks around Py particles on a SiN membrane 59
4.6. Removal of phase ramp using the MBIR approach 61
4.7. Correction of the image distortions in turned over phase images . 63
4.8. Stitching process of two perfect data sets 65
4.9. Stitching process of two perfect data sets 68
4.10. Off-axis electron hologram of as prepared spin ice 71
4.11. Electrostatic and magnetic phase image of as prepared chiral ice . 73

4.12. Histogram of the direction of the magnetic induction for as prepared artificial spin ice 74
4.13. Switching fields required to reverse magnetic state 76
4.14. Reversal of chiral ice 78
4.15. Reversal of single nanomagnet 79
4.16. Magnetic phase images of chiral ice under applied fields 80
4.17. Scheme to detect location of virtual antivortices 82
4.18. Electron hologram of 10 nm thick chiral ice 83
4.19. Magnetic and electrostatic phase shift of 10 nm thick spin ice . . . 85
4.20. Procedure used to identify position of virtual antivortices in phase images 86
4.21. Positions of virtual antivortices detected in the experimental magnetic phase image 87
4.22. Reconstruction of projected in-plane magnetisation using the MBIR approach 90
4.23. Phase shift of a single nanomagnet 91
4.24. Micromagnetic simulation of the chiral ice 91
4.25. Averaging kernel and gain maps for the chosen reconstruction parameters 93
4.26. Phase image derived from reconstructed magnetisation 94
4.27. Position of the virtual antivortices detected in the reconstructed magnetic phase image 95
4.28. Magnetic induction computed from the reconstructed magnetisation 97
4.29. Integrated magnetic induction 98
4.30. Magnetisation of simulated and reconstructed magnetisation . . . 100
4.31. Positions of virtual antivortices in chiral spin ice 101
4.32. Comparing the positions of virtual antivortices with respect to missing stray fields 103

5.1. BF image of a Py disk and their diffraction pattern 106
5.2. Cross-section of a thick Py disk 107
5.3. Influence of reference hologram on total phase 110
5.4. Electrostatic and magnetic phase shifts of a magnetic vortex in a Py disk 112
5.5. Core diameter in gradient of magnetic phase 113
5.6. Reconstructed magnetisation of a vortex state in a Py disk 114
5.7. Micromagnetic simulation of a vortex state in a Py disk 116
5.8. Vortex core diameter derived from micromagnetic simulations . . 117
5.9. Correlation between vortex core size and disk shape 118
5.10. Overview of a cross-section of a Py disk 120

5.11. HAADF STEM image and compositional map of the edge of a cross-section of a disk 120
5.12. Overview of a cross-section of a Py disk on a Si substrate 122
5.13. Magnetic phase shift of magnetic vortex in a bent disk under tilt . 123
5.14. Effect of external fields on bent Landau state 125
5.15. Vortex core displacement in dependence of applied field 126
5.16. Electrostatic and magnetic phase shifts of a cross-section of a Py disk 129

6.1. Sample for time-resolved measurements 132
6.2. Resonance spectra for vortex core dynamics 134
6.3. Resonance spectra in dependence of the saturation magnetisation 135
6.4. Schematic setup for time-resolved microscopy 136
6.5. Phase sorting for stroboscopic measurements 137
6.6. Tip of the RF magnetising holder 138
6.7. User interfaces for time-resolved experiments based on Tango . . 140
6.8. Reflections of RF magnetising holder 141
6.9. LAD diffraction on CCD camera 143
6.10. Model of the microstrip line geometry in the RF magnetising holder 145
6.11. Simulated magnetic and electrostatic field distribution in a microstrip line 147
6.12. Simulated magnetic and electrostatic fields in the magnetising holder 148
6.13. Principal component analysis 150
6.14. Locating vortex core for PCA 154
6.15. Breathing-like behaviour during vortex core gyration 154
6.16. Factors and loadings of NMF decomposition for the experiments performed at 420 MHz 156
6.17. Factors and loadings of the NMF decomposition for the experiments at 415 MHz 157
6.18. Sample geometry used for STXM measurements 161
6.19. Time-resolved STXM experiments of vortex core motion 162
6.20. Resonance frequency using time averaged images 164
6.21. Vortex core gyration imaged with the DLD 166
6.22. Correction for electron beam - magnetic field interaction 168
6.23. Velocity of the vortex core at resonance 170
6.24. Measurement of usable frequency range and temporal resolution 174

A.1. Steps in the lithography process 184
A.2. Undercut structure 184

B.1. L-curve analysis during MBIR of magnetisation 186
B.2. Application NMF to reduce noise 187

B.3. Data analysis for STXM 189
B.4. Image of a calibration sample with a periodic lattice spacing, revealing distortion of the image due to electronic issues in the imaging filter. The dark shadow shows the trajectory of the electron beam in the LAD experiments at an applied frequency of ~2 GHz (Sec. 6.6.1). 190
B.5. Core size in Fresnel defocus image 191
B.6. Calibration of scale for DLD measurements 192

List of Tables

2.1. Chiralities of magnetic vortices 15

4.1. Parameters of the chiral ice sample 54
4.2. Spatial resolution of reconstruction 92

5.1. Overview Py disks 118

6.1. Experimental setups for the investigation of breathing-like behaviour 152

Nomenclature

Acronyms / Abbreviations

Al	Aluminium
BF	Bright-field
C	Carbon
CCD	Charge-coupled device
CCW	Counter clockwise
Co	Copper
CPWG	Coplanar waveguide with ground
Cr	Chromium
CW	Clockwise
DF	Dark-field
DLD	Delay line detector
DPC	Differential phase contrast
EDX	Energy dispersive X-ray spectroscopy
EELS	Electron energy-loss spectroscopy
ER-C	Ernst Ruska-Centre
Fe	Iron
FEG	Field-emission gun
FFT	Fast Fourier transform
FOV	Field of view
FT	Fourier transform
FZJ	Forschungszentrum Jülich
GIF	Gatan imaging filter
HAADF	High-angle annular dark-field
LAD	Low-angle diffraction
LLG	Landau-Lifshitz-Gilbert
MCP	Multichannel plates
MBIR	Model-based iterative reconstruction
Ni	Nickel
NMF	Non-negative matrix factorisation

PCA	Principal component analysis
Pt	Platinum
Py	Permalloy
PSI	Paul Scherrer Institute
RF	Radio frequency
SE	Secondary electron
SEM	Scanning electron microscopy
STEM	Scanning transmission electron microscopy
STXM	Scanning transmission X-ray microscopy
TEM	Transmission electron microscopy
UTEM	Ultrafast transmission electron microscopy
VNA	Vector network analyser
WBK	Wentzel, Brillouin, Kramers
XMCD	X-ray magnetic circular dichroism

Universal constants

c	Speed of light
e	Elementary charge
h	Planck constant
$\hbar$	Reduced Planck constant
m_e	Electron rest mass
ϕ_0	Magnetic flux quantum

Roman symbols

A	Amplitude
$\mathbf{A}$	Magnetic vector potential
$\mathbf{B}$	Magnetic induction
$B_\perp$	In-plane magnetic induction
$\mathbf{E}$	Electrostatic field
E	Energy
E_{an}	Magneto-crystalline anisotropy energy
E_{ex}	Exchange energy
E_d	Dipolar energy
E_H	Zeemann energy
E_{tot}	Total energy
f	Frequency
$\mathbf{F}$	Force
$\mathbf{H}$	Magnetic field strength

$\mathbf{H_{eff}}$	Effective magnetic field strenght
$\mathbf{H_S}$	Stray fields
I	Intensity
J	Exchange constant
$\mathbf{k}$	Wave vector
k	Natural number
L	Angular moment
m	Mass
m_{RF}	RF period
$\mathbf{M}$	Magnetisation
M_s	Saturation magentisation
n	Refractive index
$\mathbf{p}$	Momentum
p_n	Phase interval
$\mathbf{q_c}$	Carrier frequency
r	Reflection coefficient
r_{rep}	Repetition rate
$\mathbf{S}$	Macrospin
t	Sample thickness
t	Time
t	Transmitted power
$\mathbf{T}$	Torque
U_b	Accelerating voltage
V	Volume
V_{el}	Electrostatic potential
$\mathbf{v}$	Velocity
w	Vortex core diameter
Z	Impedance

Greek symbols

α	Deflection angle
α_g	Phenomenological damping
β	Overlapping angle
γ	Lorentz factor
γ_g	Gyromagnetic ratio
θ	Convergence angle
μ_0	Vacuum permeability
μ_b	Bohr magneton
μ_{fc}	Fringe contrast

λ	Regularisation parameter
λ_e	Electron wave length
μ_i	Dipolar magnetic moment
τ	Time interval
τ_{exp}	Experimental temporal resolution
τ_i	Intrinsic temporal resolution
φ	Phase
φ_0	Vacuum phase shift
φ_{obj}	Object phase shift
φ_{ref}	Reference phase shift
ψ	Wave function
ψ_{obj}	Object wave function
ψ_{ref}	Reference wave function

Chapter 1.

Introduction

Magnetism and magnetic materials are omnipresent in our modern lives, with applications ranging from life science [1, 2], through energy generation/harvesting [3, 4], to information technology [5, 6]. The bit density in magnetic hard disks has increased by tens of millions during the last 50 years based on advances in data storage and processing developments [7]. Magnetic materials are remarkably attractive due to their scalability and ultrafast switching times, which can lead to high information density and the ability to manipulate them in three-dimensional structures. Nowadays, one of the main challenges in information technology is the further miniaturisation of devices without compromising their speed and fidelity, in particular with respect to thermal stability [8, 9]. In addition, efforts towards net-zero emissions[1] make more energy-efficient devices a necessity for the future [8]. One solution to these challenges is offered by the field of nanomagnetism, in particular by spintronics and magnonics [10–12]. Nanomagnetism is a discipline that deals with magnetic properties of objects and materials that have dimensions in the range from a nanometre to a few hundreds of nanometres [9, 13]. Spintronics exploits the spin degree of freedom in current in conjunction with magnetic materials, as exemplified by magnetic racetrack memories [14–16]. Magnonics refers to collective excitations of the electron spin structure and offers the prospect of magnon-based transistors that operate with nearly vanishing energy losses [17–19].

In the context of nanomagnetism, artificial spin ice (ASI) has received considerable interest due to the emergence of interesting phenomena including magnetic monopoles [20, 21], phase transitions [22, 23] and chiral dynamics [24, 25]. ASI is a metamaterial that comprises interacting single domain ferromagnets arranged

[1] International Energy Agency (2021, June 21). Net Zero by 2050 - A Roadmap for the Global Energy Sector. Retrieved from `https://iea.blob.core.windows.net/assets/4482cac7-edd6-4c03-b6a2-8e79792d16d9/NetZeroby2050-ARoadmapfortheGlobalEnergySector.pdf`

in an ordered fashion, thereby resulting in frustration by design [26, 27]. Modern nanofabrication methods allow versatile structures to be patterned that are not limited to common two-dimensional arrays of elongated magnets, but can be complex lattices or magnets of any shape [27, 28]. The magnetic state of an ASI can be controlled using external stimuli, such as magnetic fields [29], electric fields [30] and temperature gradients [31]. Based on the specific spin wave resonances of different magnetic configurations, an ASI is a promising candidate for re-programmable magnonic crystals [32, 33]. Within the ASI family, the chiral ice structure is of particular interest as a unidirectional rotation of its net magnetisation has been observed during thermal relaxation giving, rise to ratchet-like behaviour [24]. Micromagnetic simulations suggest that this observation is driven by the stray fields at the edges of the chiral ice pattern, which give rise to the formation of emergent virtual antivortices [24]. Hence, the analysis of such stray fields is essential for understanding the physical properties of chiral ice. However, the direct measurement of the in-plane stray field distribution around the constituent magnets is not simple to study and many unresolved issues remain to be answered. Experimental techniques such as superconducting quantum interference device (SQUID) magnetometry, magnetic force microscopy (MFM), magneto-optic Kerr effect (MOKE) microscopy and X-ray magnetic circular dichroism (XMCD) lack the possibility of quantitative measurements, do not provide access to stray fields or their spatial resolution is not sufficient [25, 34–36].

Another magnetic phenomenon that has been at the forefront of research studies for many years is the magnetic vortex [37–39]. It possesses two binary properties: circulation, which is the rotation of the in-plane component of the magnetisation and core polarity, which is the direction of the core relative to the plane of the vortex [9, 13]. In the context of magnetisation dynamics, vortices are particularly interesting due to their stability to large field perturbations, reproducibility and lack of stray fields [40, 41]. They offer a rich playground for tuning properties such as vortex core location, size, shape and polarity, as well as the associated eigenfrequencies of motion, which can be modified by stimuli such as applied magnetic fields [9, 13, 40]. However, access to studies of the dynamic properties of magnetic vortices requires picosecond temporal resolution accompanied by high spatial resolution (<100 nm), which is only partially available in specialised techniques such as Brillouin light scattering (BLS) [42, 43], scanning electron microscopy with polarisation analysis (SEMPA) [44] and scanning transmission X-ray microscopy (STXM) [45, 46]. These techniques are often compromised in least one of the following respects: temporal resolution, spatial resolution or compatibility with respect to structural or compositional measurements.

Transmission electron microscopy (TEM) is an ideal candidate technique for the analysis of chiral ice and magnetic vortices as it is able to meet the requirements for static and for dynamic measurements and avoids some of the drawbacks of other techniques. In TEM, interaction of the probing electrons with the material and its properties is employed to gather information about structure, electronic properties, chemical composition, morphology and electromagnetic fields with high spatial resolution [47–49]. In addition, external stimuli can be applied to samples using electric currents, temperature gradients, magnetic fields, strain, and photonic excitation [47, 49]. These properties make TEM one of the most versatile techniques in the fields of physics, chemistry, materials science and structural biology.

TEM offers several different methods to study the magnetic states and field distributions of electron-transparent samples, including differential phase contrast (DPC) imaging [50, 51], Fresnel and Foucault imaging [52] and electron holography [53, 54]. In conventional TEM, phase information about the electron wave that passed through the sample and interacted with any associated electromagnetic fields is usually lost during the recording of an image. Electron holography allows phase information to be recovered by making use of the interference of an object wave with a reference wave [53, 54]. The concept of electron holography was introduced by Dennis Gabor in 1948, with the original aim to overcome the spherical aberration that limits resolution in TEM [55, 56]. Gottfried Möllenstedt developed the electron biprism, a device that can be used to achieve the superposition of two parts of an electron wave in TEM [57]. This development facilitated the use of off-axis electron holography for the quantitative measurement of phase shift variations with high spatial resolution. Off-axis electron holography has been used successfully to map the magnetic induction field in a wide variety of magnetic samples. The technique has benefited substantially from further improvements in electron microscopy, including the introduction of electron sources with high spatial coherence [58], hardware aberration correction [59] and improvements in digital detectors [60]. Recent advances in data analysis have allowed intrinsic properties such as magnetisation and charge density to be recovered from experimentally measured phase images by using model-based iterative reconstruction (MBIR) [61, 62]. These possibilities mean that off-axis electron holography is well suited for the investigation of artificial spin ice and its stray field distribution. In order to study magnetisation dynamics in TEM, time-resolved Fresnel imaging is usually employed, based on recording defocused images [63]. By using a laser system to trigger the generation of electrons in so-called ultrafast TEM (UTEM), a temporal resolution of a few hundred femtoseconds can be achieved [64–67]. However, UTEM requires modifications

to the microscope, which limits its application to specialised instruments. This drawback can be overcome by employing a delay line detector (DLD), which assigns a time stamp to every incoming particle resulting in a three-dimensional data set that includes time [68, 69]. In principle, a DLD can be mounted on any electron microscope to improve its temporal resolution to the picosecond range. Although the technical requirements are not demanding, the DLD has rarely been used in electron microscopy.

The aims of this thesis are to gain an understanding of the magnetic states and stray field distributions of magnetic nanostructures and to improve the methodology to study them quantitatively with high spatial resolution and improved temporal resolution. Experimental measurements of the structure, chemical composition and field distribution of a chiral ice sample made from soft magnetic permalloy islands (Py, nickel (Ni) iron (Fe) alloy, $Ni_{1-x}Fe_x$ with x about 0.2) were performed using various TEM methods. These studies allowed these different properties to be correlated with each other. A methodology for the quantitative measurement of the three-dimensional magnetic induction fields of the magnets was developed, based on electron holography measurements of the phase shift and reconstruction of the magnetisation using MBIR. The locations and distributions of virtual antivortices were mapped with high precision, thereby providing a better understanding of the origin of the ratchet-like behaviour in this system. The static properties of magnetic vortices in a Py nanodisk were studied using Fresnel imaging. Special attention was paid to the implications of shape deviations of the nanodisk on magnetic states observed in different applied fields. Dynamic properties were investigated by employing high frequency excitation of the vortex core and imaged successfully with a DLD. The resonance behaviour of the vortex core was investigated and compared with results based on both STXM and more conventional TEM methods. The advantages and disadvantages of using a combination of a DLD with TEM were assessed, with respect to feasibility, temporal resolution and applicable frequency range in order to present prospects for its future applications to studies of magnetisation dynamics.

This thesis is divided into the following sections: An extensive review is given on magnetism and applied experimental techniques in Chapters 2 and 3. Chapter 4 describes the experimental methodology and presents new results on the chiral ice and virtual antivortices. Static properties of the magnetic vortex state are presented in Chapter 5. Time-resolved studies of the vortex state are presented in Chapter 6. The thesis concludes with a summary and outlook in Chapter 7.

Chapter 2.

Magnetism of nanoscale objects

This chapter describes the basic principles of the magnetism of nanoscale objects. It starts with a short overview of magnetism in general, before focusing on micromagnetism. Particular focus is placed on the systems studied in the thesis: artifical spin ice and magnetic vortices. In the case of the magnetic vortices, their static and dynamic properties are discussed in detail. In the last section, the STXM technique which provides access to the static and dynamic magnetic properties of various sample systems is introduced.

2.1. General magnetic concepts

A basic quantity in magnetism is the magnetic dipolar moment $\boldsymbol{\mu}$, which defines the magnetic properties of a material. The magnetic moment, in turn, depends on the spin angular momentum and orbital angular momentum of each electron on the atomic scale. The spin angular momentum is based on the spin of an electron only being able to align itself in two possible orientations with respect to an applied magnetic field: the spin can point either up or down in a vertical magnetic field. The orbital angular momentum results from the orbital motion of an electron around the nucleus. The intrinsic magnetic moment of an electron is given by the Bohr magneton $\mu_B = \frac{e\hbar}{2m_e}$ and can be derived classically based on the current induced by the electron on a circular trajectory. In this relation, e is the electron charge, $\hbar$ is the reduced Planck constant and m_e is the electron rest mass.

In order to describe the magnetic properties of a sample on a macroscopic scale, three vector fields are defined: the magnetisation **M**, the magnetic induction **B**

and the magnetic field strength **H**. These three fields are connected to each other by the relation

$$\mathbf{B} = \mu_0(\mathbf{H} + \mathbf{M}), \tag{2.1}$$

where, μ_0 is the permeability in vacuum. The three fields and their relation are sketched in Fig. 2.1. The magnetisation of a material results from the net magnetic moments and can be defined, on a macroscopic scale, by the sum of the magnetic moments over their volume V: $\mathbf{M} = \sum_i \frac{\mu_i}{V}$. Thus, it is only present inside the magnetic material. The highest possible magnetisation of a material is its saturation magnetisation M_S. The magnetisation is an intrinsic material property, as it depends on the magnetic moment. Nevertheless, magnetic induction is often referred to as magnetism in colloquial language. Magnetic field lines associated with magnetic induction have to be closed, *i.e.* the lines have to form continuous loops. In contrast, the magnetic field strength has sources and sinks due to discontinuities in the magnetisation. In small objects, the surfaces often act as discontinuities. One can consider that magnetic charges accumulate at the discontinuities and define **H**, similar to electric charges defining the electric field **E**. In contrast to electric charges, magnetic charges only appear in pairs and magnetic monopoles have never been observed. **H** is affected by the magnetic material of the sample, as well as by all of the magnetic material surrounding it. It can be split into two parts: demagnetising fields inside the material and stray fields outside it. These fields oppose on another. In addition to Eq. 2.1, there is another convention in use: $\mathbf{B} = \mu_0\mathbf{H} + \mathbf{M}$ [70]. It should be noted that these difference in convention is associated with a change of units. The former convention is used with the SI units, with the magnetisation measured in $\frac{\mathrm{A}}{\mathrm{m}}$. In the latter convention, the magnetic induction and magnetisation both have units of T.

In general, there are four categories that a material can be classified into based on its magnetic properties: diamagnetism, paramagnetism, ferromagnetism and antiferromagnetism. Dia- and paramagnetic materials only exhibit magnetic fields in the presence of external fields, whereas ferro- and antiferromagnetism are also present without external fields. For ferromagnets, the Curie-Weiss law describes the temperature dependence of the magnetisation: the net magnetisation decreases with increasing temperature. Above the Curie temperature, magnetic ordering of the ferromagnet is suppressed by thermal fluctuations and the material becomes paramagnetic. Such thermal fluctuations can also affect antiferromagnets, which lose their magnetic order above the Néel temperature. The samples studied in this thesis all belong to the class of ferromagnets.

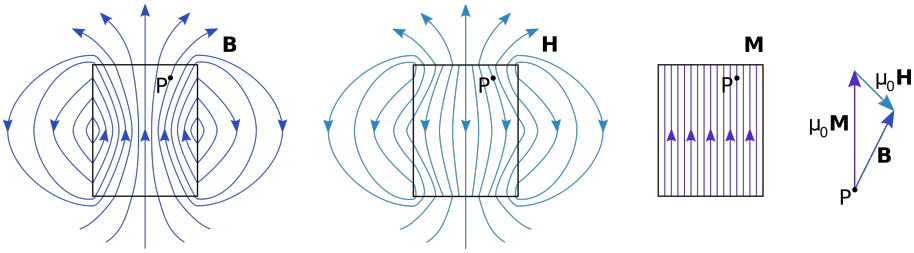

Figure 2.1.: The magnetic properties of a sample are described by three macroscopic fields: the magnetic induction **B**, the magnetic field strength **H** and the magnetisation **M**. The three fields are related by Eq. 2.1. The magnetisation arises due to the magnetic moments in the material and is only defined inside the material. The magnetic field strength is associated with magnetic charges accumulating on the surface. Inside the material, the magnetic field strength reduces the total magnetic moment and is referred to as demagnetisation field. Outside the material, it is referred to as stray field. The magnetic induction is equal to the stray field outside the material. The relation between the different fields is shown for the example of point P.

2.2. Basis of micromagnetism

Mirco- and nanoscale magnetic systems differ in several ways from their macroscopic counterparts. Different magnetic properties can have various origins: in nanoscale systems the effects of surfaces are more prominent than in bulk samples, as the surfaces break translational symmetry. Moreover, the sizes of the systems can become comparable to fundamental length scales governing magnetic states. In order to understand the magnetic properties of such systems, it is convenient to describe them in terms of energy minimisation, for example by looking at a mesoscopic length scale where the effect of the atomic structure can be neglected. Here, it is assumed that the magnitude of the magnetisation stays constant, while its direction changes. The four energy terms that dominate most nanoscale magnetic systems are the exchange energy E_{ex}, the magneto-crystalline anisotropy energy E_{an}, the Zeeman energy E_H and the dipolar energy E_d:

$$E_{tot} = E_{ex} + E_{an} + E_H + E_d. \tag{2.2}$$

In this thesis, a short introduction to the basis of micromagnetism is given. Further details can be found in [9, 13].

Spontaneous magnetisation in ferromagnets is governed by the exchange inter-

action. Even though it is very powerful, the exchange interaction decays quickly. Hence, it only has strong effects on a short range. It results from the coupling of the magnetic moments of single electrons and can be described in terms of the macrospin $\mathbf{S}$ of each atom: $E_{ex} = -J(\mathbf{S_1} \cdot \mathbf{S_2})$. The parameter J is a material-specific coupling. When J is positive, the exchange energy is minimised when the magnetic moments align parallel to each other resulting in macroscopic magnetisation. This case corresponds to ferromagnetic order. Antiferromagnetic materials have a negative J and the magnetic moments align antiparallel to each other, in order to minimise the exchange energy. Hence, there are no magnetic fields present outside the material.

The magneto-crystalline anisotropy energy is based on the interaction of the spin with the electron orbitals, which have preferential directions due to the crystal lattice. Thus, the magnetisation has a preferred direction. This energy term is minimised if the magnetic moments are aligned along the preferential direction of the crystal, which is referred to as the magnetic easy axis. In contrast, the energy is maximised if the magnetic moments are aligned along the hard axis. In polycrystalline materials, this effect is suppressed by the presence of grain boundaries. Depending on the strength of the magneto-crystalline anisotropy, different types of magnets can be defined: soft and hard magnets. Soft magnetic materials are characterised by weak magneto-crystalline anisotropy and the material can be magnetised and demagnetised more easily. Py is a prominent example of this type of material, in part due to its polycrystalline structure [13]. Hard magnetic materials do not change their magnetic state easily. Prominent examples are alloys based on samarium-cobalt and neodymium-iron-boron magnets [3].

The Zeeman energy describes the interaction of the magnetic moments with an external magnetic field. It is minimised when the magnetic moments inside the sample are aligned parallel to an external magnetic field. It can be visualised in terms of an accumulation of magnetic charges at the surface forming to exclude the external magnetic field. In contrast to electric charges in an external electric field, this exclusion is not complete, as the saturation magnetisation is finite. In soft ferromagnets, the Zeeman energy dominates magnetic interactions when an external magnetic field results in parallel alignment of the magnetisation with the external field.

The dipolar energy is sometimes referred to as the demagnetisation energy, stray field energy or magnetostatic energy. It results from the interaction of the magnetic moments with the magnetic field strength that the magnetic material induces itself and is heavily influenced by boundary conditions for finite structures.

Therefore, shape anisotropy also has to be included. Shape anisotropy arises if the magnetic state favours a specific configuration due to shape constraints.

If all of the magnetic moments are aligned, then the material is in a single domain state, which is visualised in Fig. 2.2a. This state minimises exchange energy at the cost of increasing other energy terms, *e.g.*, due to the resulting strong stray fields. These other energy terms can be reduced by dividing the magnetic material into domains (Fig 2.2b). The magnetic moments in each domain are aligned to a first approximation, but individual domains can have different directions. Domains in small samples that are made from a material with low magneto-crystalline anisotropy tend to orient themselves parallel to the surfaces of the sample. The sample size that is required to form a multidomain state depends on several properties, including the material and shape of the sample. Domain walls form at the borders of the domains. Competition between exchange and anisotropy energy results in a finite domain wall size. One consequence of the formation of magnetic domains is that not all materials possess magnetic fields that can be measured, even though the constitute elements are magnetic. The application of an external magnetic fields results in an alignment of the magnetic moments as the Zeeman energy is minimised. Several domains may then merge to form larger domains. This alignment is removed when the material is heated due to the thermal motion of the atoms and domains may then form again. The dipolar energy can be reduced by minimising the formation of discontinuities of the magnetic fields. Closure domains may therefore form, where the magnetic moments follow closed loops parallel to the surface of the sample, as shown in Fig. 2.2c. Such closed loops can be formed by several domains effectively working as one macrospin, or by magnetic moments within a single domain. When they are formed by several domains separated by domain walls, they may form a called Landau state [71], while magnetic vortices may result for the single domain case [9].

Even in a single domain that is not in a closure state, the magnetic moments are usually not aligned perfectly, but may be canted. This canting can be induced, for example, by shape or crystallographic variations of the material or impurities. Even in perfect materials, such canting may be present because the stray field of each magnetic moment depends on its position within the material. For example, the magnetic moments may follow a C or S-shape. If a single domain is small enough, superparamagnetic switching may arise. Here, thermal motion is sufficient to overcome the energy barrier for flipping the macrospin of the domain even at room temperature. The magnetisation of the domain may then change over time in a random manner. The material will appear to be non-magnetic as long as the measurement time is longer than the switching time.

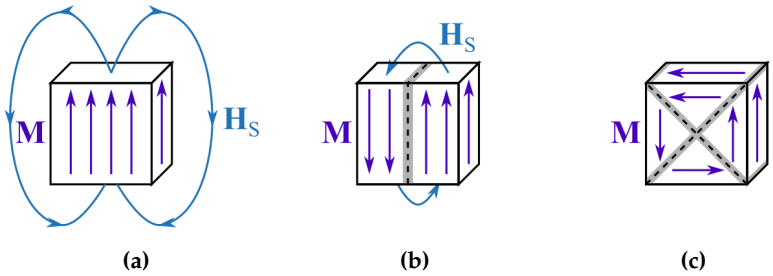

Figure 2.2.: Formation of magnetic domains. (a) Single domain state of the magnetisation **M** with large stray fields $\mathbf{H_S}$ (b) Formation of two domains, reducing the stray fields. The domains are separated by a domain wall of finite size (grey region). (c) Flux closure minimising the stray fields.

The dependence of domain structure on material size is exemplified by considering a sphere. Its magnetic properties depend strongly on its diameter, as there are typically two different magnetic ground states for a hard magnetic material and three for a soft one. These different states are a result of balancing the four energy terms. Small particles are typically in a single domain state. Furthermore, they are in the superparamagnetic switching regime if the particle is sufficiently small. In contrast, several domains are formed if the diameter is large enough. Soft magnetic materials exhibit an intermediate state for diameters in the regime between single and multi domain states corresponding to a closure domain. Here, the magnetic moments curl to form a vortex state. A magnetic vortex in a Py disk will be discussed in more detail in Sec. 2.4.1. The example of a sphere illustrates that the magnetic properties of a system can be adjusted by designing specific nanostructures. This freedom of design is utilised in complex structures such as artificial spin ice.

2.3. Artificial spin ice

In the previous section, the focus was on the magnetic properties of a single object or particle. The addition of more particles that can interact allows for a variety of other phenomena, one of which is magnetic frustration. Frustration is a ubiquitous phenomenon in systems that range from neural networks to structural glasses and is not limited to magnetic nanostructures [26]. In simplified terms, frustration is the inability of a system to satisfy all competing interactions simultaneously. This inability can lead to complex structures, which are associated

with large degeneracy at low temperature and disorder. New and interesting physical phenomena may arise from frustration, such as emergent magnetic monopoles [27,72–74]. Frustration can result from, *e.g.*, intrinsic structural disorder in a spin glass or a regular geometry with carefully balanced interactions in artificial spin ice [75]. The latter system is inspired by water ice and is explained in detail in this section.

The most common and ordinary example of frustration is present in water ice. In water ice, each oxygen atom is covalently bonded to two hydrogen atoms. Furthermore, each oxygen atom is bonded to four surrounding oxygen atoms *via* one hydrogen atom each. The two covalently bonded hydrogen atoms are located closer to the oxygen atom than the hydrogen atoms that are covalently bonded to the neighbouring oxygen atoms. In other words, every oxygen atom is bonded to four hydrogen atoms and has two strong and two weak bonds, forming a periodic lattice. This behaviour is referred to as the ice rule and was first described by Bernal and Fowler in 1933 [76]. Frustration arises as the bonds have different strengths and the hydrogen atoms are not located in central positions. Pauling applied the ice rule to explain the residual entropy of water at zero temperature [77].

The study of geometrically frustrated magnetic systems started in 1997 with the discovery of such behaviour in rare earth pyrochlore structures by Harris et al. [78]. In these systems, magnetic ions form a lattice of corner-sharing tetrahedra. Each ion has a large magnetic moment and can be considered as a classical, binary Ising spin. The crystal field enforces a configuration where the two spins point towards the centre and two away from it (two in, two out) in the lowest energy state, effectively minimising the spin-spin interaction. This configuration corresponds to the ice rule. The lowest energy state can be achieved by six different configurations. Thus, the system is degenerate. Nevertheless, the experimental study of geometric frustration in these systems is not straightforward, since it is challenging to image the atomic spins directly.

A solution to the issue of experimental studies is to use a model system with submicron-sized magnetic islands called artificial spin ice. Artificial spin ice describes a class of metamaterials that consists of interacting nanomagnets arranged in specific geometries. The geometry is chosen in such a way that it leads to geometric frustration by design. The most common systems are two-dimensional arrays fabricated by electron-beam lithography [75]. The constituent nanomagnets typically each have a thickness of a few tens of nanometres and lateral dimensions of approximately 500 nm [75]. The nanomagnets are often shaped as long ellipses, in such a way that they form a single domain and suppress

thermal fluctuations at room temperature. In most studies, the nanomagnets are made of Py, which has nearly no magneto-crystalline anisotropy, making shape anisotropy dominant [26]. Hence, the magnetisation of a nanomagnet is aligned with the long axis, giving rise to a large, Ising-like macrospin with two antiparallel states and almost classical behaviour. If the nanomagnets are placed in close proximity, then dipolar coupling will result in an influence of the nanomagnets on each other. Consequently, the nanomagnets form an interacting many-body spin system, with effects such as collective switching [27]. Besides the analogy the ice rule in particle-based ice and specific designed artificial spin ice systems, the frustration and energies are fundamentally different and the analogy does not always hold for more complex geometries. More details can be found in reviews on artificial spin ice [27,28,73,75].

Frustration in artificial spin ice arises from competition between dipolar coupling of the nanomagnets, which cannot be satisfied simultaneously due to spatial constraints. For example, a system can be considered in which four nanomagnets intersect at their ends. This intersection is referred to as a vertex. The topological charge is the difference between the macrospins pointing towards the vertex and away from it. The lowest energy state corresponds to a minimisation of topological charges which is often enforced by nearest neighbour spin interactions. All configurations that lead to the lowest energy state are said to obey the spin ice rule. Lattices of nanomagnets with an even coordination number, *i.e.* an even number of intersecting nanomagnets, will prefer to have zero topological charge at each vertex. Square ice is a common example of this class of artificial spin ice and is shown in Fig. 2.3a. Here, four nanomagnets intersect at an angle of 90°. According to the spin ice rule, two macrospins point towards the centre of the vertex and two away from it in the ground state, since the dipolar interaction prefers a head-to-tail alignment at each vertex. This configuration can be achieved by six different arrangements of the spins. It has been found that that 70% of the vertices obey the ice rule [26]. However, the distance between all nanomagnets at the vertices is not the same as the spacing between nanomagnets in a row is larger than between those with a 90° angle. This imbalance results in different strengths of the dipolar interaction, partly lifting the degeneracy of the ground state. This uneven particle spacing is absent in the kagome lattice. Here, three nanomagnets intersect at each vertex, mimicking a honeycomb structure, as shown in Fig. 2.3b. Therefore, every vertex has a coordination number of ±1 in the ground state. Here, the interaction between the three nanomagnets is equal.

An advantage of artificial spin ice, in addition to its macroscopic size, is that it can mimic the behaviour of rare earth pyrochlores at a specific temperature and

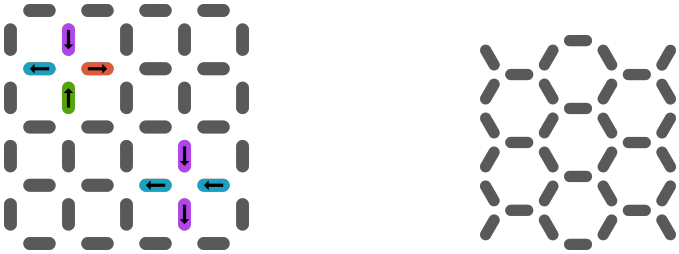

(a) (b)

Figure 2.3.: Spin ice lattices consisting of single domain ferromagnets. Two common examples are (a) square ice and (b) kagome ice. The coloured nanomagnets in (a) represent two possible configurations for the ground state obeying the ice rule.

field [73]. Its degrees of freedom are tuneable and individually observable, in contrast to a continuous thin film [73]. A manifold of magnetic configurations can be achieved by interactions between the nanomagnets and their response to an external field, depending on the specific design. The thermal barrier and mesoscopic size of artificial spin ice allows for characterisation using standard microscopy techniques, such as magnetic force microscopy, Lorentz microscopy and X-ray based techniques that include photoemission electron microscopy [74]. One of the most famous discoveries is that of emergent magnetic monopoles [72,79]. Magnetic monopoles constitute a violation of the spin ice rule and and can be thought of as an alternation of the underlying order, rather than disorder. In addition to static characterisation, artificial spin ice displays non-trivial avalanche dynamics, with typical resonant frequencies in the few GHz regime [27, 28, 74]. Its high-frequency dynamics make it a promising candidate for programmable magnonic crystals with a defined band structure [27, 28, 74]. In the future, a combination of improved fabrication and characterisation techniques with new geometries and materials may result in applications in computation, data storage, encryption and reconfigurable microwave circuits [27, 28, 32, 33]. This progress may meet the demand for faster, smaller, and more efficient devices.

2.4. Magnetic vortex state

The magnetic vortex state was introduced in Sec. 2.2. Its the static and dynamic properties are now discussed in more detail.

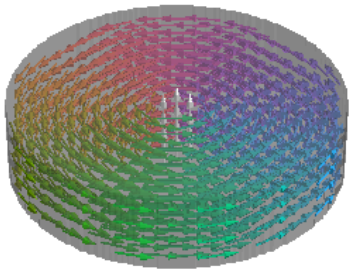

Figure 2.4.: Magnetic vortex supported in a disk. The in-plane component rotates following the disk's shape. The vortex core points out of the plane, as depicted by white arrows at the centre of the disk. Adapted from [82]

2.4.1. Description of a static magnetic vortex state

A magnetic vortex is the magnetic ground state for a disk with radius is sufficiently larger than its thickness, while its overall dimensions are small enough, *i.e.*, typically radii up to several hundreds of nanometres for soft magnetic materials [80]. A schematic diagram of a magnetic vortex in a disk is shown in Fig. 2.4. In a thin structure, the stray field and thus the dipolar energy is decreased by aligning the magnetisation parallel to the surface. In-plane alignment leads to rotation of the magnetisation within a disk. The sense of rotation is described by the circulation, which can be either clockwise or counterclockwise. At the centre, a singularity would be produced by the rotation, leading to large exchange energy, such a singularity is avoided by canting the magnetic moments along the cylinder axis, thereby allowing parallel alignment of the moments to form a vortex core. The polarity is the direction of the vortex core and is either parallel or antiparallel to the cylinder axis. Both the circulation and the polarity are binary properties, which together define the chirality of the vortex. The possible combinations of circulation and polarity are summarised in Table 2.1. As a result of its magnetic structure, a magnetic vortex has little stray field and is magnetically stable due to minimisation of the dipolar and exchange energy. These two properties, combined with the possibility to fabricate disks using lithographical processes, make vortices a promising candidate for a number of applications, such as ultra-high density recording media, miniature magnetic field sensors and spintronic logic devices [81].

When an in-plane magnetic field is applied to a disk that supports a magnetic vortex state, the vortex core is shifted perpendicular to the external magnetic field, in order to increase the number of magnetic moments aligned with the

Table 2.1.: The chirality of a vortex is described by the two binary properties polarity and circulation. CW is used for clockwise rotation of the in-plane magnetisation and CCW for counterclockwise rotation.

Polarity	Circulation
+1 (up)	−1 (CW)
+1 (up)	+1 (CCW)
−1 (down)	−1 (CW)
−1 (down)	+1 (CCW)

external magnetic fields. The symmetry of the vortex is then broken. If the external magnetic field is sufficiently large, the vortex core will be annihilated and the disk will be uniformly magnetised. When applying an out-of-plane field, the magnetic moments will also prefer to align parallel to the applied field. The direction of the field with respect to the polarity now has a major effect. If the polarity and the external field are parallel, then the vortex core will increase in size. In case of an antiparallel field, the vortex core may switch its polarity if the strength of the applied field is sufficient.

Magnetic vortices have similar resonance properties to Landau states. However, a Landau state possesses domain walls, in contrast to a domain-wall-free vortex. The presence of domain walls can affect the response of the vortex to external stimuli [83]. Disk-like samples are chosen in the presented work, in order to study their magnetic vortex core dynamics.

2.4.2. Magnetic vortex core dynamics

Magnetic vortex core motion can be induced by displacing the core from its equilibrium position and allowing the magnetic state to relax or by further displacing it in a different direction. Displacement of the vortex core can, for example, be achieved by applying an external magnetic field or driving a current through the disk. The vortex core motion can be described using the phenomenological Landau–Lifshitz–Gilbert (LLG) equation. The LLG equation is not limited to vortex core dynamics, but can also be used to study dynamic states, *e.g.*, spin waves in ferromagnets. Considering an average over the volume of an object, the magnetic torque $\mathbf{T}$ acting on the object can be expressed in the form $\mathbf{T} = \mathbf{M} \times \mathbf{H}_{\mathbf{eff}}$. The effective field $\mathbf{H}_{\mathbf{eff}}$ is a combination of the externally applied field and the demagnetisation field of the object itself. The magnetic torque can also be related to the change in angular momentum $\mathbf{L}$ *via* $\mathbf{T} = \frac{d\mathbf{L}}{dt}$. By using the gyromagnetic ratio

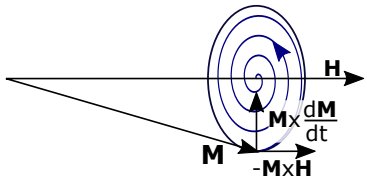

Figure 2.5.: Visualisation of magnetic vortex core motion described by the LLG equation. The spiral trajectory of the magnetisation results from precession and a damping term.

γ_g with $\mathbf{M} = -\gamma_g \mathbf{L}$, the undamped motion of the magnetisation can be derived using the expression $\frac{d\mathbf{M}}{dt} = -\gamma_g \mathbf{M} \times \mathbf{H}_{\mathbf{eff}}$. This equation describes the precession of the magnetisation around the effective field. In order to take damping into account, a phenomenological term is typically added, in order to describe the relaxation of the magnetisation towards the effective field in the form:

$$\frac{d\mathbf{M}}{dt} = -\gamma_g \mathbf{M} \times \mathbf{H}_{\text{eff}} + \frac{\alpha_g}{M_S} \mathbf{M} \times \frac{d\mathbf{M}}{dt}, \tag{2.3}$$

where the standard damping constant is α_g [84]. The magnetisation vector then follows a spiral-like trajectory about the effective external magnetic field, as shown in Fig. 2.5.

When displacing the vortex core by applying a stimulus of limited duration, the vortex core starts to move along a circular trajectory in a perfect material without damping, *i.e.*, in the absence of defects, such that the stimulus does not corrupt the vortex state. The resonance frequency of the motion is linearly dependent on the aspect ratio, given by the thickness of the disk divided by its radius for aspect ratios well below 1 [85]. Therefore, the resonance frequency can be increased by increasing the thickness or decreasing the radius of the disk. Typical resonance frequencies for vortex core gyration are below 1 GHz for disks where thickness is much smaller than their diameter [86].

The resonance of a vortex core in response to an external stimulus can be divided into two phases: linear acceleration of the vortex during the stimulus and gyroscopic rotation afterwards [87]. The resulting motion can be explained in a hand-waving manner for the model system of a Landau state. Consider a vortex that has clockwise circulation and a vortex core pointing up, *i.e.*, a left-handed vortex (Fig. 2.6a). When the field is first applied, precession of the vortex core dominates over damping in the field direction (*cf.* Eq. 2.3) during the first

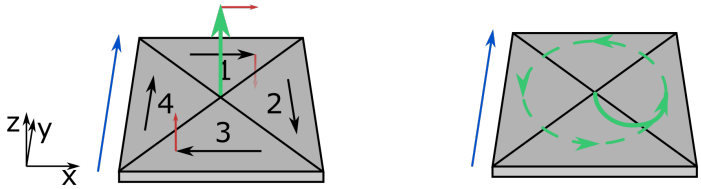

Figure 2.6.: Spiral trajectory of a magnetic vortex core in a sample that supports the Landau state under excitation by an external magnetic field. (a) The orientation of the magnetic domains is depicted by black arrows. The green arrow corresponds to the orientation of the vortex core and the blue arrow to the external magnetic field. The red arrows indicate the direction of the torque acting on the two domain perpendicular to the external magnetic field and the vortex core. (b) The green solid line shows the spiral trajectory of the vortex at the beginning of the excitation. The dashed line symbolises the trajectory under resonant microwave excitation. Adapted from Ref. [87]

sub-nanosecond time frame. Therefore, the vortex core experiences a torque in the direction of the magnetic moments in domain 1. The magnetic moments in domain 1 experience a torque downwards in -z direction, *i.e.* antiparallel to the vortex core and in domain 3 upwards in +z direction, *i.e.* parallel to the vortex core. The torque results in antiparallel motion of the magnetic vortex core with respect to the applied field. After initial precession, alignment of all domains parallel to the external field dominates the motion of the vortex core. Therefore, the domain 4 increases in size while domain 2 decreases resulting in a shift of the vortex core towards the right, perpendicular to the applied field. This combination of fast downward motion and slower motion towards the right results in a spiral trajectory of the vortex core (see solid line in Fig. 2.6b). In total, the sense of the rotation of the vortex core depends not only on the circulation of the vortex, but also on its chirality. During continuous excitation of the vortex core with a microwave magnetic field, the vortex core motion may reach a stable, circular trajectory (see dashed line in Fig. 2.6b). The radius of the trajectory is maximised if the driving frequency is equivalent to the eigenfrequency of the sample. The sample is then said to be in resonance.

A magnetic vortex core can be switched statically by applying an out-of-plane magnetic field. Large fields are typically required, as a vortex core is magnetically very stable. However, smaller in-plane magnetic fields can also be employed to achieve switching. Here, the change in direction of an in-plane field at microwave frequencies is exploited. Fast motion of the magnetic moments then results in the

creation of a vortex-antivortex pair if the excitation is strong enough [88]. The vortex has an opposite polarity to the original core and the antivortex annihilates with the original vortex leaving, the newly-created vortex behind. In a sub-micron-sized disk, the entire process can take as little as 50 ps when using a pulse of 100 ps and an 80 mT field strength [89]. Therefore, only small pulses are required to inverse the polarity of the vortex core. This inversion of the polarity results in an inversion of the direction of motion of the vortex gyration, which would have negative effects on stroboscopic experiments studying the vortex core gyration. There, the vortex core gyration is required to not vary over several cycles (*cf.* Sec. 3.4). Therefore, the applied fields have to be smaller than the threshold required for switching the polarity.

The literature contains several reports of experiments and theoretical work on magnetic vortex core dynamics [40, 63, 81, 83, 85–87]. For example, Choe et al. demonstrated that the polarisation of a magnetic vortex core affects its sense of rotation using photoemission electron microscopy [87]. Guslienko et al. used micromagnetic simulations to show that the eigenfrequency of vortex excitations states scales linearly with the aspect ratio of disk thickness relative to its radius for aspect ratios that are much smaller than 1 [85]. Such a linear dependency was also suggested by Novosad et al. based on an analytical theory and micromagnetic simulation in support of experimental results [81]. They investigated up to 40-nm-thin Py disks with diameters of 1 or 2 μm on a coplanar waveguide using a vector network analyser [81]. Pollard et al. were the first to demonstrate vortex core dynamics excited by magnetic stimuli and imaged inside a TEM [63]. They drove a current through a micrometer-sized square magnetic element and used the radius of the vortex core gyration to determine the non-adiabatic spin torque [63].

2.5. Measurement magnetisation dynamics employing X-rays

Magnetic properties of nanoscale objects can be imaged using scanning X-ray transmission microscopy (STXM), where the absorption of photon penetrating the sample is imaged for each position while scanning the sample. Both, the shape and the elemental composition of the sample can be measured, as the absorption of the X-rays is element-specific. In a synchroton, X-rays are generated by accelerating electrons close to the speed of light on a circular orbit. Undulators, which comprise magnets of alternating polarity, force the electrons on a

slalom course, thereby producing X-rays that have discreet wavelengths. The X-rays are focused to a spot by using a Fresnel zone plate and an order-selecting aperture. The sample is positioned in the focal plane and moved to record two-dimensional information. The complete measurement setup is in vacuum to prevent interaction between the X-rays and molecules in the air.

In order to obtain magnetic information, STXM employs X-ray magnetic circular dichroism (XMCD) as a contrast mechanism. XMCD was pioneered by Gisela Schütz and co-workers in 1987 [90]. XMCD allows the band structure of elements to be probed by light. For the ferromagnets Fe, cobalt (Co) and Ni, the 3d states carry most of the magnetic moments, as minimisation of the exchange energy resulting from parallel alignment of the spins outweighs the increase in kinetic energy. The imbalance of up and down spins in this band can be measured using circularly-polarised light, for which the absorption cross section is proportional to the transition probability of the photoelectrons from their initial to their final state. Due to the imbalance, the absorption cross section for left and right polarised light differs. For example, the absorption of left circularly polarised light is stronger than the absorption of right circularly polarised light at the L_3 edge when the magnetisation is parallel to the direction of motion of the photons. This process is shown schematically in Fig. 2.7a. In this example, the magnetisation and the direction of motion of the photons are directed downwards[1]. The splitting of the *d* band is shown for the extreme case that the density of states for spin up electrons is shifted completely below the Fermi level. Thus, only the excitation of spin down photoelectrons is allowed. The probability to excite those at the L_3 edge is higher for left polarised light than for right polarised light. Therefore, left polarised light is absorbed more strongly. For the L_2 edge, the probability to excite spin down photoelectrons is higher for right polarised light than for left polarised light. Since XMCD depends on the band structure, measurements of magnetisation is element specific. Nevertheless, only the out-of-plane magnetisation can be measured because the photons are only sensitive to magnetic moments that are parallel or antiparallel.

In order to visualise the direction of the out-of-plane magnetisation in the sample, the band structure is probed at a specific energy, *e.g.*, at the L_3 or the L_2 edge. First, the absorption is measured for right and then for left polarised light. Afterwards, the difference in absorption is plotted. If the out-of-plane magnetisation of the sample is aligned parallel to the direction of motion of the photons, then the sample will have a negative difference in absorption. Conversely it will have a positive difference if they are aligned antiparallel. If the magnetisation

[1] The magnetic moments are aligned antiparallel to the electron spin.

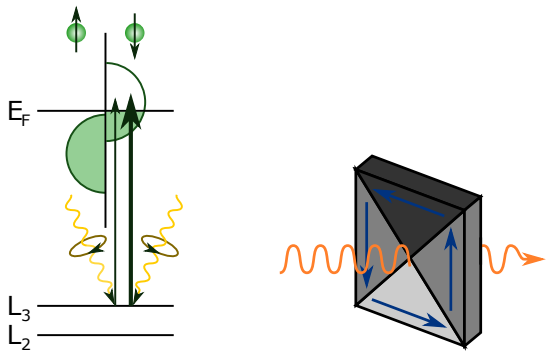

Figure 2.7.: Principle and practise of XMCD. (a) Spin-dependent absorption of photons in a ferromagnet. Circularly-polarised light excites photoelectrons from the L_3 and L_2 edges into 3d states. The 3d state is shown for the extreme case, when only valences for spin down electrons are present. This latter are more likely to be generated by left circularly-polarised light than by right circularly-polarised light. Hence, photon absorption is a measure of the band structure, which governs the magnetic properties. Image adapted from [91]. (b) The difference between absorption spectra recorded at a fixed energy can be used for imaging magnetic states. For a Landau state, the sample needs to be tilted to cant the magnetic moments towards the photon direction. Depending on the parallel or antiparallel alignment of the magnetisation with respect to the photon direction, the domain absorbs differently and appears either dark or bright in the final difference image. Domains with perpendicular alignment to the photons cannot be probed.

is perpendicular to the direction of motion of the photons, then there is no difference in the absorption spectra. An example XMCD image is shown in Fig. 2.7b for a particle in a Landau state mounted at 30° with respect to the photons. Due to the tilt, the in-plane magnetisation of the state can be imaged. A negative difference in the absorption spectra is encoded as dark contrast and a positive difference as bright contrast. The direction of magnetisation of the two grey domains cannot be read off directly as they could either point up or down. Nevertheless, their direction can be established based on a knowledge that the in-plane magnetisation of the Landau state is rotating. Furthermore, these domains can be imaged experimentally by rotating the sample 90 ° so that they are parallel to the photon direction.

By using a combination of STXM and XMCD, 20 to 30 nm spatial resolution can

typically be achieved, while recent developments allow for 7 nm spatial resolution [92]. The highest spatial resolution requires long exposure times, as the photons arrive in bunches which have to be integrated to achieve sufficient imaging contrast. By exploiting the discretisation of photons in time, it is possible to achieve temporal resolution by synchronising the X-ray bunches with an external excitation and carrying out pump-probe experiments. Videos of magnetisation dynamics can then be generated, with each successive frame separated, by a few hundred ps by assigning the absorption of photons in a certain X-ray bunch to the corresponding phase of the excitation. At temporal resolution below 100 ps can be achieved, *e.g.*, at the Pollux Beamline at the Swiss Light Source [93]. In this way, the magnetisation dynamics of a vortex core and spin waves or skyrmion nucleation can be investigated [45, 94, 95].

2.6. Summary

Magnetism offers a rich and complex playground for fundamental studies and for applications. The magnetic behaviour of nanostructures depends crucially on their shape and arrangement. Two different systems have been highlighted: artificial spin ice and magnetic vortices. In the case of artificial spin ice, the material properties can be set by design, with interesting phenomena arising from frustration of the system. In contrast, magnetic vortices provide a very stable sample system, whose dynamics are accessible by using excitations with microwave magnetic fields. In order to investigate these two nanoscale phenomena, a technique with high spatial resolution is required. In particular, as shown below, the study of artificial spin ice demands quantitative analysis of the magnetic fields. High temporal resolution is required in order to study vortex core gyration. All three requirements can be met by TEM. The principles of magnetic imaging in a transmission electron microscope are described in the following chapter.

Chapter 3.

Conventional and magnetic imaging in transmission electron microscopy

This chapter introduces the experimental techniques that are applied in this thesis to measure the magnetic nanostructures that were described in the previous chapter. Particular focus is placed on the measurement of magnetic fields with a spatial resolution on the nanometre scale, both quantitatively and with improved temporal resolution on the picosecond time scale. First, conventional approaches for imaging nanostructures using TEM are described. Then, the focus shifts to two techniques for magnetic imaging: off-axis electron holography and Lorentz microscopy. A model-based iterative reconstruction technique which allows retrieval of the magnetisation is introduced. Finally, possibilities to measure magnetisation dynamics using TEM are described.

3.1. Conventional transmission electron microscopy

The structure and composition of nanostructures can be measured down to atomic spatial resolution using TEM. In this section, the instrument itself is introduced. In general, there are two different modes in which an electron microscope can be operated: using parallel illumination of the sample in TEM mode or by scanning the sample with a focused probe in scanning TEM (STEM) mode.

3.1.1. Electron-specimen interactions

In the TEM, electrons are employed to measure a wide variety of specimen properties ranging from structure to chemical composition and electromagnetic fields

based on electron-specimen interactions. These interactions can be described in term of particle/wave duality. The properties of electron optical systems are generally described in terms of classical particle trajectories of electrons in the electromagnetic fields of the microscope lenses. In a particle description, the electrons are said to scatter from the specimen. The wave aspect underlines the quantum mechanical description of microscopic effects, including probability densities, interference phenomena and the origin of spins. The electron wave is then said to be diffracted by the specimen. In order to understand the basic principles of conventional TEM, it is often sufficient to regard the electrons as particles. Scattering of electrons at the specimen is based on their interaction with the specimen due to the Coulomb interaction with electrostatic potentials of the atoms and long-range electromagnetic fields in the specimen. On the atomic length scale, the positively charged nuclei have a stronger effect for the fast electrons employed in TEM. When studying long range electromagnetic potentials, the effect of the nuclei can be neglected because it is strongly confined to the vicinity of the atomic core. When compared to X-ray or neutron based techniques, the scattering amplitude per specimen thickness is higher, which, together with higher spatial resolution, enables the analysis of significantly smaller specimen volumes. However, the effects of multiple scattering then necessarily become more significant. Single electron scattering can only be assumed for very thin specimens, or for special cases such as interactions with weak, macroscopic fields.

Depending on the specimen properties under investigation, different interactions between an incoming electron and the specimen have to be investigated using different techniques. In a simplified picture, the signals that can be detected are: the direct beam, the bremsstrahlung and elastic and inelastically scattered electrons. The direct beam consists of electrons that, in the ideal case, have not been scattered at all; in practice, weakly scattered electrons are usually also taken into account. Bremsstrahlung describes photons that are emitted as a result of deceleration of the electrons within the specimen. It is characterised by specific energy losses from inelastic interactions, which can be recorded *via* spectroscopy. The energy of the bremsstrahlung can range from close to 0 eV up to the full energy of the decelerated electron. Scattering is said to be elastic if the electrons undergo a change in momentum and negligible energy transfer. It occurs mainly in the forward direction, with typical angles below 10° for thin specimens. The scattering angle is influenced by the atomic number of the atoms in the specimen and on its thickness, density and crystal structure. Interactions with weak, macroscopic electromagnetic fields are included in this category and will be discussed in further detail in Sec. 3.2.1. Inelastic scattering events occur

when the probing electron transfers energy to the specimen. This process can have multiple origins:

- Excitation of oscillations of molecules and of phonons, *i.e.* collective lattice oscillations.
- Intra- and interband excitations of outer shell electrons and plasmons, *i.e.* the collective oscillations of loosely bound electrons in the specimen.
- Ionisation of inner shell electrons. When the gap in the shell is filled by an electron from a higher shell, the excess energy is emitted in the form of X-rays or Auger electrons.

In general, both the composition and the chemistry of the specimen have an effect on the transferred energy. Multiple analytical methods are based on the characteristic energies. However, energy transfer enhances the risk of damaging the specimen as an increasing portion of energy is deposited into the specimen. A large amount of energy is deposited into phonons, which essentially heat the specimen. In organic specimens in particular, irreversible radiation damage can be caused by excitations and ionisations.

Two important concepts are the scattering cross section and the mean free path. The cross section is a measure of the probability of interaction between an incoming electron and the specimen and is measured in units of area. The mean free path is the average distance between two scattering events. An increase in electron energy typically leads to a reduced scattering cross section and an increased mean free path. The probability of scattering increases if the density, thickness or the atomic number of the specimen increase. In addition, scattering from crystalline specimen can be enhanced at specific angles.

3.1.2. The transmission electron microscope

TEM employs elaborate schemes to probe samples with very high spatial resolution. In order to reach sub-Å spatial resolution, electron microscopes have reached a high degree of sophistication in electron optics, sources, detectors, overall stability and precision. Nevertheless, it is educational to use a light microscope to explain the basic operating principle of a TEM. Based on this analogy, a simplified model of the electron ray path in an electron microscope is depicted in Fig. 3.1.

Modern TEMs are equipped with field-emission guns (FEGs), in which a high voltage (in the kV range) between a tip and an anode is employed to extract

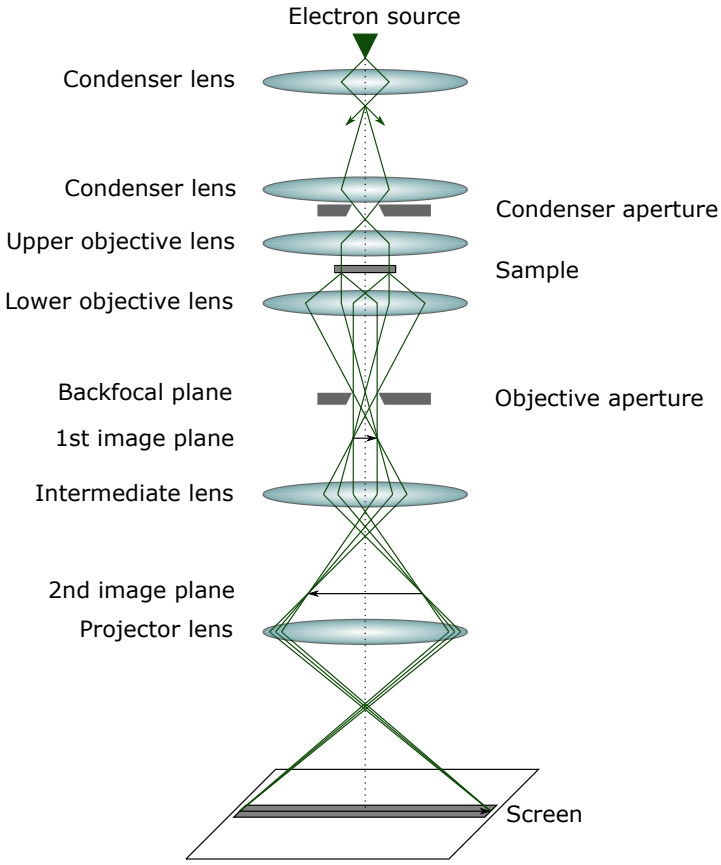

Figure 3.1.: Schematic ray diagram for a TEM. The electron path is defined by electromagnetic lenses, for example, in order to ensure parallel illumination of the sample and a focused image on the screen. Adapted from Williams and Carter [47].

electrons from a sharp metal tip. A cold FEG, the tip is at room temperature, while for a Schottky emitter the tip is heated to 1700 K. Cold FEGs offer electron beams with high spatial coherence due to their small source size and small energy spread. Schottky emitters are easier to operate, at the cost of having a larger source size and energy spread. Both types of FEG are suitable for off-axis electron holography and Lorentz microscopy experiments, which require good coherence and high brightness. Other types of guns use thermionic sources, in which a tungsten or LaB_6 tip is heated to 1700 or 2700 K, respectively, to extract electrons without applying a high voltage. However, the coherence of these tips, which is one of the key requirements for quantitative magnetic imaging, is considerably lower than those of FEGs.

From the gun, the electron beam is directed towards the sample by a set of typically two or three condenser lenses. The first condenser lens (C1) creates a crossover which defines the spot size of the beam (c.f. upper part of Fig. 3.1). The second condenser lens (C2) forms a typically underfocused image of the crossover in the sample plane, resulting in nearly parallel illumination. The strength of the C2 lens sets the illuminated area. An aperture close to the C2 lens can be used to decrease the beam convergence and thus increase the coherence at the cost of reducing the electron current.

A requirement for most TEM techniques is that the sample has to be electron-transparent, *i.e.* to have a thickness well below one micrometre. The sample is mounted in a holder and can be tilted about the axis of the holder by turning the stage. A variety of sample holders are available for a manifold of applications, offering additional tilt or rotation axis and options to modify the sample environment or to apply stimuli to the sample. For example, a sample can be cooled or heated below or above its Curie temperature for magnetic characterisation. Moreover, microwave magnetic fields can be applied to the sample in order to induce magnetisation dynamics.

The objective lens determines the coarse magnification and consists of an upper and lower pole piece. The upper pole piece acts as an additional condenser lens and improves the ability to form parallel illumination. The lower pole piece forms a strongly magnified image of the sample. An objective aperture in the back focal plane can be used to define which electrons contribute to image formation. After the objective lens, a final image can be formed on a fluorescent screen or digital detector by using the intermediate and projector lenses.

For visible light, glass lenses are used to refract light. In contrast, there is no medium that can easily be used to achieve the same effect for electron lenses.

Instead, the Lorentz force

$$\mathbf{F} = -e(\mathbf{E} + \mathbf{v} \times \mathbf{B}) \tag{3.1}$$

is utilised to change the electron trajectory by either electric or magnetic fields. In Eq. 3.1, e is the elementary charge of the electron, $\mathbf{v}$ is its velocity and $\mathbf{E}$ is the electrostatic field. Each magnetic lens consists of a soft iron pole piece with a bore for the electrons, surrounded by copper coils. The current passing through the coils determines the strength of the magnetic field in the bore. The field has axial symmetry, with components along the optical axis and in the radial direction. This field design leads to a spiral-like electron trajectory, which inverts and rotates the image. All magnetic lenses act as convex lenses and deflect electrons towards the optical axis. In practice, several lenses and apertures are usually combined to achieve the required magnification, as well as variability in the optical setup for different methods.

The electrons that are used to illuminate a TEM sample are accelerated to high energy and should be coherent in order to achieve the best possible spatial resolution. An estimate of the spatial resolution is given by the Rayleigh criterion, which is also known as the Abbe limit. It describes the smallest distance between two points that can be distinguished by the expression $\delta = \frac{0.61 \cdot \lambda_e}{n \cdot \sin \theta}$, where λ_e is the wavelength of the electrons, n is the refractive index of the medium the beam is travelling through and θ is the aperture angle. The typical accelerating voltage for electrons U_b is in the range of a few 100 kV. It can be connected *via* $eU_b = \frac{1}{2} m_e v^2$ to the speed of the electrons v using a non-relativistic ansatz, resulting in a theoretical resolution limit of ∼4 pm for an accelerating voltage of 100 kV, which is well below the limit of 50 nm for optical techniques using visible light. In practice, the spatial resolution of a TEM is limited primarily by spherical and chromatic aberration of the imaging lenses, as well as by the finite coherence of the electron beam. The former limitation results from the fact that electrons have different focal lengths when they travel at different distances from the optical axis or have different energies. Such electron optical aberrations can be corrected and controlled by using a sophisticated arrangement of multipole lenses below or above the objective lens. The microscope is then referred to as being aberration corrected [59]. Other aberrations include astigmatism, which is the result of non-perfect lenses and can be corrected by quadropole lenses, or so-called stigmators. Moreover, all of the lenses act as apertures and diffract the electron beam due to their finite size.

In addition to using parallel illumination, a TEM the can usually also be operated in STEM mode. Here, a highly convergent beam is concentrated on a single spot and scanned across the sample. Scanning is achieved by using deflection

scan coils, which are located above the objective aperture and move the beam, while keeping the direction of motion parallel to the optical axis. The aberration corrector in a STEM-optimised microscope is located above the objective lens to correct the electron beam that is focused on the sample. The size of the spot can be tuned well below typical interatomic distances. For a thin sample, the origin of the resulting signals is the illuminated spot. The electron beam is scanned across the sample from one position to the next, giving the technique its name.

As a result of the different interaction mechanisms between the electron beam and the sample, it is possible to perform element-specific investigations. Such analyses are often performed in STEM mode using different imaging and spectroscopy detectors. The detectors that are used to record the primary electron beam are located below the sample and can be divided into two groups: bright-field (BF) and dark-field (DF) detectors. BF detectors are located on the optical axis and mostly record the unscattered electron beam. In contrast, DF detectors are typically annular, centred on the optical axis and record the scattered electron beam over a range of different angles. High-angle annular dark-field (HAADF) detectors are often employed because they provide element-sensitive images. These detectors are located at higher angles where phonon excitation dominates scattering. The scattered intensity increases in strength with atomic number and hence enables so-called Z-contrast imaging [96]. Nevertheless, HAADF detectors need to cover large solid angles due to the small differential scattering cross sections of the recorded signals.

As described in the previous section, the energy loss of the electrons after interaction with the sample depends on the sample properties. Therefore, the measurement of the energy loss of the transmitted beam allows the chemical structure of the sample to be determined in great detail by using electron energy-loss spectroscopy (EELS). EELS measurements are performed by utilising energy filters, which disperse the electron beam according the the energy of the electrons. Alternatively, energy dispersive X-ray spectroscopy (EDX) allows the chemical structure of the sample to be determined by recording the energy spectrum of photons emitted from the sample. The photons are emitted because the incident electron ionises electrons from the inner shells of atoms. Subsequently, an electron from an outer shell may occupy the free state in the inner shell. During this process, a photon may be emitted to carry the energy that corresponds to the difference in binding energy between the two states. These energy differences are element-specific. Therefore, the emission spectrum can be assigned to specific elements. The combination of STEM, HAADF, EELS and EDX allows for imaging the structure of the sample with atomic spatial resolution and enables element specific mapping of thin samples.

3.2. Off-axis electron holography

Off-axis electron holography offers quantitative access to the electrostatic potential and magnetic field of a sample in the TEM by recording an intensity distribution containing information about the phase of the electron wavefunction below the sample. In this section, the interaction between the probing electrons and electromagnetic fields is first introduced first. It is shown how the magnetic properties of a sample are encoded in the phase of the electrons. It is then described how magnetic information can be retrieved from the phase. Finally, details of the experimental setup and approaches for separating magnetic and electric contributions to the recorded signal are outlined. The resulting magnetic phase shift can be used to obtain the in-plane magnetic induction, from which magnetisation in the sample can subsequently be determined.

3.2.1. Scattering of electrons by electromagnetic fields

In addition to the electron-specimen interactions described above (c.f 3.1.1), electrons interact with longer-range electromagnetic fields. In order to understand the electron-electromagnetic field interaction in more detail, it is convenient to describe the electrons in a wave picture. De Broglie postulated in 1924 that electrons can be treated as quanta of an electron wave with momentum

$$\mathbf{p} = m\mathbf{v} = \hbar\mathbf{k}, \tag{3.2}$$

where m is the relativistic mass of an electron and $\mathbf{k}$ is the wavevector [97]. The magnitude of the wavevector is related to the wavelength λ_e of the electrons *via* $|\mathbf{k}| = 2\pi/\lambda_e$. Thus, relativistic momentum p can be attributed to electrons with $p = \frac{h}{\lambda_e}$, in analogy to light quanta.

Electrons inside the TEM reach relativistic velocities. Therefore, a description of the propagation of an electron requires a relativistic treatment. Two assumptions are typically made: (i) strong scattering of electrons by the electric potential in close vicinity to atomic cores can be neglected and (ii) that electron spin can be neglected. The first assumption is valid because the core region is small compared to the volume the electrons interact with [98]. The second assumption is justified as the coupling of the spin of the electron wave with the magnetic field of the specimen is small [98]. The Klein-Gordon equation is used as a starting point, in order to understand the influence of electromagnetic fields on electron

beam propagation [98]:

$$(E - V_{el})^2\psi(\mathbf{r}, z) = (c^2\hat{\mathbf{p}}^2 + m_e^2c^4)\psi(\mathbf{r}, z), \tag{3.3}$$

where E is the total energy of the system, V_{el} is the electrostatic potential energy, c is the speed of light in vacuum and $\hat{\mathbf{p}}$ is the momentum operator. A cylindrical coordinate system is chosen so that the z direction is oriented parallel to the direction of the unscattered electron beam. Rearranging the terms (*cf.* Ref. [99] for more details) and neglecting terms in V_{el}^2 as $E \gg V_{el}$ results in the following equation:

$$[\frac{\hat{\mathbf{p}}^2}{2\gamma m_e} + V_{el}(\mathbf{r}, z)]\psi(\mathbf{r}, z) = E^\star\psi(\mathbf{r}, z), \tag{3.4}$$

where $E^\star = \frac{E^2 - m_e^2c^4}{2\gamma m_e c^2}$ is relativistic kinetic energy and $\gamma = \frac{1}{\sqrt{1-(\frac{v}{c})^2}}$ is the Lorentz factor. The assumption $E \gg V_{el}$ is usually valid for the electrostatic potential inside the TEM and specimen. However, it breaks down close to strong electric potentials in the vicinity of the atomic core.

Equation 3.4 can be solved by a plane wave ansatz, which takes the form

$$\begin{aligned}\psi(z) &= \psi_0 \exp(i\varphi(z)) \\ &= \psi_0 \exp[i\int_{z_0}^{z} dz'\, k(z')] = \psi_0 \exp[\frac{i}{\hbar}\int_{z_0}^{z} dz'\, p(z')]\end{aligned} \tag{3.5}$$

in the one-dimensional case. The solution for the electrostatic contributions to the phase shift

$$\varphi_{el}(\mathbf{r}, z) = \frac{1}{\hbar}\int_{z_0}^{z} dz'\ \sqrt{2\gamma m_e(E^\star - V_{el}(\mathbf{r}, z'))} = \frac{1}{\hbar}\int_{z_0}^{z} dz'\,[\hbar k - \frac{\hbar k}{2E^\star}V(\mathbf{r}, z')] \tag{3.6}$$

can be found when neglecting the magnetic vector potential and using the WKB (Wentzel, Kramers, Brillouin) approximation. This approximation required the potential to vary slowly, *i.e.* to be constant on the order of magnitude of the de Broglie wavelength of the electrons, resulting in slow modification of the amplitude of the wave. In addition, it is still assumed that $V \ll E^\star$ holds.

In general, the canonical momentum

$$\mathbf{p}' = m\mathbf{v} - e\mathbf{A} \tag{3.7}$$

has to be chosen in order to take the magnetic field into account. This modification

results in an additional contribution to the phase shift due to the magnetic vector potential, which can also be approximated using the WKB approximation. In total, the phase shift can be written in the form

$$\begin{aligned}\varphi(\mathbf{r},z) &= \frac{1}{\hbar}\int_{z_0}^{z} dz'\,\hbar k - \frac{1}{\hbar}\int_{z_0}^{z} dz'\,\frac{\hbar k}{2E^{\star}}V_{el}(\mathbf{r},z') + \frac{1}{\hbar}\int_{z_0}^{z} dz'\,eA_z(\mathbf{r},z') \\ &= \varphi_0 - C_E\int_{z_0}^{z} dz'\,V_{el}(\mathbf{r},z') + \frac{\pi}{\phi_0}\int_{z_0}^{z} dz'\,A_z(\mathbf{r},z'). \end{aligned} \tag{3.8}$$

The first term corresponds to the phase shift of an electron wave travelling through vacuum, while the second and third terms represent the contributions of the electrostatic and magnetic potentials, respectively. The prefactor $C_E = \frac{e\gamma m_e}{\hbar^2 k}$ takes a value of $6.526\,\mathrm{rad\,V^{-1}\,\mu m^{-1}}$ for electrons accelerated with 300 kV, while $\phi_0 = \frac{\pi\hbar}{e} = 2.068\cdot 10^{-15}\,\mathrm{Wb}$ is the magnetic flux quantum. A full derivation of Eq. 3.8 can be found in Ref. [100]. It should be noted that only the in-plane component of the magnetic field perpendicular to the electron beam direction is measured, as the phase shift is only sensitive to A_z and

$$\mathbf{B} = \nabla \times \mathbf{A}. \tag{3.9}$$

The electrostatic contribution to the phase shift is sensitive to the accelerating voltage of the microscope, with higher beam energies resulting in a smaller contribution to the total phase shift.

Equation 3.8 confirms that the electrostatic and magnetic field can be analysed by measuring the phase shift. However, the phase shift cannot easily be accessed using standard imaging techniques, which record the intensity $I(r) = |(\psi(r))|^2$. A solution to this problem is offered by electron holography, which was originally proposed by D. Gabor [55, 56]. The technique was further improved by G. Möllenstedt and H. Wahl, who introduced off-axis mode of electron holography [101]. Here, an interference pattern is created by overlapping an electron wave that passed through the specimen (object wave) with one that typically passed only through vacuum (reference wave). The overlap is achieved by using a Möllenstedt biprism (see Sec. 3.2.3 for further details). The reference wave should ideally be free of field perturbations, which can introduce artefacts. The phase shift information is encoded in the fringes of the interference pattern. The difference between the phase shift of the object and reference waves

$$\Delta\varphi(\mathbf{r}) = \varphi_{ref}(\mathbf{r}) - \varphi_{obj}(\mathbf{r}) \tag{3.10}$$

is recorded. The phase shift of the electron wave in regions of vacuum, φ_0, cancels

out. The integral over the magnetic vector potential can be rewritten in terms of the magnetic induction using Eq. 3.9 and Stokes' theorem as

$$\oint_{\delta\Sigma} d\mathbf{l}\,\mathbf{A} = \iint_{\Sigma} d\mathbf{S}\,\mathbf{B} \tag{3.11}$$

where the start and end points of the integral along z are connected in field-free space to form a closed line $\delta\Sigma$ containing area Σ. The contributions of the electrostatic potential and in-plane magnetic induction can be written in the simplified form

$$\varphi(x) = C_E V(x) t(x) - \frac{e}{\hbar}\int dx\, B_\perp(x) t(x) \tag{3.12}$$

if neither the electrostatic potential nor the in-plane magnetic induction vary in the direction of the electron beam through the of the thickness of the specimen t. If the electrostatic contribution to the phase does not vary across the region of interest or can be subtracted, then the projected in-plane magnetic flux density can be visualised in the form of contour lines by making use of the expression:

$$\frac{d\varphi(x)}{dx} = -\frac{et(x)}{\hbar} B_\perp(x). \tag{3.13}$$

Visualisation of the strength and direction of the magnetic induction can then be obtained by calculating cosine of a chosen multiple of the magnetic contribution to the phase shift.

3.2.2. Reconstruction of phase information

So far, it has been shown how information about the electrostatic and magnetic properties of a sample can be recorded in the form of a phase image. Now, this information needs to be extracted from the phase. In a first step, the phase has to be obtained from a complex wavefunction reconstructed from a hologram. In general, a wavefunction $\psi(\mathbf{r}) = A(\mathbf{r})e^{i\varphi(\mathbf{r})}$ has the amplitude $A(\mathbf{r})$ and phase $\varphi(\mathbf{r})$. Wave aberrations influence both the amplitude and the phase. The total intensity of an off-axis electron hologram can be written in the form

$$\begin{aligned} I_{hol}(\mathbf{r}) &= |\psi_{obj}(\mathbf{r}) + \psi_{ref}(\mathbf{r})|^2 \\ &= 1 + A^2(\mathbf{r}) + 2\mu_{fc} A(\mathbf{r}) \cos(2\pi \mathbf{q_c}\mathbf{r} + \varphi(\mathbf{r})), \end{aligned} \tag{3.14}$$

where the carrier frequency $|\mathbf{q_c}| \approx k\beta$, the overlapping angle β between the object and reference wave. The fringe contrast is μ_{fc} and it is assumed that $\psi_{ref} = 1$.

The fringe contrast μ_{fc} is crucial for electron holography, as it limits the smallest detectable phase shift. In practice, it is determined by the coherence of the electron source, inelastic scattering and the detector pointspread function (*cf.* Sec. 3.2.3). A representative off-axis electron hologram is shown in the second row of Fig. 3.2. The rest of the figure describes, the reconstruction process for a simulated magnetic vortex.

A hologram is typically reconstructed by calculating its Fourier transform, followed by masking one sideband, placing it at the origin of the Fourier space and performing an inverse Fourier transform. This procedure is described by the equation

$$\begin{aligned} FT\{I_{hol}(\mathbf{r})\} &= FT\{1 + A^2(\mathbf{r})\} + FT\{\mu_{fc}A(\mathbf{r})e^{i\varphi(\mathbf{r})}e^{i2\mathbf{q_c}\mathbf{r}}\} + FT\{\mu_{fc}A(\mathbf{r})e^{-i\varphi(\mathbf{r})}e^{-i2\mathbf{q_c}\mathbf{r}}\} \\ &= \delta(\mathbf{q}) \; + FT\{A^2(\mathbf{r})\} \\ &\quad + FT\{\mu_{fc}A(\mathbf{r})e^{i\varphi(\mathbf{r})}\} \otimes \delta(\mathbf{q} - \mathbf{q_c}) \\ &\quad + FT\{\mu_{fc}A(\mathbf{r})e^{-i\varphi(\mathbf{r})}\} \otimes \delta(\mathbf{q} + \mathbf{q_c}). \end{aligned} \tag{3.15}$$

There are three distinct regions in the Fourier transform (*cf.* third row in Fig. 3.2). The first two terms are contained within the centreband which is located at the centre of the Fourier transfrom. The delta function term results from the uniform intensity of the reference wave, while the second term is the Fourier transform of a conventional BF TEM image. The third and fourth terms are termed sidebands and are shifted by $\pm\mathbf{q_c}$ with respect to the centreband. Each sideband contains information about the full complex wavefunction. They are complex conjugates of each other.

On one of the sidebands is centred in Fourier space, a virtual aperture is used to cut out information from the centreband and an inverse Fourier transform is performed to retrieve the complex wavefunction. The spatial resolution of this wavefunction depends on the radius of the aperture, which defines the spatial frequencies that are retained in the selected sideband. The size of the aperture cannot be extended indefinitely. As more noise is added when the aperture size is increased and the centre band may also be included, resulting in high frequency artefacts. Therefore, an optimal aperture size has to be chosen as a trade-off between spatial resolution, signal to noise ratio and artefacts. As the electrostatic and magnetic contribution to the phase shift are often smooth and do not vary rapidly across a sample, most relevant information may be contained in the lower spatial frequencies and a smaller aperture may be applicable. Nevertheless, a sudden cut-off in information at the edges of the aperture may result in artefacts, especially at the edges of reconstructed images. Such artefacts can be reduced

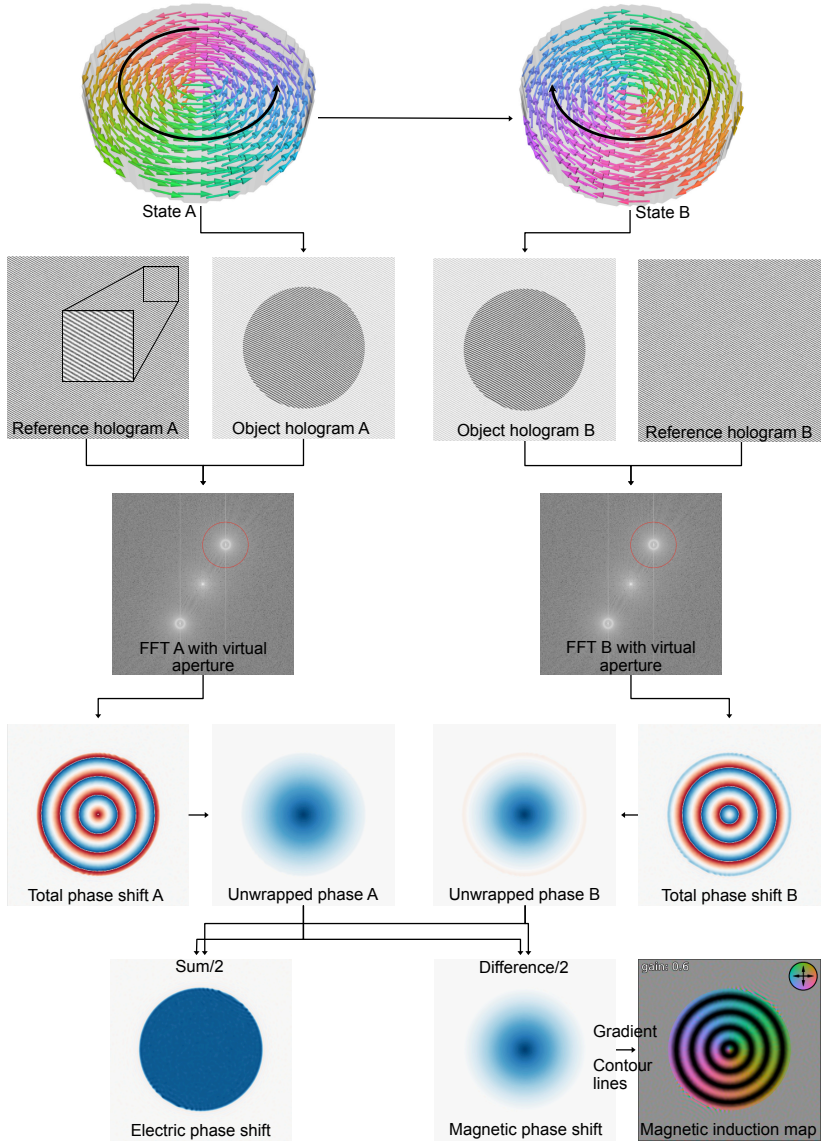

Figure 3.2.: Reconstruction process for off-axis electron holography of a magnetic vortex imaged in opposite magnetic states A and B. The phase is retrieved from each hologram by using Fourier transforms and a virtual aperture. The magnetic and the electrostatic contributions to the phase shift are determined from the phase images reconstructed for the two opposite magnetic states of the vortex.

by using an aperture with smoother edges. Consequently, the aperture size and shape have to be chosen with care, according to the specific specimen. The reconstructed image wave, which is obtained by inverse Fourier transform takes the form $\psi_{rec}(\mathbf{r}) = \mu_{fc} A e^{i\varphi(\mathbf{r})}$. The amplitude and phase can then be obtained using the relations $A(\mathbf{r}) = |\psi_{rec}(\mathbf{r})|$ and $\varphi = \arctan(\frac{Im\{\psi_{rec}(\mathbf{r})\}}{Re\{\psi_{rec}(\mathbf{r})\}})$. Discontinuities in the reconstructed phase may arise, as it is calculated module 2π. These discontinuities can be removed by using an unwrapping algorithm [102]. Only electrons that are coherent with the unscattered reference wave contribute to the interference fringes, even though they are also associated with small scattering angles. However, they do contribute to the background noise in the hologram and should therefore ideally be removed by using energy filtering to record holograms.

Distortions in a holographic interference pattern affect the quality of the phase information that can be extracted from it. Such distortions may arise from imperfections in the projector lens system or the camera. If the distortions result in high spatial frequency artefacts, then they can sometimes be distinguished from the desired magnetic signal by using Fourier filtering. In practice, distortions are usually removed more easily by recording a reference hologram from a vacuum area, as they often vary slowly over time. The reference hologram is ideally recorded with the same imaging parameters directly after the object hologram, in order to maintain the same conditions. The undistorted object wavefunction can then be obtained by performing a complex division of the object wavefunction by the reconstructed vacuum wavefunction from the reference hologram. The acquisition of a vacuum reference hologram offers an additional advantage, as it can be used to determine the true position of the centre of the sideband. For a hologram recorded from a sample, the brightest spot in the sideband does not necessarily represent its true centre. Misidentification of the centre of the sideband during reconstruction then results in an additional phase ramp. Hence, it is common practice to use a vacuum reference hologram to determine the centre of the sideband although care is required if it is perturbed by long-range fringing fields.

3.2.3. Experimental setup

The experimental setup used for conventional TEM imposes a major restriction on magnetic samples because the magnetic field of the conventional objective lens is approximately 2 T at an accelerating voltage of 200 kV (FEI Tecnai G2, S-TWIN pole piece) in the electron beam direction at the sample position. Such a large field would saturate most magnetic samples. A solution is to set the objective

lens to a low value that corresponds to nearly magnetic-field-free conditions and to instead use a so-called Lorentz lens to form the image. The Lorentz lens is located below the sample position, such that its magnetic field does not extend to the specimen significantly (see Fig. 3.3a). Aberration correction takes place below the Lorentz lens. The drawback of using a Lorentz lens is that it has a longer focal length and poorer spatial resolution than the conventional objective lens.

In off-axis electron holography, the beam is split into a reference wave and an object wave by inserting a Möllenstedt biprism into the beam path, as shown in Fig. 3.3a. The biprism is a thin metallic wire, to which a positive voltage is usually applied to overlap the two beam to form an interference pattern on the imaging detector. The biprism is located close to a conjugate image plane and can be mounted to a stage that usually holds the diffraction apertures. The image plane may need to be lowered slightly using the lenses to achieve a relative tilt of the reference and object waves towards each other. The addition of multiple biprisms to the condenser and projection lens systems of the electron microscope provides different options to vary the overlap width and fringe spacing and to remove artefacts.

The biprism voltage is chosen based on a balance between different competing factors. The highest spatial frequency that can be reconstructed q_{max} is determined by the pacing of the interference fringes. According to Eq. 3.15, for a strong phase object, the centreband has a maximum radius of $2 \times q_{max}$ when each sideband has a maximum radius of q_{max}.[1] Consequently, the carrier frequency q_c should be at least three times larger than q_{max}. Likewise, the size of the virtual aperture during reconstruction should be 1/3 of the carrier frequency to preserve as many high spatial frequencies as possible. In practice, it is convenient to refer to the fringe spacing $s = \frac{1}{q_c}$, which can be measured during an experiment. In this way the resolution of the constructed phase can be optimised to ensure that it is possible to detect the desired features. In practice, the resolution can be improved by increasing the biprism voltage, as it is proportional to the carrier frequency. The field of view is then enlarged and the Fresnel fringes at the edges of the biprism wire are also decreased. However, the increased overlap width decreases the fringe contrast, as the coherence of the electron source is limited. This decrease in fringe contrast results in an increase in noise in the reconstructed image. A measure of the fringe contrast can be obtained by taking a line scan across a hologram recorded from a vacuum region and applying the

[1] $FT\{A^2\} = FT\{A\} * FT\{A\}$. A function convoluted with itself results in a triangular function that has 2x the radius as the new radius

formula $\mu_{fc} = \frac{I_{max}-I_{min}}{I_{max}+I_{min}}$. I_{max} and I_{min} are the highest and lowest intensities of the fringes measured from the linescan. The fringes also need to be large enough to be resolvable by the pixels of the detector. Considering all of these factors, the biprism voltage needs to be chosen as a balance between resolution and the contrast. Typical biprism voltages used for electron holography of magnetic fields are on the order of 50 - 200 V.

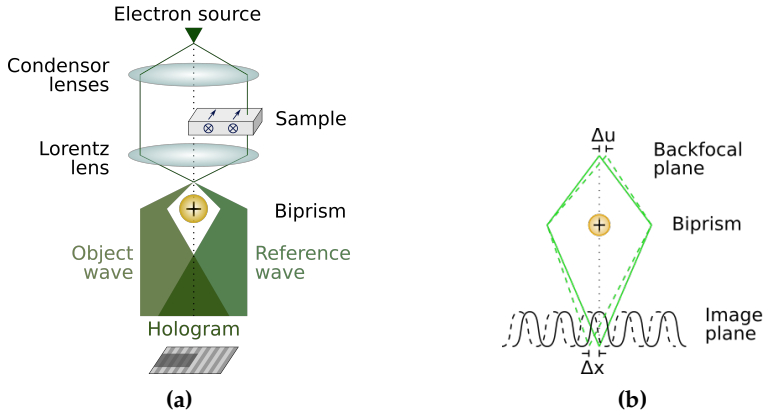

Figure 3.3.: Setup for off-axis electron holography. (a) Schematic ray diagram with a bisprim used to split the electron wave into two parts, the object wave and the reference wave and to overlap them. The overlap gives rise to interference fringes. Magnetic properties of the sample are encoded in the phase shift, which can be measured from the interference fringes. (b) Schematic diagram showing the importance of spatial coherence. A small shift in the backfocal plane results in a shift of the interference pattern and therefore in a reduction of the contrast. Adapted from Ref. [103].

As stated above, the coherence of the electron beam is a key requirement for electron holography. Its importance is highlighted in Fig. 3.3b which shows that a small shift in the backfocal plane due to instabilities results in a shift of the interference fringes in the first image plane and lower fringe contrast. The coherence of the electrons can be improved by using a high brightness field emission gun and by spreading the illumination as far as possible, *i.e.*, by demagnifying the electron source. However, a spread electron beam reduces the current density, resulting in lower dose at the detector for a given acquisition time and hence a lower signal to noise ratio. Fortunately, high coherence is only required in a direction perpendicular to the biprism to obtain the best possible fringe contrast. Therefore, elliptical rather than circular illumination is often used in off-axis

electron holography. The use of elliptical illumination provides a compromise between coherence in one direction and a sufficient signal. It can be is achieved by overfocusing the condenser lens perpendicular to the biprism using the condenser stigmators, while keeping the direction parallel to the biprism as narrow as possible. If the number of counts is still too low for reconstruction, then the acquisition time can be increased. However, an increase in acquisition time may also result in a loss of coherence, for example due to mechanical instabilities of the biprism wire or drift of the beam and/or the sample. An optimal balance between biprism voltage, illumination conditions and acquisition time therefore needs to be determined for each sample and targeted spatial resolution. Several others factors can have an influence on hologram quality, *e.g.*, the finite size of the electron source, the energy spread of the beam and the point spread function of the detector.

3.2.4. Separation of electrostatic and magnetic contributions to the phase

It was shown that the phase of the electron wave contains both electrostatic and magnetic contributions. In order to separate these contributions, two phase images can be recorded, between which the relative contributions of the magnetic and electrostatic phase shifts are different. Once separation is performed, magnetic induction maps can be visualised by generating contour lines from the magnetic contribution to the phase, while its gradient can be used to determine the direction of the projected in-plane magnetic field (Fig. 3.2).

The electrostatic and magnetic contributions to the phase shift can be achieved by different means. One possibility is to heat the sample above a critical temperature at which magnetic order disappears and to take a difference between the resulting phase images. However, heating may impose the risk of changing the composition of the sample evaporating parts of it or changing the electrostatic-beam-induced charging of the specimen.

A common approach is to reverse the magnetic contribution to the phase by magnetising the sample first in one direction and then in the opposite direction, as depicted in Fig. 3.4a. Half of the difference and half of the sum of the resulting phase shifts can then be used to determine the magnetic and the electrostatic contributions, respectively. The magnetisation in the sample can be reversed by turning the sample using the stage tilt to as high an angle as possible and turning on the magnetic field of the objective lens. The field can reach values

of more than 1.5 T in an FEI Titan type microscope with a C-TWIN lens at 300 kV, which is usually enough to saturate most samples. The objective lens is then turned off, the sample is tilted back and is investigated in magnetic-field-free conditions. However, this approach does not guarantee that perfect reversal of the magnetisation in the sample will occur.

Another option is to turn the sample over by 180° (see Fig. 3.4b). This approach is equivalent to reversing the direction of the electron beam which reverses the integration trajectory in Eq. 3.5 and Eq. 3.7. The electrostatic contribution to the phase shift is unchanged, while the sign of the magnetic contribution to the phase shift changes. Hence, the two contributions can again be separated by taking half of their difference or half of their sum. There are two possibilities to turn a sample over. The first option is to take the sample out of the microscope, flip it over and insert it again. This approach has a number of drawbacks. First, the sample is subjected to the residual fields present around the objective lens pole piece when removing and re-inserting it. Second, the sample is also likely to rotate inside the holder. This rotation then needs to be corrected during data processing. A more reliable option is to use a holder that is specifically designed to turn the sample over by precisely 180° [104]. The advantage of flipping the sample is that the intrinsic state of the sample can be imaged several times as there is no need to alter the magnetic state of the sample, *e.g.* by magnetising it. Nevertheless, it requires accurate turning by 180°, as a slight error in tilt will affect the outline of the sample in projection. Special care also has to be taken to correct for projection distortions, as these pose a significant problem when registering the two phase maps against each other during numerical evaluation [104]. Within the scope of this thesis, both turning the sample over and magnetising it are employed for different experiments.

3.2.5. Model-based iterative reconstruction of magnetisation

Although projected magnetic vector potential along the beam direction and therefore the in-plane magnetic induction can be retrieved from a phase image recorded using off-axis electron holography, the magnetisation is the intrinsic material property and the source of the magnetic vector potential. Thus, it is of interest to reconstruct the magnetisation itself, for example to calculate the three-dimensional stray field distribution that is induced by the magnetisation. In the scope of this thesis, the projected in-plane magnetisation is reconstructed for this purpose (Sec. 4.6). This section provides a concise introduction into the underlying considerations and methods of the MBIR approach in the special

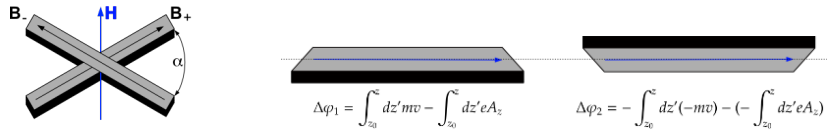

(a) **(b)**

Figure 3.4.: Two approaches for of the electrostatic and magnetic contributions to the phase shift. (a) In the first approach, a vertical magnetic field **H** is applied to a tilted sample. The sample is first turned by $\frac{\alpha}{2}$ and then by -$\frac{\alpha}{2}$ effectively reversing the magnetisation from state $\mathbf{B}_+$ to $\mathbf{B}_-$. (b) In the second approach, the sample is turned by 180° about the dashed tilt axis. In both cases, the sign of the magnetic contribution to the phase shift is reversed relative to the electrostatic contribution.

case of a two-dimensional reconstruction, *i.e.* only reconstructing the in-plane magnetisation projected along the electron beam direction. A full physical and mathematical background of the MBIR approach can be found in Ref. [61].

The phase shift of the electrons can be derived from a given magnetisation distribution *via* a forward model. The magnetisation of the sample is the source of the three-dimensional vector potential, which has a long-range nature. Electrons carry the information about the projected z component of the magnetic vector potential (see Fig. 3.3a). This projection can be treated as a simple sum of the successive contributions to the phase shift in the z direction as the deflection of the electron beam is weak. Hence, the phase shift of the probing electrons on the screen carries information about the projected in-plane magnetisation. These physical processes can be reproduced numerically and the phase shift of the electrons can be calculated for a given magnetisation distribution. However, the inverse, *i.e.* going from a given phase shift back to the magnetisation distribution, cannot be solved directly because:

- Projection along the z direction results in a loss of information;
- Experimental measurements are often noisy and an inverse algorithm cannot inherently establish if a given phase shift is a result of the true magnetisation or the noise. The influence of the noise may also be amplified in this step.[2];

[2]The electron phase shift is linked to the integration of the z component of the magnetic vector potential along the z direction (see Eq. 3.12). Hence, the reverse direction requires a derivative, which amplifies noise.

- Contributions to the phase from magnetic regions of the sample that are outside the field of view (FOV) may affect the phase inside the FOV due to the long-range nature of the magnetic vector potential. Neglecting contributions from outside the FOV may erroneously attribute the phase shift induced by them to regions of the sample inside the FOV.
- The vector potential associated with regions of the sample that are inside the FOV may extend outside the FOV. Since the vector potential outside the FOV is not recorded, information is lost. Although there are different approaches for retrieving the lost information, *e.g.* by assuming that the vector potential outside the FOV is zero, they typically result in edge artefacts.

The advantage of using model-based reconstruction is that it can take into account these measurement limitations when retrieving the magnetisation distribution from a given phase image. Successful retrieval is then possible by including *a priori* information in the reconstruction algorithm because of different mechanisms as explained in the following section. The ferromagnetic exchange energy (*cf.* Sec. 2.2) favours a smooth magnetisation distribution where neighbouring pixels do not vary strongly in magnitude and direction. Regularisation can be used to enforce this criterion. Here, the Tikhonov regularisation is chosen [61, 105]. The smaller the regularisation parameter is chosen, the more likely it is that the magnetisation distribution is fitted to noise. If the parameter is too large, then the magnetic moment distribution may be smoothed. Thus, the optimal regularisation parameter has to be chosen carefully (see Appendix B.1 for further details). Contributions from interactions other than the exchange energy, *e.g.* Dzyaloshinskii–Moriya interaction, are neglected with this approach. While this results in a failure of this approach for complex magnetic system, this assumption allows to reconstruct the magnetic state of magnetic vortices and artificial spin ice. Another advantage of the model-based approach is that contributions to the phase from particles that are outside the FOV can be considered, either by assuming that they contribute to a linear phase ramp or by introducing buffer pixels in the model. Moreover, it is possible to include *a priori* knowledge about where the sample is in the model. This knowledge can be used to define the edges of the magnetisation distribution correctly, as well as to speed up the computation. Finally, the loss of information on the edges of the FOV do not affect the reconstruction as a few supporting points outside of the known particle edges are sufficient to model stray fields. However, the loss of information due to projection in a single direction cannot be compensated. Therefore, contributions to the magnetisation whose phase shifts cancel, resulting in zero phase shift, cannot be resolved and spheres are interpreted as cylinders.

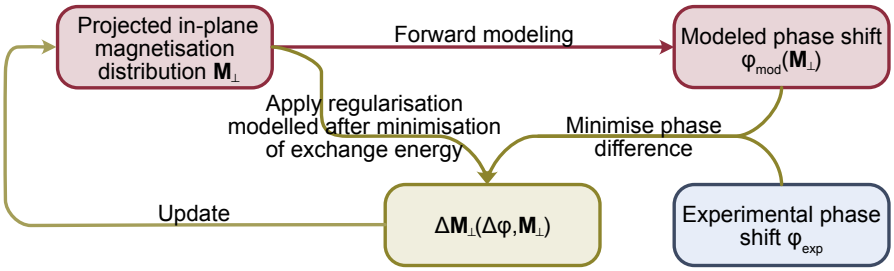

Figure 3.5.: Basic workflow for model-based iterative reconstruction of the projected in-plane magnetisation. The forward model is used to compute the phase shift for a given magnetisation distribution. The computed phase shift is compared to an experimentally measured phase image. The difference between the experimental and modelled phase shift, as well as the regularisation term, which is modelled after the exchange interaction, are minimised and used to improve the guess for the magnetisation distribution.

The model-based approach allows to solve the modified inverse problem numerically. However, this task takes significant computational time due to the use of large matrices, in particular due to the three-dimensional nature of the magnetisation distribution and the magnetic vector potential. Therefore, the modified inverse problem is replaced by an iterative minimisation approach. Using this approach, the difference between the phase shift produced by an assumed magnetisation distribution due to the forward model and an experimentally measured phase map is minimised by updating the magnetisation distribution it reproduces the experimental phase shift. In addition to compliance with the experimental data, this minimisation approach takes the constrain of the parallel alignment due to the regularisation into account. Fig. 3.5 shows an outline of the complete minimisation process including the forward model. In practise, the iteration may be stopped before minimisation is complete due to computational time constrains. This abortion results in a further smoothing of the reconstructed magnetisation distribution in addition to the input of the exchange energy. Nevertheless, the MBIR approach offers access to the projected in-plane magnetisation distribution corresponding to a measured phase image. This approach can be further extended to retrieve the three-dimensional magnetisation distribution by measuring the phase shift while tilting the sample to access different components of the magnetic vector potential [61].

3.3. Lorentz microscopy

This section describes an easier technique for magnetic imaging than off-axis electron holography: Lorentz microscopy, which is often used as an umbrella term for several different techniques for the investigation of magnetic domain structure in TEM.

As described above, electrons experience a Lorentz force when they interact with an electromagnetic field (*cf.* Eq. 3.1). The magnetic field of a sample deflects an electron beam perpendicular to both the magnetic field and the electron travelling direction. The deflection angle can be approximated as

$$\alpha = \frac{e\lambda_e}{h} B_\perp t \tag{3.16}$$

for an in-plane magnetic field $B_\perp$ in a sample of thickness t. In general, the deflection angle depends not only on the magnetic induction of the sample, but also on the stray fields above and below it. Typical deflection angles are on the order of a few tens of μrad for electrons that have been accelerated by 300 kV and pass through a sample of thickness 100 nm containing an in-plane field of 1 T. Very thin samples provide a smaller deflection angle with Fresnel fringes from the edges of a sample that has a small lateral size may conceal the magnetic contrast. In addition to deflection by the Lorentz force, electrons can also be deflected by elastic Bragg reflection at atomic planes of the crystal lattice of the specimen. Typical deflection angles for Bragg reflection are on the order of a few mrad, which is much larger than that expected from deflection by the Lorentz force.

Differently magnetised magnetic domains in a sample give rise to deflection of an incident electron beam in different directions. This deflection can be measured in a number of ways. The use of an aperture to only record electrons that have been deflected in a certain direction referred to as Foucault imaging. In Fresnel imaging the divergence and convergence of electrons deflected by different magnetic domains in defocused images is used to visualise the positions of magnetic domain walls as shown schematically in Fig. 3.6a. The electron beam converges or diverges at the positions of magnetic domain walls, giving rise to bright or dark contrast out of focus (see Fig. 3.6b). Where electrons converge interference fringes may appear, according to the wave picture of electron imaging. Going from overfocus to underfocus conditions reverses the dark and bright contrast. This change in contrast can be used to access if it is magnetic in origin. Phase can

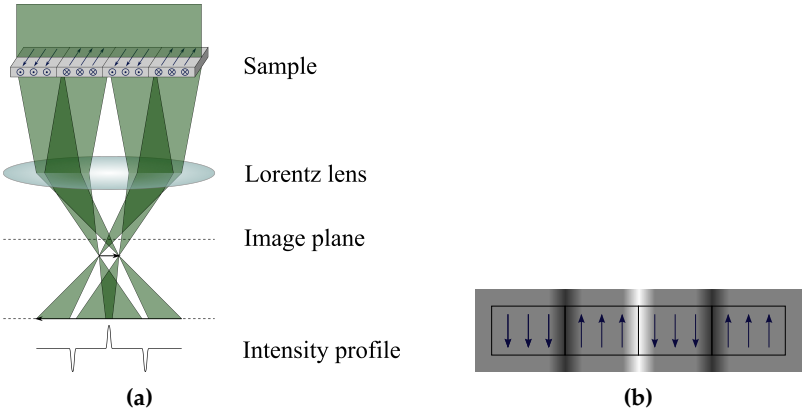

Figure 3.6.: Fresnel mode of Lorentz microscopy. (a) Schematic diagram illuminating contrast formation. The electron beam is deflected by the magnetic domains in the sample due to the Lorentz force. The deflection gives rise to bright and dark contrast at the positions of the magnetic domain walls when imaging out of focus. The figure illustrates this effect for the case of underfocused conditions. Adapted from Ref. [52] (b) Underfocused Fresnel image for the sample shown in a).

be obtained by recording several images at various defocus values and using the transport of intensity equation [106].

Fresnel imaging is often used to extract information about the positions of magnetic domain walls, their nucleation point, and pinning sites. It is easy to implement, offers a large field of view and enables real-time imaging. For example, a biprism is not needed for Fresnel imaging and the demand for coherent illumination is more relaxed. Nevertheless, a Lorentz lens is usually used, just as for off-axis electron holography. The use of out-of-focus images results in the need to calibrate the magnification of the microscope as a function of defocus. Real-time imaging is limited by the acquisition time needed to record sufficiently high contrast. Typical minimal acquisition times are on the order of 40 ms [52]. Therefore, only quasi-static behaviour can be investigated without further modification of the electron microscope. In the following section, such modifications are described, in order to push the temporal resolution below this limit and to enable true dynamic experiments.

In addition to TEM-based phase contrast techniques, it is also possible to measure electromagnetic fields in STEM mode by employing techniques such as DPC

imaging [50,51]. Here, the deflection of the electron beam is measured by using a segmented or pixelated detector at each scan point. The deflection is then related to the projected electromagnetic fields experienced by the electron beam.

3.4. Time-resolved microscopy

Magnetisation dynamics in general and the motion of magnetic vortex cores in particular can be imaged using different TEM techniques. The three most common approaches involve the use of: a) a pulsed electron source, b) an electron beam chopper and c) a fast detector. The first technique are often referred to as ultrafast transmission electron microscopy (UTEM). The imaging time of a single shot can be below the nanosecond range for all three techniques. The signal to noise ratio in a single image is therefore often not sufficient. Thus, stroboscopic pump-probe experiments are also carried out to increase the contrast. Here, imaging of the sample (the probe) is synchronised with excitation of the dynamics (the pump). Once, the dynamics have been recorded, another measurement over the complete time is started again and the individual images corresponding to the same excitation state are added up. The drawback of such a stroboscopic method is that it requires the dynamics of the system to be very stable and repeatable over many cycles without changing. Further details on the basics of pump-probe techniques may be found in Ref. [107].

The best temporal resolution is offered by a pulsed electron source. In this approach, the tip is modified to only emit electrons when it is excited by a short laser pulse, as shown schematically in Fig. 3.7a. Commercial systems can reach a time duration of 1.2 ps for a single electron pulse with a repetition rate of up to 1 MHz.[3] The time duration of a single pulse determines the temporal resolution, while the repetition rate determines how much time is required to capture the full dynamics with sufficient sampling in the time domain and sufficient contrast. Custom-built systems have been shown to reach time durations of 200 fs with a repetition rate of 800 kHz [66] or 400 fs with 2 MHz [108]. The drawback of this technique is that it requires a specialised electron gun. Hence, it is challenging to implement it and it is still only realised a small number of laboratories. Less severe modifications when using required for a beam chopper, as shown in Fig. 3.7b. Fast choppers for high energy electron beams can be realised by electromagnetic fields, which are typically introduced below the condenser system.

[3] JEOL Ltd. (2021, March 08). Luminary Ultrafast TEM / Dynamic TEM. Retrieved from `www.jeol.co.jp/en/products/detail/Ultrafast_Dynamic-TEM.html`

The electromagnetic fields deflect the electron beam and are driven in the radio frequency (RF) regime to generate specific trajectories. The deflected beam is blocked by an aperture, which creates short electron pulses. The time duration and the repetition rate depend on the deflection scheme and the aperture. Commercial systems reach time durations of 100 ns with repetition rates of 500 kHz[4], while custom-built systems can reach 750 fs with 75 MHz [**?**]. The latter repetition rate is much better than that of a pulsed electron source and is therefore able to sample finer dynamics for the same measurement time. However, the temporal resolution is significantly worse.

The third option is a fast detector. Delay line detectors (DLDs) offer a temporal resolution in the range of 200 ps.[5] Here, an array of multichannel plates (MCPs) creates charge clouds by multiplying incident single electrons. Two perpendicular meanders act as anodes detecting the arrival of the charge clouds and converting them into electric signals. The signals are extracted at both ends of each meander. The position and time of the incident electron are determined from the delay time of the signal arriving at both ends (see Fig. 3.7c). Two meanders are needed to detect the x and y positions of each incident electron. DLDs are single electron detectors, which assign a three-dimensional stamp (x position, y position and time) to each electron. This stamp is used to generate images that can be averaged over set time intervals. Another advantage of using a DLD is that it can record images continuously, thereby reducing the total measurement time. Moreover, it decreases the dose, that the sample is exposed to compared to approaches that pulse the beam after the electron-specimen interaction [110]. The most important advantages over the first two techniques are that the installation of a DLD on a microscope column is easy to realise and that it does not compromise the beam quality. Thus, this method is chosen to image magnetic vortex core dynamics in this thesis. More details about the implementation of the DLD, as well as the synchronisation with the excitation of the dynamics, are given in Ch. 6.

In this thesis, vortex motion is excited using microwave electromagnetic fields in a dedicated RF magnetising holder designed by Dr. Benjamin Zingsem [111]. The holder design is based on a coplanar waveguide with ground (CPWG) and a cartridge that acts like a waveguide [111]. The cartridge is made of brass and the sample is inserted into it [111]. Two holes in the cartridge ensure that the electron beam can pass through it at the sample position [111]. Further details

[4]JEOL Ltd. (2021, March 08). Electrostatic Dose Modulator (EDM). Retrieved from `www.jeol.co.jp/en/products/detail/EDM.html`

[5]Surface Concept GmbH (2021, March 08). Delayline Detectors. Retrieved from `www.surface-concept.com/downloads/info/delaylinedetectors.pdf`

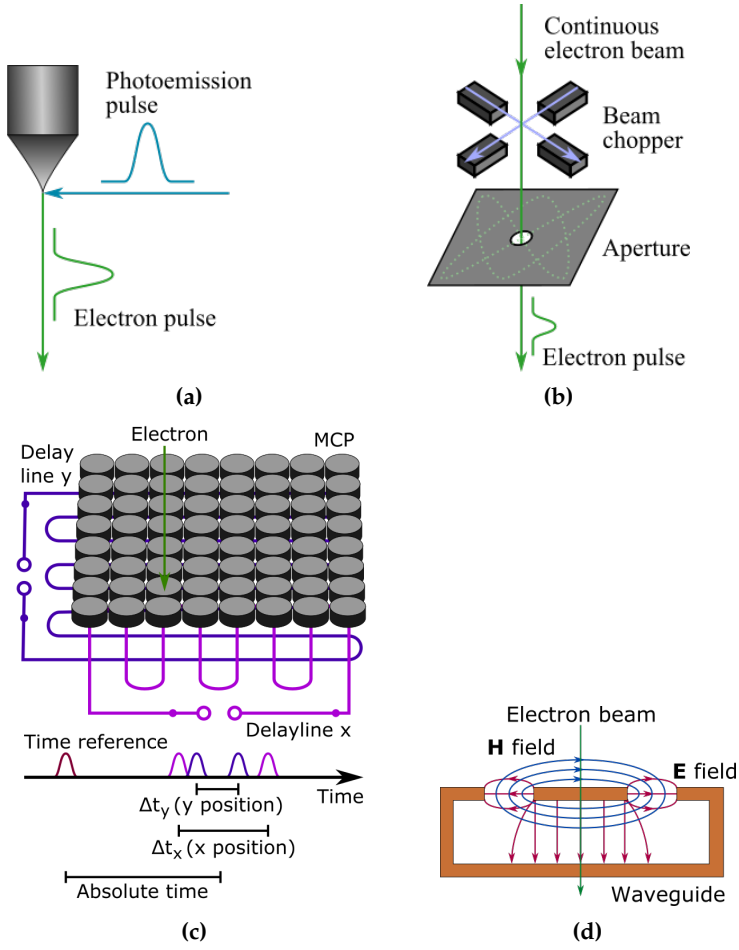

Figure 3.7.: Examples of methods of time-resolved TEM. In each case, the pulse generation or read out needs to be synchronised with excitation of the sample. (a) Pulsed electron source. (b) Electron beam chopper. (c) Fast, single electron detector. (d) Cartridge for magnetic field generation.

and a characterisation of the holder can be found in Sec. 6.2.2 and Sec. 6.2.3. RF currents are applied to the cartridge using an RF generator. The RF current induces microwave electromagnetic fields at the sample position (see. Fig. 3.7d). The main component of the magnetic field is in the plane of the sample, while the electric component is along the electron beam direction in an idealised picture. The cartridge reflects the electromagnetic waves of the electron current back towards the RF generator. These reflections results in the formation of standing waves inside the cartridge. The amplitude of the induced in-plane magnetic field is then increased if an antinode is formed at the position of the sample. Although, the reflected wave of the electron current reaches the RF generator, it is not built to handle reflected waves and the generated RF signal may be alternated as a result. Nonetheless, the RF magnetising holder demonstrates how microwave magnetic fields can be generated using a simple and elegant home-built solutions.

3.5. Summary

The transmission electron microscope is a versatile tool for the study of sample properties that include structure and composition down to the atomic scale. The interaction of the electron beam with a sample results in a multitude of different signals. The microscope conditions and detectors can be optimised to record different signals, depending on the property under investigation.

Even the electromagnetic fields become accessible quantitatively by not only recording the image intensity but the full wavefunction using a technique such as off-axis electron holography. Here, a biprism is used to split the beam into two partial waves, only one of which passed through the sample. The waves are subsequently overlapped to form an interference pattern, from which the phase can be retrieved. The phase, in turn, encodes the electromagnetic properties of the sample. In combination with a MBIR approach, not only the magnetic induction but also the magnetisation, which is an intrinsic property of the material, can be reconstructed quantitatively. Off-axis electron holography is applied in the following chapters to the study of artificial spin ice and magnetic vortices (*cf.* Ch. 4 and 5). An alternative approach to image the magnetic properties of a sample in the TEM is Fresnel imaging. The advantage of this technique is that it enables real-time imaging. It is used in Ch. 6 in combination with a DLD and an RF magnetising holder to study the time-resolved motion of a magnetic vortex core.

Chapter 4.

Quantitative measurement of virtual antivortices in artificial spin ice

Magnetic spin ice is receiving increasing attention experimentally and theoretically due to its unique physics which is based on frustration in such systems [27]. Here, a specific class of spin ice is investigated: chiral ice. Chiral ice shows peculiar dynamic behaviour driven by the distribution of stray fields at the edges of the pattern [24]. Off-axis electron holography is one of the few techniques that can be used to image these stray fields quantitatively.

This chapter first provides an overview of the theoretical background of chiral spin ice, as well as the required sample preparation. The techniques that are required for the advanced data analysis of electron holograms are then introduced and applied to investigate the magnetic state of the initial, not saturated samples and switching of the pattern. Finally, the stray fields of the chiral ice are probed and compared with theoretical predictions.

4.1. Theoretical background of chiral ice

In general, chirality is a property of an object, which describes the fact that it cannot be superimposed onto its mirror image. It is present in a variety of systems, ranging from a snail shell to elementary particles. Dynamic chirality refers to a preferred sense of rotation and holds for chiral and non-chiral objects. Chiral spin ice is a special case of the general concept of artificial spin ice. Here, nanomagnets are arranged in a two-dimensional lattice, with four nanomagnets meeting at a 90° angle with respect to each other at each vertex (Fig. 4.1a). The positioning of the individual nanomagnets makes it impossible to superimpose them onto their mirror image, in contrast to the more common square ice.

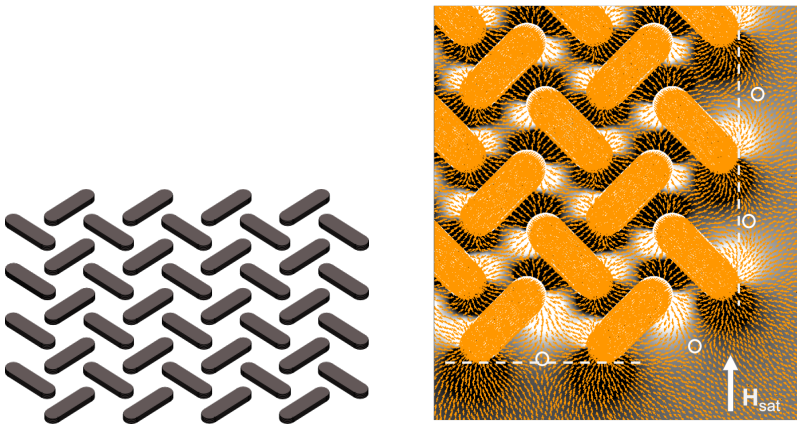

(a) (b)

Figure 4.1.: Chiral ice. (a) Schematic diagram showing an oblique view of a chiral ice consists of nanomagnets ordered in a specific arrangement that cannot be superimposed onto its mirror image. (b) Magnetic induction induced by a chiral ice pattern at remanence. The saturation field $\mathbf{H}_{\mathrm{sat}}$ was applied parallel to the right edge pointing upwards. The orange arrows indicate the direction of the magnetic induction. The magnetic induction inside the nanomagnets opposes the direction of the stray fields outside them. The dark and light contrast encodes the direction of the x component of the magnetic induction. The positions of virtual antivortices are indicated by white circles. They are located closer to the lower edge than to the right edge. The dashed lines are guide to the eye to indicate the edges of the pattern. Simulation and image by S. Gliga.

Gliga *et al.* showed that the rotation of the net magnetisation at the vertices of chiral ice has a unique direction after applying and removing a sufficiently large external magnetic field and then allowing thermally activated relaxation at room temperature [24]. The ratchet effect was confirmed by photoemission spectroscopy measurements [24]. The thicknesses of the nanomagnets were designed in such a way that their energy barrier was small enough to allow for switching at room temperature. Studies of the stray field arrangement using micromagnetic simulations revealed that the stray fields revolve around specific points (Fig. 4.1b), which are referred to as virtual antivortices, since they are not located inside the magnetic material itself [24]. Within the nanomagnet lattice, the virtual antivortices are arranged symmetrically. However, this symmetry is broken at the edges of the nanomagnet lattice, leading to an asymmetrical topology of the stray fields. The simulations revealed that this asymmetry is the reason for the ratchet effect [24]. However, the virtual antivortices could not be studied by the photoemission spectroscopy measurements since this technique does not provide direct information about the magnetic fields outside of the magnetic material itself.

4.2. Sample fabrication

Samples of chiral spin ice were prepared by S. Finizio at the Paul Scherrer Institute (PSI, Switzerland) by a standard electron beam lithography process using a double layer resist system (*cf.* Appendix A). Py was chosen as the material owing its very low magneto-crystalline anisotropy [13]. The nanomagnets were patterned onto a 100 µm x 100 µm large, 20 nm thick SiN membrane supported on a Si chip. The nanomagnets were designed to have sizes of 470 nm x 170 nm with a centre-to-centre distance of 424 nm. The thicknesses of the nanomagnets were designed to be 10 or 15 nm. The Py was deposited by thermal evaporation. The Ni content of the pellets used for evaporation was higher than the desired composition of $Fe_{17}Ni_{83}$, in order to compensate for the higher vapour pressure of Fe than of Ni at the same temperature [112]. A thin chromium (Cr) layer was deposited below and on top of the patterned structure using thermal evaporation. The layer below the Py increases adhesion of the Py to the membrane, while the layer on top protects the structures from oxidation. Nevertheless, the Cr was only applied directly onto the particles, leaving their sides unprotected. Therefore, a 10 nm aluminium (Al) layer was also deposited over the whole membrane by electron beam deposition in the Helmholtz Nanofacility cleanroom [113]. For Al deposition, the sample was stuck to the wafer using kapton tape to avoid

Table 4.1.: Parameters of the chiral ice samples. The first row gives the sample ID. Micromagnetic simulations of a structure with similar dimensions were compared to the experimental samples.

	si_18_45	si_10_45	si_10_45R	si_10_38	Micro-magnetic simulation
Pattern	chiral ice	chiral ice	mirror image of chiral ice	in-between state	chiral ice
Length [nm]	484	477	482	473	470
Width [nm]	183	183	182	171	170
Thickness [nm]	18	10	10	10	10
Centre-to-centre distance [nm]	446	457	454	456	424

breaking the membrane by clamping. Kapton is stable over a wide temperature range and does not outgas in vacuum [114]. After taking the samples out of the vacuum chamber, the first few nm of the Al oxidise, forming a protection layer over the sample. Another advantage of using continuous Al is that it reduces charging of the insulating SiN membrane when imaging the samples using an electron beam. Moreover, Al is a light metal and thus does not scatter the electron beam strongly. The latter point is important for off-axis electron holography experiments, where high coherence of the electron beam is desired.

In this thesis, chiral ice samples are investigated with nominal thicknesses of the Py islands of 15 and 10 nm. For the 10-nm-thick sample, three different patterns were fabricated: classical chiral ice, its mirror pattern and a state in-between the chiral ice. The chiral ice can be obtained from the square ice distribution by rotating every nanomagnet by an angle of 45°. The mirror pattern is achieved by mirroring the chiral ice at one edge. The chiral ice and its mirror pattern cannot be superimposed. The in-between state is obtained from the square ice by rotating every nanomagnet by an angle of 38°. This rotation angle corresponds to the transition between the square ice and chiral ice characteristics, but has a preference towards the chiral ice. Fig. 4.2 shows scanning electron microscopy (SEM) images of the various patterns taken in secondary electron (SE) mode. In the experimental setup, the samples are mounted upside down. Therefore, all images shown below are mirror images of the SEM images shown here. An overview of all of the samples is given in Table 4.1. Here, the actual thickness is given as measured in the next step of the analysis.

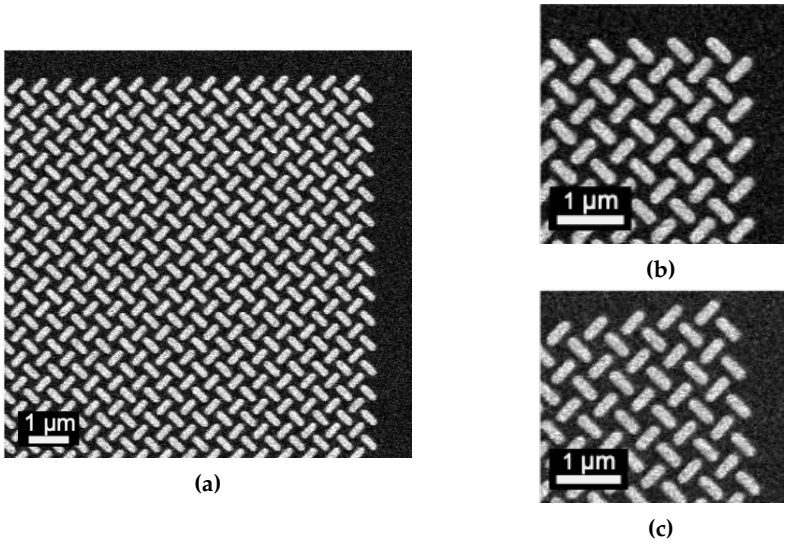

(a) (b) (c)

Figure 4.2.: SEM images taken in SE mode of chiral ice patterns. (a) Overview image of classical chiral ice; (b) Close up of the mirror pattern of chiral ice; (c) Close up of the in-between state. The images are taken by S. Finizio.

In order to further assess the quality of the sample fabrication, the thicknesses and chemical compositions of the samples were investigated in cross-section. One sample was investigated for each thickness, as all samples of the same thickness were deposited together and should have the same properties. Cross sections were prepared in a dual-beam focused ion beam (FIB) system and investigated using HAADF and EDX spectroscopy in a probe-aberration-corrected transmission electron microscope (FEI Titan G2 60-200) operated at 200 kV [115]. All sample preparation by FIB milling shown in this and the following chapters was carried out by M. Kruth (ER-C, FZJ), including SEM studies. A. Kovács (ER-C, FZJ) performed the STEM, HAADF imaging and EDX measurements. Images of a cross-section of a 10-nm-thick sample are shown in Fig. 4.3. The HAADF image shows that the particle has a stripe-like geometry, with a mostly uniform thickness. The thickness of the particle is measured to be 10 nm, which is consistent with the nominal thickness. Nevertheless, it becomes thinner at both ends. The platinum/carbon (Pt/C) on top of the Al capping layer is the protective layer deposited during the FIB milling. The chemical composition was measured by EDX and shown in Fig. 4.3b. Figure 4.3c shows a profile of the chemical composition of the nanomagnet. Before generating the linescan, the image was smoothed using a Gaussian filter and an averaging filter. The linescan reveals 65% Ni and 35% Fe, which is a higher Fe content than expected. A higher Fe content has been shown to increase saturation magnetisation [116]. Moreover, a small amount of oxygen is present throughout the sample and the surfaces of the particles are oxidised. Oxidation reduces the magnetic thickness of the particles compared to the thickness measured using HAADF STEM. The same analysis was performed for a nominally 15-nm-thick sample. Here, it can be seen that the composition is similar to the 10 nm thick samples (*cf.* Fig. 4.4). However, the thickness is close to 18 nm and thus 20% thicker than the nominal value. Moreover, there is slight bending of the nanomagnets, whose origin is discussed in Sec. 5.3.1.

4.3. Data analysis

In off-axis electron holography experiments, phase information needs to be extracted from recorded holograms and further processed to obtain information about the magnetic properties of the sample. Data analysis was performed in Python using customised scripts employing the HyperSpy package [118] and the Pyramid package based on Ref. [61]. However, these packages do not offer all of the required functionalities for full data analysis. Therefore, several custom-made functions were also used. These functions offer distortion correc-

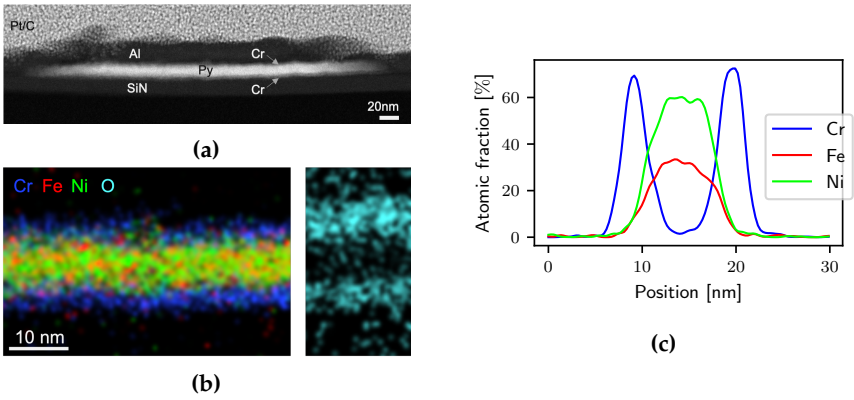

Figure 4.3.: Cross-sectional view of a nominally 10-nm-thick Py nanomagnet. (a) HAADF STEM image; (b) Compositional maps of the central region of the Py island; (c) Averaged compositional line profile across the particle. The thickness of the Py island is measured to be 10 nm with a chemical composition of approximately $Ni_{65}Fe_{35}$. Adapted from [117]

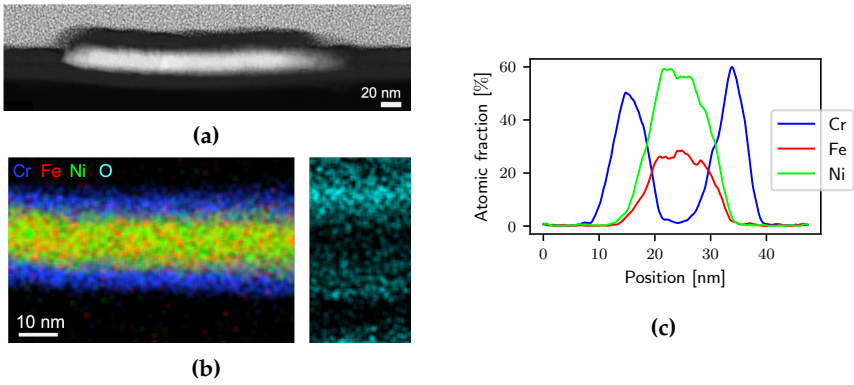

Figure 4.4.: Cross-sectional view of a nominally 15-nm-thick Py nanomagnet. (a) HAADF STEM image; (b) Compositional maps of the central region of the Py island; (c) Averaged compositional line profile across the particle. The thickness of the Py island is measured to be 18 nm with a chemical composition of approximately $Ni_{65}Fe_{35}$.

tion, stitching, and automated particle detection, as described in this chapter. In addition, it is shown how to compute the three-dimensional magnetic induction from a known magnetisation distribution.

4.3.1. Automated detection of particles

A knowledge of the positions of the particles in spin ice samples is essential, *e.g.* for reconstruction of the magnetisation. Usually, masks are required to mark regions that contain magnetic material [61]. These masks can be created on the basis of amplitude images or electrostatic phase shift maps. However, this procedure may leads to subjective or inaccurate results if it is carried out manually. Hence, an automated particle detection algorithm based on the application of a threshold to electrostatic phase images was developed. The resulting masks could be corrected by hand if individual pixels were not assigned correctly.

The starting point for the detection of the particles is the electrostatic contribution to the phase images. Figure 4.5a shows a representative electrostatic phase image of Py islands in a chiral ice configuration on a SiN membrane. It contains two dominant values of the electrostatic phase shift: one for the Py particles and one for the membrane. Figure 4.5b shows a histogram generated from the electrostatic phase image that contains the two peaks. The threshold between the two peaks is detected following Otsu's method [119]. Here, the image is separated into two classes: the particles and the membrane. The threshold is determined in such a way that the variance in each class is as low as possible, while the variance between the two classes is as large as possible. This method works as long as the two classes have little overlap, which is the case for the Py particles on the SiN membrane. The detected threshold is indicated as a red line in the histogram in Fig. 4.5b. All of the pixels in the electrostatic phase image that have a smaller value than the threshold are attributed to the SiN membrane, while all of the pixels with a larger value are attributed to the Py particles. The resulting mask is shown in Fig. 4.5c.

The mask incorrectly attributes several pixels on the SiN membrane to the Py particles due to the presence crystal grains of Al, noise and small dirt particles on the membrane. Moreover, the Py islands have apparent holes, where pixels are attributed to the SiN membrane. Therefore, the mask needs to be processed further. First, the particle regions are made smaller using binary erosion (Fig. 4.5d) to reduce the size of the faulty pixels at the cost of reducing the size of the correctly detected particles at the same time. Then, the residual faulty pixels are removed by comparing the mask with a median-filtered version of itself

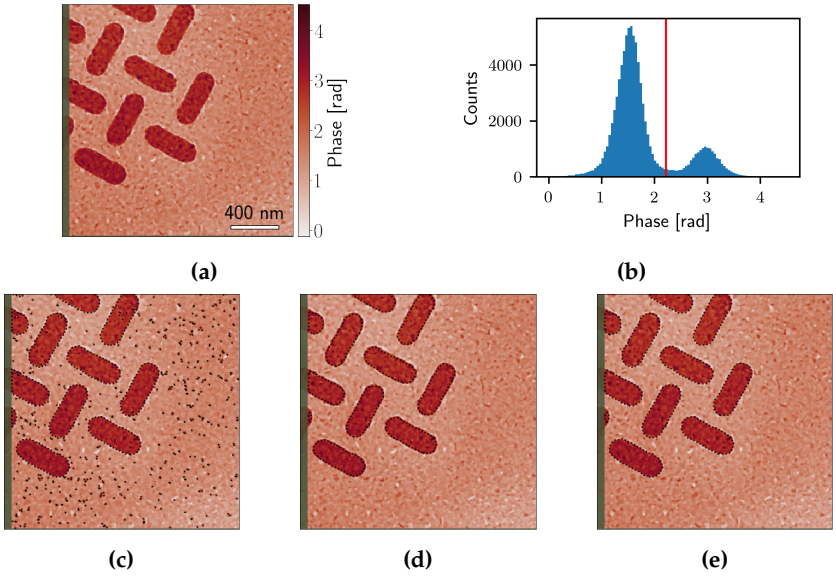

Figure 4.5.: Automated detection of masks around particles deposited on a SiN membrane for sample si_10_45 (Table 4.1). (a) An electrostatic phase image is used as input to determine the positions of the particles. (b) Histogram of the electrostatic phase image with the selected threshold between particles and the membrane marked in red. (c) Phase image and mask after applying the threshold. (d) Phase image mask after binary erosion to remove outliers. (e) Phase image and mask after binary dilation to account for previous erosion.

[120]. Afterwards, the particles are enlarged again by binary dilation (Fig. 4.5e). This approach closes the residual holes inside the particles, while compensating for making the area smaller by the earlier erosion. The resulting mask is in good agreement with the visible edges of the particles. The small dirt on the membrane is then also not attributed to the mask. Nevertheless, there are still small deviations between the detected mask and the visible edges of the sample, which have to be corrected by hand. In this way, particle detection is reliable and speeds up data analysis significantly by omitting the time-consuming task of drawing a mask manually.

4.3.2. Removal of a phase ramp in the presence of magnetic stray fields

Magnetic phase shift images often contain a phase ramp due to, *e.g.*, slight misdetection of the side band position. This phase ramp has to be removed before analysing the magnetic properties of the sample. It is normally removed by fitting a linear function to a region outside the magnetic material. However, the ramp may overlap with the long-range magnetic stray field of the particles inside and outside of the FOV. In the case of spin ice samples, this effect is more significant than for a magnetic vortex, as vortices do not have stray fields (see Sec. 2.4.1). Therefore, a more sophisticated approach was used here to remove the phase ramp. This approach is based on MBIR, which can fit a linear phase ramp while considering the stray field at the same time (*cf.* Sec. 3.2.5). A small regularisation parameter of $\lambda = 1 \cdot 10^{-8}$ was chosen to ensure high compliance with the measured phase and minimal regularisation. Another advantage of this approach is that is does not require a large area without magnetic material, which is usually required to fit a linear function. Therefore, it is possible to image more Py islands within the FOV.

Figure 4.6 shows an example of phase ramp removal from experimental data recorded from a chiral spin ice (sample si_18_45) using MBIR. Figure 4.6a shows the original magnetic phase image, while Fig. 4.6b shows the phase ramp and offset detected by the MBIR algorithm. The corrected magnetic image map (Fig. 4.6c) is obtained by subtracting the fitted phase ramp and offset from the original image. The effect of the correction can be seen in the resulting magnetic induction maps. Figure 4.6d shows a magnetic induction map before correction and Fig. 4.6e after correction. After correction, the phase contours are parallel to the long axes of the Py particles. Such parallel alignment is reasonable, as the particles are expected to have an Ising-like magnetic states.

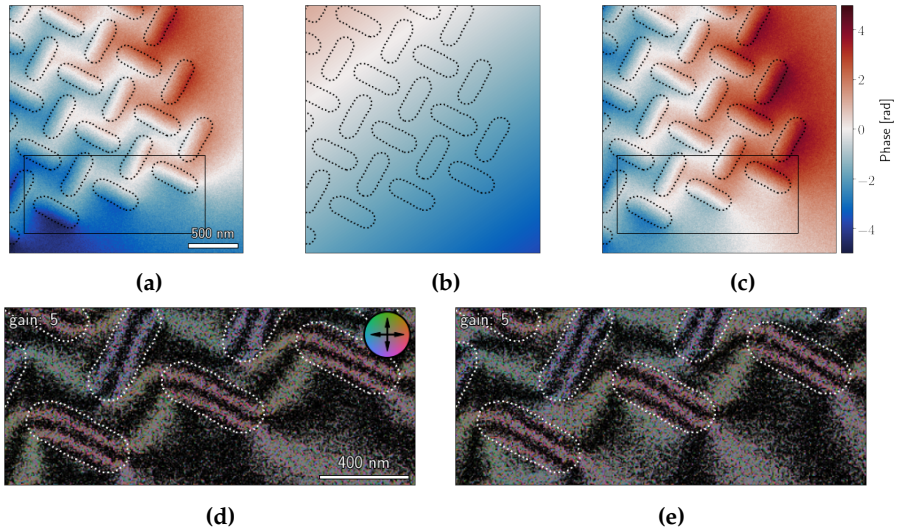

Figure 4.6.: Removal of phase ramp using the MBIR algorithm. (a) Magnetic phase image before phase ramp correction; (b) Detected phase ramp; (c) Magnetic phase image after correction. (d) and (e) show corresponding magnetic induction maps (d) before and (e) after removal of the phase ramp for the region marked with a black rectangle in (a) and (c), respectively.

4.3.3. Image distortions and warping of phase images

One way to separate magnetic and the electrostatic contribution to the phase is to turn the sample over inside the microscope (*cf.* Sec. 3.2.4). However, each image is then distorted by the optical system of the electron microscope. These distortions have to be corrected in order to remove the resulting artefacts [104]. Only if the distortions are minor can physical turning over of the sample be compensated simply by flipping the phase images about the holder axis during data analysis. Here, the holder axis is located at -17° with respect to the *x*-axis of the phase image. Therefore, turning during data analysis is divided into two steps. First, one of the phase images is mirrored at the *x*-axis. Second, this phase image is rotated by -34° to compensate for rotation of the holder axis. Then, the two phase images are aligned and compared to retrieve the electrostatic and magnetic contribution to the phase.

In general, the image distortions are not negligible. In addition, change with respect to the sample between direction the two phase images when the sample is turned over. Correction for the distortions is challenging, as they are unknown and complicated across the FOV. A pragmatic approach is to warp the images until they match each other. Here, it is assumed that the first phase image is correct. The digitally flipped over phase image is then warped to match the first one. For warping, several equivalent positions are marked on both images. A representative selection of such points is shown in Fig. 4.7 on an example phase image. Phase images A and B show the total phase of a chiral ice sample before and after turning respectively. In both images, features on the particles are used to identify identical locations by marking them by hand. Phase image B is first rotated to make identification of these locations easier. The best results are be obtained when setting markers across the full FOV. The markers are used to estimate an affine transformation that maps the points onto each other. Affine transformations preserve straight lines and keeps them parallel if they are parallel in the original image. The influence of a single marker depends on its distance from the other markers, as the larger the distance is the more weight the marker has in the transformation. Hence, its positioning is important. An inverse affine transformation is applied to phase image B, in order to obtain phase image B_{corr}, as shown at the lower right of Fig. 4.7. The lower left image shows the sum of phase image A and B_{corr} and corresponds to twice the electrostatic contribution to the phase. In this case, the warping achieved a good match, as the particles do not show significant distortions or contrast variations.

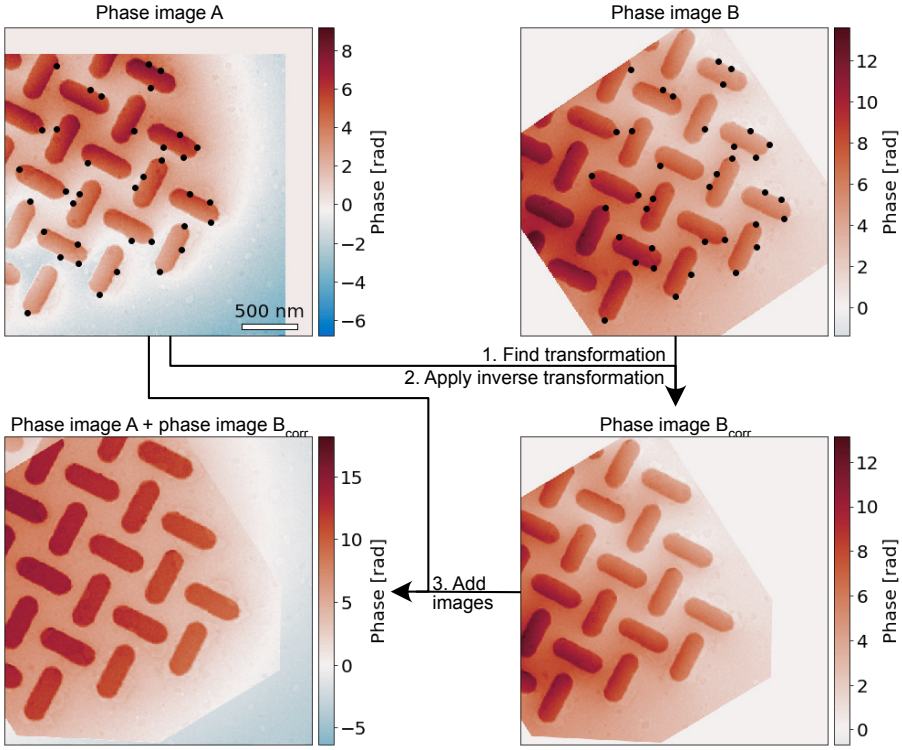

Figure 4.7.: Illustration of removal of distortions from a pair of phase images. Phase images A and B were recorded before and after turning the sample over. Dots mark identical locations and are used to estimate an affine transformation. An inverse transformation is applied to phase image B to create phase image B_{corr}. The sum of images A and B_{corr} corresponds to twice the electrostatic contribution to the phase.

4.3.4. Stitching of multiple phase images

The study of spin ice samples using off-axis electron holography requires the analysis of multiple individual nanomagnets which requires using a large FOV without compromising spatial resolution. However, a large FOV in a single hologram requires large biprism voltage, which reduce the signal to noise ratio in the reconstructed phase image (see Sec. 3.2.3). In practice, the FOV is usually limited to approximately 2x2 μm^2 in Lorentz mode, when studying internal fields of particles in chiral spin ice structures. Therefore, multiple holograms from adjacent areas need to be recorded and the resulting magnetic phase images or reconstructed magnetisation distributions combined into larger images. Such a stitching routine is described in this section for a simulated magnetic phase shift of a small chiral lattice. Two regions are initially cut from this phase image (Fig. 4.8a and Fig. 4.8b). Each of the two smaller phase image has a size of 622x562 $pixel^2$ and they share an overlap of 60x312 $pixel^2$. For each of the phase images, the corresponding particle mask is known since it is defined for the simulation. These masks are similar to those detected for experimental images in Sec. 4.3.1. However, it is assumed that the alignment of the two phase images is unknown. The starting point for the demonstration of stitching is therefore the two phase images, with their corresponding masks but an unknown alignment. The first step required for stitching the two phase images together is to determine the shift between them. As magnetic phase images do not offer clear features that can be used for the alignment, binary particle masks are employed because of their sharp boundaries, which can be used as features for alignment procedures. In each mask, an overlapping area is specified. It is necessary to indicate the overlap by hand as the program cannot match the particles in both images because they are too similar. The masks are represented by dotted lines and the overlap regions by the black squares in Fig. 4.8a and Fig. 4.8b. The shift between the images is determined by a cross correlation with single pixel accuracy. The two phase images are then stitched together by shifting one of them with respect to the other one. In the region where the phase images overlap, the average of the magnetic phase shift of each pixel is calculated and used in the stitched image. Figure 4.8c shows the result of the stitching process. The resulting phase image is in good agreement with the initial large phase image confirming the success of the stitching process.

In practice, experimental phase images are not as perfect as simulated ones and may be corrupted in different ways. The three main issues are as follows:

- Imperfect masks: Masks are often created from electrostatic phase images. However, it is often impossible to create a mask with single pixel accuracy,

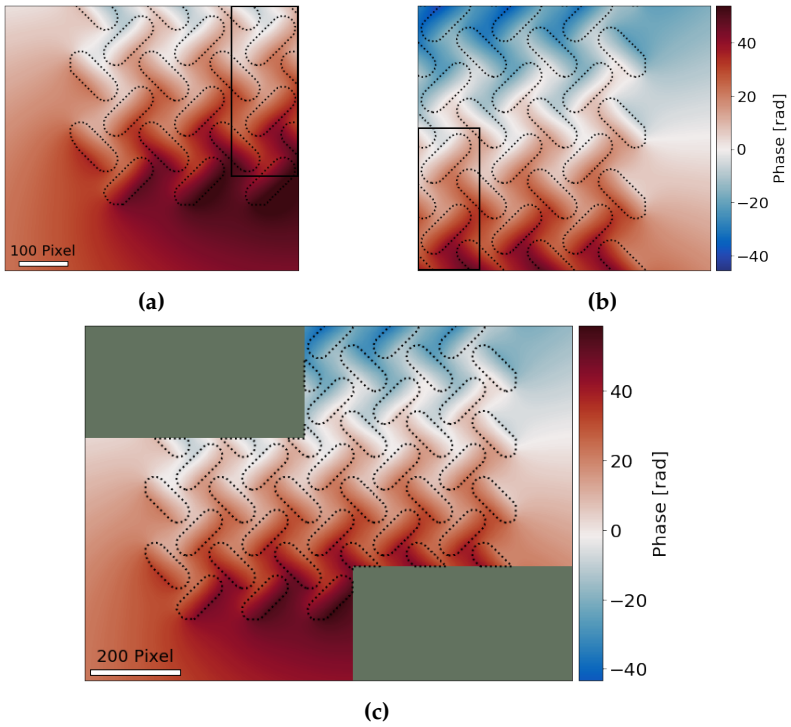

Figure 4.8.: Stitching process of phase images. (a) and (b) Two simulated phase images with an overlap (black rectangles). The overlap region is identified by hand. (c) The two phase images are stitched together after using the image shift determined from the mask. See text for details.

as the edges of the particles are not perfectly sharp.

- Residual phase ramps and offsets between the phase images: These can originate from inaccurate determination of the sideband position or stray fields, which differ between the images and could not be corrected perfectly. For spin ice, the stray fields have a major effect on data analysis, as the stray fields of nanomagnets that are outside the FOV affect the phase shift inside of the FOV. In addition, correction of the phase ramp for each experimental phase image includes an arbitrary choice of phase offset.

- Noise: Noise is present in all phase images even though its level varies from experiment to experiment. For chiral ice, the signal to noise ratio is low due to small (<1 rad) magnetic phase shifts of the thin nanomagnets.

The influence of these imperfections was first investigated by impairing the original masks and adding a phase ramp to the second phase image of 4.8 mrad/pixel in the x direction and -3.5 mrad/pixel in the y direction. In addition, a phase image with random values following a Gaussian distribution was generated using a mean of 0 and a sigma of 1 pixel. This random phase image was added to represent noise in the original phase image. Figures 4.9a and 4.9b show the impaired phase images. A confidence map was created to exclude regions, where the magnetic phase shift is not trustworthy, from the analysis. For experimental data, these region may be a result of the need to align the two total phase images leaving areas at the edges where only information from one phase image is present. In order to exclude those regions, the confidence there was set to 0, while it was set to 1 in the rest of the phase image. The image shift between the two phase images was determined using the corrupted masks. Reassuringly, the image shift was still detected perfectly (Fig. 4.9c). Afterwards, the phase images were stitched together using the image shift. During stitching, the phase offset and ramp had to be corrected in the second phase image. For correction, a two-dimensional linear function was fitted to the difference between the two magnetic phase images in the overlap region, with the fitting constants describing the phase offset and ramp. Subsequently, the fitted ramp and offset were subtracted from the entire second phase images. Finally, the average of both magnetic phases is taken in the overlap region. The resulting phase images is shown in Fig. 4.9c. The initial phase image (*i.e.* with noise but without a phase ramp or offset) was subtracted from the framed area in order to assess the error resulting from fitting the phase ramp and offset (*cf.* Fig. 4.9d). The error in the fitted phase ramp is determined to be 5.1 mrad/pixel in the x direction and -3.5 mrad/pixel in the y direction, which would result in an overall error in the phase ramp of 138.1 and 18.9 mrad in the x and the y direction,s respectively.

This error in the phase ramp is negligible compared to the overall phase shift of 80 rad. Therefore, the stitching routine is considered to be stable and can be applied to experimental data without introducing significant artefacts.

The effect of an incorrect image shift was also investigated by deliberately shifting one of the images. The phase images are shifted by 2 pixels in the x and the y directions. As before, the simulated phase images and masks included noise and a phase offset to reproduce the conditions found in experimental phase images. Figure 4.9e shows the resulting combined phase images, in which the deliberate image shift is too small to be recognisable by eye. Nevertheless, it corrupts the fitted phase offset and ramp. The phase ramp was determined to be 3.0 mrad/pixel in the x direction and -3.3 mrad/pixel in the y direction, which is a larger deviation from the nominal values (4.8 mrad/pixel in the x direction and -3.5 mrad/pixel in the y direction) compared to the unshifted case. The error is made visible by subtracting the known phase from the stitched image (Fig. 4.9f). The misfit in the x direction is more severe because there is a smaller overlap compared to the y direction. Overall, there is an error due to the phase ramp of 0.9 rad in the x direction and 0.1 rad in the y direction. Both phase ramps are still small when compared to the overall magnetic phase shift. Nevertheless, this misfit will increase cumulatively if another image is stitched next to the first two. Therefore, it is important to determine the image shift with the possible available accuracy. The use of cross correlation to determine the image shift has proven to be stable in the presence of noise. Therefore, an error in the image shift is not expected to be an issue for stitching the experimental phase images.

4.3.5. Computation of magnetic induction from a known magnetisation distribution

A knowledge of the stray fields of spin ice elements is essential in order to locate the position of virtual antivortices. Off-axis electron holography can be used to obtain this information quantitatively when combining it with the MBIR algorithm. First, the magnetisation of the spin ice is reconstructed using the MBIR introduced in Sec. 3.2.5. Second, the magnetic vector potential and magnetic induction are calculated from the reconstructed magnetisation. The resulting magnetic induction provides the required information about stray fields.

Computation of the magnetic induction is achieved by expressing the magnetic

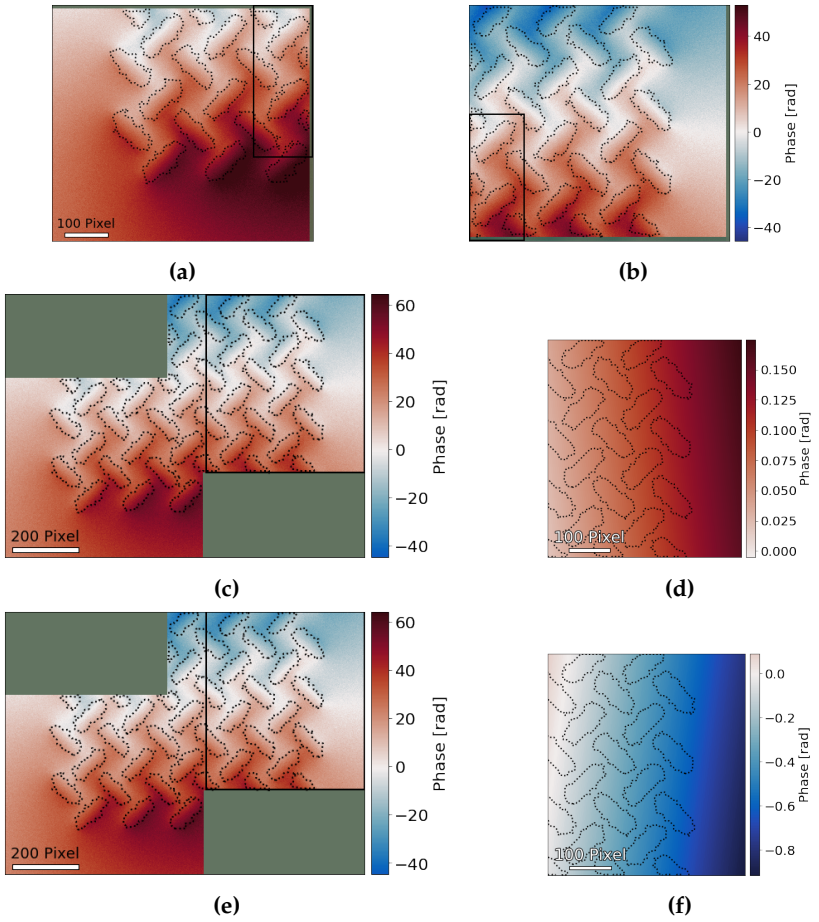

Figure 4.9.: Stitching process of phase images. (a, b) Two simulated phase images with an overlap (black rectangles). The overlap region is identified by hand. The phase shift and the masks are corrupted by noise. In addition, a phase ramp is added to phase image (b). (c) The images are stitched together. The image shift is still determined correctly, despite the use of impaired masks. (d) Difference between the marked region in (c) and the original phase phase (Fig. 4.8a) revealing a small residual phase ramp. (e) Phase images from (a) and (b) stitched together with an intentional misfit of 2 pixels in the x and 2 pixels in the y directions. (f) Difference between the black framed region in (e) and the original phase image showing a larger error in the residual phase shift compared to use of the correct image shift.

vector potential **A** as an integral of the magnetisation, in the form [121]

$$\mathbf{A}(\mathbf{r}) = \frac{\mu_0}{4\pi} \int d\mathbf{r}' \mathbf{M}(\mathbf{r}') \times \frac{\mathbf{r} - \mathbf{r}'}{|\mathbf{r} - \mathbf{r}'|^3}. \tag{4.1}$$

A closer look at the vector product reveals that **A** is a convolution of the magnetisation **M** with the kernel $\frac{\mu_0}{4\pi}\frac{\mathbf{r}}{|\mathbf{r}|^3}$. Thus, a convolution in Fourier space can be used to yield the three-dimensional Fourier transform of the vector potential: $\mathcal{F}_3\{\mathbf{A}(\mathbf{r})\} = \frac{\mu_0}{4\pi}\mathcal{F}_3\{\mathbf{M}(\mathbf{r})\} \times \mathcal{F}_3\{\frac{\mathbf{r}}{|\mathbf{r}|^3}\}$. The magnetic vector potential can therefore be obtained by taking the inverse three-dimensional Fourier transform of this expression. The magnetic induction **B** can then be calculated from the magnetic vector potential according to Eq. 3.9.

During data analysis, only the projected in-plane distribution of **M** is retrieved using off-axis electron holography in the presented work. Hence, the three-dimensional distribution of **B** can be retrieved only based on a two-dimensional distribution **M**. Fortunately, spin ice samples are sufficiently thin to assume that within each nanomagnet **M** along the z direction is constant. Before computation of **A** and **B**, a three-dimensional pixel array needs to be defined typically in the form of a three dimensional data cube. The central slice contains the information about **M**. A pixel to nm conversion in the x and the y directions is obtained from the **M** array. The corresponding conversion in the z direction is obtained from the thickness of the sample, such that the projected distribution of **M** is contained in a single slice. Empty slices are included above and below the middle slice to created three-dimensional array. **A** and the **B** are then computed using Eq. 4.1 and Eq. 3.9. In this way, the required information about the stray fields is retrieved in all three dimensions. Each slice contains the distribution of **B** averaged over a distance equivalent to the thickness of that slice which corresponds to the thickness of the sample. The stray fields can be interpreted for each single slice or they can be integrated over all slices. Integration along the z direction corresponds to the accumulation of phase shift which is experienced by electrons travelling through the sample in the TEM. Hence, the stray fields integrated along the z direction can be compared to the experimental magnetic phase images. The data cube is large enough to account for their long-range nature.

4.4. Initial magnetic state of chiral ice

In a first step, the initial magnetic state of the 18-nm-thick sample (si_18_45, *cf.* Table 4.1) was investigated using off-axis electron holography. In order to not alter its magnetic properties, the approach of turning the sample over was used to separate the electrostatic and the magnetic contributions phase shift by using a dedicated holder [104]. In order to image many nanomagnets over a large FOV, several holograms were recorded and their resulting electrostatic and magnetic phase images were stitched together after reconstruction. The experimental procedure can be summarised as follow:

1. Acquisition of multiple holograms with overlapping regions of the sample. The size of the overlap was chosen to balance the demand to image as many particles as possible, *i.e.* using a small overlap, with the requirement imposed by stitching the images together later. A large overlap is needed to detect the image shift and to correct the phase ramp and offset. Figure 4.10 shows an off-axis electron hologram recorded at 6.900x magnification and 190 V biprism voltage. This setup results in an interference fringe spacing of 1.4 nm.

2. Acquisition of reference hologram. The spin ice samples typically have no vacuum area that can be used to record a reference hologram. Therefore, the sample was partially retracted using the dedicated holder to record the reference hologram [104]. Successive holograms should be recorded immediately after each other to ensure that the imaging conditions change as little as possible.

3. Turning the sample over inside the microscope using the holder to avoid exposing the sample to the residual stray field of the objective lens [104].

4. Acquisition of multiple holograms at the same position as the holograms taken in step 1), taking into account that the turning axis of the holder is rotated with respect to the x and the y directions of the detector. The image is rotated, in addition to being flipped.

5. Acquisition of reference hologram by retracting the sample.

After recording the holograms, the magnetic induction was reconstructed. First, the complex wavefunction were reconstructed, using the reference holograms to locate the sideband position and remove camera distortions. A slight Gaussian filter was applied to the complex wavefunctions, in order to reduce noise. The total phase was extracted from the complex wavefunction and unwrapped using

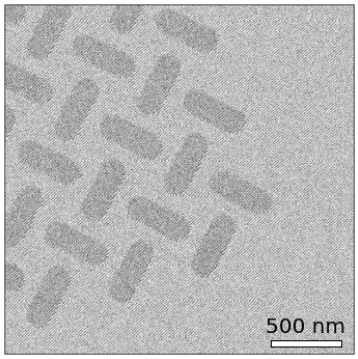

Figure 4.10.: Off-axis electron hologram of the initial state of spin ice si_18_45 sample recorded using a biprism voltage of 190 V at 6.900x magnification.

suitable algorithms available in the HyperSpy package [118]. The electrostatic and magnetic contributions to the phase were then obtained from the total phase images by adding or subtracting half of the phase images of the same region. In this step, the second phase image was flipped over and warped to match the first phase image (*cf.* Sec. 4.3.3). Both the magnetic and the electrostatic contribution to the phase may have phase ramps. For the electrostatic contribution, the phase distribution should be flat outside the Py islands, since it only depends on the mean inner potential (MIP) of the SiN membrane. Therefore, a linear function in the x and y directions can be fitted to the membrane area and used to remove the phase ramp. For the magnetic contribution, the nanomagnets induce stray fields that extend into the membrane region. Thus, a simple fitting of a linear function is not appropriate. Instead, the MBIR algorithm was employed to remove the phase ramp, taking the induced stray fields into account (see Sec. 4.3.2). The last step involves stitching the multiple phase images together (*cf.* Sec. 4.3.4). For this purpose, a mask of all of the particles in the individual images was created using the routine described in Sec. 4.3.1.

A final stitched electrostatic phase image is shown in Fig. 4.11a. A slight residual phase ramp, with the phase increasing towards the lower left corner, is apparent across the large FOV. Nevertheless, it is sufficiently small to be able to clearly distinguish the nanomagnets from the SiN membrane. The electrostatic phase shift is similar for each nanomagnet, indicating a homogeneous thickness distribution (see close-up in Fig. 4.11a). Figure 4.11b shows a corresponding magnetic phase shift, which can be used to determine the local direction of the projected in-plane magnetic induction by computing its gradient according to Eq. 3.13 (Fig. 4.11c).

The magnetic induction follows the long axis for each particle, as expected due to the shape anisotropy of the sample (*cf.* Sec. 2.3). The net magnetic induction points upwards along the right edge of the pattern, suggesting that the chiral ice sample may have been exposed to an external magnetic field between its preparation and this investigation. The magnetic stray fields inside the pattern follow a zigzag pattern, connecting the magnetic field lines between the nanomagnets in each row. Interestingly, five of the particles oppose the net alignment (marked by white ellipses in Fig. 4.11c). The switching mechanism of the nanoparticles is investigated in detail in Sec. 4.5.1.

The direction of the magnetic induction with respect to the long axes of the nanomagnets was further investigated by looking at the angular distribution of the induction. The grey histogram in Fig. 4.12 shows the direction of the magnetic induction for each pixel. Two peaks can be identified, corresponding to the majority of the particles pointing in the direction of the net magnetic induction, but along their length. The peak at 117 ° is slightly higher than the peak at 26 ° all of the particles whose long axis points towards the upper left corner following the net magnetic induction while five of the particles point into the upper right corner oppose it (Fig. 4.11c). These five particles correspond to the peak at 201°. The resulting disorder has an effect on the magnetic induction of the surrounding particles. For example, the magnetic induction of a yellow particle in between two red ones in the centre of the magnetic induction map (Fig. 4.11c) is canted with respect to the long axis of the particle. In order to investigate this canting, the average direction of the magnetic induction was computed for each particle.[1] The average direction of the magnetic induction for each particle is shown in colour in the form of a histogram in Fig. 4.12. The selection of these corresponds to the colours used to visualise the direction of the magnetic induction (Fig. 4.11c). The peaks at 26° and 117° are rather sharp, while that at 201° is spread over a wider range. The particles that deviate the most from the centre of the peak are close to these opposing the net magnetic induction direction. This deviation underlines the importance of taking magnetostatic interactions and stray fields into account during data analysis, as they can have strong effects on the magnetic state of the surrounding particles.

[1] In order to compute this average, the components of the magnetic induction were converted into complex numbers and averaged before converting them back to polar coordinates. This step is necessary because standard averaging algorithms cannot take into account the fact that particles at 350° contribute to the peak as at 30°.

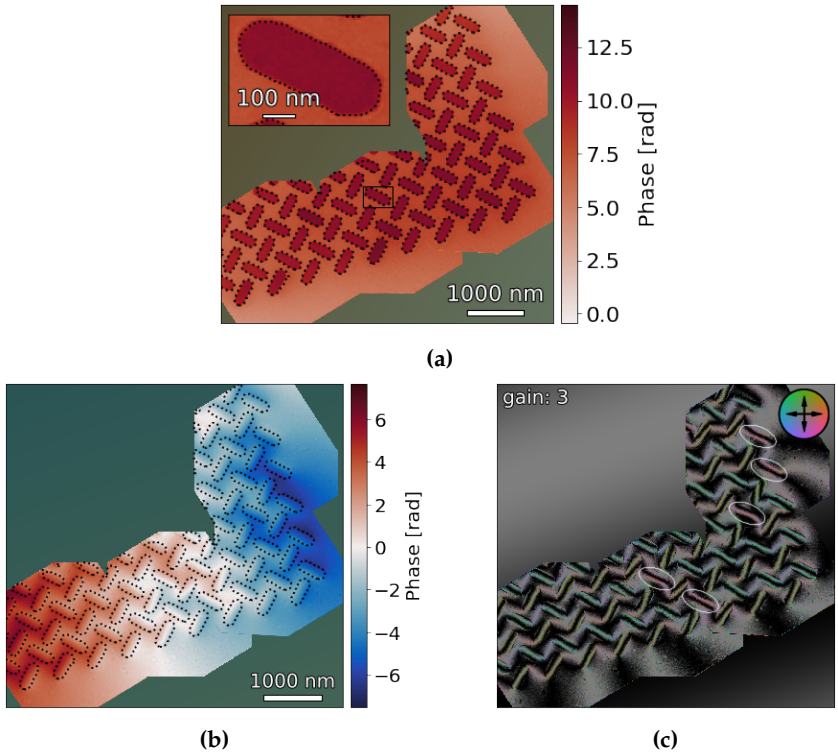

Figure 4.11.: Electrostatic and magnetic contributions to the phase for the initial state of chiral ice (si_18_45). In each case, four phase images are stitched together. (a) Electrostatic phase image in which the individual particles can be distinguished. The positions of the particles are indicated by dotted lines. The inset shows a close-up of the particle indicated by a rectangle. (b) Magnetic phase shift and (c) corresponding magnetic induction map. Most particles follow the overall net magnetic induction (pointing upwards). Interestingly, five particles (indicated by white ellipses) oppose the net magnetic induction, also affecting the direction of the magnetic induction in neighbouring particles.

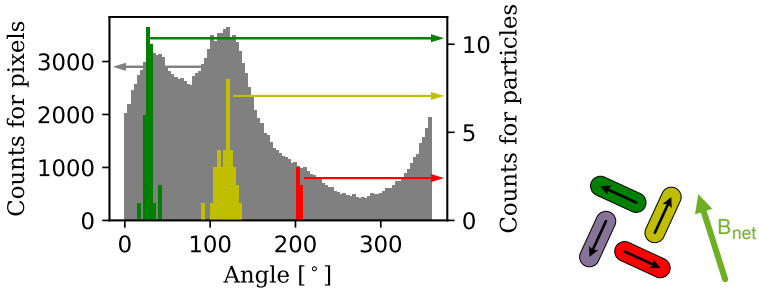

Figure 4.12.: Histogram showing the direction of the magnetic induction (Fig. 4.11c) for each pixel in grey and the average magnetic induction for each particle in colour. Particles belonging to the green peak follow the net magnetic induction, while particles belonging to the red peak oppose it, as indicated by the legend on the right. The yellow peak are spread over a wide range of angles because they are affected by the magnetic induction of the particles opposing the net magnetic induction.

4.5. Effect of external magnetic field on chiral ice

In the previous section, the effect of nanomagnets opposing the net magnetic induction is discussed. This effect has to be prevented from appearing for the analysis of the virtual antivortices. Therefore, the field required to switch all nanomagnets is investigated in the next step. The consequences of the sample oxidation are shown by studying emergent vortices within the nanomagnets. This analysis was carried out using the same sample as above (si_18_45).

4.5.1. Magnetic fields required for switching of artificial spin ice pattern

The switching field that is required to flip all of the nanomagnets was determined for the case when the external field is applied parallel to the edge of the pattern, *i.e.*, at 45° angle to the long axes of the nanomagnets. Off-axis electron holograms were recorded at remanence after applying different external magnetic fields with the objective lens to a tilted sample. The magnetic and the electrostatic contributions to the phase were separated by recording pairs of holograms between which the magnetisation of the nanomagnets was saturated in opposite directions. In order to obtain sufficient statistics, several phase images were

stitched together, just as in the case of the initial state of sample (*cf.* Sec. 4.4). The workflow for data acquisition included the following steps:

1. The sample was mounted in the holder in such a way that the edge of the pattern was parallel to the tilt axis of the holder.
2. The sample was tilted to -75° in zero field and a vertical magnetic field of 1.5 T was applied using the objective lens of the microsope, corresponding to an in-plane component of the applied field of approximately 1.45 T, which is sufficient to saturate the sample in one direction. The sample was tilted back to 0° in zero field and multiple holograms of one corner of the pattern were recorded at a magnification of 6,900x using a biprism voltage of 203 V.
3. The sample was tilted to +75° in zero field and a vertical magnetic field of 1.5 T was applied using the objective lens. Subsequently, the sample was tilted back to 0° in zero field and holograms were recorded at the same positions as in the first step.
4. The sample was tilted to -75° in zero field and saturated using the objective lens. Subsequently, it was tilted to +75° in zero field, a smaller magnetic field was applied, the sample was tilted back to 0° in zero field and holograms were recorded at the same positions as before. This step was repeated for applied vertical fields of 17.5, 20, 22.5, 25 and 30 mT, corresponding to in-plane components of the applied field of 16.9, 19.3, 21.7, 24.1 and 29.0 mT, respectively.

The first step during data analysis was to determine the electrostatic contribution to the phase from holograms recorded after saturating the sample in opposite directions. Just as for the initial-state-measurements, the total phase shift was reconstructed by applying a small Gaussian filter to each complex wave function to reduce noise in the phase images. During this process, image distortions did not need to be corrected as the sample had not been turned over. Only the image shift was determined by performing a cross correlation of the two phase images. After cross correlation, half of the sum of the two total phase images was calculated to obtain the electrostatic phase shift. The magnetic phase shift for each value of applied field was retrieved by subtracting the electrostatic phase shift from the total phase shift. Finally, the phase ramp and offset were removed by the MBIR approach (see Sec. 4.3.2) and the individual phase images were stitched together (see Sec. 4.3.4)

Figure 4.13a shows a magnetic induction map corresponding to a magnetic state after saturation with a 1.45 T in-plane field. The magnetic induction field lines inside the particles are aligned in response to the direction of the saturation field,

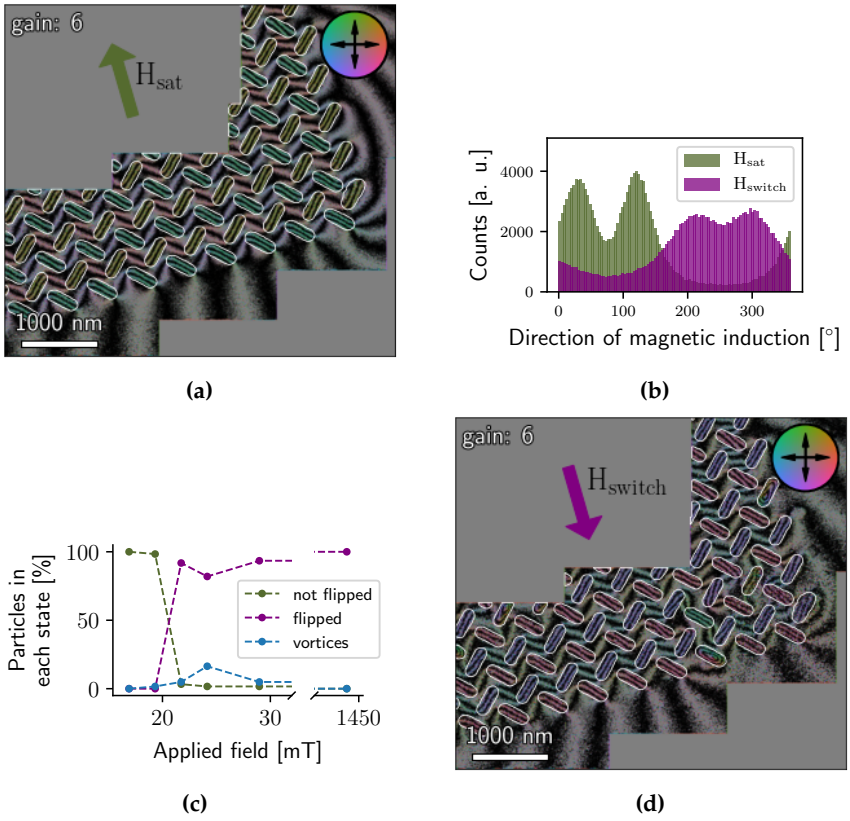

Figure 4.13.: Magnetic switching of chiral ice sample si_18_45. (a) Magnetic induction map using a 1.45 T field H_{sat}. The magnetic induction follows a zigzag pattern, while it aligned with the applied field inside the particles (outlined by white ellipses). (b) Plot of the directional dependence of the induction inside the particles after saturation in green (H_{sat}) and after applying a field of 21.7 mT in the opposite direction in purple (H_{switch}). (c) Percentage of particles flipped after saturating the sample and applying a switching field in the opposite direction. (d) Magnetic induction map after applying a switching field of 21.7 mT in the opposite direction.

while the stray fields between them follow a zigzag-like pattern, connecting the magnetic induction inside the particles in each row of particles. Figure 4.13b shows the average direction of the magnetic induction in each particle labelled H_{sat}. The two peaks correspond to the two different orientations of the particles with respect to the direction of the applied field. The peaks are sharp, as a result of the good alignment of the magnetic induction inside each particle with respect to the saturation field on applying a switching field opposing the saturation field. It is found that neither 16.9 nor 19.3 mT is sufficient to switch the magnetic state of the particles as illustrated in Fig. 4.13c. The particles only reversed after applying a switching field of 21.7 mT. Figures 4.13d and 4.13b show a magnetic induction map for the reversed state and the direction of the magnetic induction inside of the particles, respectively. The distribution (H_{switch} in Fig. 4.13b) is broader than that for the fully saturated state, as the applied 21.7 mT field is not sufficient to align the particles perfectly. It is noteworthy that two particles are not flipped, as seen in the induction map. The small fields that are required to change the magnetic state of the sample underlines the importance of realising magnetic-field-free condition at the sample position for the investigation of chiral ice samples.

A closer look at the magnetic phase image recorded after applying a field of 21.7 mT (Fig. 4.13d) reveals the emergence of magnetic vortices in some nanomagnets that are located at the edge of the pattern (*e.g.* the third nanomagnet from the right in the lowest row in Fig. 4.13d). Such vortex states are unexpected, since the nanomagnets are designed to have Ising-like macrospins. Figure 4.13c shows that flipping is not complete even for an applied field of 29.0 mT and that vortices are then still present. The vortices disappear when the sample is completely saturated. Reversal of the nanomagnets is investigated in more detail in the following section.

4.5.2. Driving mechanism of magnetic reversal of nanomagnets

The process by which magnetic field switching takes place in individual nanomagnets was investigated with the help of micromagnetic simulations provided by Sebastian Gliga (PSI, Switzerland) using a finite element micromagnetic simulation software [122]. The results reveal that the nanomagnets are too large to reverse through coherent rotation of the magnetisation (Fig. 4.14). Instead, reversal is mediated by the motion of two half antivortices around the edges of the nanomagnets. Three steps can be distinguished: (1) creation of the half

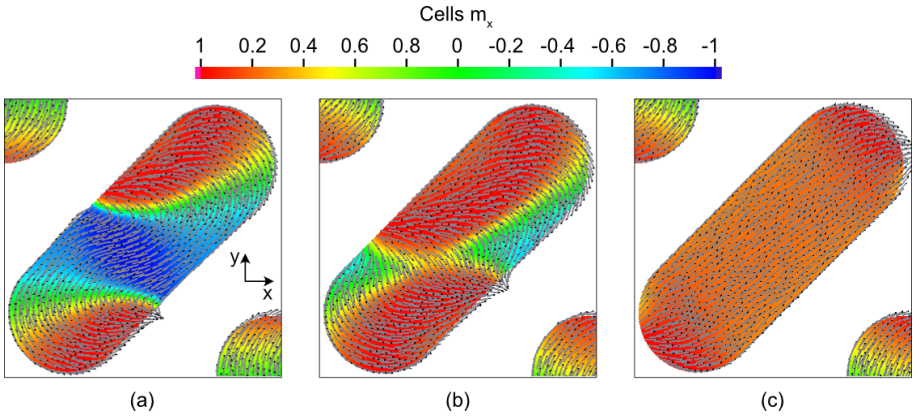

Figure 4.14.: Micromagnetic simulation of magnetisation reversal in a single nanomagnet in chiral ice. The arrows indicate the orientation of the magnetisation, while the colour represents the amplitude of the x component of the magnetisation. (a) The reversal process is initiated by the formation of two half antivortices. (b) The two half antivortices move towards the end of the nanomagnet. (c) The direction of the nanomagnet is reversed.

antivortices, (2) movement of the half antivortices towards opposite ends of the nanomagnets, and (3) completion of reversal. Creation of the two half antivortices most likely results from virtual antivortices in the stray fields partially entering the nanomagnets to form an S-shaped magnetisation distribution. The half antivortices then move towards opposite ends of the nanomagnets, similarly to zip fasteners, while the magnetic moments within the nanomagnet turn in response to the applied field.

In addition to reversal *via* two half antivortices, complete vortices may appear within the nanomagnets during the reversal process (Fig. 4.13d). Micromagnetic simulations reveal that the nucleation of vortices during switching can be favourable if: (1) the magnetostatic interaction with neighbouring nanomagnets is weak or only partially present, *e.g.* at the edges of the pattern and (2) the inversion symmetry of the magnetisation distribution is broken. The second case can be excluded for the idealised shape of the nanomagnets considered in the simulations. However, in practice the nanomagnets are subject to imperfections due to the fabrication process, which can break inversion symmetry. Figure 4.15 depicts the switching of a perfect single nanomagnet in the absence of neighbouring nanomagnets. The saturation field is applied parallel to the long axis

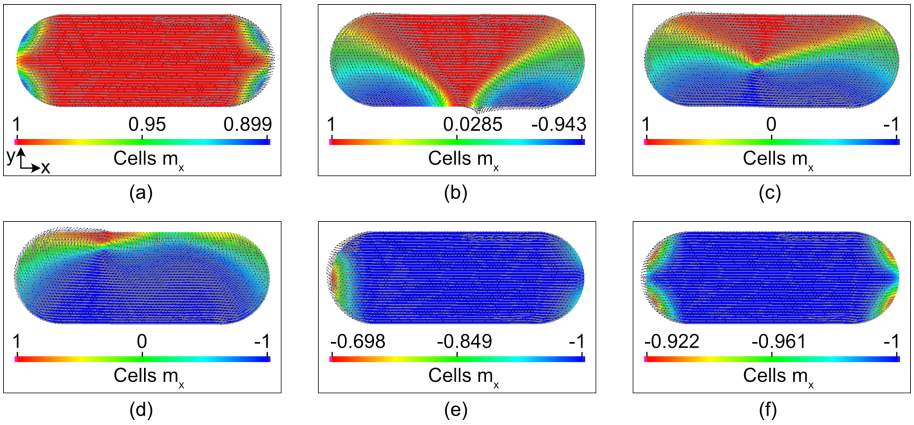

Figure 4.15.: Micromagnetic simulation of magnetisation reversal in a single nanomagnet in the presence of a magnetic field applied parallel to its long axis. The arrows indicate the orientation of the magnetisation, while the colour represents the amplitude of the x component of the magnetisation. (a) Initial state; (b) Formation of two half antivortices; (c) Formation of a vortex; (d) Movement of the vortex towards the opposite edge; (e) Movement of the vortex towards one side of the nanomagnet and (f) the vortex is expelled.

of the nanomagnet and its initial state is highly symmetrical (Fig. 4.15a). The magnetisation of the nanomagnet does not switch until rounding errors due to the finite precision of the saved numbers in the computation break the inversion symmetry. Then, two half vortices form on the same edge of the nanomagnet (Fig. 4.15b). These half vortices move towards each other and nucleate a single vortex (Fig. 4.15c). The single vortex moves closer to the opposing side of the nanomagnet (Fig. 4.15d), before it is expelled at one of the edges (Fig. 4.15e and Fig. 4.15f).

In addition to shape imperfections due to fabrication (*cf.* Sec. 4.2), Py oxidises over time introducing defects that also break inversion symmetry. Therefore, in practice more nanomagnets switch through the nucleation of a single vortex as shown in Fig. 4.15, than through the nucleation of two half vortices (Fig. 4.14). Evidence for changes in the switching process can be observed experimentally when studying samples six months after their fabrication. A larger number of vortices is then stabilised when applying fields in the regime required for switching. Figure 4.16a shows a magnetic induction map for chiral ice after a magnetic field of 20 mT had been applied parallel to the edge of the pattern, while Fig. 4.16b shows a corresponding magnetic induction map for a 25 mT magnetic

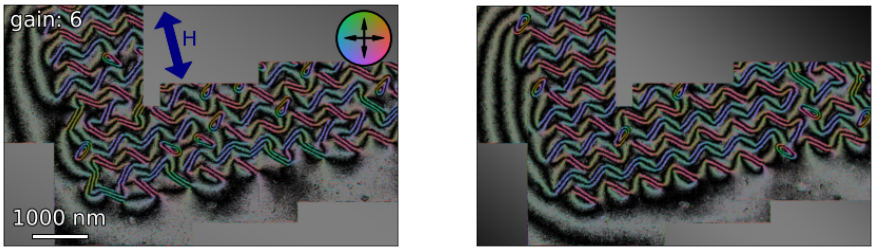

(a) **(b)**

Figure 4.16.: Magnetic phase images of chiral ice (si_18_45) studied six months after sample preparation. The blue arrow indicates the direction of the applied field. The sample was first saturated downwards before applying (a) 20 mT and (b) 25 mT fields in the opposite direction and recording holograms in zero field. The relative number of particles in vortex states increased from 7% in earlier measurements (Fig. 4.13d) to 16% (20 mT) and 9% (25 mT). Adapted from [117]

field. For both experiments, the sample was first saturated using the objective lens at a +90° sample tilt. Then, the sample was tilted to −90° in zero field and chosen smaller fields were applied. A magnetic field of 20 mT was found to be sufficient to switch some of the nanomagnets. The reversal process started at different positions in the pattern in successive experiments starting with the same saturated state. During reversal, several vortices formed within the sample. Most of the nanomagnets that had been in vortex states fully switched after applying a field of 25 mT. Interestingly, the relative number of vortices increased to 16% for a 20 mT applied field and 9% for a 25 mT applied field, when compared with the experiments performed shortly after sample fabrication, when a maximum of 7% of the nanomagnets were in vortex states (*cf.* 4.13d). The results suggest that reversal through the nucleation of a vortex is more likely for an imperfect sample that does not have a perfect elliptical shape or contains defects. This observation is in good agreement with the simulation results, indicating that inversion symmetry plays a major role in the reversal process.

The reversal process was not fully reproducible. For example, in Fig. 4.16, some of the particles that switched at 20 mT are in vortex states or are not switched at 25 mT. It should be noted that the sample was saturated between the measurements. The results indicate that nanomagnet reversal is a complicated process, which depends on many parameters and conditions. These findings are in good agreement with reports on the reversal of 20-nm-thick Py ellipses [123].

The measurements reported above show remanent magnetic states recorded after the application and removal of an external field. Hence, the reversal process should be complete and magnetic vortices should no longer be stable during imaging. Nevertheless, the vortices are present in recorded the magnetic induction maps. Experimentally, it is found that the appearance of stable vortices increased with time increasing since deposition of the samples. This stability may result from the vortices that are induced during reversal being pinned to physical defects or non-uniform magnetic properties due to oxidation. The stable vortices affect the overall magnetisation pattern of the chiral ice, as they reduce stray fields and have an effect on the overall stray field distribution, which can compromise the investigation of the distribution of virtual antivortices. A possible solution is to decrease the sample thickness, which makes the nucleation of vortices more difficult. Although a smaller thickness will reduce the magnetic signal, the benefit of reducing the formation of vortices outweighs the disadvantage of the smaller signal. Hence, a smaller thickness of 10 nm was chosen for the study of stray fields.

4.6. Detection of virtual antivortices

The primary aim of the investigation of chiral spin ice is the detection of the positions of virtual antivortices at the edges of three different patterns: chiral ice, its mirror image and an in-between state. The detection routine is summarised in Fig. 4.17. First, multiple holograms are recorded from the edge of the pattern at identical locations after magnetising the sample in opposite directions. Then, the electrostatic and the magnetic contributions to the phase are separated, a single large magnetisation map is made using MBIR and the stitching procedure is applied. Up to this point in the analysis, only the projected in-plane magnetic induction and magnetisation are considered. Then, the three-dimensional magnetic induction is computed, from which the positions of virtual antivortices are determined. Finally, the positions of virtual antivortices in the different patterns are compared with each other and with micromagnetic simulations.

4.6.1. Magnetic state of saturated artificial spin ice

The first step in the detection of virtual antivortices is the acquisition of off-axis electron holograms from the three different samples (si_10_45, si_10_45R, si_10_38, *cf.* Table 4.1). In order to prevent the formation of vortices within the

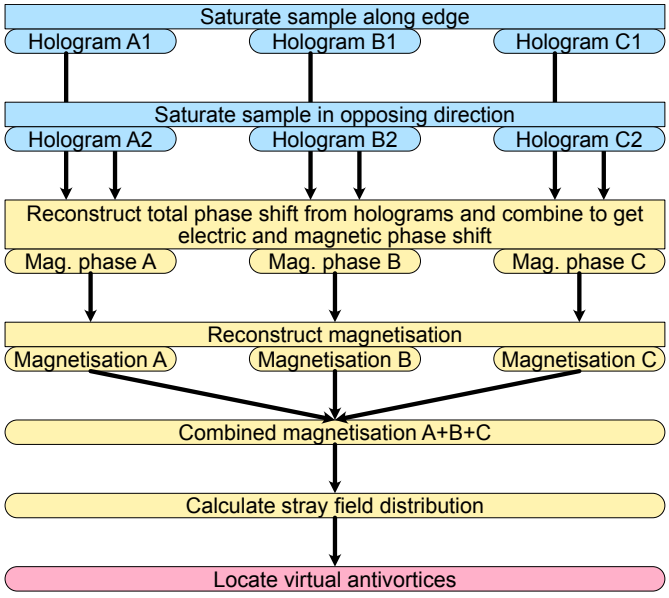

Figure 4.17.: Overview of the steps used to locate the positions of virtual antivortices from experimental results (blue), involving data analysis (yellow) and detection (red).

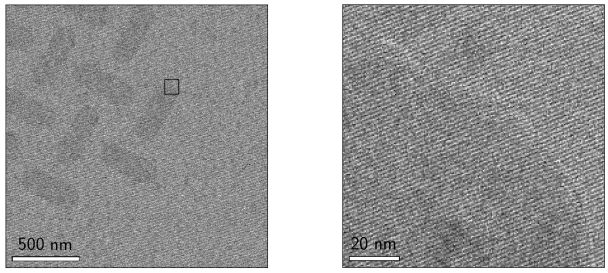

Figure 4.18.: Representative off-axis electron hologram of the 10-nm-thick chiral ice sample si_10_45 recorded using a biprism voltage of 156 V at 8,900x magnification with a fringe spacing of 1.6 nm. (a) Object hologram. The region indicated in the rectangle in (a) is magnified in (b). Adapted from [117]

nanomagnets, samples with a nominal thickness of 10 nm were investigated only a week after preparation. In contrast to earlier experiments, a higher magnification of 8900x was chosen to compensate for the weak signal limiting the spatial resolution. An example hologram is shown in Fig. 4.18a. The contrast of the nanomagnets is low owing to their thickness. The magnified image in Fig. 4.18b shows holographic interference fringes in one of the elements. The three samples were saturated by tilting then to ±75° and magnetising then parallel to the edge of the pattern using the objective lens. Multiple holograms were recorded after turning the objective lens off and tilting the sample back using a biprism voltage of 156 V, which resulted in an interference fringe spacing of 1.6 nm. The overlap width in the holograms was chosen to be just large enough to allow for the alignment of adjacent holograms. The use of small overlap region has the advantage that the number of virtual antivortices that can be imaged is increased. Nevertheless, the overlap is too small to allow for the correction of the phase ramp and offset between adjacent magnetic phase images. Instead, the reconstructed magnetisation maps were stitched together during data analysis, as the magnetisation is an intrinsic property of the material and hence equal in adjacent maps.

In a second step, the electrostatic and magnetic contribution to the phase were separated at each position using the procedure described in Section 4.4. As mentioned above, the magnetic induction here refers only to the projected in-plane magnetic induction. First, the total phase images and amplitude were reconstructed from the holograms after applying a small Gaussian filter to the complex wavefunction. The phase images were aligned by applying cross correlation to

the amplitude images. Half of the sum and half fo the difference of the two total phase images were used to generate the electrostatic and magnetic phase images, respectively. Figure 4.19a shows an example of an electrostatic phase image after removing a phase ramp for the chiral ice pattern (sample si_10_45). The average value of the electrostatic phase shift in the particles is 1.43 rad based on this value, the MIP of Py can be determined to be 22.9 V by applying Eq. 3.12 and assuming that the measured thickness of 10 nm (Fig. 4.3) is the magnetic thickness. This value is smaller than the value of 26±3 V measured for Py in the literature [124]. This difference can be explained by the higher Fe content in the present samples than the nominal composition (Sec. 4.2). Besides the chemical composition, the reduced MIP can be the result of a smaller magnetic thickness than the measured thickness, *e.g.* due to oxidation. In the next step, a mask was generated for each nanomagnet automatically from the electrostatic phase image (*cf.* Sec. 4.3.1) and corrected by reassigning individual pixels by hand. The corresponding magnetic phase shift is shown in Fig. 4.19b and the magnetic induction map is shown in Fig. 4.19c. The magnetic induction inside the particles is consistent with the applied field direction, with the induction lines following a zigzag pattern. Outside the pattern, the stray field distribution is complex. The magnetic phase shift is not yet phase-ramp-corrected here because this correction is performed automatically during reconstructing of the magnetisation of the nanomagnets (see Sec. 4.6.2).

The positions of virtual antivortices can be detected from the magnetic phase images. This detection is influenced by noise as taking the gradient of the magnetic phase image results in an increase of the phase error. Therefore, the magnetic phase image was first smoothed with a Gaussian filter using $\sigma = 20$ nm. The gradient was then computed to gain a value proportional to the x and y component of the projected in-plane magnetic induction, $B_{proj,x}$ and $B_{proj,y}$. The positions of virtual antivortices correspond to the positions of local minima of the projected in-plane magnetic induction as $B_{proj,x} = B_{proj,y} = 0$ T. Hence, it is sufficient to localise these minima. The amplitude of the projected in-plane magnetic induction was computed and inverted, as the automatic peak detection in Python routines can only locate maxima and not minima. Before the maxima could be found, the data had to be processed further. This process is shown in Fig. 4.20. First, the maxima were enhanced by a maximum filter (Fig. 4.20a). This step is necessary to ensure that the positions of the virtual antivortices can be separated from the regions further from the pattern, where the projected in-plane magnetic induction tends to zero. The nanomagnets and their surroundings were then masked out, as local variations (*e.g.*, from misfits of the mask) can result in sharp, but locally restricted changes in the projected in-plane magnetic

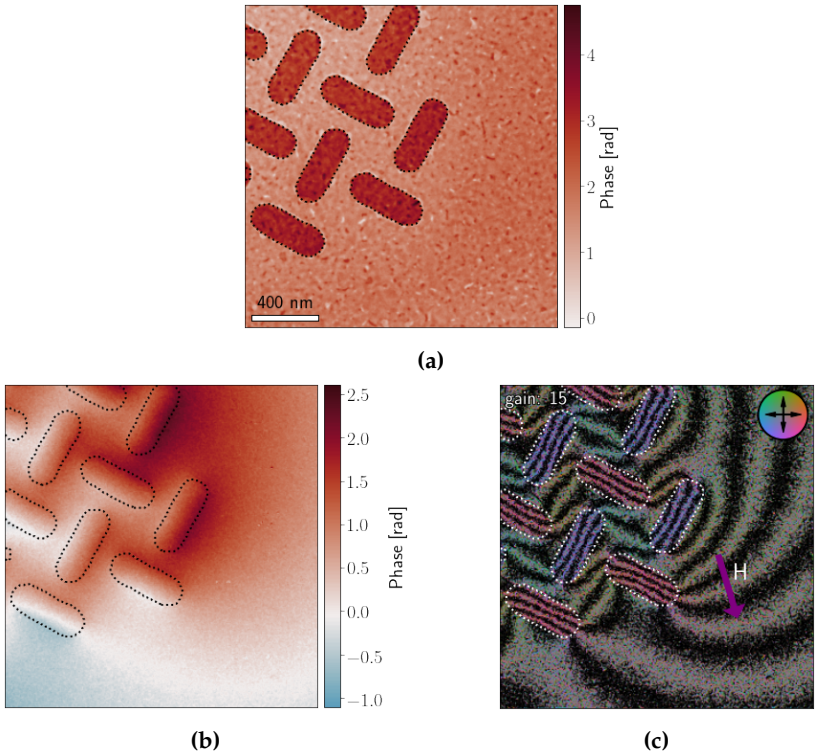

Figure 4.19.: Electrostatic and magnetic contribution to the phase for 10-nm-thick chiral ice. (a) Electrostatic phase shift, which was used to create a mask (dotted lines) around the particles. (b) Magnetic phase shift; (c) Magnetic induction map. The magnetic induction lines in the particles follow the direction of the applied field **H**. Adapted from [117]

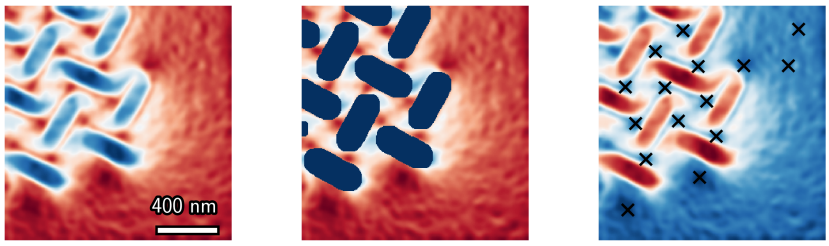

Figure 4.20.: Procedure used to identify the positions of virtual antivortices from magnetic phase images. (a) Inverted amplitude of projected in-plane magnetic induction calculated from phase shift. (b) The nanomagnets and their immediate surrounding are masked out and the positions of the maxima are enhanced. The maxima correspond to the positions of virtual antivortices. (c) Amplitude of the projected in-plane magnetic induction, with the positions of virtual antivortices marked by crosses. In (a) and (b), dark red corresponds to maxima of the inverted amplitude. In (c), dark blue corresponds to minima of the original amplitude.

induction (Fig. 4.20b). The last step is the localisation of the maxima and thus of the virtual antivortices (Fig. 4.20c). Figure 4.21 shows the position of the virtual antivortices, as well as isolines for $B_{proj,x} = 0\,\mathrm{T}$ and $B_{proj,y} = 0\,\mathrm{T}$. The isolines outside the pattern are noisy. The positions of the virtual antivortices are not always located correctly at intersections of the isolines. Close to the pattern, the amplitude of the projected in-plane magnetic induction increases and noise has a negligible effect on the signal. Here, the virtual antivortices are correctly located at the intersections. Nevertheless, the positions of the virtual antivortices do not correspond to the theoretical predictions for chiral spin ice, as the virtual antivortices at both edges have the same distance to the edge of the pattern (*cf.* Sec. 4.1). Hence, a better understanding of the stray field distribution induced by the magnetisation is required to resolve this contradiction. Therefore, the magnetisation was reconstructed using the MBIR algorithm. The advantages of reconstructing the magnetisation are that the noise is reduced by regularisation and the three-dimensional magnetic induction becomes accessible.

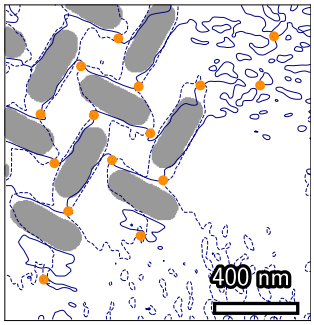

Figure 4.21.: Positions of virtual antivortices detected in the experimental magnetic phase image. A mask of the particles is superimposed by isolines for $B_{proj,x} = 0\,\mathrm{T}$ (solid) and $B_{proj,y} = 0\,\mathrm{T}$ (dashed). The positions of virtual antivortices are indicated by orange dots.

4.6.2. Reconstruction of the magnetisation

The projected in-plane magnetisation in each magnetic phase image was reconstructed using the MBIR algorithm introduced in Sec. 3.2.5. The reconstructed magnetisation is integrated along the electron beam trajectory and thus over the whole thickness of the sample. Only the projected in-plane magnetisation is reconstructed. Three-dimensional reconstruction of the magnetisation would require a tomographic measurement [61, 125]. Nevertheless, for the chiral ice samples the in-plane magnetisation components are present in each nanomagnet. Hence, a knowledge of the projected in-plane magnetisation is sufficient. The MBIR algorithm requires a magnetic phase image and a mask with the positions of the particles as input. The mask is used as *a priori* knowledge, because magnetisation can only be present inside the nanomagnets. In addition, a confidence mask is used to specify pixels in the phase image that contain untrustworthy information. Furthermore, the reconstruction can take phase ramps into account, as explained in Sec. 4.3.2. Magnetic stray fields originating from particles outside the FOV introduce additional variations in phase in the magnetic phase image, affecting measurement of the positions of virtual antivortices, where the relative phase is weak. Hence, a buffer layer was introduced around the phase images. This buffer layer is treated as a magnetic area, in which the magnetisation is allowed to vary. A gap between the buffer layer and the particles ensures that the magnetisation of the nanomagnets is disjoint from the buffer region. This separation is important for regularisation, which constrains the smoothness of

connected magnetic regions.[2] The confidence map in the region of the buffer layer labels it as untrustworthy, as it is not present in the experiment. Stray fields of nanomagnets that are close to the FOV but outside it result in a local increase in apparent magnetisation in the buffer layer. The magnetisation in the nanomagnets close to the edges of the FOV is therefore not increased as much as it would be without using a buffer layer. Both an overall linear phase ramp, (*e.g.* due to an error in the sideband detection) can also be corrected using the buffer layer by adjusting the magnetisation inside it in such a way that it resembles a linear phase ramp. Respectively, a closed loop of the magnetisation inside the buffer results in a constant phase shift inside the loop and thus is employed to compensate for phase offsets.

After including the buffer layer, an L-curve analysis was performed to determine the best regularisation parameter (see Appendix B.1). The resulting L-curve is shown in Fig. 4.22a. The aim of the investigation is the detection of virtual antivortices with high spatial resolution. Therefore, a regularisation parameter of $\lambda = 0.1$ was chosen to reduce the effect of smoothing. Figure 4.22b shows the reconstructed magnetisation in the nanomagnets for the 10-nm-thick chiral ice sample. The magnetisation inside the buffer layer increases at the top and left edges of the pattern, as a result of the stray fields of particles outside the FOV. The saturation magnetisation was retrieved by dividing the projected magnetisation by the thickness of the nanomagnets t. Here and in the following analysis, the magnetic thickness was assumed to be the measured thickness of $t = 10\,\mathrm{nm}$. The resulting magnetic saturation polarisation $\mu_0 M_{xy}$ is measured to be $0.73 \pm 0.07\,\mathrm{T}$ (Fig. 4.22c), which is lower than the magnetic polarisation of 1 T measured for a 180-nm-thick Py disk [126]. This difference can be attributed to a combination of different factors. The chemical composition deviates from the nominal value (*cf.* Sec. 4.2). Since the nanomagnets are Fe-rich, the saturation magnetisation is expected to be higher [116]. However, this increase is compensated by two other factors. First, the nanomagnets may be thinner magnetically than their nominal value. In the literature [127], it was shown that there is a threshold thickness below which the saturation magnetisation decreases rapidly. This finding is attributed to a lower magnetisation in surface layers [127]. Second, surface oxidation (*cf.* Sec. 4.2) results in an additional decrease in magnetic thickness. The total measured thickness is used for calculation of the saturation magnetisation, this difference results in a underestimation of the saturation magnetisation. Regions where the measured magnetic polarisation exceeds 1 T are mainly concentrated at the edges of the mask and in nanomagnets that are not

[2] The magnetisation inside the buffer region can be very different from the magnetisation in the nanomagnets, as it has to account for various effects outside of the FOV

fully in the FOV (Fig. 4.22d). The high magnetisation at the edges of the particles suggests that the mask for the particles is likely to be too small in these regions and should be adjusted [61]. The high magnetisation of particles that are not fully in the FOV shows that the use of a buffer layer is only partially sufficient to remove contributions from parts of nanomagnets that are outside the FOV but not to compensate for nanomagnets not being fully inside the FOV. Nevertheless, the use of a buffer layer minimises the flawed assignment of magnetisation from particles outside the FOV to those inside it.

The importance of removing magnetic stray fields from neighbouring nanomagnets is highlighted by studying their long-range nature. For this purpose, the reconstructed magnetisation of a single nanomagnet was isolated and the forward model was applied to simulate its magnetic phase shift (Fig. 4.23a). A line profile of the magnetic phase shift across the nanomagnet is shown in Fig. 4.23b. The overall magnetic phase shift across the nanomagnet is 1.47 rad. However, the magnetic stray fields reach as far as 1.3 μm before the phase shift drops below a value of 0.1 rad. The circle in Fig. 4.23a indicates this radius, which corresponds to the presence of several nanomagnets the pattern. Therefore, stray fields from particles outside the FOV can have a severe effect on those inside it.

The experimental results were compared with micromagnetic simulations performed by S. Gliga (PSI, Switzerland). In the simulations, a static field was applied along the edge of the pattern to saturate the nanomagnets along their long axes. In contrast, the magnetisation in a single nanomagnet in the experiments is not perfectly aligned along its long axis, (Fig. 4.24). Instead, it follows an S-shape presumably in part due to imperfections of the sample. Major contributions arise from shape imperfections due to sample preparation at the edges of the nanomagnets, as well as thickness variations and bending of nanomagnets. All of these shape imperfections can be found in a study of a cross-section of these samples (*cf.* Sec. 4.2). Nevertheless, the simulations strongly support the experimental results overall. The quality of the reconstruction was analysed further by applying diagnostic measures as explained below.

The spatial resolution of the reconstructed projected in-plane magnetisation can be determined from the full width at half maximum (FWHM) of the averaging kernel, which provides an estimate of the strength of the smoothing by the regularisation [61]. Figure 4.25a and Figure 4.25c show the averaging kernels for the x and y components of the magnetisation for a single pixel in the Py islands. The ellipses correspond to the values of the FWHM of the kernels. The FWHM takes a value of 65 nm along the long axis of each ellipse. The values of spatial resolution in the x and y directions are given in Table 4.2.

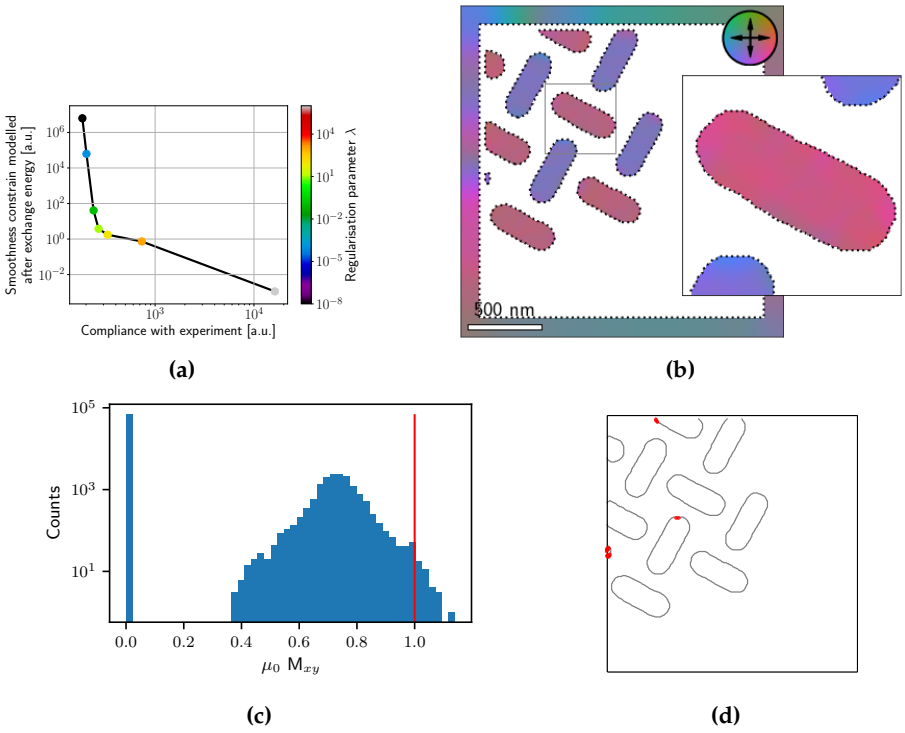

Figure 4.22.: Reconstruction of the projected in-plane magnetisation using the MBIR approach. (a) L-curve analysis showing trade-off between the compliance with experimental data on the x-axis and smoothness constrain modelled after the minimisation of the exchange energy on the y-axis. A value of $\lambda = 0.1$ is chosen for the reconstruction to preserve as much spatial resolution as possible. (b) Reconstructed projected in-plane magnetisation. The buffer region around the pattern compensates for the phase ramp, the phase offset and the presence of particles outside the FOV. The inset shows a magnified view of one particle in which curling of the magnetisation at the edges is visible. (c) Histogram of the values of magnetisation in the reconstruction. The average value of the magnetic polarisation $\mu_0 M_{xy}$ in the particles is 0.73 T. (d) Pixels where the magnetic polarisation exceeds 1 T are marked by red dots. The dots are larger than the pixel size to make them visible. See text for details. (b) and (c) adapted from [117]

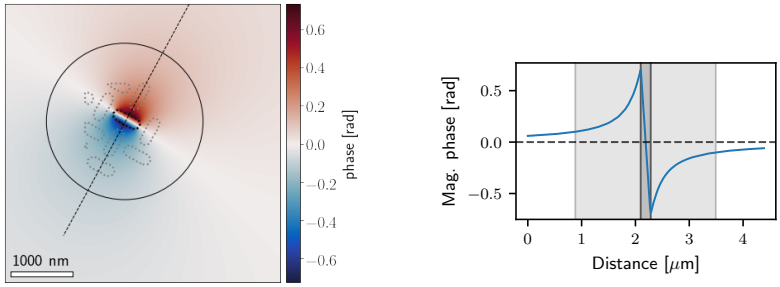

(a) **(b)**

Figure 4.23.: (a) Contributions to the magnetic phase shift from a single nanoparticle. The locations of several nanomagnets are marked by grey outlines. (b) Line profile of the phase shift along the dashed line in (a) showing that the phase only drops below a value of 0.1 rad after 1.3 μm (area marked in light grey). This distance is indicated by a circle in (a). The dark grey area marks the size of the Py island.

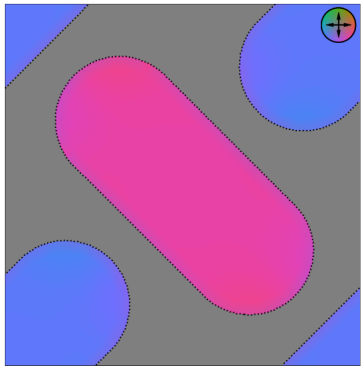

Figure 4.24.: Close up on a single particle from the micromagnetic simulation of the chiral ice pattern revealing parallel magnetisation along the long axis of the particle. Adapted from [117]

Table 4.2.: Spatial resolution of the reconstruction of the projected in-plane magnetisation at the centre of a nanomagnets is approximated by the FWHM of the averaging kernel shown in Fig. 4.25.

Vector component	x resolution [nm]	y resolution [nm]
x component	64.3	31.0
y component	30.5	63.0

The gain maps shown in Fig. 4.25b and Fig. 4.25d indicate how much a single pixel is affected by information from surrounding pixels during reconstruction. It can be seen that the neighbouring pixels have a strong effect on a chosen pixel. Nevertheless, the chosen regularisation parameter is small enough to avoid averaging over a complete particle (see Appendix. B.1). The quality of the reconstruction can also be assessed by comparing the measured magnetic phase image to a phase image generated from the reconstructed magnetisation by employing the forward model used in the MBIR algorithm [61]. Figure 4.26a shows the resulting calculated phase image. The magnetisation in the buffer pixels is included in the computation to reproduce the phase ramp and offset in the experimental data. This calculated phase image is less affected by noise than the experimental magnetic phase images owing to the regularisation used in the reconstruction. The difference between the calculated experimentally measured phase images are dominated by noise and does not show any specific features, as shown seen in Fig. 4.26b. Only a few deviations in the membrane region are present due to dirt particles on the membrane or the detector. The noise level of $\sigma = 0.05\,\mathrm{rad}$ in the corresponding histogram (Fig. 4.26c) can be attributed to phase noise in the experimental image, which is filtered out by regularisation. It is much smaller than the magnetic phase shift of 1.5 rad of a single nanomagnet. A close-up of the difference image at the position of one of the particles reveals only noise (Fig. 4.26d), with no bright or dark features at the edges of the particle that would indicate an error in the mask.

Such a reconstructed phase images of the projected in-plane magnetic induction can be used to determine the positions of virtual antivortices, just as for the experimental phase images as discussed in Sec. 4.6.1. Here, only the magnetisation of the particles is taken into account and the phase shift induced by the buffer pixels is neglected. Gaussian filtering is not necessary, as the data are already smoothed by regularisation. The advantage of using regularisation for filtering is that it has a physical meaning, as it is related to minimisation of the energy of the exchange interaction. The detection of virtual antivortices then delivers better results than detection from experimental phase images, both as a result of

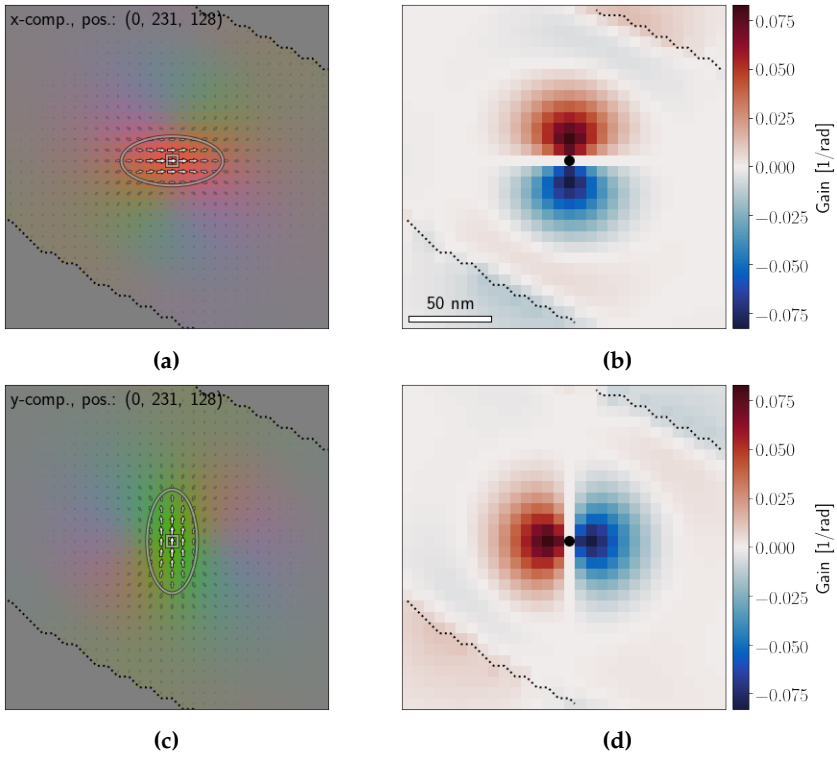

Figure 4.25.: Determination of the spatial resolution resulting from the use of the MBIR approach. (a) Averaging kernel for the x component of the magnetisation. The ellipse corresponds to the FWHM of the averaging kernel. The FWHM corresponds to a length of approximately 65 nm, providing an estimate for the spatial resolution. (b) Gain map for the x component, showing the influence of each pixel in the experimental phase image on the chosen pixel marked with a black dot. (c) Averaging kernel and (d) gain map for the y component.

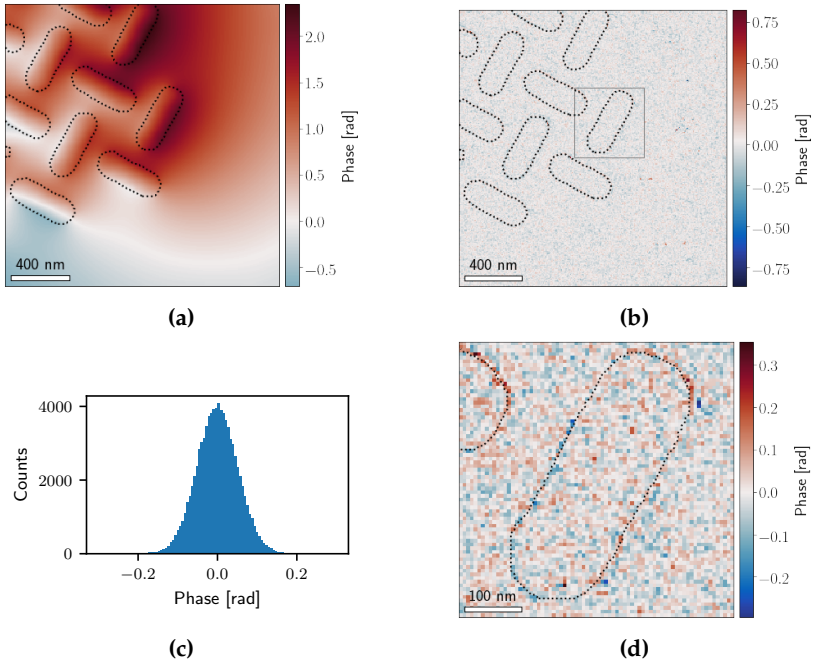

Figure 4.26.: Phase image calculated from the reconstructed magnetisation and its deviation from the experimental phase image. (a) Calculated phase image. (b) Difference between the reconstructed and experimental phase images, dominated by noise in the experimental phase image. (c) Histogram of the phase difference between the two images. (d) Close up of the difference image at the position marked by a grey box in (b). The difference image is dominated by noise.

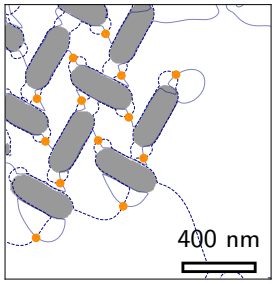

Figure 4.27.: Positions of virtual antivortices in the reconstructed magnetic phase. A mask of the particles (in grey) is superimposed on isolines for $B_{proj,x} = 0\,\mathrm{T}$ (solid) and $B_{proj,y} = 0\,\mathrm{T}$ (dashed). The position of the virtual antivortices are marked in orange.

noise filtering and because computed stray fields are not subjected to noise from the underlying SiN membrane. In this case, the positions of antivortices coincide with the crossings of isolines for $B_{proj,x} = 0\,\mathrm{T}$ and $B_{proj,y} = 0\,\mathrm{T}$. These positions are close to these seen in the experimental phase image (Fig. 4.21). Nevertheless, they still do not correspond to theoretical predictions (*cf.* Sec. 4.1). Hence, an even deeper understanding in terms of the magnetic induction of the sample is necessary.

4.6.3. Determination of the three-dimensional magnetic induction from the reconstructed magnetisation

The magnetic induction of a known magnetisation distribution can be calculated numerically as described in Sec. 4.3.5. In contrast to the previous analysis, this calculation will give access to the three-dimensional stray field distribution. Here, 500 empty slices were added above and below the sample, with each slice corresponding to the thickness of the nanomagnets. Therefore, the magnetic induction below is always integrated over the sample thickness. In this way, a three-dimensional volume was generated with 2323 x 2323 x 9100 nm^3 in x, y, and z directions, respectively. The three-dimensional magnetic induction was then computed at the position of each pixel in the datacube. Figure 4.28 shows examples of B_x, B_y and B_z at different heights above the sample plane. Within the sample plane, the x component of the magnetic induction alternates in successive rows of nanomagnets, as the particles point in different directions, while the y

component inside the nanomagnets points along the direction of the external field as expected. The z component is negligible, as there are no stray fields pointing along the beam direction at the height of the nanomagnets. Above or below the plane of the nanomagnets, the z component adopts higher values. Nevertheless, it does not affect the experimental results, as the electron beam is only sensitive to the in-plane component of the magnetic induction (cf. Eq. 3.8). The y component becomes uniform further above or below the plane of the nanomagnets while the x component becomes negligible. The magnetic induction is symmetrical with respect to the sample plane. Hence, the B-field distribution is the same when going a certain distance either above or below the sample. The shape of the stray field far from the nanomagnet array is comparable to the stray field of a single magnetic dipole. This behaviour is expected, as the sample appears to be a uniformly magnetised thin film from far away.

When the electron beam travels through the sample, it experiences the in-plane magnetic induction in the sample and that of the stray fields around it. A magnetic phase image records the in-plane magnetic induction integrated along the beam direction over the full distance of the stray fields. An example of the over the full stray field distance integrated $B_{proj,x}$ and $B_{proj,y}$ fields that the electrons are subjected to is shown in Fig. 4.29, together with the amplitude of the in-plane magnetic induction. The images are thresholded to increase the visibility of the stray fields. The same images were used to detect the positions of virtual antivortices. The advantage of this approach is that computation of the phase gradient is no longer required and hence the noise is reduced. The isolines for $B_{proj,x} = 0\,\mathrm{T}$ and $B_{proj,y} = 0\,\mathrm{T}$ coincide with minima in the amplitude. The positions of the virtual antivortices are in good agreement with the positions detected in the reconstructed phase images, but still not with the theoretical prediction. The reason for this contradiction can be understood by taking a closer look at the stray fields above and below the plane of the sample (*cf.* Fig 4.28). The y component of the magnetic induction integrated only over the thickness of the nanoparticle only alternates its direction at the right edge up to a height of 135 nm above or below the sample. This alternation is required for the formation of the virtual antivortices. Therefore, virtual antivortices are only present close to the plane of the sample. In contrast, above and below the sample the stray fields become uniform over the FOV. The electron beam is sensitive to such uniform stray fields, which are superimposed with the alternating stray fields close to the sample and shift the positions of the virtual antivortices in a projection over the full distance of the magnetic induction, as seen by the electron beam. Consequently, there is no contradiction between the theoretical prediction and the experimental results as they correspond to two different cases: first to stray fields in the sample plane

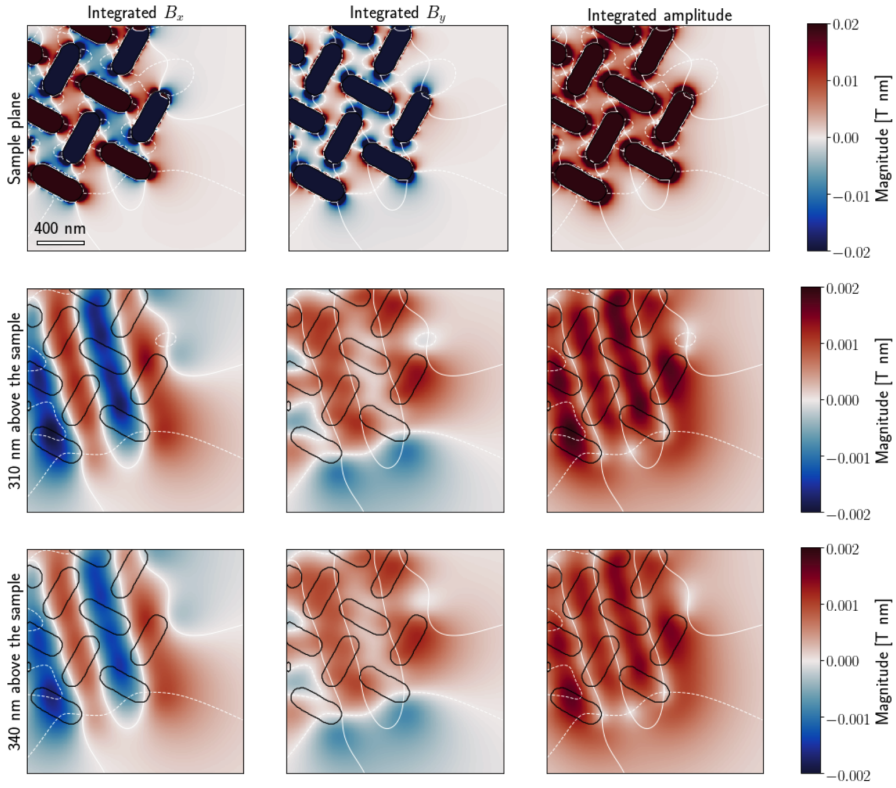

Figure 4.28.: X and y components and amplitude of the calculated magnetic induction at different heights above the sample plane. Each image is integrated over the thickness of the particles t. The images are thresholded to increase the contrast of the stray fields. Virtual antivortices are present at the crossings of isolines for $B_x t = 0\,\mathrm{T\,nm}$ (solid white line) and $B_y t = 0\,\mathrm{T\,nm}$ (dashed white line) only in the vicinity of the particles. The magnetic induction above and below the sample is symmetrical with respect to the sample plane. The black lines outline the edges of the nanomagnets.

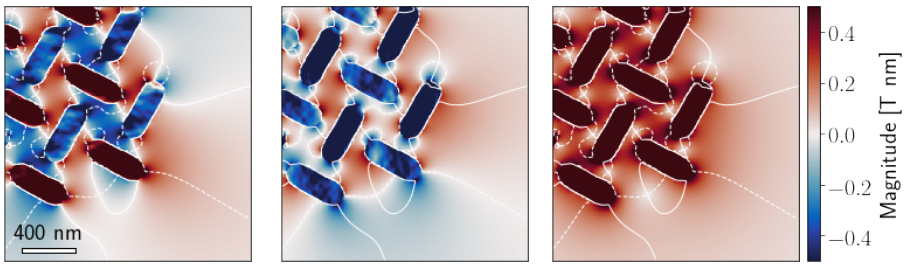

(a) (b) (c)

Figure 4.29.: Magnitude of the magnetic induction integrated along the electron beam direction over the full distance of the calculated stray fields for (a) the x and (b) the y component, as well as for c) the amplitude. The magnitude is clipped to 0.5 T nm to improve the contrast of the stray fields. The solid lines are isolines for $B_{proj,x} = 0$ T, while the dashed lines are isolines for $B_{proj,y} = 0$ T. Their intersections mark the position of the virtual antivortices.

and second to a projection of the stray fields along the full z direction. In order to compare them, the positions of the virtual antivortices in the plane of the sample can be determined from the magnetic induction computed from the experimental data as described below.

4.6.4. Determination of virtual antivortex positions

Before detecting the positions of virtual antivortices in the sample plane, several magnetisation maps were combined to increase the number of vortices that would be detected and to reduce the influence of missing stray fields from particles outside the FOV. The magnetisation maps were stitched together, as shown for samples si_10_45, si_10_45R and si_10_38 in Fig. 4.30 together with a simulated magnetisation map of a chiral pattern. In contrast to stitching magnetic phase images, correction of the phase offset and ramp is not necessary when stitching the magnetisation and a smaller overlap region is required. Hence, more virtual antivortices can be detected from the same number of holograms. However, the shape of the mask becomes very important as there is a steep change in magnetisation when going from the saturation magnetisation of the particles to zero outside them. Therefore, it was decided not to average the magnetisation of the particles, which are present in both images, but to assume that one of the measurements is correct. As the magnetisation of the particles at the edges

of the pattern has large uncertainties due to the missing stray fields, the stitching method can result in a steep change on magnetisation inside particles that are stitched together from two individual magnetisation maps. This artefact is present in all of the experimental magnetisation maps. The overall magnetisation follows the external magnetic field, which was applied parallel to the right edge pointing downwards (Fig. 4.30). The magnetic induction maps that were computed from the stitched magnetisation maps are not heavily affected by these artefacts and the positions of the virtual antivortices can still be determined.

Before computing the magnetic induction for each sample, empty pixels were added around the maps in the x and y directions so that computation of the stray fields was not restricted to the area that contained particles. In contrast to the previous computation of the magnetic induction, only the stray field distribution in the sample plane is of interest. Hence, there is no need to add empty slices above and below the sample.[3] In the resulting magnetic induction map, the positions of the antivortices can be detected, as described above for the integrated magnetic induction maps (Sec. 4.6.1). Their positions coincide with isolines for the x and y components of the magnetic induction being zero (*cf.* Fig. 4.31). In order to compare the experimental results with the simulation, the virtual antivortices were detected using the same approach in the simulated magnetisation distribution, as shown in Fig. 4.31c.

The positions of the antivortices in sample si_10_45 show a clear difference between the bottom and right edges (Fig. 4.31a). At the bottom edge, the virtual antivortices are located close to the edge of the pattern, whereas they are shifted away from the right edge. The experimental stray field distribution is consistent with the simulated distribution. Even the observation that the virtual antivortices on the right side are located closer to the edge of the pattern when going further from the bottom corner is reproduced in the simulation. Therefore, the theoretical prediction for the stray fields is consistent with the experimental results. In the sample with the mirror pattern (si_10_45R), a similar distribution of virtual antivortices is expected as for the chiral ice. The primary difference is that the location of the virtual antivortices on the right side is mirrored when compared with the chiral ice. This behaviour can be seen at the left edge of the simulated pattern, as shown in Fig. 4.31b. Here, the virtual antivortices at the bottom edge are located closer to the pattern than at the right edge. At the right edge, their positions shift towards the edge in the upward direction. This finding further underlines that the detection of the positions of the virtual antivortices in

[3] However, the calculation requires a three dimensional input to compute three dimensional vectors. Therefore, one empty slice above and below the sample plan had been added.

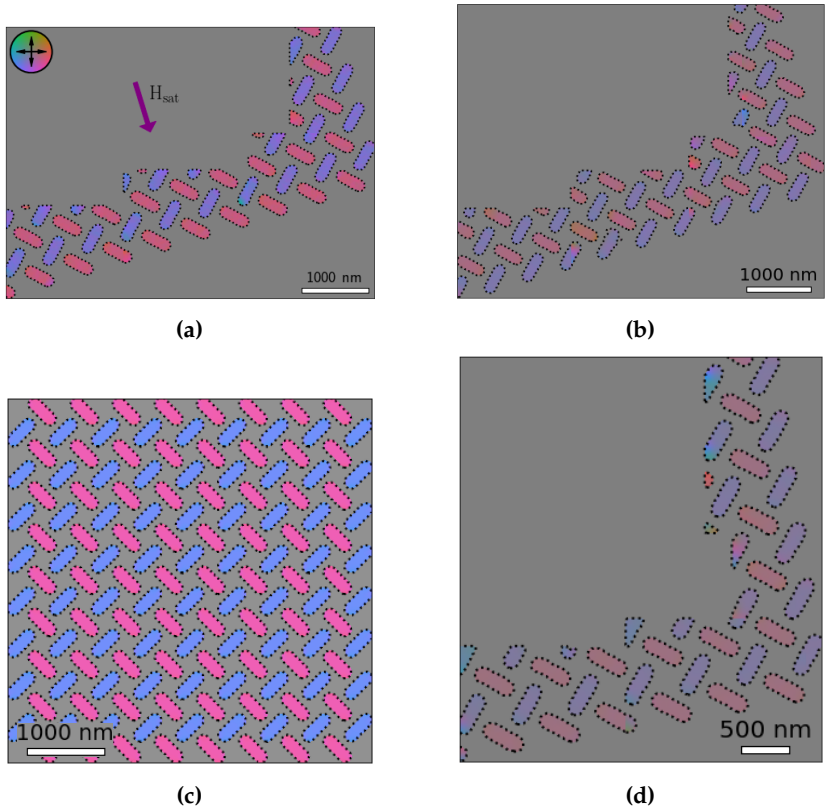

Figure 4.30.: Projected in-plane magnetisation for (a) sample si_10_45, (b) sample si_10_45R, (c) a simulation for chiral ice and d) sample si_10_38. The magnetisation is oriented along the external field, which was applied pointing downwards. The sharp transitions of the magnetisation inside some of the particles are artefacts of stitching multiple measurements together. See text for details.

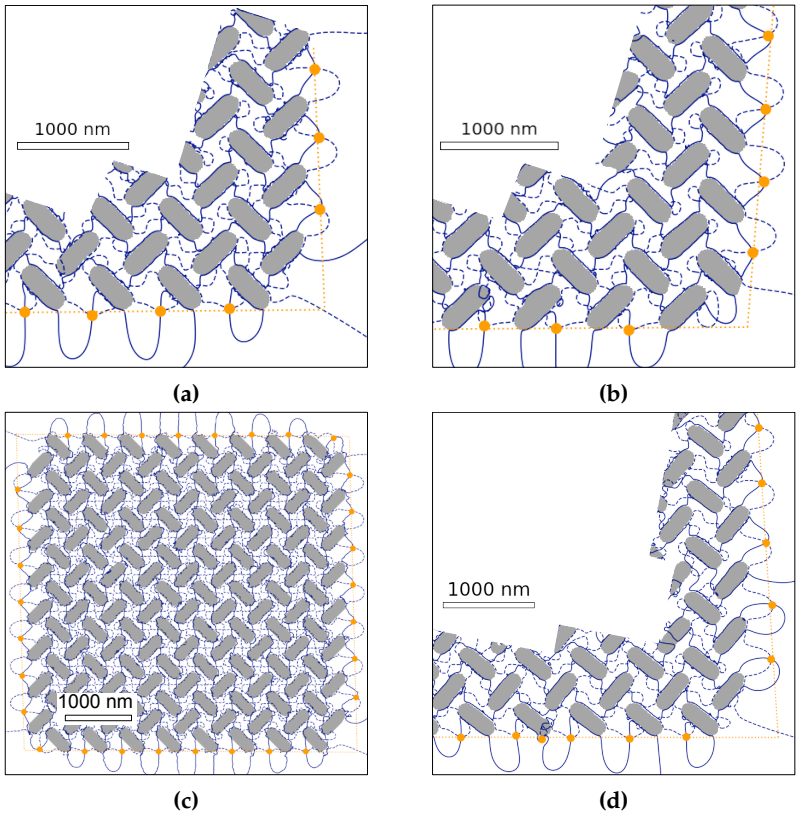

Figure 4.31.: Positions of virtual antivortices (indicated by the orange dots), with respect to the nanomagnets (grey). The antivortices were directly in the sample plane. (a) Classic chiral ice, sample si_10_45. (b) Mirror pattern, sample si_10_45R. (c) Simulation for chiral ice. (d) In-between state, sample si_10_38. Isolines for $B_x t = 0\,\mathrm{T\,nm}$ (solid) and $B_y t = 0\,\mathrm{T\,nm}$ (dashed) are shown in blue. The dotted orange lines are guides to the eye to indicate the difference between the distance of the antivortices to the edge of the pattern at the bottom and right edges.

chiral spin ice is successful. However, the shift of the virtual antivortices in both samples is slightly stronger than in the simulation. This difference is thought to result from the effect of missing stray fields generated by particles outside the measured FOV and is discussed in the following section. Before this discussion, a closer look is taken at the last sample, which corresponds to an in-between state of the chiral ice and the more common square ice [27]. The resulting distribution of virtual antivortices is similar to the distribution for the chiral ice (Fig. 4.31d). Nevertheless, the stray fields are not as well ordered as in the chiral ice. This observation of disorder underlines the fact that spin ice can be used to achieve specific magnetic states by design.

4.6.5. Effect of missing stray fields on the positions of virtual antivortices

The shift in the positions of the virtual antivortices on the right side towards the pattern in the case of the chiral ice (Fig. 4.31a) and away from it for the mirror sample (Fig. 4.31b) is stronger in the experimental results than in the simulation (Fig. 4.31c). The reason for this shift can be understood by studying the influence of stray fields outside the FOV. For this purpose, the positions of the virtual antivortices along an edge in the simulation were determined for two different cases. First, the magnetisation of all of the antivortices was included during detection, regardless of whether or not the particles were located in the chosen FOV, as shown by red crosses in Fig. 4.30c. Second, only the magnetisation of the nanomagnets in the image was used to compute the magnetic induction (see blue crosses in Fig. 4.32). The positions of the virtual antivortices were then determined for both cases. The results are shown in Fig. 4.32. The positions of the virtual antivortices inside the FOV are very similar in the two cases. However, the position of the top right antivortex differs significantly. In the second case, the antivortex is already close to the edge of the pattern. When no stray fields are induced by particles above the edge of the FOV, the magnetic induction corresponds to the induction present at the top edge of the pattern where no nanomagnets are present above the edge of the pattern. Therefore, the missing stray fields need to be taken into account when looking at the positions of virtual antivortices close to the edge of the FOV.

The experimental results correspond to the second case, where only the magnetisation of nanoparticles inside the FOV is considered. For computation of the magnetic induction, only the reconstructed magnetisation of the nanomagnets inside the FOV was considered. The detected positions of the virtual antivortices

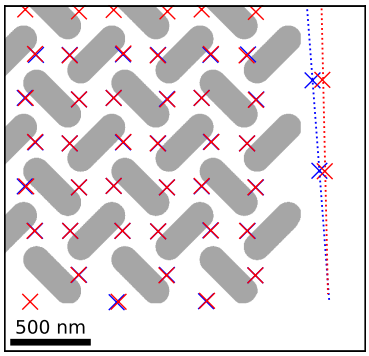

Figure 4.32.: Positions of the virtual antivortices indicated for two cases. Red crosses: the magnetic induction was computed from the complete magnetisation shown in Fig. 4.30c. Blue crosses: only the magnetisation of the displayed particles was used to compute the magnetic induction. The dashed lines are linear fits to the position of the virtual antivortices for both cases. The positions of virtual antivortices at the right edge of the pattern shifts towards the edge when only particles inside the image are considered.

correspond to the positions that they would have if there were no other nanomagnets present outside the FOV. Therefore, they do not correspond perfectly to the true distribution of virtual antivortices present in the sample. The detection of virtual antivortices using the reconstructed magnetic induction is only possible approach that does not suffer from the shift of the antivortices induced by integration of the magnetic phase over the electron beam path. As shown above, the latter approach would result in an overall shift of all of the virtual antivortices. Meanwhile, the effect of the missing stray fields is only present at the edges of the FOV and can be overcome by taking several measurements around the edge of the pattern. In this way, the influence of the missing stray fields can be reduced, as the relative number of virtual antivortices close to the edge is reduced, when compared to the total number of virtual antivortices. Importantly, the trend that antivortices are located further away at edges parallel to the direction of the applied field then at edges perpendicular to the direction of the applied field is verified for the chiral ice sample. Consequently, the theoretical predictions on the underlying mechanism of the ratchet effect are verified experimentally [24].

4.7. Summary

In this chapter, the formation of virtual antivortices in chiral spin ice is verified experimentally. The asymmetrical distribution of the virtual antivortices at the edges of the pattern is the driving mechanism behind the ratchet behaviour, *i.e.* a unique rotation direction of the net magnetisation at the vertices, during thermal relaxation. An analysis of the formation of virtual antivortices was first developed, including an understanding of the switching behaviour and effects of oxidation of the nanomagnets. Their positions were then detected experimentally using off-axis electron holography and MBIR of the magnetisation. Subsequently, the magnetic induction induced by the reconstructed magnetisation was computed to determine the locations of the virtual antivortices. It was shown that, it is important to consider the three-dimensional distribution and long-range nature of the magnetic stray field of the sample. In particular, a projection of the stray field along the electron beam direction results in a shift of the positions at which virtual antivortices are detected. Significantly, the results need to be interpreted carefully due to the effect of missing stray fields from nanomagnets that are outside the FOV. Nevertheless, it was possible to verify that the positions of virtual antivortices differ at edges that are parallel to the saturation field and perpendicular to it.

Chapter 5.

Magnetic vortices in Py disks

Magnetic vortices can be used as a model system for exploring non-standard magnetic characterisation methods thanks to their simple geometry and stability, as introduced in Sec. 2.4.1. Here, the static properties of magnetic vortices in Py disks are studied, in order to access their suitability for later dynamic experiments. The Py disks are patterned lithographically and the quality of their fabrication is first assessed. Their magnetic properties are then investigated, with a special focus on their vortex cores, using the techniques that were developed for the analysis of the artificial spin ice. In the last section, shape deviations from a flat disk geometry are highlighted and their implications for magnetic properties and data analysis are discussed.

5.1. Sample preparation and structure

The Py disks were fabricated by S. Finizio (PSI) on SiN membranes, following the same procedure as for the chiral ice samples (for details see Sec. 4.2). Several disks were analysed, ranging from 50 to 200 nm in thickness and from 750 to 1500 nm in diameter. In these range, the disks are expected to support magnetic vortices. For each sample, nine disks were fabricated on a SiN membrane in a 3x3 configuration, in order to increase the chance of having a viable disk on the membrane. The spacing between the disks was chosen to be 25 μm, in order to avoid shadowing from both the holder and adjacent disks. On the one hand, the disks should be located as close to the centre of the membrane as possible to avoid shadowing by the holder edge when tilting to high angles. On the other hand, their spacing should be as large as possible to prevent the disks from shadowing each other at high tilt angles. In order to increase the accessible tilt range further, the membranes were specifically fabricated by Silson Ltd. to be as

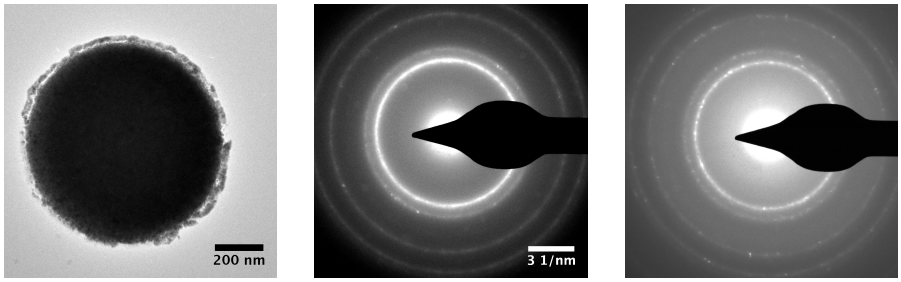

(a) (b) (c)

Figure 5.1.: Py disk that hosts a magnetic vortex. (a) BF TEM image, revealing the presence of residual material around the disk. (b) Diffraction pattern recorded from the disk, showing rings with bright spots characteristic of a polycrystalline structure. (c) Diffraction pattern recorded with the disk tilted by 25°, revealing no preferred texture of the Py.

thin and large as possible without breaking during the fabrication process. The best compromise proved to be a thickness of 20 nm and a size of 100 μm x 100 μm. In the last fabrication step, a 10-nm-thick layer of Al was deposited over the full membrane in order to reduce electron-beam-induced charging in the Helmholtz Nanofacility cleanroom [113].

Figure 5.1a shows a BF TEM image of a Py disk with a nominal thickness of 175 nm and a nominal diameter of 750 nm. Its true diameter is measured to be 815 nm. Residual material can be seen around the edges of the disk. It is likely to be residual electron resist or Py that was not lifted up, resulting from of an imperfect fabrication process. In addition, some Py may have been deposited there during fabrication. The latter possibility will be discussed in Sec. 5.3.1. The Py has a polycrystalline structure as revealed by the electron diffraction ring pattern shown in Fig. 5.1b, which was recorded by using a selected area aperture to image only the Py disk. The grains are randomly oriented, as no texture is observed in a diffraction pattern recorded with the sample tilted by 25° (Fig. 5.1c).

The structure and composition of the Py was investigated in cross-section. Figure 5.2a shows an HAADF STEM image of a cross-section of the nominally 175-nm-thick sample. The true sample thickness of the Py is measured to be 164 nm. The deviation may have been resulted from an inaccuracy in the quartz balance used to control the Py thickness during deposition. The cross-section reveals columnar growth of the Py grains, which is likely to have been induced by

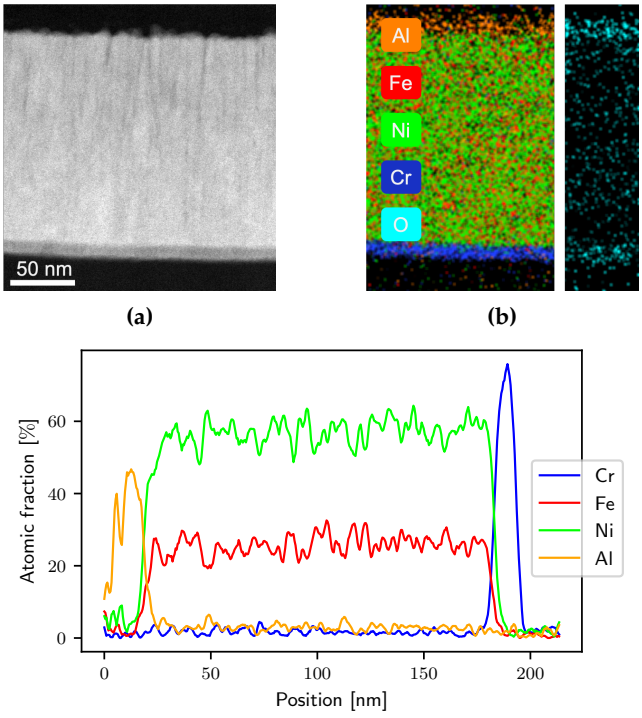

Figure 5.2.: Cross-section of a Py disk of a nominal thickness of 175 nm. (a) HAADF STEM image reveals a columnar grain structure and that the Py disk is 164 nm thick. The ADF detector semi-angle used was 69 mrad. (b) Combined elemental map obtained using STEM EDX spectrum imaging. (c) Integrated linescans across the EDX map shows homogenous Ni and Fe distributions in the Py layer. The EDX measurement indicates that the Py layer composition corresponds to Ni ~70 % and Fe ~30 %.

the crystal structure of the underlying Cr adhesion layer. The column diameter is in the range of 5 to 10 nm. In the chemical map shown in Fig. 5.2b, one can see that Fe and Ni are distributed uniformly in the Py. An integrated linescan across the layers shows that the Fe and Ni are distributed equally through the thickness of the sample (Fig. 5.2c). The Py layer contains approximately 70% Ni and 30% Fe. As in the case of the artificial spin ice samples (*cf.* Ch. 4), the measured deviation in composition from the standard Ni to Fe ratio of 81 to 19 affects the saturation magnetisation. Oxidation of the surface of the disk results in a reduction of the magnetic volume. The deviation in chemical composition and the presence of oxidation are consistent with the observations for the spin ice nanomagnets, where both effects were present (*cf.* Sec. 4.2). Nevertheless, a magnetic vortex state is still expected to form in of the disk, as it is stabilised by a competition between exchange and dipolar energy (*cf.* Ch. 2).

5.2. Reconstruction of the projected in-plane magnetic induction and magnetisation of magnetic vortices

The magnetic properties of vortices were discussed theoretically above (*cf.* Sec. 2.4.1). In the next section, their properties are analysed experimentally and discussed in the light of deviations from the ideal model. The projected in-plane magnetic induction and magnetisation of a single disk are reconstructed and the results are compared to micromagnetic simulations. Finally, the relationship between the sample geometry and the shape of the core of the magnetic vortex is analysed.

5.2.1. Influence of the reference hologram on phase reconstruction

The Py disk that was investigated in detail had a nominal thickness of 100 nm and a nominal diameter of 1 μm. The true diameter of the disk was measured to be 1086 ± 12 nm from a radial profile of the object hologram. Before analysis of the magnetic state, the influence of reference holograms on the reconstruction was evaluated, as shown in Fig. 5.3. There are three different choices for a reference hologram when studying these samples: taking no reference hologram, recording it from the SiN membrane and recording it from vacuum. For the last option, the sample and holder have to be retracted from the electron beam, as

there is no vacuum region available on the sample. A representative object hologram and different reference holograms are shown in Fig. 5.3a to 5.3c for a magnification of 14.5 kx and an applied biprism voltage of 80 V. These parameters correspond to a holographic interference fringe spacing of approximately 3.5 nm. The corresponding total phase images are shown in Fig. 5.3d, 5.3e, and 5.3f, respectively. The total phase images are similar and the choice of reference hologram does not seem to have a strong influence on the result. A uniform phase ramp due to charging and an error in the detection of the sideband position can be removed in each case on the assumption that the phase shift is constant outside the disk. These assumptions hold, as magnetic vortices do not possess significant magnetic stray fields. In addition, the region with Fresnel fringes from the edges of the biprism needs to be excluded (*cf.* Fig. 5.3g). It would be possible to move these fringes out of the field of view by increasing the biprism voltage. However, this would result in weaker fringe contrast, which is already compromised by the thickness of the disk.

A quantitative overview of the effect of using different reference holograms was obtained from the phase noise in the total phase images of the SiN region. Figure 5.3h shows histograms of the total phase inside the marked blue regions in Fig. 5.3g. The standard deviations of the three distributions are 0.87 ± 0.01 rad for the reconstruction with a vacuum reference hologram, 0.88 ± 0.01 rad for a reference hologram on SiN and 0.87 ± 0.01 rad without a reference hologram. Therefore, the choice of reference hologram does not have a major effect on the phase noise, in large part due to the excellent performance of the direct electron detector used to record the holograms and the high stability of the electron microscope. However, the disadvantage of not using a reference hologram is that potential image distortions arising from the physical setup (*cf.* Sec. 3.2.2) are not corrected, affecting the reconstruction of magnetic and electrostatic contributions to the phase. Thus, a reference hologram recorded from vacuum was employed for these kinds of experiments.

5.2.2. Off-axis electron holography of magnetic vortices and reconstruction of the projected in-plane magnetisation

The magnetic properties of the disk introduced in section 5.1 are now analysed for the as-prepared state. A turning over experiment was performed to separate the magnetic and electrostatic contributions to the phase shift by using a dedicated specimen holder to record two object holograms, between which the sample was flipped [104]. Reference holograms were recorded from vacuum after the

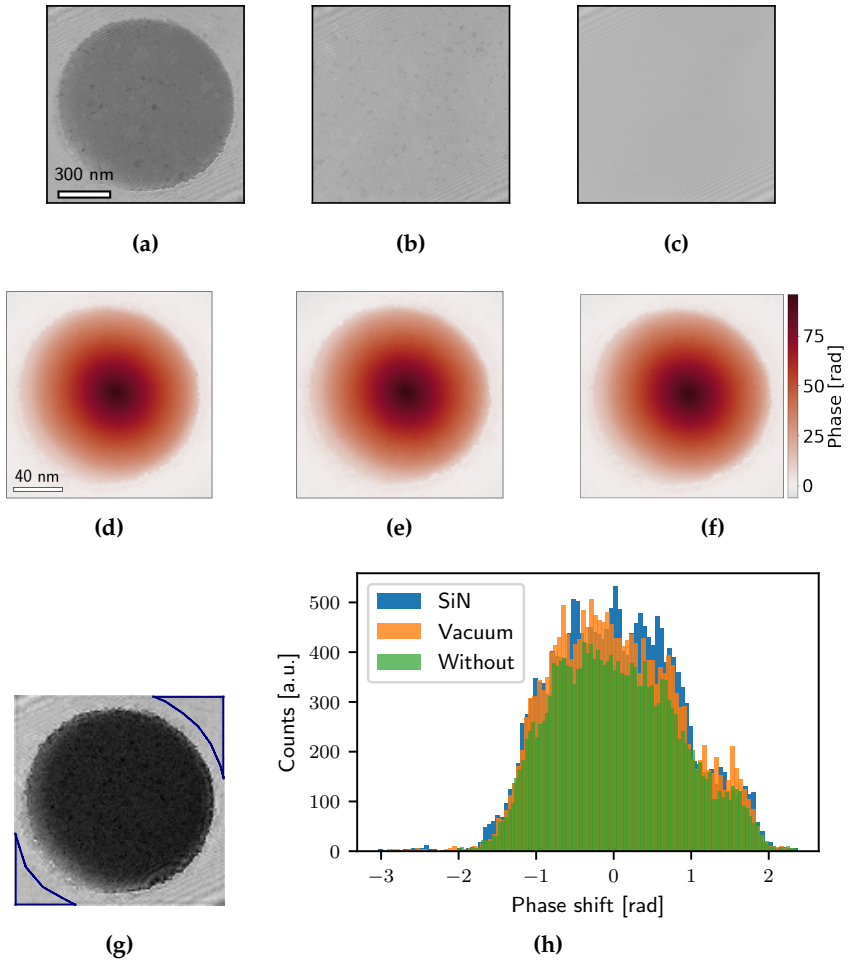

Figure 5.3.: Influence of the choice of reference hologram on the total phase. (a) Object hologram of a Py disk of nominal thickness 100 nm. (b) Reference hologram recorded form a SiN region. (c) Reference hologram recorded from vacuum. (d) - (f) Reconstructed total phase shift images obtained using (d) no reference and (e,f) reference holograms recorded from (e) SiN and (f) vacuum. (g) Reconstructed amplitude image of the disk. (h) Histograms of the phase distribution measured in the marked blue regions in (g). There is only a small difference between the widths of the different histograms.

sample was removed from the beam path. During data analysis, the total phase shift was first reconstructed for each object hologram. The total phase image corresponds to the turned over experiment has to be flipped digitally, in order to match it with the original total phase image. Digital turning was achieved by first flipping the image about the x axis and then rotating it by $-32°$. The angle was determined from the relationship between the holder tilt axis with the x and y axis of the electron camera. The shift in x and y directions between the first total phase image and the digitally flipped phase image were obtained from a cross correlation performed on the corresponding amplitude images, which were also digitally turned over. The advantage of using the amplitude images is that they do not differ, unlike the total phase images, which contain the magnetic contribution to the phase. It was not possible to warp the total phase images as was done for the spin ice (c.f Sec. 4.3.3) due to the lack of distinct features for round disks. The electrostatic and magnetic contributions to the phase were finally retrieved by calculating half of the sum and half of the difference of the original and tuned over phase shift images, respectively.

Figure 5.4a shows the resulting electrostatic contributions to the phase shift. It can be seen that the sample has a reasonably uniform thickness across the disk. The decrease in phase shift on the lower left side of the disk, which is evident in the line scan across the electrostatic phase shift shown in Fig. 5.4b, corresponds to a local reduction in the thickness of the disk, which may have resulted from a tilt of the sample during Py deposition, with respect to the Py source. The electron beam resist could then have shadowed this part of the disk. The thickness of the disk was determined from the mean electrostatic phase shift in the region where the sample thickness was homogeneous, based on the value for the MIP of 22.9 V determined for the spin ice sample (*cf.* Sec. 4.6.1). The inferred thickness is approximately 143 nm, which is thicker than the nominal value of 100 nm. This deviation is likely to result from several factors. First, thickness control during Py deposition is not error-prone because the quartz balance used to measure the deposition rate is not perfectly calibrated. Second, the Cr adhesion and capping layer are included in the measured thickness. Third, the ratio of membrane and capping/adhesion layer to Py thickness is much smaller than that in the spin ice. Forth, the composition of Ni and Fe in the thick Py disk is different than that of the thin Py nanomagnets in the spin ice.

The grey areas in Fig. 5.4a indicate regions where the confidence was set to 0. In these regions, the two aligned images do not overlap and the electrostatic contribution to the phase shift cannot be determined. This area results from the need to virtually flip the second phase image about the holder axis to compensate for physical turning the sample over inside the microscope. The outline of the

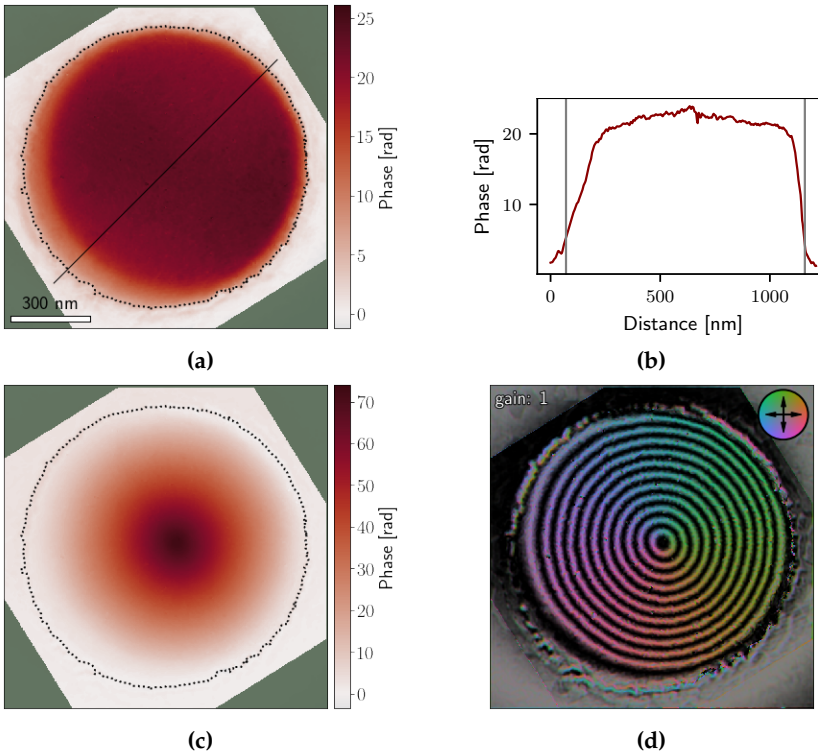

Figure 5.4.: Electrostatic and magnetic contributions to the phase shift for a magnetic vortex in a Py disk of a nominal thickness of 100 nm. (a) The electrostatic phase shift reveals a uniform thickness across a large part of the disk. The small phase shift variations visible at the lower left edge indicate the presence of thickness variations. The grey area indicates regions that are not taken into account in the analysis. The dotted line marks the edge of the disk. (b) Linescan across the electrostatic phase shift along the black line marked in (a). The grey lines indicate the borders of the disk indicated in (a). (c) Magnetic contribution to the phase shift. (d) Magnetic induction map, showing counterclockwise rotation of the vortex.

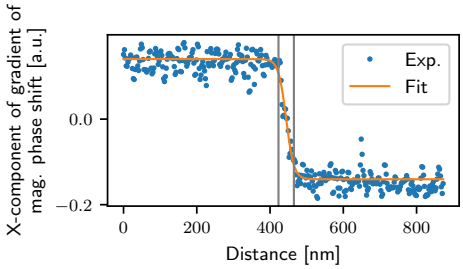

Figure 5.5.: Line profile through the y component of gradient of the magnetic contribution to the phase shift (blue). The core diameter is determined to be 42 ± 4 nm by a fit (orange). The grey lines indicate the fitted core diameter. See text for details.

disk was detected by setting a threshold for the minimum electrostatic phase shift for the particle and is indicated by a dotted line (see Sec. 4.3.1).

The magnetic phase shift and corresponding magnetic induction map are shown in Fig. 5.4c and 5.4d, respectively. The magnetic phase shift contains a peak at the centre of the disk (Fig. 5.4c), as expected for a magnetic vortex that rotates counterclockwise, as seen in the magnetic induction map (Fig. 5.4d). The size of the core is estimated by looking at the line profile of the y component of the gradient of the magnetic contribution to the phase shift. This gradient is a measure of the in-plane magnetic induction. The vortex core diameter w can be extracted from the line profile at the core position according to

$$y = a \cdot \tanh(\frac{x - x_0}{w/2}), \tag{5.1}$$

where x_0 is the x position of the vortex core [128]. Fitting Eq. 5.1 to the experimental line profile gives a vortex core diameter of $w = 42 \pm 4$ nm (Fig. 5.5). The line profile is averaged over 10 nm in the x direction in order to smooth the data. This is likely to result in a slight overestimation of the vortex core size.

The projected in-plane magnetisation of the disk was reconstructed using the MBIR algorithm (*cf.* Sec. 3.2.5), in order to compare it to a simulated magnetisation distribution. Here, a regularisation of 1 was chosen during the reconstruction. The resulting projected in-plane magnetisation is shown in Fig. 5.6a, with a counterclockwise rotation of the magnetic moments. The thickness variations at the edge of the disk (Fig. 5.4a) result in a decrease in the projected in-plane magnetisation on the left side of the disk. In addition, local thickness variations result in a shift of the vortex core in the opposite direction, *i.e.* towards the right side.

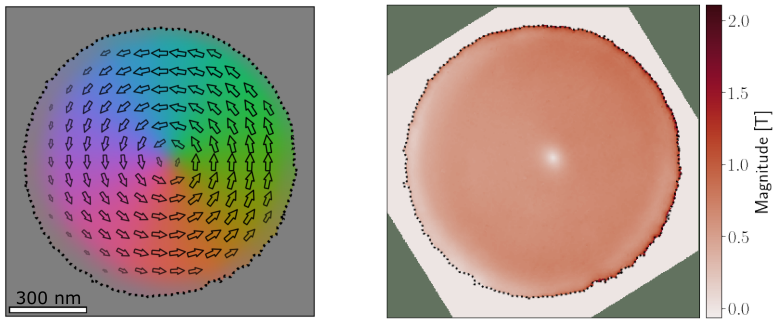

(a) **(b)**

Figure 5.6.: Projected in-plane magnetisation reconstructed inside a Py disk of a nominal thickness of 100 nm using the MBIR approach. (a) Direction and magnitude of the projected in-plane magnetisation. The magnitude is encoded in the brightness of the colours as well as in the length of the arrows. The projected in-plane magnetisation is consistent with counterclockwise rotation of a magnetic vortex. (b) Magnitude of the projected in-plane magnetic polarisation normalised to the measured thickness at each pixel.

In order to take the thickness variation into account when analysing the magnitude of the magnetisation, the magnitude of the projected in-plane magnetisation was normalised to the measured thickness of the disk at each pixel based on a thickness map calculated from the electrostatic contribution to the phase shift. Figure 5.6b shows the resulting normalised magnitude of the projected in-plane magnetisation. The magnetic vortex core is clearly visible due to the decrease in the magnitude of the projected in-plane magnetisation. The normalised projected in-plane magnetisation is approximately constant over the radius of the disk. However, it sometimes decreases or increases along the edges of the disk. Right at the edges of the disk, these variations can be a result of a not perfect mask during the reconstruction of the magnetisation. The variations further inside the disk may result from shape imperfections and will be discussed in Sec. 5.3.1. The average normalised in-plane magnetic polarisation is 0.66 T in the homogeneous regions. This value is lower than the saturation magnetic polarisation the spin ice samples of 0.73 T (*cf.* Sec. 4.6.2), even though both samples were prepared using the same recipe and using similar materials for evaporation. This discrepancy may result from different effects: (i) the effective composition of the Py material corresponds to a (65/35) Ni/Fe ratio for the spin ice samples and 70/30 for the disks, (ii) oxidation of the samples decreases their magnetic thickness, (iii) their total thickness is different meaning that the relative influence of the adhesion

and capping layers on the measured electrostatic phase shift varies between the thick Py disks and the thin spin ice samples.

5.2.3. Comparison of reconstructed magnetisation with micromagnetic simulations

In addition to the experimental analysis, the magnetic vortex state in the Py disk was compared with by micromagnetic simulations provided by Sebastian Gliga (PSI). The simulations were performed for a 160-nm-thick disk with a diameter of 1500 nm and nominal composition $Ni_{81}Fe_{19}$. The dimensions of the disk correspond to those of the disk used for the vortex gyration experiments (*cf.* Ch. 6). The parameters were set up in such a way that a clockwise in-plane rotation was achieved, with the core of the disk pointing upwards. The resulting magnetisation distribution is shown in Fig. 5.7a. The vortex core is too small to be visualised in the image of the full disk. Therefore, two cross-sections were generated at the core position in the *xy*-plane and the *xz*-plane (see Fig. 5.7b and Fig. 5.7b). The cross-sections correspond to a cube with dimensions of $300 \times 300 \times 160\,\mathrm{nm}^3$. The vortex core is visible in the cross-section in the *xy*-plane as a gradual decrease of the magnitude of the in-plane magnetisation. The cross-section in the *xz*-plane reveals the reason for this gradual decrease. The vortex core has a barrel-like shape, rather than having a sharp transition from in-plane magnetisation to the out-of-plane core. This configuration reduces the exchange interaction by slightly canting adjacent magnetic moments with respect to each other. At the top and bottom surfaces of the disk, the magnetisation is further tilted parallel to the surface, thereby minimising magnetic stray fields and resulting in the final barrel shape. The vortex core diameter is estimated to be 61.5 ± 0.1 by fitting Eq. 5.1 to a linescan through the *y* component of the magnetic polarisation in Fig. 5.7 (Fig. 5.8). This distance corresponds approximately to the outer diameter of the barrel-like shape (grey lines in Fig. 5.7c).

A comparison of the simulated magnetisation with the reconstructed projected in-plane magnetisation for the 143-nm-thick disk underlines the importance of using both methods. On the one hand, the simulation reveals the barrel-like shape of the core. This information is lost in the present experiment, which only records the projected in-plane magnetisation. On the other hand, the disk is not perfect in reality, as assumed in the simulation. For example, the thickness variation of the Py disk results in a shift of the vortex core away from the centre of the disk. This shift is in present for the idealised disk in the simulations.

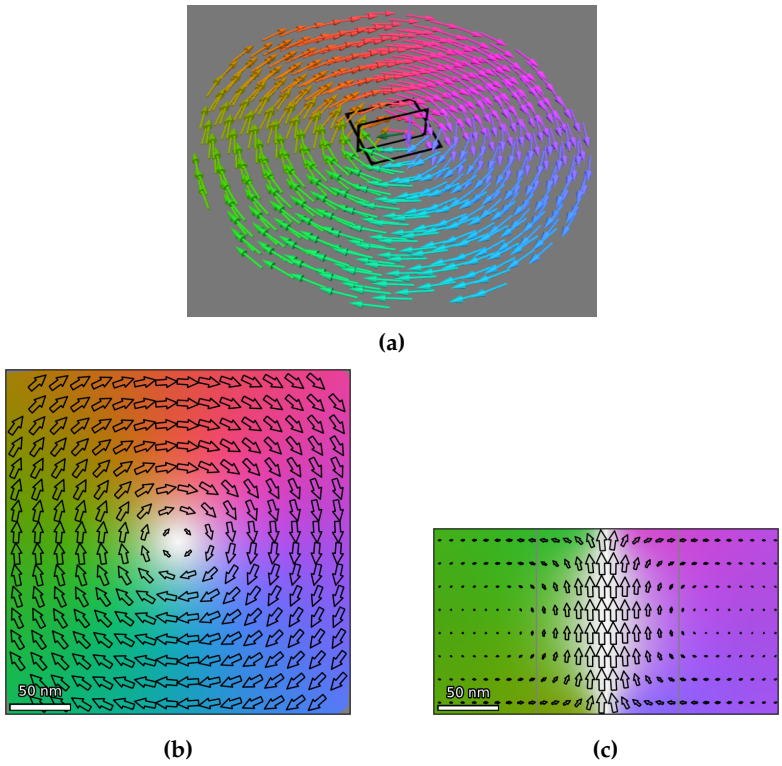

Figure 5.7.: Micromagnetic simulation of a vortex state in a Py disk with a diameter of 1.5 µm and a thickness of 160 nm. (a) Three-dimensional representation of the magnetisation in the disk, with the black rectangles outlining the positions of the slices shown in (b) and (c). (b) *xy*-plane and (c) *xz*-plane sections in the middle of the disk. The colours encode the rotation of the magnetisation in all images. The white colour shows the direction of the out-of-plane magnetisation at the magnetic vortex core. The arrows in (a) describe the three-dimensional distribution of the magnetisation, while the arrows in (b) only show the magnetisation in the *xy*-plane and (c) in the *xz*-plane correspondingly. The length of the arrows encodes the magnitude of the magnetisation. The magnetic vortex exhibits clockwise in-plane rotation, with its core pointing upwards. The core itself has a barrel-like shape and is larger in the centre than at the surfaces of the disk. The grey lines indicate the diameter of the vortex core determined according to Fig. 5.8.

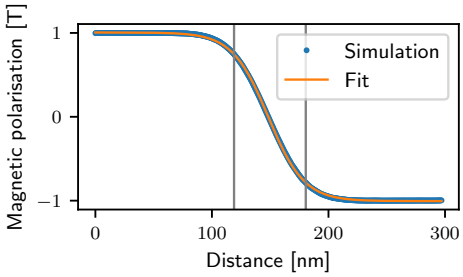

Figure 5.8.: Linescan through the y component of the magnetic polarisation shown in Fig. 5.8 (blue). The vortex core size is fitted according to Eq. 5.1 (orange) and estimated to be 61.5 ± 0.1 nm. The grey lines indicate the vortex core size.

Therefore, simulations and experiments have to be combined in order to fully understand the magnetic properties of vortices in Py disks.

5.2.4. Dependence of core shape on the thickness and diameter of the disk

As seen above, the thickness of the disk has an influence on the vortex core size. This relationship is further studied in this section, as the vortex core is of central importance for subsequent dynamic experiments (see Ch. 6). In the literature [86], it has been shown that the radius of the core increases with increasing disk thickness if the exchange length (5 nm for Py [129]) is sufficiently smaller than the disk thickness. At the same time, a change in the diameter of the disk does not have a significant effect on the radius of the core [86]. This behaviour was investigated experimentally probed by measuring the vortex core sizes of disks with various geometries. A hologram was recorded and reconstructed for each disk. An overview of the investigated samples is given in Table 5.1. The diameter of all disks were measured using a radial profile. The uncertainty of the diameter mainly depends on the different magnifications the holograms were recorded with.

The diameter of the core was determined by using the procedure that was described in Sec. 5.2.2, *i.e.* from the gradient of the phase shift. In contrast to the previous analysis, the profile was taken from the total phase image for all experiments except the value at a nominal thickness of 100 nm. The restrict to the total phase shift avoids the need for a turning over experiment and is justified as

Table 5.1.: Overview of investigated Py disk samples. Six different samples were analysed experimentally.

nominal thickness [nm]	measured diameter [nm]
50	1281 ± 16
50	1596 ± 31
100	1086 ± 12
150	1085 ± 49
150	1425 ± 34
175	1658 ± 65

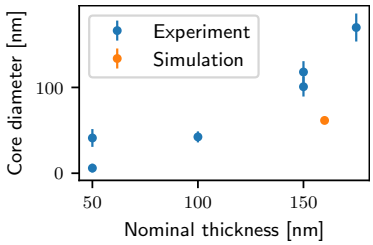

Figure 5.9.: Vortex core radius plotted against nominal disk thickness for the disks listed in Table 5.1. The core radius increases with disk thickness. The orange point corresponds to the measured from a micromagnetic simulation core size for comparison.

the vortex core area is sufficiently flat. Therefore, the total phase is dominated by the local change in magnetic phase shift in these regions. Figure 5.9 shows the dependence of vortex core size on disk thickness, while neglecting the disk diameter. The core size increases with disk thickness, as expected. The orange dot in Fig. 5.9 corresponds to the core diameter determined from the magnetic simulations. This diameter is smaller than the experimental. The deviation might be a result of several factors. Firstly, the average in-plane magnetic polarisation is with 0.66 T smaller than the nominal value of 1 T. Secondly, the true magnetic thickness is not known. Thirdly, there are shape deviations which will be discussed in the following section.

In contrast to disk thickness, the diameter of the Py disks has a less significant influence the size of the vortex core as long as the disk diameter is much larger than the core diameter. This dependence can be seen when comparing measurements from Py disks, that have the same nominal thickness of 50 and 150 nm while varying in diameter around 300 nm and 340 nm, respectively (Fig. 5.9 and Table 5.1). However, only the nominal value for the thickness can be compared which re-

stricts the further analysis. Nevertheless, this finding is in good agreement with literature on the properties of vortices in disks [86].

5.3. Effect of the three-dimensional shape of the disks

So far, the magnetic properties of the disks have been studied in projection and it was assumed that the disks are flat. However, a cross-sectional study of a disk reveals that the disks in fact have a curved shape. In this section, the origin of the shape variation and its effect on the magnetic properties of the disk are investigated.

5.3.1. Shape variations of the Py disks

The shapes of the Py disks were investigated by studying cross-sections of three different disks prepared using FIB milling. Figure 5.10 shows an overview image of a cross-section of a nominally 175-nm-thick disk that has a nominal diameter of 1500 nm. The thickness and diameter of the Py disk are measured to be ~164 nm and ~1600 nm, *i.e.* smaller and larger than the nominal values, respectively (*cf.* Sec. 5.1). The most striking and unexpected feature is the bent shape of the disk, whose edges are peeled away from the membrane. The cross-section was prepared by first depositing C on top of the SiN membrane and then Pt on the lower part. The cross-section was then cut out using FIB milling. In order to exclude the possibility that the bending is an artefact of cross-section preparation, two additional cross-sections of different disks were prepared by FIB milling using slightly different preparation steps. For the second cross-section, first the Pt on the back side and then the C on the front side were deposited before cutting. For the third cross-section, first a C protection layer was deposited on top of the Py structure on the SiN membrane. Then, the membrane with the Py structure was lifted up and attached onto a Si crystal. In the final step, a cross-section of the Py structure was cut from of the stack containing the sample and the Si crystal. The two additional cross-sections exhibited similar bending (not shown), suggesting that the bending has been present before the cross-section was cut.

Chemically sensitive HAADF STEM images and EDX maps were recorded from the cross-section of the Py disk, in order to investigate the origin of the bending

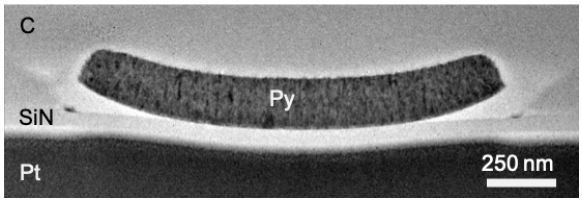

Figure 5.10.: Overview BF TEM image of a cross-section cut from a Py disk, revealing that the disk has peeled from the membrane and bent upwards at its edges. The disk has a nominal thickness of 175 nm and a nominal diameter of 1500 nm. It is measured to be ~164 nm thick, with a diameter of ~1600 nm.

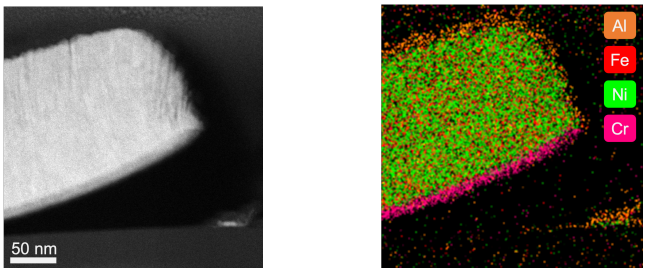

(a) **(b)**

Figure 5.11.: Edge of a 164-nm-thick Py disk. (a) HAADF STEM image revealing that the columnar growth at the edges points upwards. (b) EDX composition map. The Cr has peeled off and Al is present along the edge of the disk.

(Fig. 5.11). Small particles next to the disk are present on all of the samples. They consist of Ni and Fe, with an Al or Cr capping layer on top of them. Most importantly, there is no Cr adhesion layer beneath the particle. The Py therefore had to be deposited after the adhesion layer had already peeled off, suggesting that the bending already happened during Py deposition. A possible explanation is that some Py adhered to the electron beam resist that was used to define shape of the disks and was redeposited on the membrane when the resist was washed off. However, there should then not be a continuous capping layer on top of the particle, making such redeposition unlikely. Another indication that the bending took place during deposition is the presence of an Al capping layer along the edge of the Py disk (Fig. 5.11b). It is likely that the capping layer can only be deposited along this edge if the disk is already bent before Al deposition is started.

The bending of thin Py particles on SiN has been reported previously [130]. The effect was attributed to the significantly different thermal expansion coefficients

of Py and SiN ($10.5 \cdot 10^{-6}$ to $2.6 - 3.3 \cdot 10^{-6}$ K^{-1}), resulting in mechanical stress [130]. The mechanical stress is released when the disk is peeled off the membrane. The adhesion of Cr to Py is observed to be stronger than to SiN, as the Cr is also peeled off. This difference in thermal expansion is relevant because the Py pellets are heated to 1500°C to deposit Py on the sample. As the electron beam resist on the sample does not reflow during deposition, it can be excluded that the sample temperature exceeds 120°C. However, a substantial amount of heat will still be deposited in the Py disk and the SiN membrane. The hypothesis that a difference in thermal expansion is the driving mechanism for the bending is supported by a study of a cross-section of a 120-nm-thick Py disk deposited on a Si substrate with a SiN layer. A DF SEM image of the cross-section shows a flat disk with only minor bending at the edges of the sample (see Fig. 5.12). This sample was patterned in the same way as the Py disks on the membrane, *i.e.* including a Cr adhesion layer. Here, the Si substrate acted as a heat reservoir, dissipating heat from the disk and membrane. Therefore, the Si substrate prevents an overall heating of the Py disk and the SiN membrane and consequently the bending due to thermal expansion. The C layer on top of the disk was first deposited using electron-beam-induced deposition and subsequently using an ion-beam-induced deposition. The two methods result in darker and brighter contrast of the C layer in the DF SEM image. The bright contrast at the edges of the disks can be attributed to C contamination accumulating when these regions were exposed to a stronger electron beam dose while focusing the electron beam on the sample for imaging. In addition to the different thermal expansion coefficients, other reasons may result in bending of the disks, *e.g.* tensile strain introduced during growth due to a lattice mismatch of the different elements. This possibility can be excluded, since the disk on a Si substrate with a SiN membrane is not bent. Hence, a difference in thermal expansion coefficients is the most likely source of the bending.

5.3.2. Movement of vortex core with sample tilt

Bending of the disk causes a number of different effects on the recorded phase image and on the magnetic response of the disk with the tilt angle. Both situations should be considered in the study of vortex core dynamics, as the sample may be tilted with respect to the applied field or the electron beam (see Ch. 6). The effects are demonstrated by tilting the sample investigated in Sec. 5.2.2 to 50°. This tilt angle is chosen as it offers the best compromise between tilting as far as possible to maximise the in-plane component of the applied field, while the core is not yet affected by unwrapping errors arising from the increase in projected

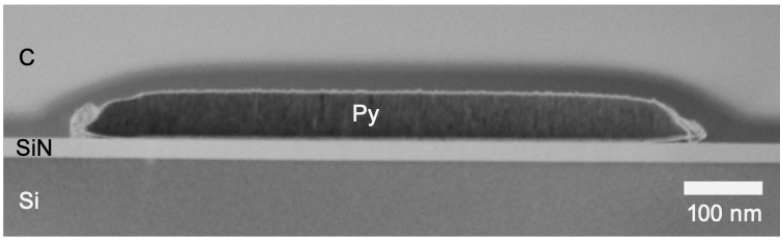

Figure 5.12.: DF SEM image of a Py disk prepared on a Si substrate. The nominal thickness and diameter of the disk are 100 and 1500 nm, respectively, while they are measured to be ~110 and ~1500 nm, respectively. Here, no significant bending of the disk can be observed. See text for details.

sample thickness. Apart from the tilt angle, the other experimental parameters remain the same (*cf.* Sec. 5.2.2). As before, the magnetic phase shift was extracted using a turning over experiment. A resulting magnetic induction map is shown in Fig. 5.13a. The first visible effect is the presence of unwrapping errors at the lower edge of the sample due to increased noise in the phase measurement. These unwrapping errors occur in the region where the sample is tilted upwards most strongly in the z direction (Fig. 5.13b). The upwards tilt increases the distance through which the electron beam travels in the sample due to bending, as shown on the right side of Fig. 5.13b. This increase in thickness results in a weaker signal and a decrease in signal-to-noise ratio. In addition, a half ring can be seen below the sample in the area framed in grey in Fig. 5.13a. This ring can be attributed to the presence of the small Py particles, which are deposited underneath the disk and can be observed in cross-section (Fig. 5.10 and Fig. 5.13b). The upper half of the ring is not visible in the magnetic induction map (Fig. 5.13a), as its contribution to the phase shift is negligible compared to the magnetic phase shift of the thick Py disk, *i.e.* the thick Py disk shadows the upper half of the ring. Another effect that can be seen in the magnetic induction map is a shift of the vortex core. The blue line indicates the long axis of an ellipse fitted to the outlines of the projected disk. The vortex core is expected to lie on this axis. The observed shift is a geometrical effect and only appears in projection. The reason for the shift is visualised in Fig. 5.13b: due to the curvature of the disk, the middle of the disk in the x direction does not correspond to the centre of the disk where the vortex core is situated. Therefore, the vortex core is shifted towards the upwards-tilted part of the disk in a projection in the z direction. If the disk were perfectly flat, the vortex core would stay in the middle of the disk even in the presence of sample tilt. Hence, it would not be possible to explain the shift for a magnetic vortex in a perfectly flat disk.

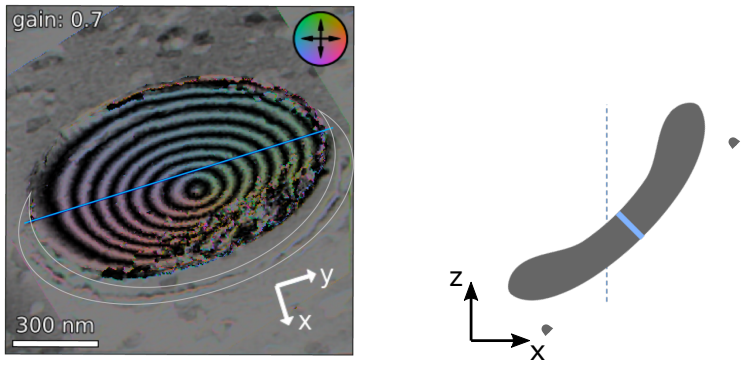

(a) (b)

Figure 5.13.: Influence of shape deviations on the projected magnetic induction. (a) Magnetic induction map of a Py disk (Sec. 5.2.2) investigated in Sec. 5.2.2 at a 50° tilt angle. The blue line depicts the long axis of the fitted ellipse at which the vortex core should be located in for a flat shape. The unwrapping errors at the lower edge are due to an increase in projected thickness. The half ring below the disk (marked by grey lines) can be attributed to the small particles next to the disk seen in cross-section. (b) Schematic sketch of a side view of the disk under tilt. The dashed line indicates the middle of the sample along the x direction. The blue region inside the disk indicates the position of the vortex core. The vortex core is shifted with respect to the x axis for a bent disk. When looking along z direction, the small particles at the left side are shadowed by the Py disk, while it is visible on the right side.

In addition to the apparent shift of the vortex core in a titled Py disk studied at remanence, it can also be displaced by applying an external magnetic field according to Dietrich *et al.* [130]. The effects of in-plane and out-of-plane external fields on a vortex core are visualised in Fig. 5.14, based on their argumentation. For simplicity, a square sample in a Landau state is shown in the schematic figures. Figures 5.14a and 5.14b show top and side views of a square sample, which is bent on both sides. An out-of-plane magnetic field $\mathbf{H}_{\mathrm{oop}}$ applied to this bent sample would have components parallel and perpendicular to the sample surface at the edges of the sample. Thus, the bent sample would experience an effective in-plane magnetic field due to the applied out-of-plane field $\mathbf{H}_{\mathrm{oop}}$. The effective in-plane field is indicated by green arrows in the top view. The direction of the effective in-plane field is radial away from the centre. However, the position of the vortex core is not affected by the effective radial in-plane field, as the core is situated in the centre of the disk, where these fields are negligible. The situation changes when applying an additional external in-plane field $\mathbf{H}_{\mathrm{ip}}$, as shown in Fig. 5.14c. Note the difference between the external applied in-plane field $\mathbf{H}_{\mathrm{ip}}$ pointing in the same direction at every point of the sample while the effective in-plane component of $\mathbf{H}_{\mathrm{oop}}$ is radial, as shown in Fig. 5.14b. The presence of the external in-plane field $\mathbf{H}_{\mathrm{ip}}$ results in a shift of the vortex core to the right side, as the magnetic moments align with the external in-plane field and the left domain grows in size. The vortex core is no longer situated in the centre of the disk, but moves towards its edge. There, $\mathbf{H}_{\mathrm{oop}}$ has a strong effective in-plane component in the radial direction. This component points towards the right edge at the position to which the vortex core is shifted. Thus, the magnetic moments align parallel to the effective field and the vortex core is shifted downwards. The latter shift would not be expected in a flat sample, in which an applied out-of-plane field should only result in an increase or decrease of the vortex core size, but not in a shift. For the disks under investigation, the edges are the regions where bending is strongest. Thus, the effective in-plane magnetic field due to the applied out-of-plane external field $\mathbf{H}_{\mathrm{oop}}$ is expected to have the largest effect at these positions.

This phenomenon of vortex core displacement in an applied field in the presence bending of the disk may affect the study of vortex core gyration in Ch. 6. Therefore, the applied field strength and vortex core displacement that are required to move the vortex core were studied for a sample with a thickness of 119 ± 12 nm and a diameter of 1489 ± 40 nm, as shown in Fig. 5.15. The thickness is measured in cross section and the diameter looking at the radial profile of the object hologram. This sample was tilted to 25° and various external magnetic fields were applied in the electron beam direction using the objective lens of the

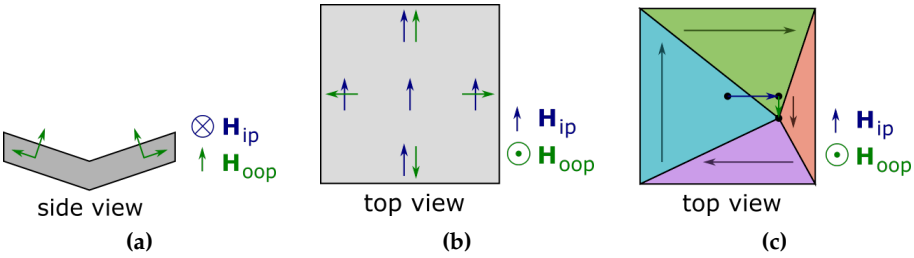

Figure 5.14.: Schematic overview of the effect of external in-plane and out-of-plane fields on a bent sample in a Landau state [130]. (a) and (b) Sketches of a bent square sample (in side view and top view, respectively) and the applied magnetic fields. (c) The magnetic state and the shift of the core due to these fields. The in-plane field $\mathbf{H}_{ip}$ results in a shift of the core perpendicular to the field. The out-of-plane field $\mathbf{H}_{oop}$ can be divided into components parallel to the surface and perpendicular to it. The out-of-plane field $\mathbf{H}_{oop}$ has an effective in-plane component, resulting in an additional shift of the core perpendicular to the effective field.

microscope. Due to the sample tilt, the external field can be divided into an in-plane and an out-of-plane component with respect to the disk. The in-plane component is perpendicular to the tilt axis and is therefore perpendicular to the long axis of the ellipse that represents the outline of the tilted disk in projection. Off-axis electron holograms were recorded in applied fields of 0 to 150 mT. Figure 5.15a shows the resulting magnetic induction maps of the total phase shift for various applied fields. Here, it is assumed that the electrostatic contributions to the phase shift is constant across the disk, which holds for most parts of the disk except at its very edges. It was found that the vortex core moves along the long axis of the ellipse as the applied field increases. At fields of 100 and 150 mT, the vortex core develops a C-shaped structure as it moves closer to the edge of the disk, as reported previously [131]. At a field of 150 mT, the vortex core moves not only along the long axis, but also towards the lower edge of the disk. Here, the change in direction of the magnetic field lines might result from a competition of the magnetic moments aligning themselves according to the applied in-plane and according to the applied out-of-plane field in combination with the effect of shape deviations.

The phase images for all applied fields were aligned with respect to each other by using the corresponding amplitude images. The vortex core position was then detected in each phase image by filtering for pixels with the largest total phase shift and then determining the centre of mass in the filtered images. The

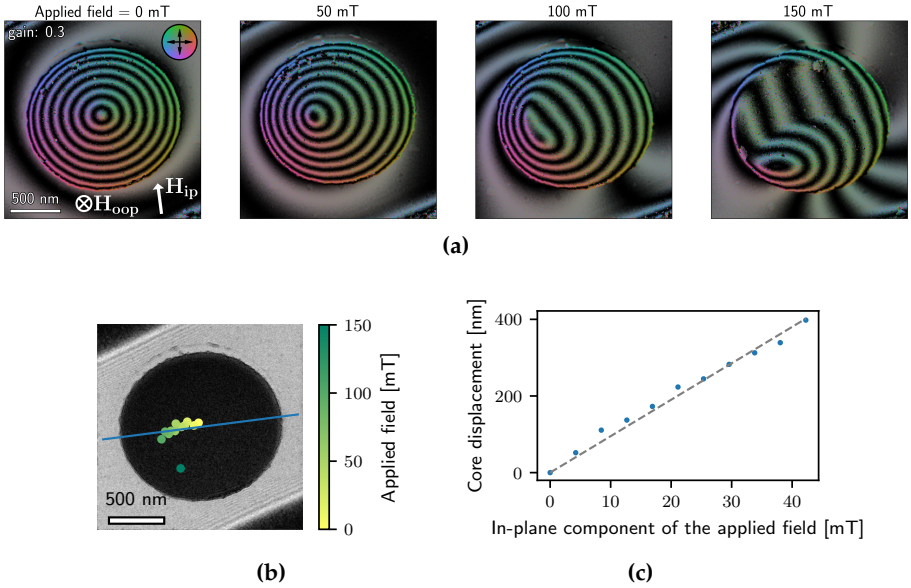

Figure 5.15.: Vortex core displacement as a function of applied field for a disk with a thickness of 120 nm. The sample is tilted by 25° and various magnetic fields are applied along the electron beam direction. The applied field has an in-plane component $\mathbf{H}_{ip}$ and an out-of-plane component $\mathbf{H}_{oop}$. (a) Magnetic induction maps showing the total phase shift recorded in different applied fields indicated. (b) Position of the vortex core plotted on an amplitude image of the Py disk. The blue line indicates the tilt axis of the sample. The vortex core is displaced parallel to the tilt axis up to fields of 100 mT. At an applied field of 150 mT, the vortex core is also displaced perpendicular to the tilt axis. (c) Displacement of the vortex core placed as a function of the in-plane component of the applied field. The dashed line shows a linear for to the points.

resulting positions are plotted in Fig. 5.15b as a function of applied field, using the amplitude image of the disk at 0 mT as a background. The blue line in the image indicates the tilt axis of the ellipse. If the disk were not bent, then the vortex core would be expected to be displaced along the tilt axis towards the edge of the disk. Such a displacement can be seen for magnetic fields up to 100 mT. A total applied field of 100 mT corresponds to an in-plane component of 42 mT and an out-of-plane component of 91 mT. Here, the shift of the core along the axis displays a slight trend towards the lower edge of the sample. At an applied field of 150 mT, the vortex core is clearly displaced from the long axis. This displacement may result from the effect of the out-of-plane component of the applied field or thickness variations of the disk close to its edge. The results suggest that the vortex core gyration will not be affected by bending of the disk if no additional out-of-plane field is applied, the applied in-plane field is smaller than 100 mT and the sample is not tilted. During the vortex core gyration experiments, an in-plane field and an out-of-plane field are applied simultaneously (*cf.* Ch. 6). The applied in-plane field is on the order of a few tens of a mT. Therefore, the vortex core is only slightly deflected and it is located close to the centre of the disk at each point of its gyration. Hence, the applied out-of-plane field is not expected to result in an additional shift of the vortex core.

In the dynamic experiments, it is important that the vortex core motion is not hindered by pinning. The origin of pinning is the minimisation of total energy (*cf.* Sec. 2.2), which may involve alignment of the magnetisation with respect to local anisotropy within the polycrystalline domains of Py, as shown by Uhlig *et al.* [132]. In other words, a difference in local anisotropy of the domains may affect the vortex core position. In the latter study, it was not possible to associate the positions of the pinning sites with the physical morphology of the sample using Lorentz microscopy or time-resolved Kerr microscopy [132, 133]. Nevertheless, the role of grain boundaries as pinning sites has been demonstrated experimentally using UTEM [134]. In the literature, it has been suggested that surface roughness is the dominant pinning source and that pinning is strongest if the features have a length scale similar to the vortex core diameter [135]. As the dynamic experiments that are present below are carried out for disks that have a thickness of approximately 150 nm, the vortex core has a diameter of approximately 80 nm (*cf.* Sec. 5.2.4). Therefore, vortex core gyration should not be affected significantly by pinning because the surface roughness is much smaller (*cf.* Fig. 5.2). In order to verify this assumption experimentally, the displacement of the vortex core was investigated to assess the dependence of pinning of the vortex core on its position. Figure 5.15c shows the displacement of the vortex core with respect to the core position plotted as a function of

the in-plane component of the applied field. Here, only the regime where the vortex core is displaced along the long axis is considered. The displacement has an approximately linear dependence on applied in-plane field. This linearity implies that the vortex core is able to move smoothly and that no strong pinning sites are present. The dynamic investigation of vortex core motion is therefore not expected to be hindered by pinning.

5.3.3. Magnetic state of a cross-section

The Py disk was further investigated by studying its magnetic properties in cross-section. Large impurities, *e.g.* due to a contaminated Py source, would affect the electrostatic and magnetic contributions to the phase shift and could act as pinning centres. The phase shifts were retrieved by performing a turning over experiment at a magnification of 11.5 kx using biprism voltage of 135 V, which corresponds to a holographic interference spacing of 1.5 nm. The regions where the two total phase images did not overlap were excluded by using a confidence matrix in the MBIR approach. A phase ramp in the electrostatic phase shift was removed by fitting a linear function to the phase in the C support above the Py and assuming that the electrostatic phase shift is constant in this region. A mask of the particle was drawn by defining a minimum value for the electrostatic phase shift of the Py. For the magnetic phase shift, a phase ramp was removed using the MBIR approach (*cf.* Sec 4.3.2). The resulting electrostatic and magnetic phase shift images are shown in Fig. 5.16.

The electrostatic phase shift shown in Fig. 5.16a is in good agreement with the previously presented results acquired using conventional electron microscopy (*cf.* Sec. 5.1). The Pt support at the bottom, the SiN membrane, the Py disk and the C layer at the top can be distinguished. The dark and bright contrast below the disk is located inside the SiN membrane and might result from charging being different when the sample is turned over. In addition, the Cr adhesion layer is visible at the bottom of the disk. Inside the disk, the columnar growth structure can be seen in the form of local variations of the electrostatic phase shift (inset in Fig. 5.16a). The lack of image alignment artefacts indicates that the routine that was used to warp one image to fit the other worked well. At the same time, no unexpected features are visible in the electrostatic phase shift, suggesting that there are no significant impurities in the sample. These results are in good agreement with EDX STEM analysis, which also revealed no impurities in the Py (Fig. 5.2 and Fig. 5.11).

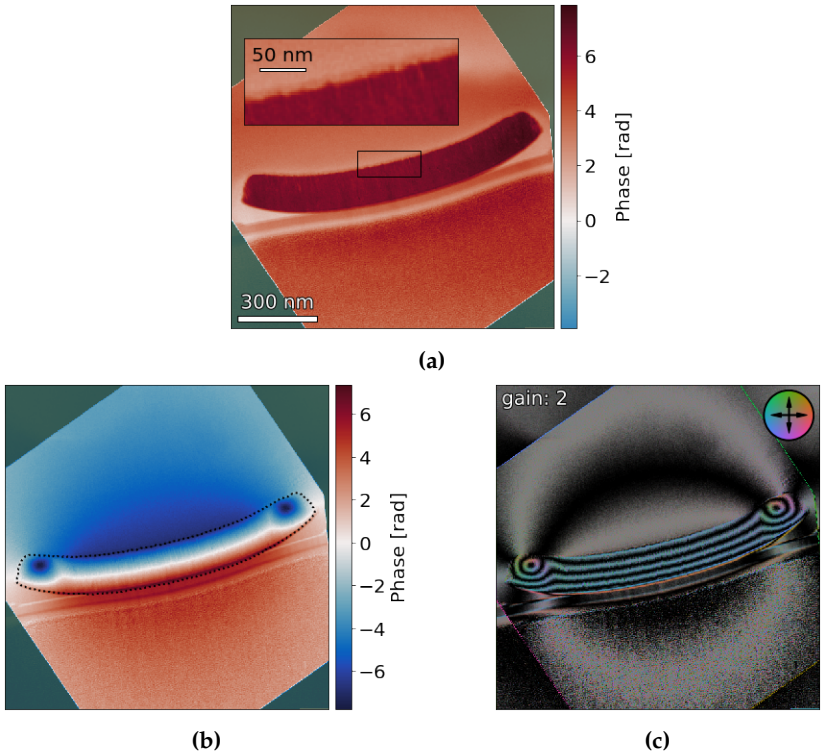

Figure 5.16.: Electrostatic and magnetic contributions to the phase shift measured from a cross-section of a 164-nm-thick Py disk shown in Fig. 5.10. (a) Electrostatic phase shift, showing bending of the disk and adhesion layer at the bottom. The inset shows a close up, in which the columnar structure of the Py is visible. The black box indicates the area of the inset. (b) Magnetic phase shift and (c) magnetic induction map of the cross-section. The formation of the vortices results from minimisation of the stray field and is fostered by the bent shape.

The magnetic phase shift and corresponding magnetic induction map (Fig. 5.16b and Fig. 5.16c) reveal that the magnetic induction follows the shape of the disk inside the Py island (Fig. 5.16c), with the shape anisotropy dominating the magnetic configuration. Surprisingly, both ends of the cross-sections contain magnetic vortices of the same chirality. The vortices minimise magnetic stray fields outside the cross-section, at the cost of increasing the exchange interaction. The formation of such vortices is fostered by bending of the disk and by the comparable thin thickness of the cross-section. Due to the latter point, it is not possible to predict if these vortices exist in the full disk as well. In Fig. 5.16b and Fig. 5.16c, there are no unexpected alterations of the magnetic phase shift resulting from possible impurities, further indicating that such disks are suitable for the dynamic experiments that are presented in the next chapter.

5.4. Summary

The presence of a magnetic vortex was experimentally demonstrated in circular Py disks with varying dimensions. The structures and compositions of the disks were first investigated revealing columnar growth of the Py in cross-section. It was also shown that there are no significant impurities are present within the disks. Reconstruction of the magnetisation of a magnetic vortex was presented for a nominal 100-nm-thick Py disk revealing variations due to the fact that such disks does not have ideal geometries. Micromagnetic simulations revealed that the magnetic vortex core is a barrel-shaped. The properties of the core with respect to the disk geometry were studied. It was found that the diameter of the core increases with increasing disk thickness while being approximately independent of disk diameter. Cross-sectional studies revealed Py disks fabricated on SiN membranes is bent during deposition of the Py on the Cr adhesion layer. The bent structure results in a shift of the magnetic vortex core away from the centre in case the sample is imaged under tilted conditions. It is shown that this bending does not affect the displacement of the vortex core in an applied field, so long as the core is not displaced to the edge of the disk and so long as the applied fields. This information is important for dynamic experiments (Ch. 6), as a field in a similar regime is sufficient to bring the vortex core to resonance when it is applied as an in-plane microwave magnetic field. Hence, bending of the disks is not expected to compromise the investigation of vortex core motion presented in the next chapter. It was also demonstrated displacement of the vortex core by external fields is not compromised by the presence of pinning sites.

Chapter 6.

Dynamic imaging using a fast readout detector in a transmission electron microscope

Transmission electron microscopy offers access to a wide range of material properties, from structure and chemical composition to magnetic properties. In standard electron microscopes, these properties can only be imaged statically or, at best, on a ms timescale. Here, an approach is developed that can be used to improve temporal resolution by using a delay line detector (DLD) while maintaining the imaging properties of a transmission electron microscope. It is demonstrated by investigating the dynamics of a magnetic vortex core excited by a magnetising specimen holder. Similar magnetic vortices were investigated statically in the previous chapter, in order to ensure their suitability for the dynamic experiments. In this chapter, the sample is first described, followed by description of the general setup for time-resolved TEM using a DLD. The main concepts that are required for the data analysis are then highlighted, before investigating the breathing-like behaviour of the vortex core experimentally. This behaviour is unexpected and its origin and consequences are discussed. In the next section, the resonance behaviour of the vortex core is investigated using different methods, including STXM, static TEM and time-resolved TEM employing the DLD. The results are discussed and the advantages and disadvantages of each technique are compared. Finally, the limits of the DLD are assessed and the approach is compared with UTEM.

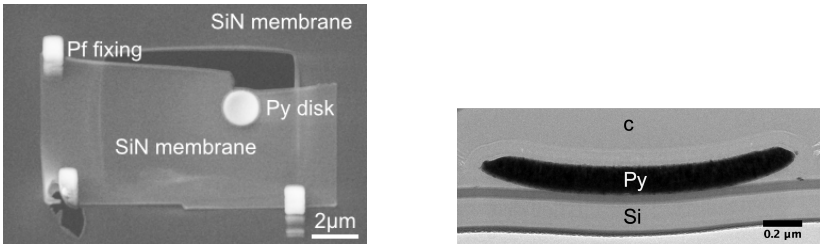

(a) **(b)**

Figure 6.1.: Py disk used for time-resolved microscopy experiments. (a) SE SEM image of the Py disk transferred onto a chip that is compatible with the RF magnetising specimen holder. (b) Cross-sectional BF TEM image revealing bending of the Py disk. C was deposited on the sample to stabilise the Py disk before cutting the cross-section.

6.1. Fabrication and expected features of the sample

Vortex core dynamics in a soft magnetic Py nanostructure were investigated in a single sample. Unless otherwise stated, this specific sample was used in all of the experiments described in this chapter. The sample is a Py disk with a thickness of ~130 nm and a diameter of ~1600 nm deposited on an electron-transparent SiN membrane. The thickness was measured in cross-section. These are similar dimensions to those of the Py disk whose static vortex core properties were studied in Ch. 5. Figure 6.1a shows an SEM image of the Py disk that was used for dynamic experiments after an additional preparation step, which is explained at the end of this section. The Py disk was first prepared in the same way as for samples on standard TEM substrates (see Sec. 5.1). It had similar static magnetic properties to those of the Py disks investigated in Ch. 5. These properties are expected to be affect by bending of the Py disk, which is also seen in a cross-sectional view of the presented sample (see. Fig. 6.1b).[1] The cross-section was prepared by transferring the membrane with the Py disk onto a Si crystal and depositing C protection layers before and after the transfer, before cutting the cross-section. It was shown in the previous chapter that bending does not significantly affect the response of the vortex core to applied in-plane and out-of-plane fields. Therefore, vortex core dynamic experiments were carried out without taking such additional effects into account during analysis.

The expected dynamic behaviour of the vortex core in the presence applied

[1] The cross-section was cut after the vortex core gyration experiments.

magnetic field was first investigated using micromagnetic simulations. All of the micromagnetic simulations in this chapter were performed by B. Zingsem (University of Duisburg-Essen) and are based on the Landau-Lifshifts-Gilbert equation within the MuMax^3 framework [136, 137]. The thickness of the Py disk in the simulation was set to 160 nm in order to compensate for the bending of the Py disk which increases the distance from the edges to the membrane. The residual parameters were set to a disk diameter of 1.675 µm, a saturation magnetisation of $8 \cdot 10^5$ A/m, an exchange stiffness of $1.32 \cdot 10^{-11}$J/m, g-factor of 2.1 $\mu_B/\hbar$, a damping coefficient of 0.016, an applied out-of-plane magnetic field of 20 mT and an applied in-plane oscillating magnetic field of an amplitude of 0.1 mT. First, the vortex core resonance was probed by studying the dependence of the deflection of the magnetic moments on the applied frequency. The resulting curve is shown in Fig. 6.2a. A sharp resonance is revealed around 400 MHz in good agreement with results reported in the literature [86]. In addition, a second resonance is found at 1 GHz. The trajectory of the vortex core at resonance at 400 MHz was simulated as a function of applied microwave magnetic field amplitude. Figure 6.2b shows the trajectory of the vortex core in the central slice of the Py disk, *i.e.* at a height of 80 nm from the bottom of the disk. The averaged trajectory through the thickness of the disk follows the same trend, but it is smeared out because the vortex core position at the top and bottom of the disk is shifted with respect to each other. The diameter of the gyration increases from about 26 nm for an applied field of 0.1 mT to 70 nm for an applied field of 1 mT. The trajectory follows an approximately circular shape for the smaller applied field and a more elliptical shape for the higher applied field.[2] In both cases, a transition time is required to reach stable motion. The transition time for 0.1 mT is 30 ns, while it increases to 60 ns for 1 mT. Both transition periods are too small to be resolved using a stroboscopic measurement of the vortex core motion, *e.g.* by STXM. The small radius of the vortex core gyration, which is in the nm regime, requires the use of measurement techniques that have sufficient spatial resolution. Fresnel defocus imaging provides the required spatial resolution.

The influence on the dynamic properties of the vortex core of the saturation magnetisation of the sample was investigated, as it can change over time due to oxidation or heating during an experiment. Resonance spectra were simulated for an applied static out-of-plane field of 100 mT and an applied power of 10 mT for different saturation magnetisation values. First, the saturation magnetisation was set to the standard value of $M_s = 8 \cdot 10^5$ A/m [138], resulting in the spectrum shown in Fig. 6.3. The resonance frequency was observed 390 MHz. The resonance frequency is slightly reduced, but significantly broadened when

[2] The reason for the elliptical trajectory is not understood yet.

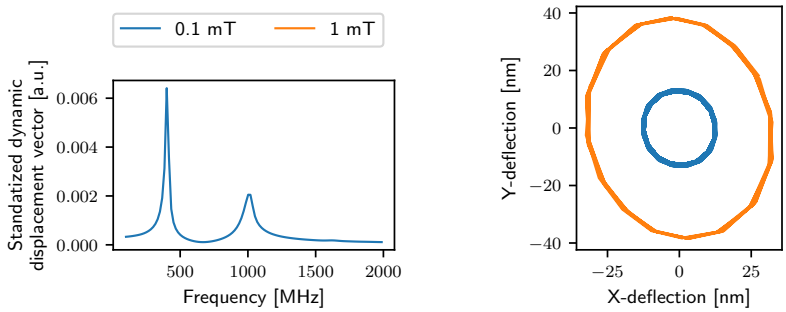

Figure 6.2.: Micromagnetic simulation of vortex core resonance in a 160-nm-thick Py disk of 1600 nm diameter in a 20 mT applied out-of-plane field. (a) The resonance spectrum shows a sharp resonance at 400 MHz and a second resonance at 1 GHz. (b) Deflection of the vortex core in the middle of the Py disk plotted for two different values of the amplitude of the applied microwave field. For an applied field of 0.1 mT, a circluar trajectory with a radius of 10 nm is observed. The radius of the trajectory increases at an applied field of 1 mT and becomes elliptical. Both trajectories are shown after an initial transition period that is required to reach stable trajectories. Figure adapted from [82].

compared to the applied field of 20 mT and applied power of 0.1 mT considered above. Resonance spectra for reduced saturation magnetisation values of 0.99% M_s and 0.95% M_s are also plotted in Fig. 6.3. It can be seen that the saturation magnetisation has a large impact on the resonance, which is shifted to higher frequencies and broadened for 0.99% M_s. If the saturation magnetisation is decreased further, then the resonance frequency is shifted to even higher frequencies, while developing additional features. The strong influence of the saturation magnetisation, as well as the sample conditions and other effects that may change the magnetic properties of the sample, has to be considered in the interpretation of the results.

The magnetisation holder that was used for these experiments (see below) requires a substrate with dimensions of 4x10 mm^2 (*cf.* Sec.6.2.1), in contrast to the standard TEM support that was used in previous experiments. Therefore, the Py disk was transferred onto the required rectangular Si substrate with the underlying SiN membrane using FIB milling: the Py disk with part of the membrane was cut out and placed over a precut hole in the membrane of the rectangular substrate. Care was taken so that the Py disk was not subjected to this Ga beam during the process, in order to prevent the implantation of Ga. The successfully

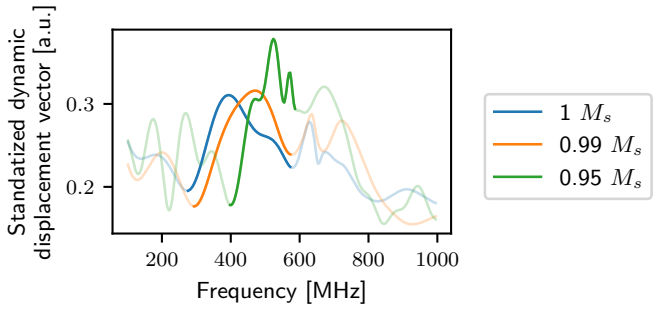

Figure 6.3.: Micromagnetic simulations of resonance spectra of the vortex core for different values of saturation magnetisation for an applied microwave field of 10 mT, an applied out-of-plane field of 100 mT, a saturation magnetisation of $8 \cdot 10^5$ A/m and a Py thickness of 160 nm. With decreasing saturation magnetisation, the resonance frequency increases and broadens.

transferred sample is shown in Fig. 6.1a. The transfer imposes further challenges, in addition to preventing Ga implantation. For example, the Pt that was used to fix the lifted out SiN membrane onto the supporting SiN membrane is only attached at two points. A third connection between the membranes was destroyed by sputtering during fabrication. The membrane itself sags due to the weight of the Py disk. Furthermore, the need to cut blindly to prevent Ga implantation while being close to the Py disk requires very good instrument control to not destroy the sample. Regardless of these challenges, the transfer was successful and the Py disk sample was used for the following dynamic experiments.

6.2. Experimental setup for time-resolved microscopy

In this section, the experimental setup for time-resolved TEM is introduced. The primary focus is on the components that are required to achieve the required temporal resolution: the DLD, the electronics for the excitation and the synchronisation of these two components. The RF magnetising holder is then characterised experimentally and its properties are evaluated based on simulations, in order to improve the understanding of the experimental results.

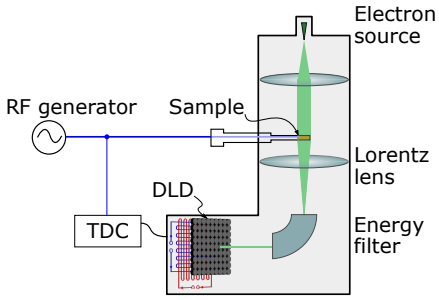

Figure 6.4.: Schematic diagram showing the setup for time-resolved experiments using a DLD in a transmission electron microscope. An RF generator provides a microwave current that is directed to a cartridge at the tip of the holder, in order to generate a microwave magnetic field at the sample position. Images are recorded using a DLD mounted at the end of an energy filter. The TDC of the DLD receives a small part of the microwave current and uses it as a reference signal. Adapted from [82].

6.2.1. Overview of general setup

The setup consists of the three main components: the microscope, the holder and the detector. Their interaction is visualised schematically in Fig. 6.4. An RF generator (HP8657B, HP8671B or R&S SMR 20) generates a microwave current. The power of the current can be increased using an amplifier (SPIN PA233b A), before the current is split into two parts by a resistive divider (custom-built by Simon Däster (ETH Zurich)). The largest part of the current is directed towards the RF magnetising holder. At the tip of the holder, the RF current generates a microwave magnetic field that is used to excite the vortex and to deflect the electron beam. The DLD is employed to image the dynamic excitations and is mounted at the end of an energy filter (Gatan Tridiem 865 ER imaging filter (GIF)). The time-to-digital converter (TDC) of the DLD receives the second part of the microwave current and used it as a start signal, to achieve synchronisation between the excitation of the sample and the detector. The frequency of the microwave current has to be divided, in order to match the requirements of the TDC. This division was achieved by using a frequency splitter that was custom-built by S. Däster (ETH Zurich). The division factor can be set to a value of 2^x, where x is a natural number smaller than 6. A factor of 64 was chosen for the presented experiments. The final images are generated by adding up the electrons that arrive during the same phase of the excitation period.

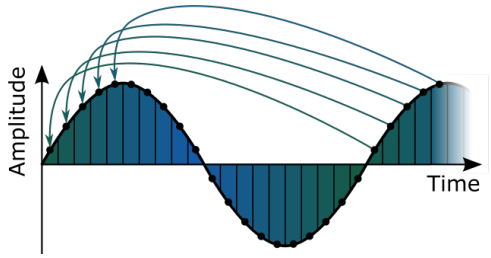

Figure 6.5.: Phase sorting for stroboscopic measurements. Events recorded after the first excitation are mapped onto equivalent phases during the each cycle.

The DLD, in combination with the TDC, records images by measuring the arrival time of each electron and the location where the electron hit the detector. A three-dimensional dataset of (x, y, t) is therefore generated. The time is measured in intervals of $\tau = 6.858711\,\text{ps}$, where τ is set by the TDC. The experiments are carried out stroboscopically to increase the signal to noise ratio. All events that correspond to the same phase of the RF excitation cycle are summed up to generate a single image for each phase interval, as shown schematically in Fig. 6.5. Mathematically, this approach is equivalent to the number of time steps $t_n = t/\tau$ being mapped onto one RF period by $m_{RF} = \frac{1}{f_{RF}\cdot\tau}$, where f_{RF} is the applied RF frequency. Accordingly, the phase intervals correspond to $p_n = t_n mod\, m_{RF}$ in units of $\frac{2\pi}{p_n}$. In this way, the dataset is converted into (x, y, p_n) values. This procedure of mapping time onto phase intervals is only possible if m_{RF} is a natural number. Otherwise, the length of the intervals is not well-defined, resulting in misassignment of the incoming electrons. Therefore, the RF frequencies were constrained to $f_{RF} = \frac{1}{\tau k}$, where k is a natural number and is quantised. Hence, it is not possible to set the RF frequency arbitrarily.

The magnetising holder used in the experiments was built by B. Zingsem (University of Duisburg-Essen) [111]. The principle of electromagnetic field generation is introduced in Sec. 3.4. The holder is based on a brass cartridge, which acts as a coplanar waveguide with a ground. The sample is placed inside the cartridge, as shown in Fig. 6.6. The cartridge and the holder have small holes at the position of the SiN membrane allowing electrons to pass through them. The cartridge is mounted by using a set screw, which pushes the cartridge against the inner wire of the RF cable. The pressure of the screw needs to be adjusted, in order to ensure a good connection between the cartridge and the RF cable, while not breaking the screw or bending the wire. The connection to the ground is made *via* the tip of the holder, which connects the cartridge to the outer wire of the RF cable. In

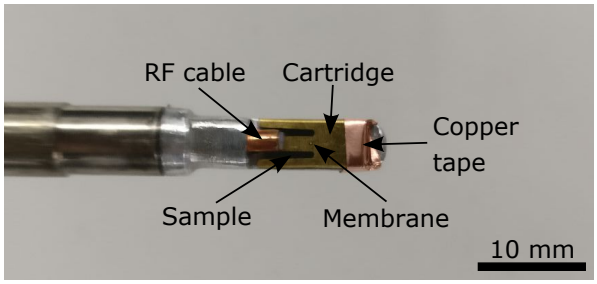

Figure 6.6.: Tip of the RF magnetising holder consisting of a cartridge with the sample inside it. Both components are pressed against the RF cable by a set screw from the bottom and also attached to the tip by using copper tape. The cartridge and the holder have holes at the position of the membrane.

order to further secure the sample on the holder, the cartridge is attached to the holder by using copper tape at the tip.

The DLD, RF generator and the microscope were controlled by a Tango server and dedicated scripts programmed in Python. A graphical user interface (GUI) was developed for convenience to control all three components (*cf.* Fig. 6.7a). For the DLD, a live view is available and the exposure time can be set. The live view is a sum image over all events that take place during the exposure time. A region of interest (ROI) can be chosen, as well as spatial binning in the x and y directions. Options to record and subtract a background image are also available. Background removal is particularly helpful if the signal to noise ratio is low. The excitation frequency is automatically applied to the DLD, as well as to the RF generator. The number of phase intervals depends on the RF frequency and on the duration of an interval given by the DLD ($\tau = 6.858711$ ps). Since the total number of intervals may become large for small frequencies, time binning can be applied in steps of 2^l, where l is a natural number and $l = 0$ corresponds to no binning. The RF generator can be turned on or off and its frequency and power can be set. As before, the set frequency is applied to the RF generator and to the DLD. On the microscope, it is possible to control the stage in the x and y directions and to open and close the column valve. In addition, the pressure in the projection chamber is constantly monitored. A pressure that is too high in the projection chamber risks breaking the MCPs of the DLD. Three squares in the GUI are colour coded to represent the status of the DLD, the RF generator and the microscope. Light green corresponds to the device being connected to the Tango server, yellow to the device not being connected and red to other issues. For the DLD, a dark green signal indicates that an image is being recorded. The advantage of using

a Tango server is that it easily adaptable for different kinds of devices [139]. Therefore, it is possible to extend its functionalities, e.g. for controlling different excitation stimuli using additional devices. Experimental proof of this flexibilty is demonstrated by the simplicity with which the different frequency generators can be exchanged during the experiment. Software development was mainly carried out by S. Däster and Yves Acremann (ETH Zurich), who also provided the required hardware for the server.

The RF measurements were performed using Jupyter notebooks. In this way, the measurements can be automated, they act as a lab book and preliminary data analysis is possible immediately. The standard procedure consists of five steps. First, the closest allowed frequency to the desired frequency and time binning are calculated taking the possibilities for quantisation into account. Then, the chosen frequency is applied to the DLD and the RF generator and an exposure time is chosen. Finally, images are recorded and saved in hdf5 format. Each file is assigned a unique number. The saved file consists of a three-dimensional array, which is made up of a single image for each phase interval. An example of the code used to perform a time-resolved experiment is given in Fig. 6.7b. A background image is generated in the same way. The recorded background can be applied to a live view image in the GUI. However, one has to take care that the number of phase intervals is the same for the live view and the background image. This precaution can be implemented during data analysis in the Jupyter notebooks by subtracting the background for each image for a single phase interval individually. For longer measurements, it is possible to write scripts in the Jupyter notebooks to perform these steps automatically, e.g. a script to record vortex gyration at multiple frequencies. During all of the experiments, the pressure in the projection chamber was monitored so that the column valve could be closed if the pressure rose, in order to protect the MCP from damage. After each successful experiment, the column valve was also closed automatically. Similar automation can be used to record data from multiple sample positions, or by performing multiple measurements with short exposure times to improve the signal to noise ratio further. Hence, a combination of Tango with Jupyter notebooks provides a powerful and flexible tool to control time-resolved experiments.

6.2.2. Experimental characterisation of the magnetising holder

The properties of the RF magnetising holder were first characterised in order to understand its influence on of the time-resolved measurements. First, the reflections of the holder were measured by using a vector network analyser (VNA)

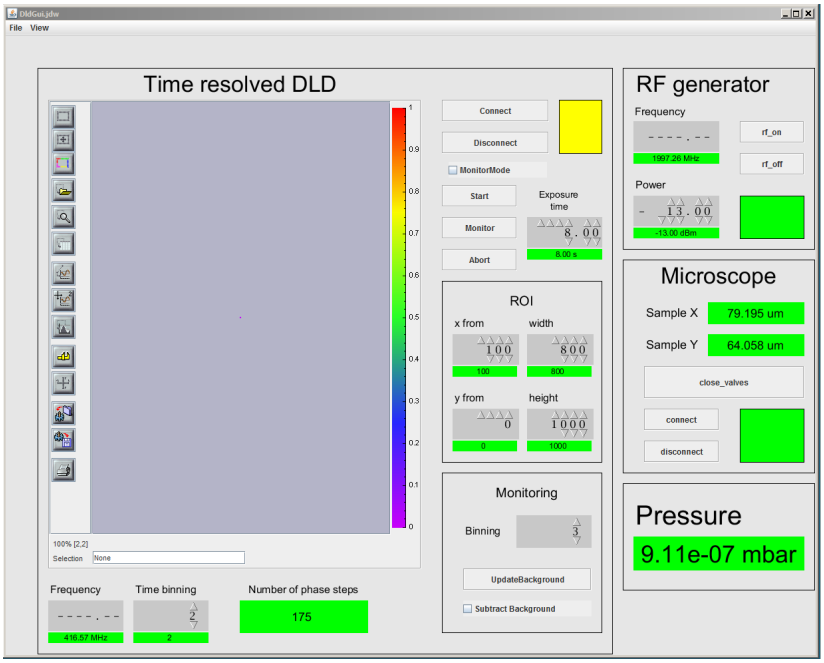

(a)

```
findClosestFrequency(415, binning=2)
```

```
414.2045190282971
```

```
client.setFrequency(414.2045190282971)
```

```
# Image
client.clear()
exposureTime = 120.
client.exposeAndWait(exposureTime)
client.receiveXyt()
# store it: (# 32)
print("hdf5 number: " + str(client.storeHdf5()))
```

```
hdf5 number: 33
```

(b)

Figure 6.7.: User interfaces for time-resolved experiments based on Tango. (a) GUI for time-resolved experiments used to control the DLD, RF generator and microscope at the same time. For each component, different parameters such as applied frequency can be set and a live view of a sum image can be monitored. (b) Example code for recording a time-resolved measurement using a Jupyter notebook. First, all of the input parameters are set. Then, the measurement is performed and the results are saved.

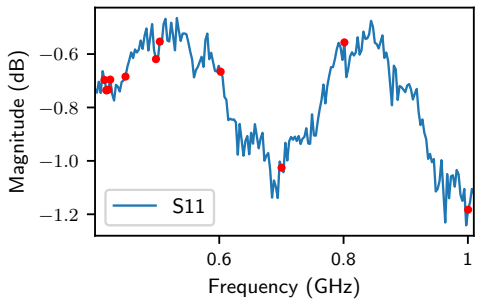

Figure 6.8.: Reflections of RF current applied to the RF magnetising holder measured with a VNA. The blue line corresponds to the S11 parameters, while the red dots indicate frequencies used in later LAD measurements (*cf.*Fig. 6.9).

(R&S ZVL). A VNA is a precise measurement tool, which can be used to generate an RF current and to probe its transmission and reflections. B. Breitkreutz and H. Soltner (FZJ) performed the measurements. The results are given in terms of S-parameters. The S11 parameter corresponds to direct reflections in the device under test [140]. Figure 6.8 shows reflections of the RF magnetising holder up to 1 GHz. It can be seen that nearly the complete power is reflected, with a small modulation by a standing wave. The high amount of reflected power may cause issues for the RF generator used in the experiments, as the RF generator is not designed to handle reflected power, especially considering the 30 dBm amplification used for some experiments. It is possible that the generator will turn off RF generation for a short time whenever the reflected power is high in order to protect itself from damage, or that the generated RF wave will not have the characteristics of a pure sinusoidal wave. Hence, it is beneficial to use a circulator before the holder. A circulator has three ports. It allows the RF current to be conducted from port one to port two, but conducts the current entering at port two to port three. Port three can be terminated with a terminator, or an oscilloscope can be used to measure the reflected wave. In this way, the reflected power cannot reach the RF generator which is protected from damage.

In addition to measuring reflected power, the magnetic field at the sample position was probed by making use of the electron beam - electromagnetic field interaction. Here, a standard charge-coupled device (CCD) camera without temporal resolution is employed to image the electron beam, since a time-integrated measurement is sufficient. Otherwise, the setup was kept as close as possible to that used for the time-resolved experiments. In particular, the electronics, con-

sisting of an RF generator and an amplifier, were used in the same configurations. Furthermore, a substrate without a sample on the membrane was inserted into the cartridge of the holder. The presence of a substrate is important, since it influences the conductance of the RF current and the resulting microwave magnetic field. The measurements were performed using low-angle diffraction (LAD) in magnetic-field-free conditions [141]. The principle of LAD is similar to that of Lorentz microscopy. In the presented experiment, the electron beam is subjected to electromagnetic fields induced by the holder. The magnetic fields result in a deflection of the electron beam, according to the Lorentz force (*cf.* Eq. 3.1). All electrons that experience the same deflection are converged onto the same spot in the back focal plane (*cf.* Fig. 3.1). In diffraction mode, the back focal plane is projected onto the camera by the projection system. Camera lengths in the range of 100 to 3000 m are necessary to compensate for the small deflection angle of the electron beam, which is only at the order of a few tens of microradians and is not easily resolvable using standard diffraction techniques. Moreover, very coherent illumination conditions are necessary to access the small deflection angles. The exposure time for LAD is significantly longer than the period of the RF current and only time-integrated deflection can be recorded with the CCD camera. Thus, a straight line is expected in the images.

Representative LAD images recorded for various applied frequencies and powers are shown in Fig. 6.9a. The applied frequencies and powers correspond to those used in the experiments below (*cf.* Sec. 6.5.3 and Sec. 6.6.1). For a power of 17 dBm, the deflection follows a linear path, as expected. However, for a higher power of 23 dBm there are bright spots at the centre of the deflection (exemplary shown at 414 MHz and 23 dBm in Fig. 6.9a). The presence of these spots may result from the RF generator turning itself off due to large reflections. Such a temporary shutdown would result in a bright spot at the centre, since there is no magnetic field induced in the holder when the generator is turned off. The generated wave may also be modulated by an additional wave, which would result in the presence of bright spots at various positions in the LAD image (exemplary shown at 450 MHz and 23 dBm in Fig. 6.9a). Moreover, higher order modes of the induced microwave field may start to have an effect [140].

The magnitude of the deflection of the electron beam was studied over a wide range of frequencies up to 1 GHz, with a finer sampling around the resonance frequency of the vortex core. The magnitude was used to estimate the strength of the magnetic field at the sample position. For this purpose, it was assumed that the magnetic fields in the cartridge are uniform over the height of the cartridge and that there are no stray fields outside the cartridge. Equation 3.16 then gives the relationship between the deflection and the in-plane field. Both assumptions

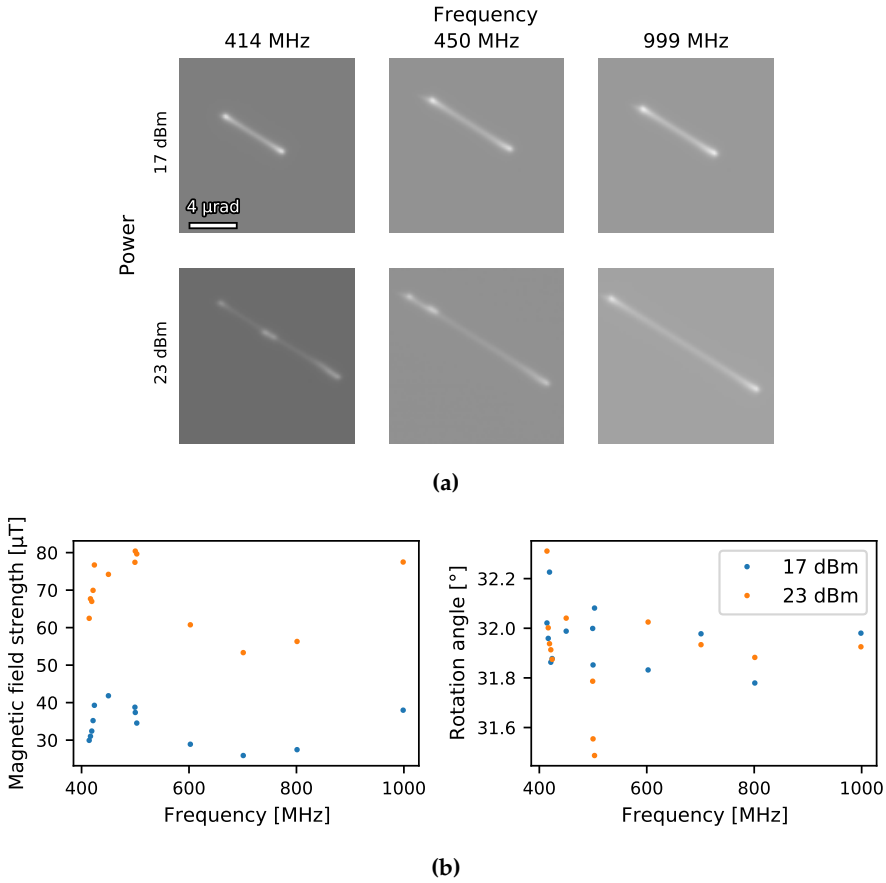

Figure 6.9.: LAD results showing deflections of the electron beam under microwave excitation applied with the RF magnetising holder. (a) LAD images recorded for various frequencies and powers. For an applied power of 17 dBm, the deflection follows a straight line. For 23 dBm, the images show bright spots at different positions. (b) Magnetic field strength (left) and rotation angle (right) plotted as a function of applied power and frequency. The magnetic field strength for 23 dBm is stronger than that for 17 dBm. However, both follow the same frequency-dependent trend. The rotation angle is constant for both powers, with only minor variations for 23 dBm.

may result in an underestimate of the magnetic field strength at the sample position. Firstly, the magnetic fields may not be perfectly uniform, but decrease with distance from the sample (Fig. 3.7d). Secondly, there are likely to be stray fields above and below the cartridge (Fig. 3.7d), which result in a deflection of the electron beam in the opposite direction to those in the cartridge. Despite these limitations, an estimate of the magnetic field is helpful to be able to interpret the experiments on vortex core gyration and to compare them with micromagnetic simulations.

Measurements of the magnetic field strength and rotation angle are shown in Fig. 6.9b, on the assumption that the thickness of the cartridge is $t = 500\,\mu$m and that the wavelength of the electrons is approximately 2 pm for an accelerating voltage of 300 kV. The measured magnetic field strength for 23 dBm is stronger than that for 17 dBm. However, both sets of measurements follow the same frequency dependence. The variation in field strength can be explained by the formation of standing waves in the cartridge. The positions of the nodes and antinodes depend on applied frequency. The strength of the magnetic field at the sample position, in turn, depends on the sample position relative to the nodes and antinodes. Moreover, irregularities in the cartridge may affect the field differently for different applied frequencies. Furthermore, all of these issues with reflected power and non-uniform field are frequency-dependent and power-dependent. The rotation angle is nearly constant in both cases, with minor variations for 23 dBm. Thus, the direction of the microwaves field in the cartridge does not change significantly with frequency. In the small frequency regime of vortex core resonance around 400 MHz, the magnetic field strength and angle are constant with applied frequency and no effects due to variations of the microwave fields are expected. The field strength is 70 μT for an applied power of 23 dBm, which is the value used for the vortex core gyration experiments (see Sec. 6.5). Bearing in mind that this is most likely an underestimate of the field strength, simulations of vortex core gyration at 100 μT are likely to be comparable to the true situation in the experiments (see. Sec. 6.1). Hence, only small gyration radii on the order of a few tens of nm are expected during the TEM experiments (*cf.* Fig. 6.2a).

In a perfect setup, the deflection of the electron beam should depend directly on the power delivered by the RF generator. However, the periodicity of standing wave formation, observed with the VNA, is not in agreement with the trend of the deflection in the LAD measurements (reflection at red dots in Fig. 6.8 does not correspond to magnetic field strength in Fig. 6.9b). This discrepancy can be explained by considering the difference between the two systems that are probed with the VNA and the LAD. In the case of the VNA the complete holder is probed, whereas LAD only measures the local microwave field at the sample

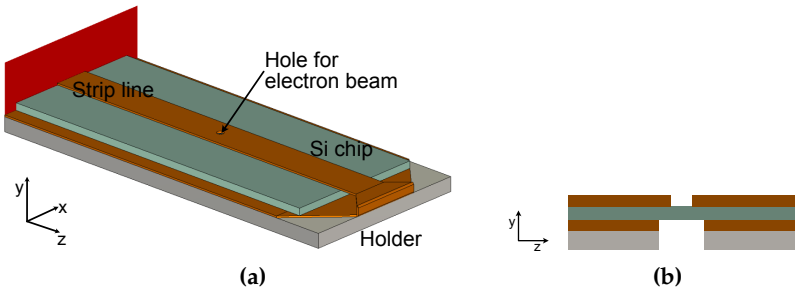

Figure 6.10.: Model of the microstrip line geometry in the RF magnetising holder. The Si substrate is indicated in cyan, the strip line in brown and the holder in grey. The small hole in the strip line indicates the position of the membrane. The red layer corresponds to the transition between the strip line and the coaxial cable. a) Isometric projection. b) Cross-sectional view (not to scale). Model and drawing by B. Breitkreutz (IKP, FZJ) and Y. Murooka (ER-C, FZJ).

position. Losses seen by the VNA may also be induced at the coaxial cable, the connections of the cable or the surrounding metal parts *via* leakage currents. Hence, it is necessary to study the local magnetic fields instead of only relying on characterising the complete holder.

6.2.3. Simulations of electromagnetic fields induced by the RF magnetising holder

The experimental characterisation of the RF magnetising holder was supported by simulations of the electromagnetic fields induced by it performed by B. Breitkreutz (IKP, FZJ) using a finite element approach. These simulations were carried out for an early version of the holder, in which the magnetic fields were not been generated by a grounded coplanar waveguide but using a strip line. A schematic diagram of the strip line and sample are shown in Fig. 6.10. The upper strip line has a width of 1 mm and a thickness of 0.05 mm, while the spacing between the upper strip line and the lower one is 0.2 mm. The amount of power radiated in a strip line is higher and the magnetic field smaller when compared with a CPWG [140, 142]. Nevertheless, the simulations provide valuable insight about the electromagnetic fields that can be expected during experiments.

As input for the finite element simulations, the impedance was determined to be approximately $Z_L = 16\,\Omega$ for the chosen dimensions of the strip line, neglecting

the presence of SiN on the chip.[3] The coaxial cable inside the holder has an impedance of $Z_C = 50\,\Omega$, which results in a reflection coefficient of $r = \frac{Z_L - Z_C}{Z_L + Z_C} \approx -52\%$ and a transmitted power from the coaxial cable to the microstrip line of $|t|^2 = 1 - |r|^2 \approx 73\%$. Therefore, only three quarters of the RF current is transmitted into the microstrip line, even under the best case assumption that there are no further losses. In addition, some of the RF power is reflected back and forth in the strip line, while losing approximately 72% of the power at every reflection at the transition to the coaxial cable. Incomplete reflection of the RF wave at the transition point results in a different electrostatic to magnetic field ratio when compared to the matched case. In order to avoid the unknown details of the transition between the coaxial cable and the holder and to simplify the simulation, it was assumed that the holder is correctly terminated, *e.g* the transition being impedance-matched with an appropriate port. Therefore, these two effects did not have to be taken into account.

In a second step, simulations were performed and the electrostatic and magnetic field distributions in cross-section at the sample position were investigated for an applied frequency of 10 GHz, as shown in Fig. 6.11. The magnetic field is approximately in-plane at the sample position, while the electrostatic field is approximately parallel to the electron beam direction. Thus, the magnetic field deflects the electron beam, while the electrostatic field only changes the energy of the electrons locally. Close examination of the power radiated by the strip line shows that only about 4% of the power is lost up to 20 GHz. Around 500 MHz, where the vortex resonance frequency is expected, only about 1% of the power is radiated. This small loss should have little effect on the propagation of the electromagnetic wave, especially considering that the CPWG design is expected to have even lower radiation losses [140, 142]. Hence, the induced magnetic field should be almost fully in-plane at the sample position.

In a third step, the field strengths of the electrostatic and magnetic field at the sample position were studied as a function of applied frequency for an applied power of 27 dBm. The expected formation of standing waves can be seen in the frequency spectra shown in Fig. 6.12. The magnetic field of the holder vanishes when an antinode is located at the sample position, for example at an applied frequency of 4.5 GHz. For frequencies below 500 MHz, the magnetic field is nearly at its maximum of 0.2 mT. While this maximum value is rather small, it is still sufficient to induce vortex core motion in a Landau state similar to the studied vortex [45]. For the electrostatic fields, the formation of a standing wave

[3] Chemandy Electronics Ltd. (2021, March 11). Microstrip Transmission Line Characteristic Impedance Calculator. Retrieved from `chemandy.com/calculators/microstrip-transmission-line-calculator-hartley27.htm`

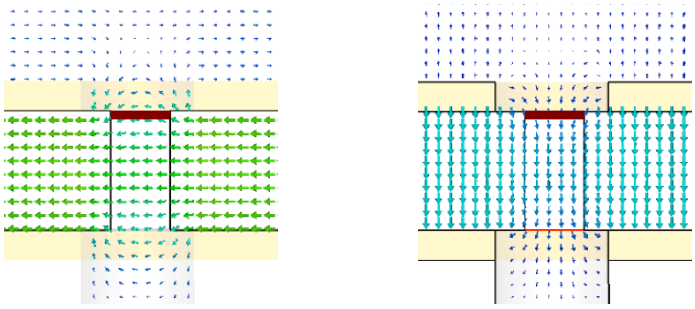

Figure 6.11.: Simulated (a) magnetic and (b) electrostatic field distributions in a microstrip line showing cross-sections of the microstrip line for an applied field of 10 GHz and a power of 27 dBm. It shows the same cross-section as Fig. 6.10b. The yellow areas correspond to the microstrip line, while the area indicated by the black lines correspond to the Si substrate. The sample is indicated by the red square. The magnetic field is approximately parallel to the sample while the electrostatic field is approximately parallel to the electron beam direction.

can also be seen in the simulations (see Fig. 6.12). The electric field is shifted in the frequency domain compared to the magnetic field. For frequencies below 500 MHz, the electrostatic field is below ~3 kV/m and should not influence the experiments because of its small magnitude and direction. In the experiments, the electric field is expected to be even smaller due to the non-perfect properties of the experimental setup resulting in even smaller fields.

Finally, the influence of the position of the sample in the microstrip line was investigated using the simulations. In practice, there may be a small gap between the lower part of the microstrip line and the sample, as the sample is clamped in the holder using a set screw. Above the sample, there is a gap of a few hundred micrometers, as there the microstrip line is bent away from the membrane there. This bending is necessary to prevent the microstrip line from touching and breaking the membrane. The position of the substrate in the microstrip line has two effects on the magnetic field strength. On the one hand, the sample may be at a position where the magnetic field has already decayed. On the other hand, the Si substrate has an effect on the propagation of the microwave current and fields. In the simulation, nine different gap sizes were considered. The smallest gap corresponds to the perfect case of no gap at all. In all other cases, the gaps above and below the sample were set to either 0.05 mm or 0.1 mm. The electrostatic field increased slightly with gap size for frequencies below 500 MHz. Over the same

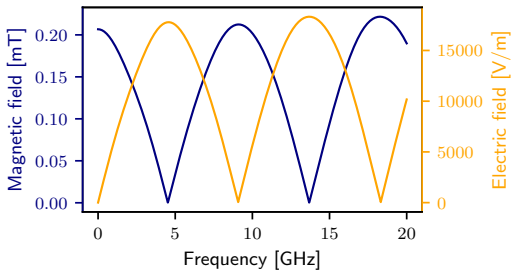

Figure 6.12.: Amplitude of the x component of the magnetic and and y component of the electrostatic field at the specimen position determined from simulations and plotted as a function of applied frequency (for directions compare with Fig. 6.10 and Fig. 6.11). Both fields form standing waves. For applied frequencies below 500 MHz, the magnetic field is close to its maximum amplitude of 0.2 mT and the electrostatic field is close to 0 $\frac{\mathrm{V}}{\mathrm{m}}$.

frequency range, the magnetic field decreased with increasing gap size down to 95 $\frac{\mathrm{A}}{\mathrm{m}}$. The lower gap was found to have a larger effect than that the upper gap. Therefore, the substrate should be mounted as close as possible to the bottom of the strip line to maximise the magnetic field. Furthermore, it should be noted that impedance mismatch will reduce the magnetic field strength. The experimental measurement of the magnetic field resulted in field values of only 55 $\frac{\mathrm{A}}{\mathrm{m}}$ for the CPWG design (*cf.* Sec. 6.2.2) which is smaller than the worst case simulation. This discrepancy shows that the simulation does not account for all experimental irregularities and mismatches. Nevertheless, the magnetic field strength is sufficient to induce vortex core motion in the Py disks in the experiments.

6.3. Basics of data analysis: Principal component analysis

Vortex core gyration was studied both with a direct electron detector and with a CCD using a conventional TEM setup with exposure times in the ms regime. In the latter case, only a time average of the motion could be imaged due to the long exposure time compared to the frequency of vortex core gyration. At the same time, the use of exposure times of only up to 0.1 s resulted in poor signal to noise ratio. The exposure time was chosen so short to capture a time-resolved image series (*cf.* Sec. 6.4.1). In order to reduce noise and to classify

up to several hundreds of images, principal component analysis (PCA) was applied to the data. PCA is a mathematical tool, which can be used to structure, simplify and illustrate large data sets by making use of statistical variables with as little as possible linear combinations of previous. These linear combinations are called principal components. Hence, the PCA reduces the dimensionality of the dataset. The principal components are ordered from highest variance to lowest variance. The variance is the squared deviation from the mean. A visualisation of the use of PCA is shown in Fig. 6.13a and Fig. 6.13b. In a simplified picture, PCA looks for the main axis on which it can map all data points with the smallest possible loss in information. In a three-dimensional case, this approach corresponds to a search for the main images that can be added up to create all other images. Here, PCA was performed by applying the machine learning module of the HyperSpy framework [118]. This frame work is capable of accounting for Possion noise, which is present in experimental images. For PCA, the framework uses the following notation: the initial dataset X is decomposed into two new datasets. The first new dataset comprises the factors A, which are the main images that all other images can be constructed from. The second dataset, which is referred to as the loading B, give the weights by which the main images need to be multiplied to reconstruct the initial images. Reconstruction takes place by matrix multiplication in the form $X = AB^T$. The components are sorted by their importance for the reconstruction. The number of components that is included in the reconstruction depends on how well the main components can be separated, as well on the noise reduction be achieved. A scree plot can be used to provide an overview of the influence of the components (Fig. 6.13c). In such a plot, the components often decay rapidly. This elbow-like shape allows the components above the linear regime to be chosen. The fewer components are considered, the smaller is the noise level. However, the use of fewer components also results in information loss. Therefore, noise reduction and information loss have to be carefully balanced against each other.

For the images analysed below, it is known that only values larger than zero are allowed, as the camera cannot record negative values of intensity. Therefore, the technique of a non-negative matrix factorisation (NMF) is a promising approach. NMF requires all elements to have non-negative values. The number of components is known in the case of gyration experiments due to physical constrains (see Sec 6.4.2). Therefore, it can be included as additional prior knowledge. Here, NMF was performed using the HyperSpy framework [118]. Both PCA and NMF are simple to apply to reduce noise and determine the main components of the gyration and their influence on each recorded image. However, they should be applied with care to avoid generating artefacts in the results.

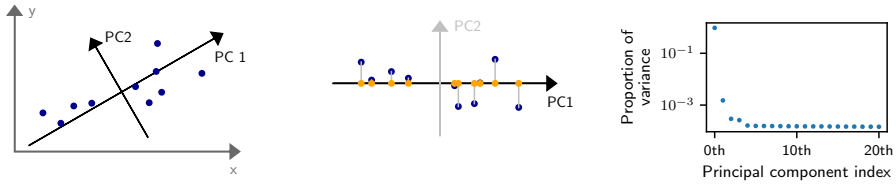

(a) (b) (c)

Figure 6.13.: Illustration of the basis of principal component analysis. (a) Data points (blue) in the original x and y coordinate system (grey). The principal components (black) are determined as new axes with as large as possible variation. (b) The data are shown with respect to the principal components. The dimensionality of the data set is reduced by projection of the data points onto the component with the highest variation (see text for details). The new data set (orange) has a reduced dimensionality. c) Example of a scree plot showing rapid decay before a linear regime.

6.4. Breathing-like behaviour of the vortex core during its gyration

In preparation for the time-resolved experiments, the parameters that are required to excite stable vortex core gyration were probed using a standard CCD camera. One of the key parameters is the magnitude of the in-plane magnetic field that is needed to excite vortex core motion and thus the applied power. In this section, it is shown, that in the case of low power, no gyration can be resolved, while at high power breathing-like behaviour of the vortex core gyration is observed. In the latter case, the state of the vortex core changes between being in motion and being stationary. In this section, the experimental setup is introduced and the steps required for of the data analysis are described. The characteristics of the observed breathing-like behaviour are presented and its consequences for the detection of vortex core resonance are discussed.

6.4.1. Experimental details

Two different experimental setups were used to determine the power required to bring the vortex core to gyration. Both approaches are based on the setup for time-resolved measurements introduced in Sec. 6.2.1. The first experiment was carried out using an image-aberration-corrected electron microscope (FEI Titan T [143])

operated at 300 kV in close-to-magnetic-field-free conditions. The chip with the Py disk was placed in the cartridge of the RF magnetising specimen holder. An RF current was applied using the same generator and amplifier as used later in the time-resolved experiments. The frequency was set to 420 MHz, which is close to the expected resonance frequency, with three different total powers of 22, 21.5 and 21 dBm. The major difference from the time-resolved experiments was that a normal CCD camera before the GIF was employed instead of a DLD. Thus, the temporal resolution was limited to a few ms, many cycles of the vortex core motion were compressed into a single image and only a time integration of the motion could be seen. For vortex core motion, time integration should result in a smeared ring rather than spots on a circular trajectory. The size of the FOV had to be balanced between two competing considerations. On the one hand, it had to be small enough to provide good spatial resolution of the vortex core. On the other hand, it had to be large to ensure that the vortex core did not drift outside the FOV, even for hundreds of consecutive images. In practice, a size of approximately 20 times the vortex core provided the best compromise. Movement of the vortex core was affected by thermal drift, as the sample and cartridge are heated up due to the RF current going through the cartridge. The objective lens of the microscope was used to apply a static out-of-plane field of -7 mT to the sample. This value of out-of-plane field was chosen to maximise the vortex core gyration radius by measuring the amplitude of the gyration during the experiment.

The second experiment was carried out using a slightly different setup in an image-aberration-corrected electron microscope (HOLO [144]) operated at 300 kV in close-to-magnetic-field-free conditions. The RF magnetising holder was again used. However, the sample was not placed inside the cartridge but inside the strip line described in Sec. 6.2.3. Therefore, the magnetic field generated at the sample position may be smaller than in the first experiment. Nevertheless, the field strength is not likely to be much smaller, as it is found to be sufficient to excite the vortex core resonance. The holder was tilted to 21° to align the sample parallel to the image plane as the sample was not mounted flat inside the magnetising specimen holder. Compared to the first experiment, a different frequency generator was used without an amplifier. The use of different excitation electronics makes it possible to exclude electronic-based effects from the results. The second experiment was carried out using a K2 detector with millisecond temporal resolution. The parameters were set up to apply an RF current at a frequency of 415 MHz and a power of 20 dBm in an out-of-plane field of 100 mT. Table 6.1 gives a concise overview of the differences between the two setups.

Both experiments were performed in the same way to ensure their comparability,

Table 6.1.: Experimental setups for the investigation of breathing-like behaviour of the vortex core. The same Py disk (*cf.* Sec. 6.1) was investigated using both setups.

	Setup 1	Setup 2
Microscope	Titan T	Titan HOLO
Camera	CCD	K2 detector
Holder tip	cartridge	strip line
RF generator	HP 8657B with a SPIN PA233B A amplifier	R&S SMR20
Applied frequency	420 MHz	415 MHz
Total applied power	22, 21.5 and 21 dBm	20 dBm
Static out-of-plane field	-7 mT	100 mT
Exposure time	0.05 s	0.1 s
Magnification	25.5k	49k
Defocus	710 µm	1.15 mm

despite the different setups. First, the sample was placed in the cartridge or strip line and loaded into the microscope using the RF magnetising holder. Then, an RF current was applied to the holder, resulting in motion of the vortex core due to the microwave magnetic fields. The microscopes were operated in Lorentz mode to visualise the position of the vortex core in Fresnel images (*cf.* 3.3). The sign of the defocus was chosen so that the vortex core appeared as a bright spot. In order to capture the breathing-like effect with the best possible temporal resolution, the exposure time was chosen to be as small as possible, while retaining sufficient contrast using a standard camera. It was not possible to adjust the contrast in such a way that that the vortex core appeared dark because it would not be visible in the noise resulting from use of a short exposure time. The microwave current was turned on before setting up each new measurement to minimise the thermal drift. Series of several hundreds of images were then recorded with as little time between individual exposures as possible, *i.e.* 0.3 s in practice, by using a script written by V. Migunov (ERC, FZJ). The recordings were started after the respective parameters were adjusted.

6.4.2. Data analysis

In order to interpret the results, several hundred images had to be processed and classified. The breathing-like behaviour manifested itself in the form of two different observations: an open state with the vortex core gyrating and a closed

state with a static vortex core. The open state took the form of a ring, with several cycles of the vortex core gyration captured in a single image. The closed state consisted one bright spot, since the vortex core was stationary. Due to the large number of images, these two states could not be differentiated manually. Therefore, a NMF algorithm was applied to the data sets (c.f Sec. 6.3). The NMF algorithm is very sensitive to image shifts between different images, which it cannot account for. Therefore, the vortex core needed to be centred carefully in every single image. The centering was performed based on detecting the centre of mass of the intensity after applying a slight Gaussian filter of 1 pixel. Only pixels with an intensity larger than 0.8 times the maximum intensity were considered when determining the centre of mass. This pre-selection was necessary because determination of the centre of mass has a bias towards the centre of the image, in particular since the signal to noise ratio is small. Therefore, small noise contributions at the edges would have a large effect on the detected position of the vortex core. As the region of the vortex core is small compared to the complete FOV, the images were cropped to the region of the vortex core in order to reduce computational time.

In the first experiment, the images were already binned to 512 x 512 pixel^2 in order to avoid running out of computer memory when taking several hundreds of images. As a first step, all dead pixels were removed, as they affect the determination of the position of the vortex core [120]. The images were then cropped so that the edge of the Py disk was no longer visible, as bright spots due to Fresnel fringes at the edge of the disk are often brighter than the vortex core and could result in its misdetection. In the next step, the vortex core was located by detecting the centre of mass twice. During the first stage, a 128x 128 pixel^2 region around the core was cut out. The core was located within this region a second time and a smaller region of size 64 x 64 pixel ^{2} was cut out. The resulting images had the centre of the vortex core aligned to the centre of the image. If the core was too close to one edge during the first location of the centre, the cropped region was expanded in the opposite direction. Therefore, the core may not be centred anymore. However, any misdetection in the first step was corrected by the second step. The sequence of step is shown in Fig. 6.14. Figure 6.15a shows representative images after centering the core for the open state and the closed state. The two states can be clearly distinguished.

Data treatment prior to NMF for the second experiment was carried out in a similar way. First, the core was located in the 3708 x 3836 pixel^2 images, using a Gaussian filter of $\sigma = 5$ pixels for detection[4] The original images were then

[4]The Gaussian filter was not applied to the image permanently.

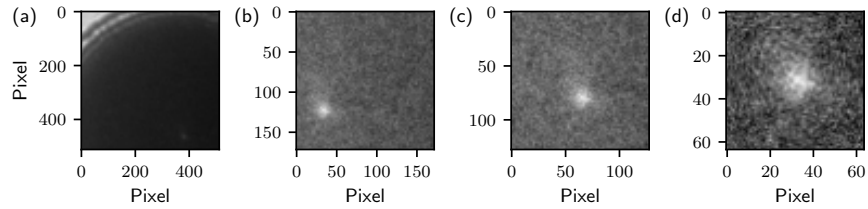

Figure 6.14.: Steps used to centre and crop images around the vortex core to ensure that there is no image shift between them. a) Remove all outliers that might be misinterpreted as the vortex core. b) Remove the edge of the Py disk from the image manually. c) Locate the vortex core and crop the image. d) Locate the vortex core in the cropped image again to increase the accuracy of the centering and crop around the core again. The images shown here correspond to the data set for 22 dBm excitation.

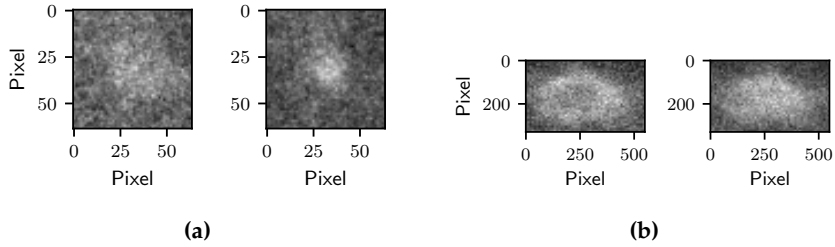

Figure 6.15.: Snapshots taken from image series revealing breathing-like behaviour during vortex core gyration. (a) First experiment for an applied power of 22 dBm. (b) Second experiment. In each case, the left image shows an open state and the right image shows a closed state.

cropped to 1024 x 512 pixel^2 around the core. The core was located for a second time to achieve better accuracy. For this step, the data was again filtered with a Gaussian filter of $\sigma = 5$ pixels. The original (not filtered) image was then cropped to 550 x 330 pixel^2 around the core. Finally, outliers in the cropped image were removed and a Gaussian filter of $\sigma = 2$ pixels was applied to the data. Changes with respect to the first data analysis were required due to the large number of pixels offered by the K2 detector. The larger number of pixels also restricted the data processing that could be performed in a reasonable time, *i.e.* a couple of minutes, for each image series. Examples of the resulting images for open and closed states are shown in Fig. 6.15b. Both states can be clearly distinguished, as for the first experiment.

The NMF algorithm was applied to the data from both experiments, with the input knowledge that two different states are expected. The NMF computed the two images that should be added together to create each image and the weight of how much of each image is required (see Appendix B.2 for a comparison of the input and reconstructed data). The two images are the factors and their weight the loadings. The loading values for each image were used to decide whether it corresponds to an open or closed state. This discrimination was performed by normalising the loadings to a range of 0 and 1. An image was defined to be in the open state if the loading for the open state was above 0.5 and the loading for the closed state below 0.5. Correspondingly, closed images were defined by a normalised loading for the open state of below 0.5 and for the closed state of above 0.5. Some images could not be categorized in either of the two states. These in-between states are likely to have resulted from the long exposure times, as the vortex core can switch between open and closed states within an acquisition, resulting in an image of the mixture of both states.

6.4.3. Characteristics and consequences of the breathing-like behaviour

Results of the NMF analysis and thus the temporal evolution of the vortex core motion are shown in Fig 6.16 for the first setup and in Fig. 6.17 for the second setup. The pixel-to-nm conversion for the first setup was defined by measuring the radius of the Py in the defocused images. Unfortunately, it was not possible to define the conversion factor for the second experiment, as there were no features that could be used to define the scale. The decomposition factors, *i.e.* the images of the different states, indicate the appearance of the open state in both experiments above a threshold for the applied power that depends on the

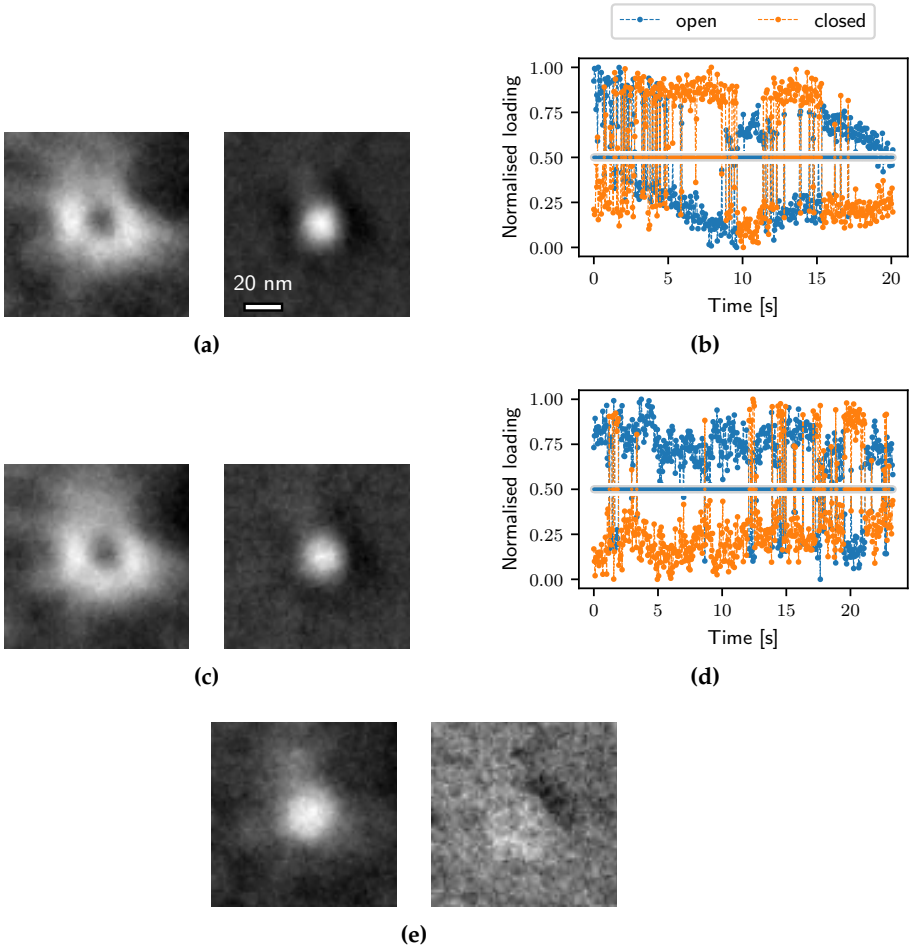

Figure 6.16.: Factors and loadings of NMF decomposition for the first experiment performed at 420 MHz and (a, b) 22 dBm; (c, d) 21.5 dBm; (e) 21 dBm. (a), (c) and (e) show the factors and (b) and (d) the normalised loadings. The inset in the centre of the loadings indicates if the respective images are classified as being in an open or closed state. For 22 and 21.5 dBm, the factors show a clear differentiation between open and closed states. At 21.5 dBm, the system stays longer in the open state than in the closed state. At 21 dBm, NMF is not able to detect a difference between the open and closed states as the vortex core is not gyrating. Instead, the second factor corresponds to misalignment between images in the series.

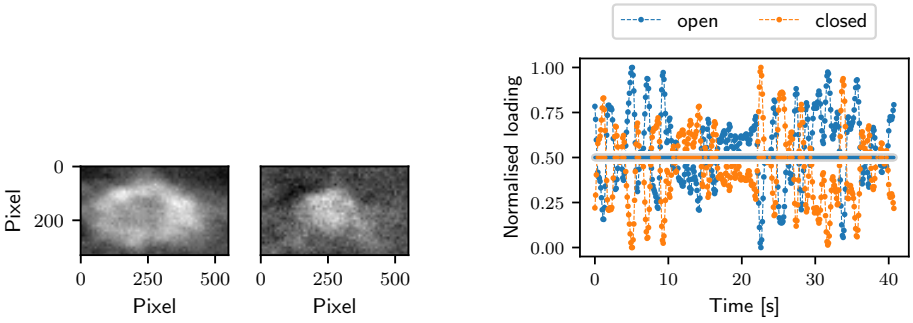

Figure 6.17.: (a) Factors and (b) loadings of NMF decomposition for the second experiment at 415 MHz and 20 dBm. The factors show a clear difference between open and closed states. The inset in the loadings whether each image in the series is classified as being in an open or closed state. The normalised loadings indicate that the system is fluctuating between open and closed states.

setup. It was found that the open state is not stable over time and a breathing-like behaviour is observed. Since the experiments are independent with exception of the specimen holder, it is unlikely that the breathing-like behaviour is an effect of the setup and is, instead, intrinsic to the sample. In the first experiment, the vortex core was observed to be in the closed state for applied powers below 21.5 dBm. At 21 dBm (Fig. 6.16e), the first decomposition factor corresponds to the closed state and the second decomposition factor shows bright and dark contrast around the core. This contrast is likely to be an artefact of the images not being aligned perfectly. Allowing for more than two factors on the NMF reveals artefacts in different directions. These artefacts underline the importance of image shift correction prior to NMF. On decreasing the applied power in the second experiment (Fig. 6.17), the breathing stopped and the vortex remained in the closed state. The disappearance of the open state shows that a certain power level is required to bring the vortex core into gyration. This behaviour is expected since the radius of the trajectory of the vortex core motion depends on the applied in-plane magnetic field. If the applied field is too low, the radius will be small and cannot be resolved in the images. Therefore, it appears as if the vortex core is not moving at all. In addition, the movement may be suppressed by pinning of the vortex core. The elliptical shape of the vortex core trajectory will be discussed in Sec. 6.5.3.

The first two measurements of the first experiment indicate different evolutions

of the breathing-like behaviour over time, as shown in Fig. 6.16. For an applied power of 22 dBm, the vortex core initially switches between open and closed states followed by two periods of no gyration (Fig. 6.16a and Fig. 6.16b). The core then forms an open state, achieving a stable trajectory. However, a clear trend towards a closed state can be observed, in agreement with the breathing-like behaviour seeming to disappear when the measurements run over a longer time. Overall, the sum of the normalised loadings is decreasing over time indicating an increase of the in-between state, *i.e.* the open and closed state cannot be differentiated due to the long exposure time. For an applied power of 21.5 dBm (Fig. 6.16c and Fig. 6.16d), the vortex core stays in an open state for a longer time than for a 22 dBm applied power. The fine details of the open state are very similar for both applied powers. This similarity indicates either the presence of pinning sites or the deflection of the electron beam by the microwave fields being similar in both cases.

There are several reasons why the vortex core gyration may stop when applying too large a power. For example, it is possible that gyration of the vortex core results in local heating of the sample. As a result of heating, the magnetic properties may be altered and the conditions required for vortex core gyration may change. The Curie temperature of Py is approximately 550°C for nanostructure elements have a thickness of above 30 nm [145]. However, such a dramatic increase in temperature is not required to change the magnetic properties. Schulz *et al.* showed that annealing a 36-nm-thick Py thin film in ultra high vacuum conditions above 300°C for 60 min results in structural changes that are visible in cross-section and a reduction in saturation magnetisation by 28% [146]. No structural changes are visible in the cross-section of the sample after the presented experiments (Fig. 6.1b). Therefore, it is unlikely that the sample heated up above 300°C even considering the differences in sample and heating. Schulz *et al.* also showed that annealing at only 100°C changes the saturation magnetisation by 3% [146]. Micromagnetic simulations showed that such small changes in saturation magnetisation can have a major impact on the resonance frequency (see Sec. 6.1). This change may be so dramatic that the gyration stops. Once the system cools down, with the SiN membrane and Si frame acting as heat sinks, the conditions for vortex core gyration may be fulfilled again and the core movement excited. Local heating may explain why the vortex core gyration decreases over time, since not all of the heat may be transported from the sample, which may heat up gradually. However, the change in saturation magnetisation has to be reversible in order to allow the system to come back into gyration.

Another potential reason for the change in vortex core motion with time is switching of the polarisation of the vortex core (*cf.* Sec. 2.4.2). The sense of rotation is

solely dependent on the polarisation of the vortex core. Hence, a switch of the polarisation would result in a short break in the motion, before the core resumes to move in the opposite direction. The switching time required to flip a vortex core is on the order of ps [89]. If the switching takes place constantly over a longer time, then it would appear as though the vortex core were not moving and remained in a closed state. This switching would not be visible experimentally as Fresnel defocus imaging only offers access to the projected in-plane magnetisation (*cf.* Sec. 3.3). Reports in the literature [147] have shown that the vortex core switching can take place multiple times in a 50-nm-thick Py disk of 16 µm diameter during the application of a ns field pulse, resulting in an overlapping of clockwise and counterclockwise vortex core motion in stroboscopic experiments. With regard to the switching fields that are required, Van Waeyenberge *et al.* [45] showed experimentally for a Landau state that short field in-plane pulses on the order of 1.5 mT in magnitude and 4 ns in duration are sufficient to switch the polarisation of a square Py element with dimensions of 1500 x 1500 x 50 nm^3, which can be brought into gyration by using a microwave magnetic field of frequency 250 MHz and amplitude 0.1 mT. These findings show that even small disturbances of the microwave excitation may be sufficient to induce spikes in the magnetic field which might switch the core. These spikes may result from malfunctioning of the excitation equipment, since the holder reflects most of the applied current back into the RF generator (*cf.* Sec. 6.2.1).

Even though the origin of the breathing-like behaviour is not yet understood, an important conclusion from the present experiments is that the power of the driving RF current has to be tuned carefully. The measurements with a DLD are carried out stroboscopically, with about 10^{11} excitation cycles per measurement. The power has to be low enough that the breathing-like behaviour does not corrupt the measurements. At the same time, a sufficiently large applied power is required to bring the vortex core into gyration. These conflicting requirements only leave a narrow window for the time-resolved measurements.

6.5. Resonance frequency of magnetic vortex cores

After the preliminary investigations of the parameters that are required to induce stable vortex gyration, resonance spectra of the Py disk were measured using three different techniques: STXM, conventional Fresnel defocus imaging and time-resolved Fresnel defocus imaging with a DLD. The results are presented separately, before comparing the advantages and disadvantages of the techniques.

6.5.1. Vortex motion studied by scanning tunnelling X-ray microscopy

In a first experiment, the resonance frequency of a Py disk was studied using the STXM method (see Sec. 2.5). A twin sample of the Py disk investigated by TEM (*cf.* Sec. 6.1) was examined with a nominal thickness of ~100 nm and diameter of ~1500 nm. It was prepared by the same technique on a 20-nm-thick SiN membrane by S. Finizio (PSI) (see Sec. 4.2). For this experiment, a Au strip line was deposited on the Py disk and used to induce microwave magnetic fields by driving an RF current through it. This setup produces an in-plane microwave magnetic field at the sample position (see Fig. 6.18). The strip line was electrically contacted by gluing it onto a PCB board using silver paste. As the magnetic vortex contains mainly in-plane magnetic fields, the sample was mounted at an angle of 30° to image the vortex core gyration [45, 126]. The sample is scanned by X-rays with a spot size of 25 nm, which defines the achievable spatial resolution. The energy of the X-rays beam was chosen to be 710 eV, which corresponds to the L_3 edge of Fe, in order to have access to the magnetic properties of the sample. The vortex core was imaged using a FOV of 20 x 20 pixel^2 for 5 different frequencies around the expected resonance frequency of 400 MHz. 17 images of the vortex core gyration were recorded for each cycle. This choice sets the accessible frequencies together with the repetition rate $r_{rep} = 500$ MHz of the X-ray illumination *via* $f = \frac{k}{17} \cdot r_{rep}$, where k is a natural number, just as for the quantisation of selectable frequencies using the DLD (see Sec. 6.2.1). Therefore, vortex core gyration was imaged at frequencies of approximately 353, 382, 412, 441 and 471 MHz. The measurement time for each frequency was in the range of 10 to 20 minutes. In order to reduce the total measurement time, the time-resolved parts of the experiment were performed with either left or right polarised light after taking static XMCD images to ensure that the sample is in the expected magnetic state.

Since the measurements were only performed with one sense of polarisation of the X-rays, the magnetic contrast was not visible directly in the time series, as the images were dominated by the thickness contrast of the sample. Thus, it was not possible to track the vortex core motion directly. Instead, magnetic contrast was obtained by generating a sum image, normalising it by the number of images and subtracting this sum image from each image in the series (see Appendix B.3 for example images). This procedure resulted in dark and light contrast, which highlighted changes between the images. These changes originate solely from the motion of the vortex core. Figure 6.19a shows examples of difference images for various stages of the excitation cycle, where dark and light contrast indicates

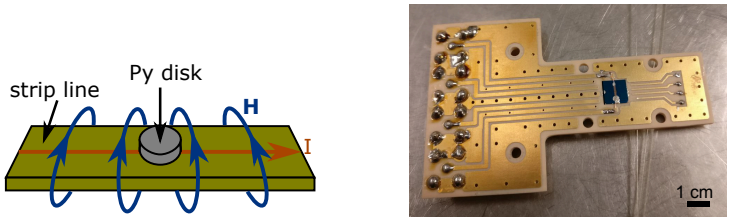

Figure 6.18.: Sample geometry used for STXM measurements. (a) Schematic diagram of the Py disk on a strip line, which generates an in-plane magnetic field **H** at the sample position when a current I is passed through. (b) Image of a sample on the chip stuck to a PCB board with silver paste. The strip line is also connected to the board with silver paste.

clockwise vortex core motion which becomes apparent in a video of the image series. A breathing-like characteristic of the vortex core motion was not observed in any measurement. Otherwise, the stroboscopic measurements would not have been possible.

The resonance frequency was determined from the magnitude of the changes in contrast in the difference images at the position of the vortex core. The position of the vortex core was first determined by finding the pixel with the highest variance over time. A 3-pixel-round mask was fitted around this position (see red circle in Fig. 6.19a). This mask had to be located in such a way that it is only subject to the bright or the dark contrast in a single image of the series. The intensity inside the mask was then determined and plotted as a function of image number. Since the vortex core motion is driven by a sinusiodal stimulus, the intensity is also expected to follow a sinusoidal function as a function of time. The period is fixed by the number of images taken per excitation cycle. Therefore, the function $b = a \cdot \sin(\frac{2\pi}{17} \cdot f + d) + e$ was fitted to the data, where b is the intensity and d and e are needed to compensate for the unknown phase shift and the intensity offset (see Appendix B.3 for further details). The amplitude a was determined for each of the applied frequencies. The normalised amplitudes are shown in blue in Fig. 6.19b. An additional measurement was performed at 353 MHz (not shown). However, it was affected by cross talk between the avalanche photodiodedetector and the microwave magnetic field of the strip line [95]. The highest amplitude corresponds to the resonance frequency. The strongest amplitude is found around 400 MHz. This frequency is in good agreement with the results obtained using micromagnetic simulations (*cf.* Sec. 6.1).

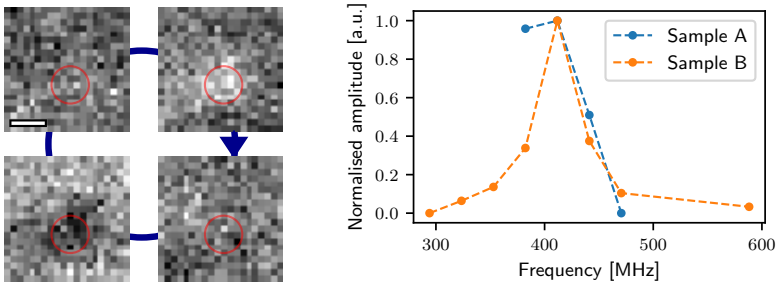

(a) **(b)**

Figure 6.19.: Time-resolved STXM experiments of vortex core motion. (a) Difference images recorded at different phases of an excitation cycle at 412 MHz. The dark and white contrast corresponds to clockwise gyration of the vortex core. The red circle indicates the region used for the sinusoidal fit. The scale bar corresponds to 100 nm. (b) Normalised amplitude of the contrast changes at the position of the vortex core for a twin of the TEM sample (sample A) and a nominally 160-nm-thick sample (sample B). Both samples have a resonance frequency by approximately 400 MHz.

In addition to cross talk, heat is a major challenge when carrying out time-resolved STXM measurements. As a result of the need to scan the sample point by point while recording a full excitation cycle stroboscopically, the measurement time for a single image series at a fixed frequency is on the order of 10 minutes, which introduces a lot of heat into the system from the RF current in the strip line.[5] At the same time, the thin SiN membrane is not sufficient to transport the heat away quickly enough. The heat may corrupt the measurements as it influences the saturation magnetisation of the Py disk, which in turn affects the resonance spectra (*cf.* Sec. 6.1). Additional issues caused by heat include thermal drift of the sample, which cannot easily be corrected by automated drift correction because the excitation cycle is measured for each pixel before moving to the next pixel and, even in a full image, the position of the core cannot be detected easily. Therefore, the FOV has to be enlarged for automated measurements, increasing the measurement time and the heat input. During these experiments performed with a twin of the TEM sample, the thermal stress introduced by heating became large enough to break the SiN membrane, thus destroying the sample.

In order to verify the first measurements, a second image series was recorded

[5] The temperature is unlikely to rise above the Curie temperature (~550°C [145]), it was possible to record magnetic signals.

from a thicker sample of nominal thickness of 160 nm for the same measurement parameters. This sample was fabricated on a 200-nm-thick SiN membrane, in order to improve heat transfer, by S. Finizio (PSI). The thicker membrane is also more resistant to thermal stress. The FOV was enlarged to 28 x 28 pixel^2. The orange line in Fig. 6.19b shows STXM measurements of the resonance frequency of the second sample. During this experiment, image series at 529 and 559 MHz were be excluded from evaluation due to cross talk, while a measurement at 470 MHz was not possible due to quantisation of the frequencies and the choice of taking 17 images per series. The resonance spectra are in good agreement with those recorded from the first sample. This agreement suggests that a change in thickness from 130 nm to nominally 160 nm does not have a strong influence on the resonance frequency. Nevertheless, the true thickness of the Py disk, as well as its degree of bending, are unknown. Regardless of the uncertainties, these results are in good agreement with micromagnetic simulations (see. Sec. 6.1).

6.5.2. Vortex core motion studied by conventional Lorentz microscopy

Although the resonance frequency of the vortex core gyration can be detected from images recorded in Fresnel mode using the CCD of the electron microscope [63], its motion cannot be resolved with the required temporal resolution using conventional Fresnel defocus imaging. Within the scope of this thesis, the resonance frequency was detected using the same setup at the Titan T as for the characterisation of breathing of the vortex core above using the same defocus value of 710 µm (see Sec. 6.4.1 for further details). The only difference in the setup was that the images were saved at their full resolution of 2048 x 2048 pixel^2. The vortex core was brought into motion by applying RF fields with frequencies of 416 to 423 MHz using a total power of 22 dBm. The images were recorded in Lorentz mode, with bright contrast indicating the position of the vortex core. The core appeared as a dot or a ring, depending on whether it was at resonance when using long exposure times of 1 s, which represent a time average over many cycles. The scale was defined by measuring the radius of the Py in the defocused images. Figure 6.20 shows the outer radius of the vortex core gyration plotted as a function of applied frequency. The outer radius of the gyration can be measured directly from the images. The insets in the plot show representative images, which have been cropped to the region of the vortex core. The largest outer radius of the gyration is ~39 nm at a frequency of 418 MHz which is consequently defined to be the resonance frequency. It can be excluded that

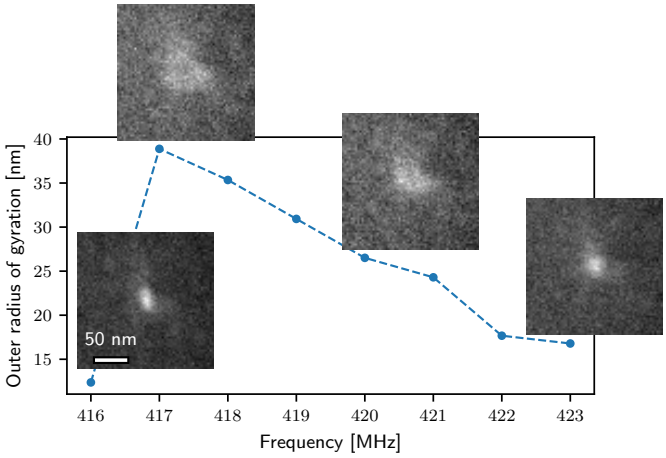

Figure 6.20.: Measurement of resonance frequency of the sample described in Sec. 6.1 using time-averaged images recorded with a defocus of 710 µm. The radius of the gyration increases at the resonance frequency, which is approximately 418 MHz. The insets show images of the gyration recorded using an exposure time of 1 s at frequencies of 416, 418, 421 and 423 MHz and an applied power of 22 dBm.

the opening is purely due to an image shift (*cf.* Sec. 6.5.3) due to two reasons. Firstly, the deflection of the image is expected to be approximately constant in this frequency range (*cf.* Sec. 6.2.2), while the images show the largest deflection close to the expected vortex core resonance. Secondly, the image shift deflects the complete image only along a line (*cf.* Sec. 6.5.3), while the vortex core gyration indicates a circular trajectory.

The measured resonance frequency is in good agreement with simulation of the vortex core motion (*cf.* Sec. 6.1), although the experimentally determined resonance frequency of 417 MHz is slightly higher than the value of 400 MHz predicted by the simulation. The higher resonance frequency suggests that the assumed thickness of 160 nm (to account for the bending of the Py disk) is not sufficient and that the effective thickness of the Py disk is even larger [85]. Moreover, other factors may affect the resonance frequency, *e.g.* heating of the sample and the variation of the saturation magnetisation (Sec. 5.2.2). The experimental resonance frequency spectrum around 400 MHz is sharper than that in the simulation. This difference may result from imperfect properties of the holder, as discussed in Sec. 6.2.1, which may affect the electromagnetic fields inside the cartridge. In contrast, the driving field and the sample are assumed to be perfect in

the simulation. This difference underlines the fact that the properties of a perfect system can be described using simulations, whereas in experiments reality may impose different constrains. The second resonance seen in the simulation close to 1 GHz is less prominent. Its absence in the experiments (not shown) illustrates that experimental parameters have to be tuned carefully in order to excite the first resonance.

6.5.3. Time-resolved electron microscopy using a delay line detector

In addition to recording time-averaged images of vortex core gyration, time-resolved motion of the vortex core was also studied using Fresnel imaging with bright contrast at the vortex core position in a Py disk using a defocus of 1 mm. The temporal resolution was defined by the DLD. The experimental setup was introduced in Sec. 6.2.1. In contrast to the previous TEM measurements, the sense of rotation of the vortex core, as well as its speed of motion at each position, are now accessible. The gyration was excited by applying microwave magnetic fields around the expected resonance frequency at an applied power of 23 dBm in a static out-of-plane field of 18 mT. All of the parameters were optimised to increase the gyration radius, while ensuring that vortex core switching did not occur [45]. In addition to the frequencies around resonance, one reference image of vortex core motion out of resonance was recorded at frequency of 450 MHz. The total integration time for each measurement was set to 2 min, which was sufficient to resolve vortex core motion, while minimising sample drift. For each chosen frequency, the excitation cycle was divided into approximately 175 phases. An image was recorded at each of these steps by adding measurements from at the corresponding phases stroboscopically.

Figure 6.21a shows snapshots of vortex core gyration recorded at various phases of the excitation cycle. A clockwise trajectory follows an elliptical shape. Each snapshot corresponds to a time average over 13 ps. Several empty images with exposure times of approximately two minutes were recorded and combined to form one image of the background. Each individual image was divided by this background image after normalisation to the exposure time to enhance the contrast of the vortex core. The motion of the core, in combination with its bright contrast, suggests that the circulation of the in-plane magnetisation of the vortex is counterclockwise. By combining this information with the clockwise motion of the vortex core, it can be inferred that the vortex core is left-handed and, hence, that the vortex core points downwards (*cf.* Sec. 2.4.2). The pixel-to-nm conversion

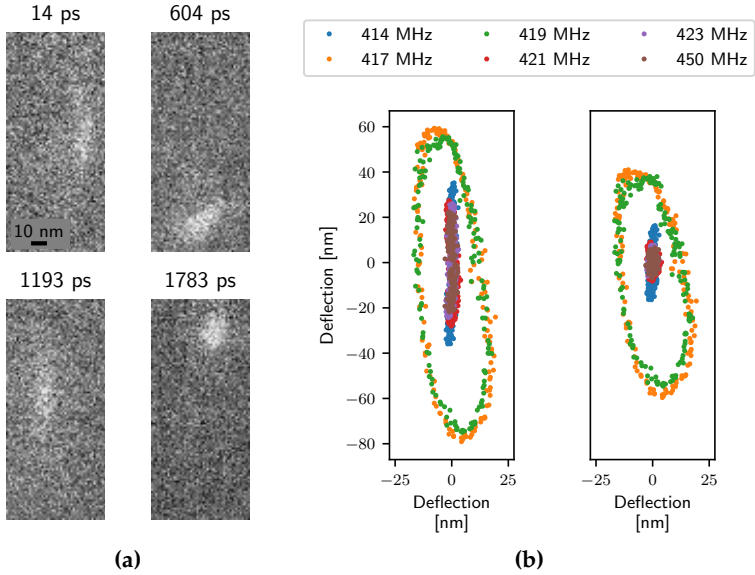

Figure 6.21.: Vortex core gyration of the sample described in Sec. 6.1 imaged with the DLD at an applied power of 23 dBm and a static out-of-plane field of 18 mT. (a) Snapshots of vortex core motion at different phases of the excitation cycle. Each image corresponds to an integration time of 13 ps. (b) Position of the vortex core at each time step for different frequencies without (left) and with (right) correction for the electron beam - microwave magnetic field interaction. An increase in gyration amplitude for a frequency around 418 MHz is observed. Figures adapted from [82].

was determined by measuring the core size out-of-resonance and compare this to the known core size from calibrated measurements (*c.f.* Appendix B.5). This method results in an error of about 10%.

The position of the vortex core was then measured in each individual image. For this purpose, a region of interest around the core trajectory was cropped from each image to speed up the data processing and to avoid issues with bright pixels (*cf.* Appendix B.4). The single snapshots were smoothed with a $\sigma = 2$ pixel Gaussian filter and thresholded to show pixels with an intensity higher than 0.8 times the maximum intensity. Finally, the centre of mass was determined for each image. The smoothing and thresholding steps were found to be necessary so that the vortex core position was not affected by noise. Figure 6.21b shows the detected vortex core positions for different applied frequencies. The measurements were rotated in such a way that the main deflection of the vortex core is aligned with the y axis. A clear distinction between the gyration amplitude in and out of resonance is visible. It can be excluded that the imaged deflection is purely based on the interaction of the electron beam with the microwave magnetic field because there are no modulations of the trajectory visible. These modulations would have to be present if the deflection was a result of only the electron beam – microwave field interaction because the presence of these modulations of the microwave excitation was shown in Sec 6.2.2. In contrast to the electron beam, the vortex core gyration in resonance does not follow small modulations of the microwave excitation instantly. Therefore, small modulations do not affect the vortex core gyration at resonance and a stable trajectory is reached.

As mentioned above, the position of the vortex core in each snapshot only not depends on the deflection of the vortex core by the applied field, but is also affected by an additional deflection of the electron beam and ultimately of the whole image (see schematic diagram in Fig. 6.22a). The image shift can partly be removed by estimating its effect using an out-of-resonance measurement, where it is assumed that the vortex core is not deflected by the applied field. Instead, the apparent motion of the vortex core in the image series results purely from the interaction of the electron beam with the applied magnetic field. This interaction follows the same excitation and also results in a sinusoidal motion along a line. The deflection due to this interaction can be estimated by fitting a sinusoidal function to the deflection in the form:

$$y_1 = y_0 + y' \tag{6.1}$$

$$y_0 = y_1 - y' = y_1 - [a \cdot \sin(b \cdot t + c) + d]. \tag{6.2}$$

Here, y_1 is the measured vortex core position which consists of the undeflected

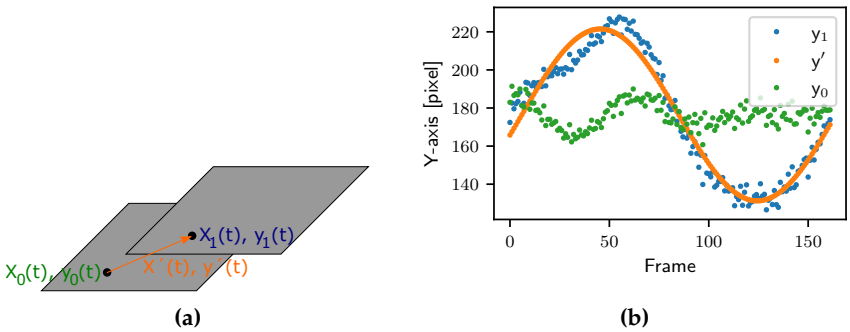

Figure 6.22.: Correction for the electron beam - magnetic field interaction. (a) A shift of the complete image results in an apparent shift of the vortex core (black dot). The image shift is induced by the interaction of the electron beam with the magnetic field. (b) A sinusiodal function y' is fitted to the measured position of the vortex core y_1 which models the image shift due to the microwave magnetic fields. The vortex core position without the image shift y_0 could then be extracted from the model (see text for details). Images adapted from [82].

position y_0 and the image shift y'. In order to estimate the effect of the image shift, a measurement out-of-resonance (at 450 MHz) is analysed. Here, it is assumed that the vortex core is stationary and the measured deflection is purely due the image shift. The image shift depends on the microwave excitation, where the amplitude a is a measure of the strength of the deflection. The parameters b, c and d are required to match the phase and offset of the sinusoidal function. The not-deflected position is determined by subtracting the fitted image shift y' from the measured vortex core position y_1. Figure 6.22b shows a plot of the deflected core position, the estimated image shift and the corrected core position for each frame in the excitation cycle. In order to correct the remaining frequencies, the parameters b, c and d were fitted for each of the applied frequencies separately as the measurements start at different phases within the excitation period. The parameter a was not fitted again as this characterises the strength of the image shift. The image shift y' was then determined from all parameters for each applied frequency and removed from the measured core position, thereby obtaining the corrected vortex core position.

The right frame in Fig. 6.21b shows the corrected vortex core positions for each frequency. A sharp vortex core resonance can be seen at 417 and 419 MHz with a gyration diameter of 23 ± 3 nm. This resonance frequency is in good agreement with the previously determined value of 418 MHz in time-averaged

images recorded on a CCD camera, with the STXM results and with in the simulations. However, unexpectedly, the vortex core motion shows a strongly elliptical trajectory. Even though elliptical trajectories for vortex core gyration have been reported previously [63], such a strong ellipticity was in a prior single experiments (Fig. 6.17) and not in the simulations (Sec. 6.1). Several effects may influence the trajectory. The main factor is the interaction of the electron beam with the microwave field. So far, it was assumed that the deflection due to this interaction is constant with respect to applied frequency. However, this assumption only holds to a first approximation. The LAD experiments performed to characterise the holder in Sec. 6.2.2 revealed that the magnitude of the deflection depends slightly on applied frequency. A possible explanation is that, the formation of standing waves inside the holder may affect the amplitude of the microwave field. The approach that was used to remove the image shift may therefore not be sophisticated enough to correct for the image shift completely. A simple approach to overcome the frequency dependence would be to pattern a non-magnetic marker in the vicinity of the Py disk and to record its motion for each value of applied frequency and power. This motion would be based solely on the interaction of the electron beam with the microwave magnetic field. In addition, the control electronics of the energy filter were broken during the experiments (see. Appendix B.4). The measured trajectory may therefore be distorted.[6] Nevertheless, the motion of the vortex core was resolved and the resonance frequency was detected successfully.

The velocity of the vortex core was determined at each time step. This information cannot be obtained from the previous experiments, either due to a lack of spatial information in STXM or due to a lack of temporal resolution in conventional TEM. By using the DLD, both spatial and temporal information is accessible. Here, the velocity at each position is defined as the distance in pixels between two adjacent frames divided by the time of a single frame of 13 ps. The average velocity is 0.2 nm/ps, which is higher than the average velocity from micromagnetic simulations of 0.03 nm/ps. The difference is likely to originate from distorted shape of the vortex core following an elliptical trajectory. The velocity at each point reveals high values along the long axis of the elliptical motion for an applied frequency of 419 MHz (see Fig. 6.23). At the top and bottom of the trajectory, the vortex core velocity is smallest. This trend is expected for an elliptical trajectory, as the motion in the x direction is compressed compared to the motion in the y direction.

[6] By using the K2 detector before the energy filter, it was confirmed that the ellipticity is also present there.

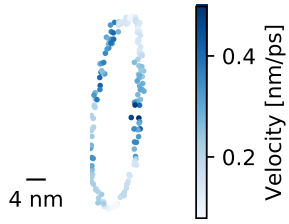

Figure 6.23.: Velocity of the vortex core under excitation at 419 MHz. The core is faster along the long axis of the ellipse than along the short axis.

Small local variations in velocity indicate where the sample has imperfections that affect the motion of the vortex core. For example, surface roughness of the sample can affect the velocity of the vortex core [148]. In addition, the vortex core may be pinned locally by internal defects in the sample [134]. Hence, the vortex core velocity can be used to probe the texture and defects in a sample by studying its variations at different positions in the sample. For this purpose, the trajectory of the vortex core can be changed by applying different static in-plane or out-of-plane magnetic fields to access all regions of the sample. This possibility highlights the prospect of combining spatial and temporal resolution in a transmission electron microscope that is equipped with a DLD to access multiple sample properties, including the influence of defects.

6.5.4. Comparison of the methods

The resonance frequency of the vortex core in a Py disk was detected successfully using three different methods. The results are in good agreement between each other and with micromagnetic simulations. The simulations predict a resonance around 400 MHz. The STXM measurements provide a value around 400 MHz, while the conventional and time-resolved Fresnel defocus measurements provide a value around 418 MHz for similar sample systems. The agreement suggests that TEM measurements using a DLD probe the resonance of the vortex core and not only the interaction of the electron beam with the microwave magnetic field. The diameter of the gyration is in good agreement between the experiments and the simulations considering the likely underestimation of the microwave amplitude (Sec. 6.2.2). It was found to be ~23 nm at an applied field of 0.07 mT in the time-resolved Fresnel defocus measurements and 20 nm in the micromagnetic simulations at an applied power of 0.1 mT. In case of the conventional Fresnel defocus measurements, only the outer diameter of the time-averaged core mo-

tion could be measured in the images and not the gyration diameter at the centre of the vortex core. The outer diameter of the gyration is ~78 nm at a similar applied magnetic field compared to the time-resolved measurements (at an applied power of 22 and 23 dBm, respectively), which is, as expected, larger than the gyration diameter. Nevertheless, it will be possible to measure the gyration diameter in the future by fine tuning the experimental setup.

As described above, the three methods different advantages and disadvantages for imaging vortex core gyration. The advantage of STXM is its easy access to high temporal and spatial resolution. At the same time, X-ray photons do not interact with the applied microwave field and can penetrate thicker materials. Therefore, it is possible to deposit a strip line on top of the sample, ensuring that the applied magnetic field is strongest at the sample position. In addition, several stimuli, *e.g.* additional static fields, can easily be applied, since there is enough space inside the sample chamber. Furthermore, STXM is element-specific, so that the magnetisation associated with a specific element can be probed. However, these advantages come at the cost of long measurement times of typically around 10 to 20 minutes. As a result, the measurement time needs to be balanced against the required temporal and spatial resolution. Moreover, the frequencies that can be applied are quantised and cannot be chosen freely. With STXM, only the magnetic properties in the beam direction measured. A measurement therefore only provides information about the out-of-plane magnetisation. In the case of a vortex, the out-of-plane magnetisation is restricted primarily to the core area and its motion can be tracked more easily from the in-plane component. Hence, the sample may need to be mounted at an angle to measure the vortex core gyration optimally. The use of sample tilt may result in a distortion of the projected image and an increases in the projected material thickness.

In contrast, conventional Fresnel defocus imaging provides direct access to in-plane magnetic properties while not being sensitive to out-of-plane magnetisation. Such measurements can be combined with a sweep of the frequency of the applied magnetic field and exposure times in the range of seconds, allowing the resonance frequency to be read directly from the images by measuring the gyration radius. Hence, the technique provides easy and fast access to detect the resonance frequency. However, these advantages come at the cost of a loss of access to temporal resolution. It is also not easily possible to determine the polarisation of the vortex core. This information would have been helpful in the analysis of the observed breathing-like behaviour, as it would have provided insight about whether the core is switching its polarity.

The combination of a fast readout detector with Fresnel defocus imaging pro-

vides a good compromise between the two techniques for studying vortex core dynamics. It offers access to the gyration of the vortex core with high temporal resolution as for STXM, but with better spatial resolution. At the same time, data analysis is straightforward, as the position of the vortex core can be determined directly and the total measurement time per frequency is significantly reduced, when compared to conventional Fresnel defocus imaging, the temporal resolution is improved dramatically. Nevertheless, the use of a DLD has some disadvantages. For example, the interaction of the electron beam with the microwave field has to be taken into account. In addition, the technique is limited to stroboscopic measurements to provide sufficient contrast. Therefore, the vortex core dynamics have to be stable and repeatable. The frequencies that can be applied are currently quantised. However, there are efforts to overcome this limitation in the future. The analysis of vortex core dynamics in the TEM can be extended to studies of other magnetic systems, as well as to time-resolved measurements of other material properties, such as strain where diffraction patterns are recorded while scanning the sample. Here, the exposure time per diffraction pattern can be reduced down to a few tens of milliseconds reducing the total exposure time of a complete scan from 2,5 h to a couple of minutes [69].

6.6. Limitations of time-resolved microscopy with a delay line detector

As mentioned above, the combination of a DLD with Fresnel defocus imaging is suitable for studying vortex core gyration, while pushing the temporal resolution of TEM. In this section, the limitations of a DLD are discussed, with a focus on its temporal resolution and applicable the frequency range. The use of a DLD is then compared to UTEM approaches based on a pulsed source or a beam deflector.

6.6.1. Temporal resolution and applicable frequency range

The temporal resolution and the frequency range of the DLD were probed using LAD mode. The same principle was applied as for characterisation of the holder, where the microwave magnetic field deflects the electron beam (see Sec. 6.2.2). A frequency range of between 100 MHz and 4 GHz was probed by using the HP8657B frequency generator for frequencies up to 2 GHz and HP8671B for higher frequencies. In both cases, a total power of 17 dBm was sufficient to

provide a resolvable deflection, while keeping the distortions of the micromagnetic field due to the experimental conditions (Sec. 6.2.2) as small as possible. The camera length was chosen to be 115 m and the spot size of the beam was approximately 300x300 pixel^2 to provide the best access for imaging the beam deflection.

Figure 6.24a shows the deflection of the electron beam measured for various applied frequencies. For each frequency, a different number of frames per excitation cycle was recorded to ensure reasonable temporal resolution, while not saving too large amount of data. 8 frames were averaged for the measurement at 100 MHz, while 2 frames were averaged for frequencies between 500 MHz and 2.5 GHz. For higher frequencies, the images were not binned in the time domain. The background was removed from the data, as explained for vortex core gyration (*cf.* Sec. 6.5.3) and the three-dimensional data set was filtered using a Gaussian filter with $\sigma = 2$ pixel. The main axis of motion was rotated so that it was aligned with the y axis and a region of interest only containing the beam deflection was cropped from the full image. The sinusoidal motion of the beam due to the excitation can be clearly seen in the images summed over the x axis. However, the motion does not follow a straight line. Instead, it is slightly bent as seen in the time-averaged images. This bending is thought to be caused primarily by the broken energy filter electronics (see Appendix B.4). In addition, higher modes may form inside the cartridge and affect the behaviour of the microwave magnetic field [140].

The highest frequency that can be resolved is defined as the frequency for which a linescan through the phase domain in the centre of the deflection still results in two maxima. The positions where the linescans were taken are indicated by red lines in Fig. 6.24a, while the resulting linescans are shown in Fig. 6.24b. The condition that two maxima need to be present is fulfilled up to 2.3 GHz. Hence, magnetisation dynamics can be studied up to this frequency.

The temporal resolution is defined as the full width at half maximum (FWHM) of the peaks in the line scan. Figure 6.24c shows the FWHM τ_{exp} plotted as a function of applied frequency. In each case, the first maximum was chosen for evaluation. For lower frequencies close to 100 MHz, the temporal resolution is limited to approximately 900 ps. The temporal resolution is then limited by the spot size of the beam on the detector, as well as by binning in the time domain. For higher frequencies, the combination of the DLD with TEM offers a temporal resolution on the order of 100 to 300 ps. In order to correct for the effect of the

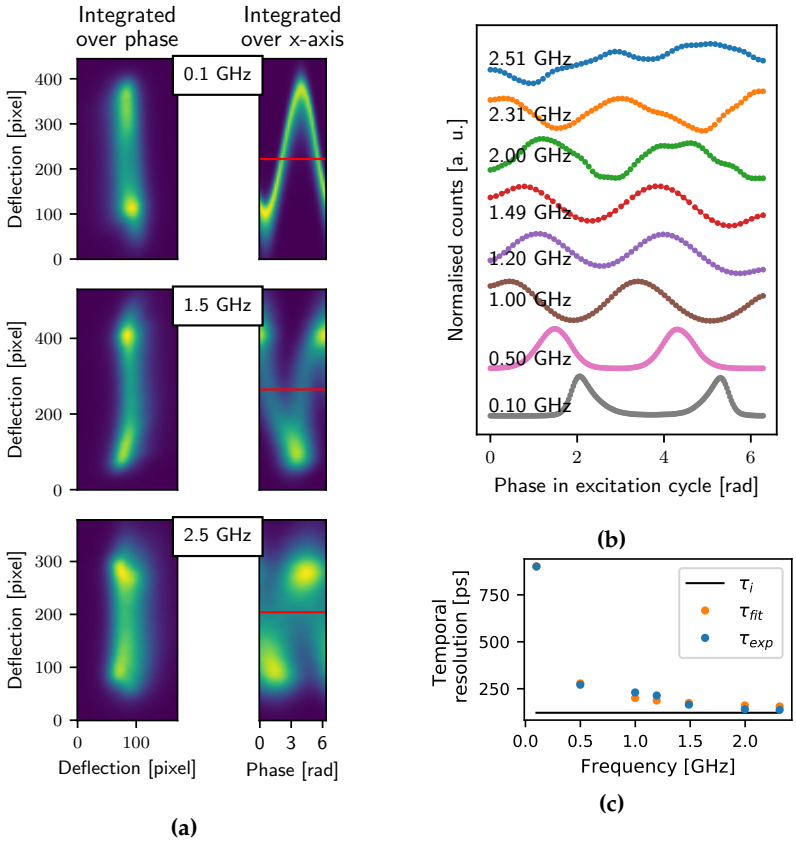

Figure 6.24.: Measurement of the usable frequency range and temporal resolution of the combination of a DLD and TEM. (a) LAD images of the deflection of the electron beam by the microwave magnetic fields for frequencies of ~0.1 GHz, ~1.5 GHz and ~2.5 GHz, revealing approximately sinusoidal motion. The left column corresponds to integration over the phase domain, while the right column corresponds to integration over the x axis. (b) Linescans recorded along the time domain of the integrated data over x at the position of the red line indicated in (a) for varying frequencies. Up to 2.3 GHz, approximately sinusoidal motion is observed, as suggested by the two peaks, indicating that dynamic measurements can be performed up to this frequency. (c) FWHM of the first peaks in the linescans in (b). τ_{exp} corresponds to the measured FWHM, which is corrected by a fit to account for the effect of the spot size to gain the intrinsic temporal resolution τ_i = 122 ps. τ_{fit} corresponds to the fitted temporal resolution. All images adapted from [82].

spot size by fitting

$$\tau_{fit} = \tau_i + \frac{\tau_{spot}}{f_{RF}} \tag{6.3}$$

where tau_i is the intrinsic temporal resolution and τ_{spot} the frequency dependent effect of the spot size. Here, the intrinsic temporal resolution is found to be 122 ps. This temporal resolution is an improvement approximately by six orders of magnitude when compared to conventional TEM imaging, albeit for stroboscopic experiments.

6.6.2. Comparison of different approaches to achieve sub-ns temporal resolution

Time-resolved electron microscopy of vortex core gyration is not only possible with a fast camera, but also based on UTEM approaches that make use of a pulsed source or a beam chopper (see. Sec. 3.4). All of these approaches offer access to transitions between two states, instead of imaging only an initial and a final state. They all rely on stroboscopic measurements to obtain enough contrast in the recorded TEM images. Thus, the process under investigation needs to be reproducible over many (typically several millions) of cycles.

UTEM offers temporal resolution in the fs regime [66, 109, 149–151]. However, the better temporal resolution comes at the cost of modifications to the illumination or condenser system of the microscope. Hence, such approaches cannot be implemented on existing microscopes easily. Moreover, the modifications may compromise the quality of the electron beam. For example, the number of electrons per pulse is reduced [108] and additional beam displacements and blurring may be introduced [152]. Hence, UTEM approaches result in challenges for techniques that require a stable and coherent electron beam, such as off-axis electron holography.

In contrast to UTEM, the implementation of DLD does not require significant modifications to a microscope and existing microscopes can easily be upgraded. In addition, it offers a number of further advantages: (i) the high quality of the electron beam offered by modern microscopes is not compromised, as the electron optics are unchanged; (ii) the sample is illuminated continuously and every electron is recorded, reducing the measurement time that is required to obtain sufficient contrast, as well as the electron dose that the sample is subjected to, when compared to methods based on pulsing the electron beam; (iii) the DLD is a single electron detector, in which the arrival time of each incident electron is

detected; (iv) a pulsed beam may result in a sample drift. Nevertheless, the DLD has a number of disadvantages. For example, the temporal resolution is currently limited to the ps regime. This limitation is imposed by several factors. On the one hand, the incident electrons can only be detected every 7 ps. On the other hand, the time that the MCP requires to pass the information that an electron has hit the MCP to the underlying meanders for position detection depends on the incident angle of the electron. This angular dependence affects the temporal resolution. Despite these limitations, the combination of a DLD with TEM can be used to push the temporal resolution of existing microscopes by approximately six orders of magnitude. The growing interest in easy-to-access temporal resolution is also exemplified by recent developments of other fast detectors. For example, the aim of the Timepix 4 detector is to reach ps temporal resolution, while maintaining a high electron dose [153].

6.7. Summary

This chapter focused on investigating vortex core dynamics in a Py disk using different techniques. Conventional Fresnel defocus imaging in the TEM revealed a breathing-like behaviour at high powers of an applied microwave field close to the resonance frequency. The breathing-like behaviour might originate from heating effects or flipping of the vortex core polarisation. Even though it is not understood yet, it shows that experimental parameters need to be tuned carefully before performing stroboscopic measurements. The vortex core resonance was then investigated using three different approaches: STXM, conventional Fresnel defocus imaging and time-resolved Fresnel defocus imaging using a DLD. The results obtained using the three techniques are consistent with each other, providing a value of the vortex core resonance of approximately 400 MHz. Nevertheless, an elliptical trajectory was observed experimentally, which was not expected based on micromagnetic simulations. With respect to the measurement techniques, the combination of a DLD with TEM offers a good compromise between imaging with STXM and conventional TEM. This combination makes it possible to achieve an intrinsic temporal resolution of 122 ps over an applied range of frequency regime up to 2.3 GHz for stroboscopic measurements. This temporal resolution is a significant improvement over conventional TEM. Moreover, existing electron microscopes can easily be upgraded, allowing access to transitions between different states for a multitude of sample systems.

Chapter 7.

Summary and outlook

Research interest in magnetic materials has been strong for many decades [1–6]. In this context, magnetic nanostructures and related physical phenomena are gaining increasing attention, in part due to discoveries of new materials and properties (e.g., magnetic skyrmions) and their promising applications in energy efficient information storage technologies [10–12]. This thesis has focused on two nanostructure systems: artificial spin ice and magnetic vortices. It has aimed to develop novel quantitative approaches to study the static and dynamic magnetic properties of these nanostructures using TEM with high spatial resolution. The existence of virtual antivortices in chiral ice and their importance for dynamic magnetic behaviour was predicted by theory, but not confirmed experimentally [24]. Magnetic vortices and their cores are used as model systems to develop new methodologies to study magnetisation dynamics with improved temporal resolution. In the present work, the use of a high frequency magnetising holder and a fast delay line detector allowed the electron beam illumination to remain unmodified.

The demonstration of the existence of virtual antivortices in chiral ice required several pre-characterisation experiments to ensure that the sample quality and experimental conditions were sufficient for the study of weak stray fields. First, the structure and chemical composition of the chiral ice sample were investigated in conventional and cross-sectional studies. It was found that the composition of the deposited magnetic islands is 65 at.% Ni and 35 at.% Fe, which deviates from the nominal composition of 83 at.% Ni and 17 at.% Fe, altering the magnetic properties. The magnetic order in the chiral ice and the magnetic flux distribution were imaged using off-axis electron holography. Model-based reconstruction of the magnetisation from the experimental phase shift revealed a reduced averaged in-plane saturation magnetic polarisation of 0.73 T in the permalloy islands, which is lower than the nominal value of 0.8 – 1 T [126, 127]. The magnetisation

switching behaviour of the complete spin ice pattern was then systematically investigated, confirming a driving mechanism for switching predicted using micromagnetic simulations. The effect of oxidation on the magnetic state of the nanomagnets, as well as on magnetisation switching, was assessed, revealing the importance of maintaining a pristine sample condition for characterisation of the virtual antivortices. By analysing the experimental phase shift and magnetisation distribution of the nanostructures, the three-dimensional stray field distribution of the chiral ice was retrieved successfully. The results revealed that virtual antivortices are present in the sample plane and that their distribution is not symmetrical with respect to the edges of the pattern matching the prediction of theoretical calculations. These studies required the development of approaches data analysis based on scripts written in the Python environment. The two most important steps were the possibility to correct for image distortions in the phase shift images that were used in turning over experiments and to increase the useable FOV of the phase maps. The image distortions were corrected by warping one phase image to fit a second phase image. An increase in the useable FOV was also achieved by stitching several magnetic phase images or magnetisation maps together.

The analysis of vortex core dynamics in permalloy disks was started with measurements of their static magnetic properties using Lorentz microscopy and off-axis electron holography following the methodology applied in the chiral ice studies. By combining experimental results and micromagnetic simulations, it was shown that the magnetic vortex core in a permalloy disk has a barrel-like shape, whose position depends on the sample geometry. For example, a non-uniform thickness profile may result in a shift of the core from the centre of the disk. The size of the vortex core increased with increasing thickness of the disk, but was approximately independent of its diameter. It was shown that the permalloy disks exhibit bending as their edges, as the deposited islands peeled away from the membrane during the fabrication process. Such shape imperfections are not expected to have an influence on vortex core dynamics observed in time-resolved experiments. Time-resolved studies of vortex core dynamics in the Py disks were carried out in real space by combining Lorentz microscopy with the use of a high-frequency specimen holder and a fast delay line detector. In contrast to UTEM, this approach does not require significant modification of the microscope, thereby retaining the high electron coherence, brightness and fluence of the electron beam available in a standard instrument. Experiments on vortex core dynamics revealed a resonance at ~418 MHz, which was confirmed by complementary STXM and conventional TEM experiments. A comparison of these complementary approaches showed that a combination of Lorentz mi-

croscopy with a fast detector offers a good compromise between the excellent temporal resolution of STXM and the spatial resolution of TEM. The limits of this combination were assessed, showing that the resonant behaviour of magnetic systems can be studied up to 2.4 GHz with a temporal resolution down to 100 ps.

Magnetic domains are of essential interest in technical application over several years, maybe most famous in magnetic hard drives [154]. The presented work utilised microwave magnetic fields to excite vortex core motion. This excitation principle can also be extended towards the excitation of domain wall motion of various systems. Domain wall motion in general is taking place on a 10 to 100 ns time-scale which is accessible by the DLD [155]. Often, the technical application of permanent magnets is limited according to Brown's paradox which states that only 20-30% of the full potential of permanent magnets are used due to their microstructure [3]. Therefore, it is essential to understand the interplay between the microstructure and domain wall motion and the underlying mechanism of magnetisation switching [156]. This information can be used to tailor specific magnetic properties for various applications, such as increasing the coercivities of permanent. An example for unusual structures are periodic domain patterns in spiral geometries stabilised by the competition between strain and shape anisotropy. These ferromagnetic structures can be patterned in non-ferromagnetic thin films such as $Fe_{60}Al_{40}$ [157]. Their domain wall motion can also be excited by microwave magnetic fields and studied with the present setup. In addition to microwave magnetic fields, further stimuli can be applied to excite the domain wall motion, e.g., driving RF or spin-polarised currents through the sample. Therefore, it is possible to image the magnetic domain wall racetrack which has great potential for non-volatile memory application [14]. These racetracks can also be realised based on magnetic skyrmions [158]. Another common stimulus is laser excitation since the optical control of the magnetic state of nanostructures is appealing as they do not depend on external fields and offer fast switching times [159].

The fact that the electron beam quality is not affected by the presented time-resolved imaging principle opens the pathway to time-resolved electron holography. Therefore, stray field dynamics become accessible, while preserving the spatial resolution of TEM. Therefore, it complements the toolset of characterisation techniques such as time-resolved STXM and UTEM approaches based on Fresnel defocus imaging. Imaging the stray field is of particular interest for interacting systems of nanomagnets, such as ASI. For square ice, it was found by Monte Carlo simulations that the interaction of the nanomagnets results in a chiral reversal during magnetic switching [160]. With the setup, not only the

switching of the nanomagnets, but also the influence of neighbouring nanomagnets can be investigated. Knowledge of the switching behaviour can then be employed to design reconfigurable Boolean logic gates in an artificial square ice like geometry where a small laser spot may be used for selective heating of individual nanomagnets [161]. Future studies of chiral ice can focus on topics that include: (i) optimisation of the chiral ice geometry and analysis of virtual antivortices to ensure switching in the deep picosecond regime; (ii) experimental studies of the effect of switching processes on resonance spectra proposed by micromagnetic simulations [29]; (iii) local control and switching by optical means to image the origin of different resonance behaviours in real space. The latter study would combine different stimuli such as laser and microwave magnetic excitation. The aim of these studies would be to contribute to the pathway towards reconfigurable magnonic crystals [33]. Nevertheless, the interest in magnetic stray fields is not limited to ASI. In biomedical applications, the local heating of hyperthermal nanoparticles, which are excited into motion, for cancer treatment is critical for a successful therapy [162]. Understanding the influence of the stray fields on the formation and motion of the clusters of interacting nanoparticles can help to improve the distribution of the nanoparticles. For time-resolved off-axis electron holography, denoising of the measurements will become an important factor as the total exposure time of stroboscopic measurements is limited by instabilities. These instabilities may be specimen or fringe drift and decrease the signal-to-noise ratio. Here, conventional and machine learning denoising algorithms, which are regularly used in medical imaging [163], offer great potential as exemplified by the presented PCA in the context of vortex core gyration and by unsupervised training of neural networks [164].

This work focussed on magnetic phenomena. Nevertheless, the methods developed here are not limited to magnetic application. As shown, off-axis electron holography is not only sensitive to the magnetic, but also to the electrostatic phase shift. Moreover, the MBIR was adapted to being able to reconstruct electric fields as well [62]. Therefore, the Python routines developed for the quantitative imaging of magnetic stray fields of chiral ice with a large field of view can be applied to image electric stray fields as well. These routines would allow imaging of large areas of semiconductors and p-n junctions and the effect of various dopants on those. The combination of DLD and TEM can also be used in a wide range of applications, for example to significantly reduce the measurement time for 4D STEM experiments where diffraction patterns are collected while scanning the sample [69,165]. In addition, there is progress towards coincidence experiments combining EELS and EDX measurements in order to remove the background in EELS measurements and enable imaging of low concentrations

of elements [166].

The presented thesis provided a pathway towards the quantitative study of magnetic stray fields in chiral ice and towards time-resolved microscopy of magnetisation dynamics exemplified by the magnetic vortex. In the future, both areas can be combined in order to study the dynamics of magnetic stray fields.

Appendix A.

Sample fabrication

The fabrication of nanostructures has advanced significantly in recent years, with advanced lithographic processes opening up a universe of possible designs on the micro- and nanoscale. A variety of specific methods make use of a beam to write a desired structure into a resist. Material is then often evaporated onto the resist. When the resist is washed away, only the desired structure is left on the substrate. In electron beam lithography, electrons are employed to write structures with a spatial resolution down to the nm scale.

The process of electron beam lithography can be divided into six steps (Fig. A.1). In the first step, the substrate is cleaned to ensure that there are no residuals left that may compromise the result (Fig. A.1a). In the second step, resist is coated onto the substrate (Fig. A.1b). It is important that the resist has a homogeneous thickness. This is usually achieved by spin coating, which involves rotating the substrate at high velocity after dropping the resist in the centre. The resist is dissolved in a solution for this purpose. The thickness of the resist can be controlled by the rotation speed and the rotation time. The desired thickness depends on the thickness of the structure to be prepared, as well as on the required spatial resolution. Two types of resist are available, depending on whether the exposed or the unexposed area should be dissolved. For electron beam lithography, most often a positive resist is used and the desired structure is exposed to keep the writing time short. After coating, the substrate is baked to drive off the solvent. In the fourth step, an electron beam is used to write the desired structure into the resist. The electron beam then locally breaks the bonds of the resist (Fig. A.1c). Typical electron energies are in the range of 50 to 100 keV. The resist is a polymer that can be dissolved more easily once it is broken into smaller segments. After writing, the resist has to be developed by immersing the sample into a solvent, which washes away the area that was exposed to the electron beam (Fig. A.1d). The solvent is chosen so that it mostly affects the exposed area and not the rest of the resist, in order to achieve clearly separated

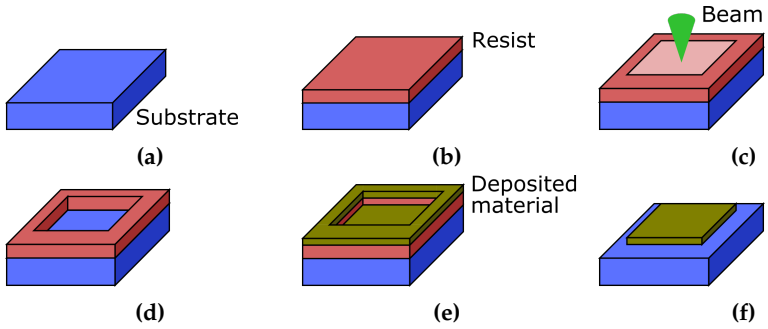

Figure A.1.: Steps in the lithography process. In the first step, the sample is cleaned (a), in the second step it is coated with a resist (b), before the resist is exposed to an electron beam (c). The exposed area is removed (d) and a material layer is deposited (e). Finally, the redundant material is removed by dissolving the resist (f).

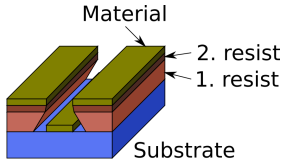

Figure A.2.: A double layer of resist can be used to form an undercut after development for electron beam lithography. The undercut breaks the continuous metal layer and improves lift-off.

regions. Subsequently, the material of interest is deposited on top of the resist (Fig. A.1e). The material only adheres to the substrate in the regions that have been exposed. In the last step, the resist is dissolved, effectively removing the excess material on top of it (Fig. A.1f), leaving only the desired structure on the substrate. This final step is referred to as lift-off. In practice, lift-off is often the most challenging part of the fabrication process. During evaporation, the material may also cover the side walls of the resist. Due to coverage of the side walls, the material in contact with the substrate may also be washed away when removing the resist. In order to counter this effect, the resist can be fabricated in such a way that the walls have an undercut (*cf.* Fig. A.2). Here, a double layer of resist is used with the thin upper layer having a larger molecular weight. The lower layer is then etched away faster during development.

Appendix B.

Data analysis

B.1. Finding unique solutions in model-based iterative reconstruction

During reconstruction of the magnetisation using the MBIR approach, regularisation based on the minimisation of the exchange energy is used as a constraint to smooth the reconstructed magnetisation. The strength of the minimisation, *i.e.* the regularisation parameter λ, has to balance regularisation with compliance to the experimental phase shift. If λ is too large, then the reconstructed magnetisation will resemble a mostly uniformly magnetised structure and will not match the experimental phase image. If λ is too small, then the algorithm will fit the magnetisation to noise. An L-curve analysis can be performed in order to find the optimal regularisation parameter [167]. In the case of magnetisation reconstruction, compliance with the experimental data is plotted against regularisation for various values of λ. Figure B.1 shows an L-curve for a simulated phase image that, includes artificial noise, for a magnetic vortex in a bar. The inflection point in the plot provides the best compromise between these two constraints. In this case the optimal parameter is $\lambda = 1e^{-4}$ and the vortex is reconstructed successfully. Decreasing the regularisation results in a magnetisation distribution that is mostly fitted to noise. Small vortices are then formed around outliers in the phase image. Too high a regularisation parameter leads to the magnetisation pointing up at the right side and down at the left side, thereby retrieving the two largest areas with parallel alignment. However, a domain wall is then formed in the centre instead of a vortex. The strength of the regularisation therefore has an effect on the spatial resolution of the magnetisation, smoothing neighbouring pixels by forcing them to be aligned parallel to each other. The larger the regularisation parameter, the more pixels are combined during smoothing and the poorer is the resulting spatial resolution. Hence, it is important to find the

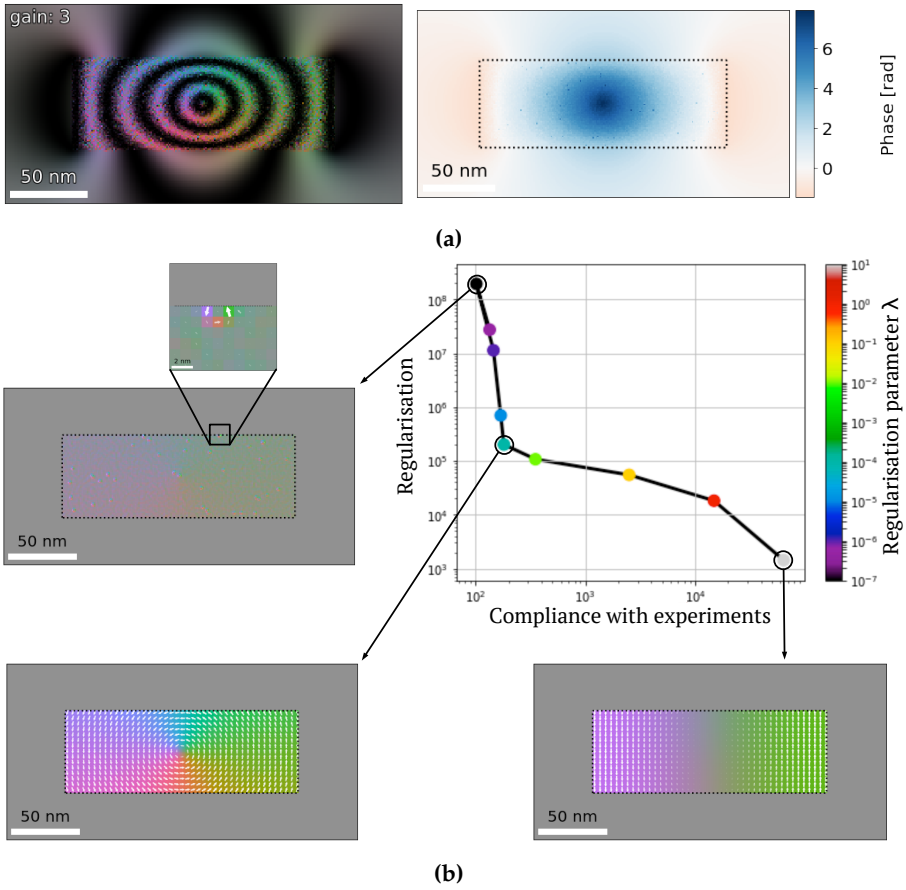

Figure B.1.: L-curve analysis during MBIR of magnetisation. (a) The right image shows the simulated magnetic phase shift of a vortex in a long bar. The left image shows a corresponding magnetic induction map. The magnetisation was reconstructed for various regularisation parameters. A compromise between compliance with the experiment and regularisation strength is plotted for different regularisation parameters in (b). The optimal regularisation strength corresponds to the inflection point in the plot. For this value of regularisation strength, the magnetic vortex is reconstructed correctly. If the regularisation is too small, then the resulting magnetisation is dominated by noise, while the vortex is smoothed away if the regularisation is too large.

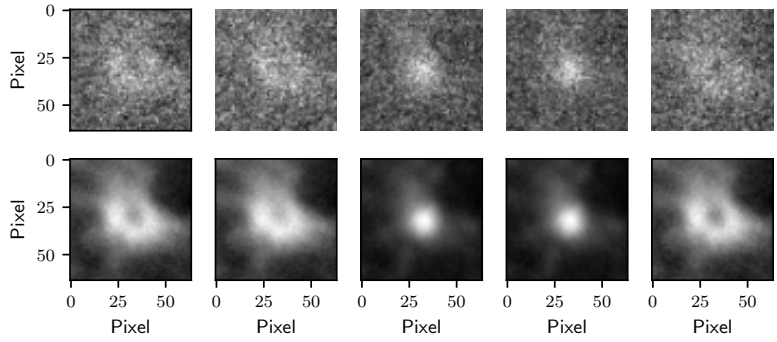

Figure B.2.: Application of NMF to a series of images to reduce noise. The top row shows images of the breathing-like behaviour of the vortex core motion (Sec. 6.4). The bottom row shows the same images after reconstruction with NMF. NMF only filters out the main features which can be reproduced by the open and closed of the breathing-like behaviour of the vortex core (Sec. 6.4). Therefore, these two states can be distinguished easier from noise after NMF.

best regularisation parameter, which neither results in a fit too noisy nor in a smoothing of the features of interest.

B.2. Principal component analysis for noise reduction

PCA can be applied to reduce noise in experimental images by filtering for the main features. In the vortex core experiments, the images can be classified as a mixture of two states, corresponding to the vortex core being in or out of resonance (Sec. 6.4). If the core is in resonance, then a ring can be seen in the images (open state), while a smeared dot (closed state), is visible if the core is out of resonance. NMF was applied with the pre-knowledge that two features are needed to reproduce the images. The constraint to use only two features results in a suppression of details that cannot be reproduced by open or closed states, as exemplified in Fig. B.2. The upper row shows original images where the vortex core was centred, but no filtering was applied. There, the core in the open state is barely visible due to noise in the background. The lower row shows the images after treatment with NMF. Here, the images are reproduced by adding products of the loadings and corresponding factors for each image in the series. The noise

in the reconstructed images is suppressed and the open state is visible. Both states can be distinguished more easily.

B.3. Data analysis for STXM

The original STXM images were dominated by the thickness contrast, as well as by an intensity gradient across the FOV. The process used to extract information about the vortex core resonance is described here for a 130-nm-thick Py disk (*cf.* Sec. 6.1) excited by an in-plane microwave magnetic field at 412 MHz. The first row in Fig. B.3a shows the original, images in which the core is not visible. From these images, the magnetic contrast has to be extracted by computing a sum image over the full image series, normalising this image by the number of images in the series and subtracting it from each image in the series. The second row in Fig. B.3a shows the images after normalisation. The black and white contrast corresponds to vortex core which becomes apparent in the difference between each image and the time average. The vortex core motion results in a circulation of the dark and bright contrast around each other. A small region around the strongest variation in contrast was masked out (black outlines the second row of Fig. B.3a). Care was required to ensure that the mask only contained either bright or dark features in each image. The total intensity of all of the pixels inside the mask was calculated at each different time step. This variation in intensity follows the sinusoidal excitation applied to excite the vortex core resonance (Fig. B.3b). Thus, a sinusoidal function can be fitted to the variation, with a pre-knowledge of the applied frequency. The variation of the amplitude of the function for different applied frequencies is used to determine the vortex core resonance (Sec. 6.5.1).

B.4. Energy filter status during DLD experiments

During the time-resolved experiments with the DLD, there were issues with the control electronics of the energy filter. These issues resulted in a distortion of the image on the DLD. Figure B.4 shows the distortion for a cross-grating grid. The straight lines of the square grid do not appear as straight lines in the image, but have a curvature that is position-dependent. These distortions are reproduced by the time-resolved vortex core gyration and LAD experiments (Sec. 6.5.3 and Sec. 6.6.1) where straight lines show the same position-dependent curvature. The dark shadow in Fig. B.4 shows the time-integrated trajectory of the electron

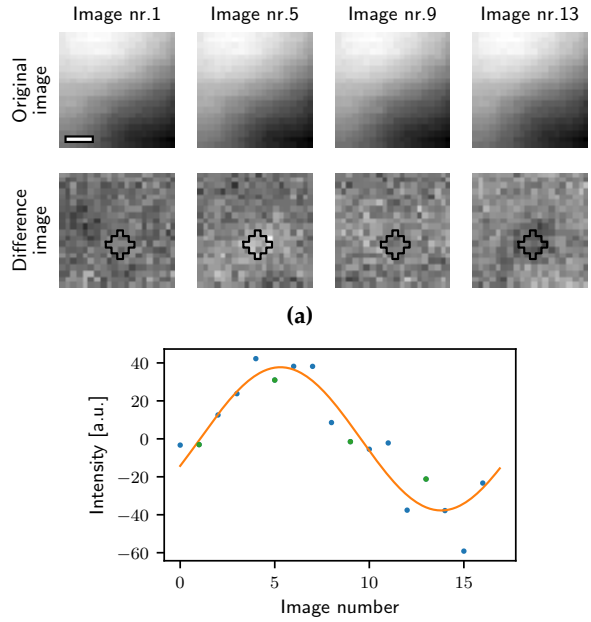

Figure B.3.: Data analysis for STXM. (a) Images recorded at four different stages of the excitation cycle are shown in the four columns. The top row shows the original recorded images. The second row shows difference images (see text for details). In the difference images, the dark and bright variations correspond to the vortex core motion. The black outlines indicate the mask in which to sum the recorded intensity. The scale bar corresponds to 100 nm. (b) Intensity of the vortex core region for all images of the series (black outlines in (a)). A sinusoidal function is fitted to the data points, in order to determine the amplitude of the contrast variations, which gives access to the amplitude of the vortex core motion. The green data points indicate the images in (a).

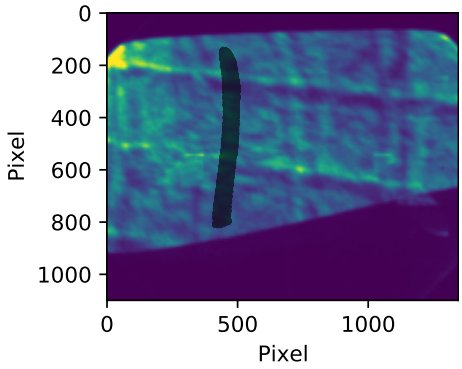

Figure B.4.: Image of a calibration sample with a periodic lattice spacing, revealing distortion of the image due to electronic issues in the imaging filter. The dark shadow shows the trajectory of the electron beam in the LAD experiments at an applied frequency of ~2 GHz (Sec. 6.6.1).

beam in the LAD experiments at an applied frequency of ~2 GHz (Sec. 6.6.1). The distortions of the trajectory follow the curvature of the gross grating grid with a stronger deflection in the top of the image. In addition to the distortions, only half of the detector is illuminated by the electron beam. Nevertheless, these constraints did not impede the vortex gyration experiments, as the change in the vortex core amplitude was sufficiently large (Sec. 6.5.3).

B.5. Calibration of DLD images

The DLD measurements were calibrated using the vortex core size in Fresnel defocus images. The procedure is described in this section. Firstly, a Fresnel images taken of the complete disk at 1 mm defocus with a K2 detector (Fig. B.5a). The pixel-to-nm conversion was converted by measuring the outer radius of the disk with a known radius of ~839 nm. Then, the distance between the central and first outer Fresnel fringe was measured to be ~12 nm (Fig. B.5b). Secondly, the same distance was measured to be 66 pixels in time-integrated Fresnel defocus images taken of the vortex core dynamics off-resonance (at 450 MHz). Figure B.6a shows the time-integrated image with the distance indicated in red. This distance was determined in Fig. B.6b from a line scan along the y direction integrated from the region marked in blue (Fig. B.6a). The distance was measured in additional time-integrated Fresnel images off-resonance and the mean conversion

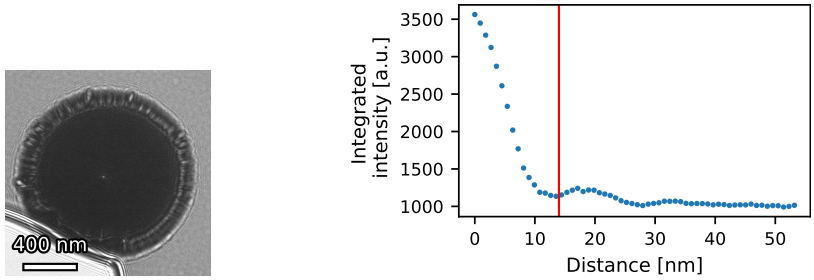

(a) (b)

Figure B.5.: Core size in Fresnel defocus image. (a) Fesnel image of disk at 1 mm defocus. The scale was calibrated by measuring the diameter of the Py disk. (b) Radial profile in core region. The distance between the centre peak and first outer fringe was measured to be ~12 nm (red line).

was determined to be 0.35 ± 0.2 nm/pixel. Thirdly, the diameter of the vortex core resonance was then measured from the time-integrated Fresnel defocus image at 417 MHz (Fresnel defocus image in Fig. B.6c and line scan in Fig. B.6d). There, the diameter was determined to be approximately 66 pixel which corresponds to 23 ± 3 nm using the conversion factor.

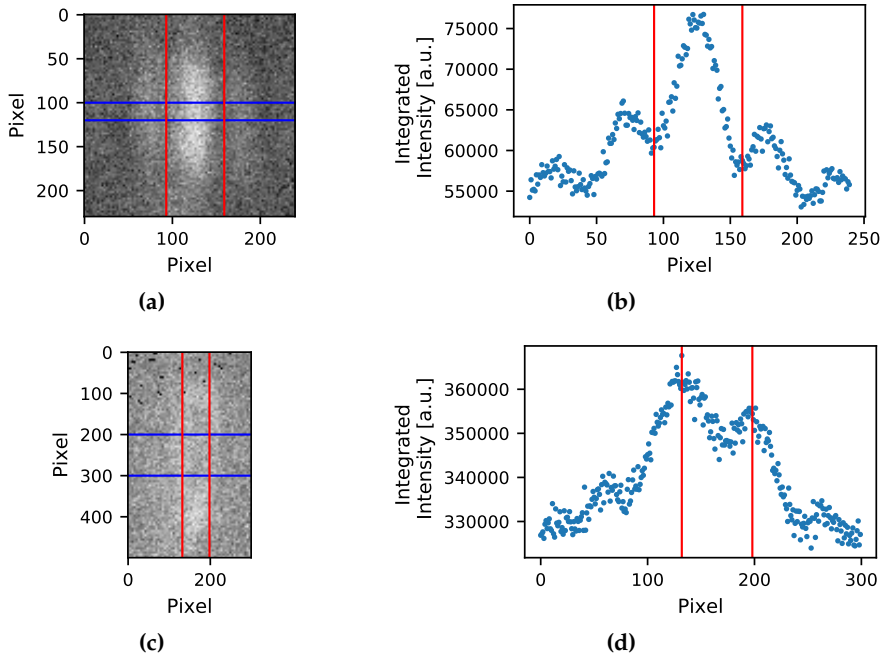

Figure B.6.: Calibration of scale for DLD measurements. (a) Time-integrated Fresnel image of the vortex core motion taken off-resonance (450 MHz) at ~1 mm defocus. (b) Integrated intensity from region indicated by blue lines in (a). The spacing between the central and first outer Fresnel fringe is measured to be 66 pixels (indicated by red lines in (a) and (b)). (c) Time-integrated Fresnel image taken in resonance (417 MHz) at ~1 mm defocus. (d) Integrated intensity from region indicated by blue lines in (c). The diameter of the vortex core gyration corresponds to 66 pixel (indicated by red lines in (c) and (d)).

Bibliography

[1] W. Andrä and H. Nowak, *Magnetism in Medicine: A Handbook*. John Wiley & Sons, 2007.

[2] M. Colombo, S. Carregal-Romero, M. F. Casula, L. Gutiérrez, M. P. Morales, I. B. Böhm, J. T. Heverhagen, D. Prosperi, and W. J. Parak, "Biological applications of magnetic nanoparticles," *Chemical Society Reviews*, vol. 41, no. 11, pp. 4306–4334, 2012.

[3] O. Gutfleisch, M. A. Willard, E. Brück, C. H. Chen, S. G. Sankar, and J. P. Liu, "Magnetic Materials and Devices for the 21st Century: Stronger, Lighter, and More Energy Efficient," *Advanced Materials*, vol. 23, no. 7, pp. 821–842, 2011.

[4] L. H. Lewis and F. Jiménez-Villacorta, "Perspectives on Permanent Magnetic Materials for Energy Conversion and Power Generation," *Metallurgical and Materials Transactions A*, vol. 44, no. 1, pp. 2–20, 2013.

[5] N. Romming, C. Hanneken, M. Menzel, J. E. Bickel, B. Wolter, K. von Bergmann, A. Kubetzka, and R. Wiesendanger, "Writing and Deleting Single Magnetic Skyrmions," *Science*, vol. 341, no. 6146, pp. 636–639, 2013.

[6] C. Altavilla and E. Ciliberto, "Chapter 3 - Magnetic Nanoparticle for Information Storage Applications," in *Inorganic Nanoparticles: Synthesis, Applications, and Perspectives*. CRC Press, 2017.

[7] D. Weller and T. McDaniel, "Media for Extremely High Density Recording," in *Advanced Magnetic Nanostructures*, D. Sellmyer and R. Skomski, Eds. Boston, MA: Springer US, 2006, pp. 295–324.

[8] P. J. Denning and T. G. Lewis, "Exponential laws of computing growth," *Communications of the ACM*, vol. 60, no. 1, pp. 54–65, 2016.

[9] A. P. Guimarães, *Principles of Nanomagnetism*, ser. NanoScience and Technology. Springer International Publishing, 2017.

[10] S. A. Wolf, D. D. Awschalom, R. A. Buhrman, J. M. Daughton, S. von Molnár, M. L. Roukes, A. Y. Chtchelkanova, and D. M. Treger, "Spintronics: A Spin-Based Electronics Vision for the Future," *Science*, vol. 294, no. 5546, pp. 1488–1495, 2001.

[11] I. Žutić, J. Fabian, and S. Das Sarma, "Spintronics: Fundamentals and applications," *Reviews of Modern Physics*, vol. 76, no. 2, pp. 323–410, 2004.

[12] V. V. Kruglyak, S. O. Demokritov, and D. Grundler, "Magnonics," *Journal of Physics D: Applied Physics*, vol. 43, no. 26, p. 264001, 2010.

[13] J. M. D. Coey, *Magnetism and Magnetic Materials*. Cambridge University press, 2010.

[14] S. S. P. Parkin, M. Hayashi, and L. Thomas, "Magnetic Domain-Wall Racetrack Memory," *Science*, vol. 320, no. 5873, pp. 190–194, 2008.

[15] S.-H. Yang, K.-S. Ryu, and S. Parkin, "Domain-wall velocities of up to 750 m s -1 driven by exchange-coupling torque in synthetic antiferromagnets," *Nature Nanotechnology*, vol. 10, no. 3, pp. 221–226, 2015.

[16] R. Tomasello, E. Martinez, R. Zivieri, L. Torres, M. Carpentieri, and G. Finocchio, "A strategy for the design of skyrmion racetrack memories," *Scientific Reports*, vol. 4, no. 1, p. 6784, 2014.

[17] A. V. Chumak, A. A. Serga, and B. Hillebrands, "Magnon transistor for all-magnon data processing," *Nature Communications*, vol. 5, no. 1, p. 4700, 2014.

[18] ——, "Magnonic crystals for data processing," *Journal of Physics D: Applied Physics*, vol. 50, no. 24, p. 244001, 2017.

[19] M. Vogel, R. Aßmann, P. Pirro, A. V. Chumak, B. Hillebrands, and G. von Freymann, "Control of Spin-Wave Propagation using Magnetisation Gradients," *Scientific Reports*, vol. 8, no. 1, p. 11099, 2018.

[20] L. A. Mól, R. L. Silva, R. C. Silva, A. R. Pereira, W. A. Moura-Melo, and B. V. Costa, "Magnetic monopole and string excitations in two-dimensional spin ice," *Journal of Applied Physics*, vol. 106, no. 6, p. 063913, 2009.

[21] S. Ladak, D. E. Read, G. K. Perkins, L. F. Cohen, and W. R. Branford, "Direct observation of magnetic monopole defects in an artificial spin-ice system," *Nature Physics*, vol. 6, no. 5, pp. 359–363, 2010.

[22] G. Möller and R. Moessner, "Magnetic multipole analysis of kagome and artificial spin-ice dipolar arrays," *Physical Review B*, vol. 80, no. 14, p. 140409, 2009.

[23] L. Anghinolfi, H. Luetkens, J. Perron, M. G. Flokstra, O. Sendetskyi, A. Suter, T. Prokscha, P. M. Derlet, S. L. Lee, and L. J. Heyderman, "Thermodynamic phase transitions in a frustrated magnetic metamaterial," *Nature Communications*, vol. 6, no. 1, p. 8278, 2015.

[24] S. Gliga, G. Hrkac, C. Donnelly, J. Büchi, A. Kleibert, J. Cui, A. Farhan, E. Kirk, R. V. Chopdekar, Y. Masaki, N. S. Bingham, A. Scholl, R. L. Stamps, and L. J. Heyderman, "Emergent dynamic chirality in a thermally driven artificial spin ratchet," *Nature Materials*, vol. 16, no. 11, pp. 1106–1111, 2017.

[25] M. Wyss, S. Gliga, D. Vasyukov, L. Ceccarelli, G. Romagnoli, J. Cui, A. Kleibert, R. L. Stamps, and M. Poggio, "Stray-Field Imaging of a Chiral Artificial Spin Ice during Magnetization Reversal," *ACS Nano*, vol. 13, no. 12, pp. 13 910–13 916, 2019.

[26] R. F. Wang, C. Nisoli, R. S. Freitas, J. Li, W. McConville, B. J. Cooley, M. S. Lund, N. Samarth, C. Leighton, V. H. Crespi, and P. Schiffer, "Artificial 'spin ice' in a geometrically frustrated lattice of nanoscale ferromagnetic islands," *Nature*, vol. 439, no. 7074, pp. 303–306, 2006.

[27] S. H. Skjærvø, C. H. Marrows, R. L. Stamps, and L. J. Heyderman, "Advances in artificial spin ice," *Nature Reviews Physics*, vol. 2, no. 1, pp. 13–28, 2020.

[28] S. Lendinez and M. B. Jungfleisch, "Magnetization dynamics in artificial spin ice," *Journal of Physics: Condensed Matter*, vol. 32, no. 1, p. 013001, 2020.

[29] S. Gliga, A. Kákay, R. Hertel, and O. G. Heinonen, "Spectral Analysis of Topological Defects in an Artificial Spin-Ice Lattice," *Physical Review Letters*, vol. 110, no. 11, p. 117205, 2013.

[30] A. C. Chavez, A. Barra, and G. P. Carman, "Voltage control of magnetic monopoles in artificial spin ice," *Journal of Physics D: Applied Physics*, vol. 51, no. 23, p. 234001, 2018.

[31] A. León, "Thermal phase transition in artificial spin ice systems induces the formation and migration of monopole-like magnetic excitations," *Physica B: Condensed Matter*, vol. 500, pp. 59–65, 2016.

[32] M. Krawczyk and D. Grundler, "Review and prospects of magnonic crystals and devices with reprogrammable band structure," *Journal of Physics: Condensed Matter*, vol. 26, no. 12, p. 123202, 2014.

[33] S. Gliga, "Dynamics of reconfigurable artificial spin ice: Toward magnonic functional materials," *APL Materials*, vol. 8, no. 4, p. 040911, 2020.

[34] K. K. Kohli, A. L. Balk, J. Li, S. Zhang, I. Gilbert, P. E. Lammert, V. H. Crespi, P. Schiffer, and N. Samarth, "Magneto-optical Kerr effect studies of square artificial spin ice," *Physical Review B*, vol. 84, no. 18, p. 180412, 2011.

[35] J. C. Gartside, D. M. Arroo, D. M. Burn, V. L. Bemmer, A. Moskalenko, L. F. Cohen, and W. R. Branford, "Realization of ground state in artificial kagome spin ice via topological defect-driven magnetic writing," *Nature Nanotechnology*, vol. 13, no. 1, pp. 53–58, 2018.

[36] A. Farhan, M. Saccone, C. F. Petersen, S. Dhuey, R. V. Chopdekar, Y.-L. Huang, N. Kent, Z. Chen, M. J. Alava, T. Lippert, A. Scholl, and S. van Dijken, "Emergent magnetic monopole dynamics in macroscopically degenerate artificial spin ice," *Science Advances*, vol. 5, no. 2, p. eaav6380, 2019.

[37] L. Landau and E. Lifshitz, "3 - On the theory of the dispersion of magnetic permeability in ferromagnetic bodies Reprinted from Physikalische Zeitschrift der Sowjetunion 8, Part 2, 153, 1935." in *Perspectives in Theoretical Physics*, L. P. Pitaevski, Ed. Amsterdam: Pergamon, 1992, pp. 51–65.

[38] T. Shinjo, T. Okuno, R. Hassdorf, †. K. Shigeto, and T. Ono, "Magnetic Vortex Core Observation in Circular Dots of Permalloy," *Science*, vol. 289, no. 5481, pp. 930–932, 2000.

[39] G. Hrkac, P. S. Keatley, M. T. Bryan, and K. Butler, "Magnetic vortex oscillators," *Journal of Physics D: Applied Physics*, vol. 48, no. 45, p. 453001, 2015.

[40] R. Antos, Y. Otani, and J. Shibata, "Magnetic Vortex Dynamics," *Journal of the Physical Society of Japan*, vol. 77, no. 3, p. 031004, 2008.

[41] K. Nakano, D. Chiba, N. Ohshima, S. Kasai, T. Sato, Y. Nakatani, K. Sekiguchi, K. Kobayashi, and T. Ono, "All-electrical operation of magnetic vortex core memory cell," *Applied Physics Letters*, vol. 99, no. 26, p. 262505, 2011.

[42] S. O. Demokritov, B. Hillebrands, and A. N. Slavin, "Brillouin light scattering studies of confined spin waves: Linear and nonlinear confinement," *Physics Reports*, vol. 348, no. 6, pp. 441–489, 2001.

[43] T. Sebastian, K. Schultheiss, B. Obry, B. Hillebrands, and H. Schultheiss, "Micro-focused Brillouin light scattering: Imaging spin waves at the nanoscale," *Frontiers in Physics*, vol. 3, 2015.

[44] R. Frömter, F. Kloodt, S. Rößler, A. Frauen, P. Staeck, D. R. Cavicchia, L. Bocklage, V. Röbisch, E. Quandt, and H. P. Oepen, "Time-resolved scanning electron microscopy with polarization analysis," *Applied Physics Letters*, vol. 108, no. 14, p. 142401, 2016.

[45] B. Van Waeyenberge, A. Puzic, H. Stoll, K. W. Chou, T. Tyliszczak, R. Hertel, M. Fähnle, H. Brückl, K. Rott, G. Reiss, I. Neudecker, D. Weiss, C. H. Back, and G. Schütz, "Magnetic vortex core reversal by excitation with short bursts of an alternating field," *Nature*, vol. 444, no. 7118, pp. 461–464, 2006.

[46] S. Bonetti, R. Kukreja, Z. Chen, D. Spoddig, K. Ollefs, C. Schöppner, R. Meckenstock, A. Ney, J. Pinto, R. Houanche, J. Frisch, J. Stöhr, H. A. Dürr, and H. Ohldag, "Microwave soft x-ray microscopy for nanoscale magnetization dynamics in the 5–10 GHz frequency range," *Review of Scientific Instruments*, vol. 86, no. 9, p. 093703, 2015.

[47] D. B. Williams and C. B. Carter, *Transmission Electron Microscopy: A Textbook for Materials Science*, 2nd ed. New York: Springer, 2009.

[48] E. Brück, Ed., *Handbook of Magnetic Materials*, 1st ed. Amsterdam, Netherlands: North Holland, 2016.

[49] P. W. Hawkes and J. C. H. Spence, *Springer Handbook of Microscopy*. Springer Nature, 2019.

[50] J. N. Chapman, R. Ploessl, and D. M. Donnet, "Differential phase contrast microscopy of magnetic materials," *Ultramicroscopy*, vol. 47, no. 4, pp. 331–338, 1992.

[51] A. Lubk and J. Zweck, "Differential phase contrast: An integral perspective," *Physical Review A*, vol. 91, no. 2, p. 023805, 2015.

[52] A. K. Petford-Long and M. D. Graef, "Lorentz Microscopy," in *Characterization of Materials*. American Cancer Society, 2012, pp. 1–15.

[53] A. Kovács and R. E. Dunin-Borkowski, "Magnetic Imaging of Nanostructures Using Off-Axis Electron Holography," in *Handbook of Magnetic Materials*. Elsevier, 2018, pp. 59–153.

[54] R. E. Dunin-Borkowski, A. Kovács, T. Kasama, M. R. McCartney, and D. J. Smith, "Electron Holography," in *Springer Handbook of Microscopy*, ser. Springer Handbooks, P. W. Hawkes and J. C. H. Spence, Eds. Cham: Springer International Publishing, 2019, pp. 767–818.

[55] D. Gabor, "A new microscopic principle," *Nature*, vol. 161, pp. 777–778, 1948.

[56] ——, "Microscopy by reconstructed wave-fronts," *Proceedings of the Royal Society of London A: Mathematical, Physical and Engineering Sciences*, vol. 197, no. 1051, pp. 454–487, 1949.

[57] G. Möllenstedt and H. Düker, "Fresnelscher Interferenzversuch mit einem Biprisma für Elektronenwellen," *Naturwissenschaften*, vol. 42, no. 2, pp. 41–41, 1955.

[58] A. V. Crewe, D. N. Eggenberger, J. Wall, and L. M. Welter, "Electron Gun Using a Field Emission Source," *Review of Scientific Instruments*, vol. 39, no. 4, pp. 576–583, 1968.

[59] M. Haider, H. Rose, S. Uhlemann, E. Schwan, B. Kabius, and K. Urban, "A spherical-aberration-corrected 200kV transmission electron microscope," *Ultramicroscopy*, vol. 75, no. 1, pp. 53–60, 1998.

[60] S. L. Y. Chang, C. Dwyer, J. Barthel, C. B. Boothroyd, and R. E. Dunin-Borkowski, "Performance of a direct detection camera for off-axis electron holography," *Ultramicroscopy*, vol. 161, pp. 90–97, 2016.

[61] J. Caron, "Model-based reconstruction of magnetisation distributions in nanostructures from electron optical phase images," Ph.D. dissertation, RWTH Aachen University, Aachen, 2018.

[62] F. Zheng, V. Migunov, J. Caron, H. Du, G. Pozzi, and R. Dunin-Borkowski, "Three-dimensional Charge Density and Electric Field Mapping of an Electrically Biased Needle Using Off-axis Electron Holography," *Microscopy and Microanalysis*, vol. 26, no. S2, pp. 1540–1542, 2020.

[63] S. Pollard, L. Huang, K. Buchanan, D. Arena, and Y. Zhu, "Direct dynamic imaging of non-adiabatic spin torque effects," *Nature Communications*, vol. 3, no. 1, p. 1028, 2012.

[64] D. J. Flannigan and A. H. Zewail, "4D Electron Microscopy: Principles and Applications," *Accounts of Chemical Research*, vol. 45, no. 10, pp. 1828–1839, 2012.

[65] L. Piazza, D. J. Masiel, T. LaGrange, B. W. Reed, B. Barwick, and F. Carbone, "Design and implementation of a fs-resolved transmission electron microscope based on thermionic gun technology," *Chemical Physics*, vol. 423, pp. 79–84, 2013.

[66] A. Feist, N. Bach, N. Rubiano da Silva, T. Danz, M. Möller, K. E. Priebe, T. Domröse, J. G. Gatzmann, S. Rost, J. Schauss, S. Strauch, R. Bormann, M. Sivis, S. Schäfer, and C. Ropers, "Ultrafast transmission electron microscopy using a laser-driven field emitter: Femtosecond resolution with a high coherence electron beam," *Ultramicroscopy*, vol. 176, pp. 63–73, 2017.

[67] J. Yang, Y. Yoshida, and H. Yasuda, "Ultrafast electron microscopy with relativistic femtosecond electron pulses," *Microscopy*, vol. 67, no. 5, pp. 291–295, 2018.

[68] A. Oelsner, O. Schmidt, M. Schicketanz, M. Klais, G. Schönhense, V. Mergel, O. Jagutzki, and H. Schmidt-Böcking, "Microspectroscopy and imaging using a delay line detector in time-of-flight photoemission microscopy," *Review of Scientific Instruments*, vol. 72, no. 10, pp. 3968–3974, 2001.

[69] K. Müller-Caspary, A. Oelsner, and P. Potapov, "Two-dimensional strain mapping in semiconductors by nano-beam electron diffraction employing a delay-line detector," *Applied Physics Letters*, vol. 107, no. 7, p. 072110, 2015.

[70] P. C. Scholten, "Which SI?" *Journal of Magnetism and Magnetic Materials*, vol. 149, no. 1, pp. 57–59, 1995.

[71] A. S. Arrott, "Dipole-dipole interactions in the computational micromagnetism of iron (1955-2010) (invited)," *Journal of Applied Physics*, vol. 109, no. 7, p. 07E135, 2011.

[72] D. J. P. Morris, D. A. Tennant, S. A. Grigera, B. Klemke, C. Castelnovo, R. Moessner, C. Czternasty, M. Meissner, K. C. Rule, J.-U. Hoffmann, K. Kiefer, S. Gerischer, D. Slobinsky, and R. S. Perry, "Dirac Strings and Magnetic Monopoles in the Spin Ice $Dy_2Ti_2O_7$," *Science*, vol. 326, no. 5951, pp. 411–414, 2009.

[73] L. J. Heyderman and R. L. Stamps, "Artificial ferroic systems: Novel functionality from structure, interactions and dynamics," *Journal of Physics: Condensed Matter*, vol. 25, no. 36, p. 363201, 2013.

[74] A. Ortiz-Ambriz, C. Nisoli, C. Reichhardt, C. J. O. Reichhardt, and P. Tierno, "Ice Rule and Emergent Frustration in Particle Ice and Beyond," *Reviews of Modern Physics*, vol. 91, no. 4, p. 041003, 2019.

[75] C. Nisoli, R. Moessner, and P. Schiffer, "*Colloquium* : Artificial spin ice: Designing and imaging magnetic frustration," *Reviews of Modern Physics*, vol. 85, no. 4, pp. 1473–1490, 2013.

[76] J. D. Bernal and R. H. Fowler, "A Theory of Water and Ionic Solution, with Particular Reference to Hydrogen and Hydroxyl Ions," *The Journal of Chemical Physics*, vol. 1, no. 8, pp. 515–548, 1933.

[77] L. Pauling, "The Structure and Entropy of Ice and of Other Crystals with Some Randomness of Atomic Arrangement," *Journal of the American Chemical Society*, vol. 57, no. 12, pp. 2680–2684, 1935.

[78] M. J. Harris, S. T. Bramwell, D. F. McMorrow, T. Zeiske, and K. W. Godfrey, "Geometrical Frustration in the Ferromagnetic Pyrochlore Ho_2Ti_2O," *Physical Review Letters*, vol. 79, no. 13, pp. 2554–2557, 1997.

[79] C. Castelnovo, R. Moessner, and S. L. Sondhi, "Magnetic monopoles in spin ice," *Nature*, vol. 451, no. 7174, pp. 42–45, 2008.

[80] E. R. P. Novais, P. Landeros, A. G. S. Barbosa, M. D. Martins, F. Garcia, and A. P. Guimarães, "Properties of magnetic nanodots with perpendicular anisotropy," *Journal of Applied Physics*, vol. 110, no. 5, p. 053917, 2011.

[81] V. Novosad, F. Y. Fradin, P. E. Roy, K. S. Buchanan, K. Y. Guslienko, and S. D. Bader, "Magnetic vortex resonance in patterned ferromagnetic dots," *Physical Review B*, vol. 72, no. 2, p. 024455, 2005.

[82] T. Weßels, S. Däster, Y. Murooka, B. Zingsem, V. Migunov, M. Kruth, S. Finizio, P.-H. Lu, A. Kovács, A. Oelsner, K. Müller-Caspary, Y. Acremann, and R. E. Dunin-Borkowski, "Continuous illumination picosecond imaging using a delay line detector in a transmission electron microscope," *Ultramicroscopy*, vol. 233, p. 113392, 2022.

[83] A. Neudert, J. McCord, R. Schäfer, R. Kaltofen, I. Mönch, H. Vinzelberg, and L. Schultz, "Bloch-line generation in cross-tie walls by fast magnetic-field pulses," *Journal of Applied Physics*, vol. 99, no. 8, p. 08F302, 2006.

[84] T. Gilbert, "A phenomenological theory of damping in ferromagnetic materials," *IEEE Transactions on Magnetics*, vol. 40, no. 6, pp. 3443–3449, 2004.

[85] K. Y. Guslienko, B. A. Ivanov, V. Novosad, Y. Otani, H. Shima, and K. Fukamichi, "Eigenfrequencies of vortex state excitations in magnetic submicron-size disks," *Journal of Applied Physics*, vol. 91, no. 10, p. 8037, 2002.

[86] N. Usov and L. Kurkina, "Magnetodynamics of vortex in thin cylindrical platelet," *Journal of Magnetism and Magnetic Materials*, vol. 242–245, pp. 1005–1008, 2002.

[87] S.-B. Choe, Y. Acremann, A. Scholl, A. Bauer, A. Doran, J. Stöhr, and H. A. Padmore, "Vortex Core-Driven Magnetization Dynamics," *Science*, vol. 304, no. 5669, pp. 420–422, 2004.

[88] R. Hertel and C. M. Schneider, "Exchange Explosions: Magnetization Dynamics during Vortex-Antivortex Annihilation," *Physical Review Letters*, vol. 97, no. 17, p. 177202, 2006.

[89] R. Hertel, S. Gliga, M. Fähnle, and C. M. Schneider, "Ultrafast Nanomagnetic Toggle Switching of Vortex Cores," *Physical Review Letters*, vol. 98, no. 11, p. 117201, 2007.

[90] G. Schütz, W. Wagner, W. Wilhelm, P. Kienle, R. Zeller, R. Frahm, and G. Materlik, "Absorption of Circularly Polarized X Rays in Iron," *Physical Review Letters*, vol. 58, no. 7, pp. 737–740, 1987.

[91] T. Funk, A. Deb, S. J. George, H. Wang, and S. P. Cramer, "X-ray magnetic circular dichroism—a high energy probe of magnetic properties," *Coordination Chemistry Reviews*, vol. 249, no. 1-2, pp. 3–30, 2005.

[92] B. Rösner, S. Finizio, F. Koch, F. Döring, V. A. Guzenko, M. Langer, E. Kirk, B. Watts, M. Meyer, J. Loroña Ornelas, A. Späth, S. Stanescu, S. Swaraj, R. Belkhou, T. Ishikawa, T. F. Keller, B. Gross, M. Poggio, R. H. Fink, J. Raabe, A. Kleibert, and C. David, "Soft x-ray microscopy with 7 nm resolution," *Optica*, vol. 7, no. 11, p. 1602, 2020.

[93] M. Baumgartner, K. Garello, J. Mendil, C. O. Avci, E. Grimaldi, C. Murer, J. Feng, M. Gabureac, C. Stamm, Y. Acremann, S. Finizio, S. Wintz, J. Raabe, and P. Gambardella, "Spatially and time-resolved magnetization dynamics driven by spin–orbit torques," *Nature Nanotechnology*, vol. 12, no. 10, pp. 980–986, 2017.

[94] S. Wintz, V. Tiberkevich, M. Weigand, J. Raabe, J. Lindner, A. Erbe, A. Slavin, and J. Fassbender, "Magnetic vortex cores as tunable spin-wave emitters," *Nature Nanotechnology*, vol. 11, no. 11, pp. 948–953, 2016.

[95] S. Finizio, K. Zeissler, S. Wintz, S. Mayr, T. Weßels, A. J. Huxtable, G. Burnell, C. H. Marrows, and J. Raabe, "Deterministic Field-Free Skyrmion Nucleation at a Nanoengineered Injector Device," *Nano Letters*, vol. 19, no. 10, pp. 7246–7255, 2019.

[96] S. J. Pennycook, "Z-contrast STEM for materials science," *Ultramicroscopy*, vol. 30, no. 1, pp. 58–69, 1989.

[97] L. Reimer and H. Kohl, *Transmission Electron Microscopy: Physics of Image Formation*, 5th ed., ser. Springer Series in Optical Sciences. New York: Springer, 2008, no. 36.

[98] A. Rother and K. Scheerschmidt, "Relativistic effects in elastic scattering of electrons in TEM," *Ultramicroscopy*, vol. 109, no. 2, pp. 154–160, 2009.

[99] D. Wolf, "Elektronen-Holographische Tomographie zur 3D-Abbildung von elektrostatischen Potentialen in Nanostrukturen," Ph.D. dissertation, Technische Universitat Dresden, Dresden, 2010.

[100] K. Keimpema, "Electron holography of nanoparticles," Ph.D. dissertation, University of Groningen, Groningen, 2008.

[101] G. Möllenstedt and H. Wahl, "Elektronenholographie und Rekonstruktion mit Laserlicht," *Naturwissenschaften*, vol. 55, no. 7, pp. 340–341, 1968.

[102] D. C. Ghigla and M. D. Pritt, *Two-Dimensional Phase Unwrapping: Theory, Algorithms, and Software*. Wiley New York, 1998, vol. 4.

[103] M. Lehmann and H. Lichte, "Tutorial on Off-Axis Electron Holography," *Microscopy and Microanalysis*, vol. 8, no. 6, pp. 447–466, 2002.

[104] P. Diehle, A. Kovács, T. Duden, R. Speen, K. Žagar Soderžnik, and R. E. Dunin-Borkowski, "A cartridge-based turning specimen holder with wireless tilt angle measurement for magnetic induction mapping in the transmission electron microscope," *Ultramicroscopy*, vol. 220, p. 113098, 2021.

[105] A. Tikhonov and V. Arsenin, *Solutions of Ill-Posed Problems*, ser. Ser. Scripta Series in Mathematics. Washington and New York: Halsted Press, 1997.

[106] M. Beleggia, M. A. Schofield, V. V. Volkov, and Y. Zhu, "On the transport of intensity technique for phase retrieval," *Ultramicroscopy*, vol. 102, no. 1, pp. 37–49, 2004.

[107] J. Gräfe, M. Weigand, B. Van Waeyenberge, A. Gangwar, F. Groß, F. Lisiecki, J. Rychly, H. Stoll, N. Träger, J. Förster, F. Stobiecki, J. Dubowik, J. Klos, M. Krawczyk, C. H. Back, E. J. Goering, and G. Schütz, "Visualizing nanoscale spin waves using MAXYMUS," in *Spintronics XII*, H.-J. M. Drouhin, J.-E. Wegrowe, and M. Razeghi, Eds. San Diego, United States: SPIE, 2019, p. 76.

[108] F. Houdellier, G. Caruso, S. Weber, M. Hÿtch, C. Gatel, and A. Arbouet, "Optimization of off-axis electron holography performed with femtosecond electron pulses," *Ultramicroscopy*, vol. 202, pp. 26–32, 2019.

[109] J. van Rens, W. Verhoeven, J. Franssen, A. Lassise, X. Stragier, E. Kieft, P. Mutsaers, and O. Luiten, "Theory and particle tracking simulations of a resonant radiofrequency deflection cavity in TM 110 mode for ultrafast electron microscopy," *Ultramicroscopy*, vol. 184, pp. 77–89, 2018.

[110] T. Wagner, T. Niermann, F. Urban, and M. Lehmann, "Nanosecond electron holography by interference gating," *Ultramicroscopy*, vol. 206, p. 112824, 2019.

[111] B. Zingsem, "Pico-second spin dynamics in nano-structures: Towards nanometer spatial resolution by Transmission electron microscopy," Ph.D. dissertation, Universität Duisburg-Essen, 2020.

[112] D. E. Gray, *American Institute of Physics Handbook*. New York: McGraw-Hill Book Company, 1972.

[113] W. Albrecht, J. Moers, and B. Hermanns, "HNF - Helmholtz Nano Facility," *Journal of large-scale research facilities JLSRF*, vol. 3, p. A112, 2017.

[114] X. F. Navick, M. Carty, M. Chapellier, G. Chardin, C. Goldbach, R. Granelli, S. Hervé, M. Karolak, G. Nollez, F. Nizery, C. Riccio, P. Starzynski, and V. Villar, "Fabrication of ultra-low radioactivity detector holders for Edelweiss-II," *Nuclear Instruments and Methods in Physics Research Section A: Accelerators, Spectrometers, Detectors and Associated Equipment*, vol. 520, no. 1, pp. 189–192, 2004.

[115] Ernst Ruska-Centre for Microscopy and Spectroscopy with Electrons, "FEI Titan G2 80-200 CREWLEY," *Journal of large-scale research facilities*, vol. 2, p. A43, 2016.

[116] R. D. Tikhonov and A. A. Cheremisinov, "Magnetization of permalloy films," *Russian Microelectronics*, vol. 46, no. 2, pp. 95–104, 2017.

[117] T. Weßels, A. Kovács, S. Gliga, S. Finizio, J. Caron, and R. E. Dunin-Borkowski, "Quantitative imaging of the magnetic field distribution in an artificial spin ice studied by off-axis electron holography," *Journal of Magnetism and Magnetic Materials*, vol. 543, p. 168535, 2022.

[118] F. de la Peña, E. Prestat, V. T. Fauske, P. Burdet, T. Furnival, P. Jokubauskas, M. Nord, T. Ostasevicius, K. E. MacArthur, D. N. Johnstone, M. Sarahan, J. Lähnemann, and J. Taillon, "Hyperspy/hyperspy: Release v1.6.1," available at doi:10.5281/zenodo.4294676, 2020.

[119] M. Sezgin and B. Sankur, "Survey over image thresholding techniques and quantitative performance evaluation," *Journal of Electronic Imaging*, vol. 13, no. 1, pp. 146–165, 2004.

[120] F. Winkler, "Absolute scale off-axis electron holography of thin dichalcogenide crystals at atomic resolution," Ph.D. dissertation, RWTH Aachen University, Aachen, 2019.

[121] M. Mansuripur, "Computation of electron diffraction patterns in Lorentz electron microscopy of thin magnetic films," *Journal of Applied Physics*, vol. 69, no. 4, pp. 2455–2464, 1991.

[122] A. Kakay, E. Westphal, and R. Hertel, "Speedup of FEM Micromagnetic Simulations With Graphical Processing Units," *IEEE Transactions on Magnetics*, vol. 46, no. 6, pp. 2303–2306, 2010.

[123] M. Schneider, J. Liszkowski, M. Rahm, W. Wegscheider, D. Weiss, H. Hoffmann, and J. Zweck, "Magnetization configurations and hysteresis loops of small permalloy ellipses," *Journal of Physics D: Applied Pysics*, vol. 36, no. 18, pp. 2239–2243, 2003.

[124] M. Beleggia, M. A. Schofield, Y. Zhu, M. Malac, Z. Liu, and M. Freeman, "Quantitative study of magnetic field distribution by electron holography and micromagnetic simulations," *Applied Physics Letters*, vol. 83, no. 7, pp. 1435–1437, 2003.

[125] D. Wolf, L. A. Rodriguez, A. Bec, C. Gatel, A. Lubk, H. Lichte, S. Bals, G. V. Tendeloo, and A. Fernan, "3D Magnetic Induction Maps of Nanoscale Materials Revealed by Electron Holographic Tomography," *Chem. Mater.*, p. 8, 2015.

[126] S. Finizio, S. Wintz, D. Bracher, E. Kirk, A. S. Semisalova, J. Förster, K. Zeissler, T. Weßels, M. Weigand, K. Lenz, A. Kleibert, and J. Raabe,

"Thick permalloy films for the imaging of spin texture dynamics in perpendicularly magnetized systems," *Physical Review B*, vol. 98, no. 10, p. 104415, 2018.

[127] K. Ounadjela, H. Lefakis, V. S. Speriousu, C. Hwang, and P. S. Alexopoulos, "Effect of surface composition observed by Auger electron spectroscopy on magnetization and magnetostriction of NiFe and NiFeRh thin films," *Journal of Applied Physics*, vol. 65, no. 3, pp. 1230–1233, 1989.

[128] M. Bode and R. Wiesendanger, "Spin-Polarized Scanning Tunneling Spectroscopy," in *Magnetic Microscopy of Nanostructures*, P. Avouris, K. von Klitzing, H. Sakaki, R. Wiesendanger, H. Hopster, and H. P. Oepen, Eds. Berlin, Heidelberg: Springer Berlin Heidelberg, 2005, pp. 203–223.

[129] J. Wang, X. Zhang, X. Lu, J. Zhang, Y. Yan, H. Ling, J. Wu, Y. Zhou, and Y. Xu, "Magnetic domain wall engineering in a nanoscale permalloy junction," *Applied Physics Letters*, vol. 111, no. 7, p. 072401, 2017.

[130] C. Dietrich, R. Hertel, M. Huber, D. Weiss, R. Schäfer, and J. Zweck, "Influence of perpendicular magnetic fields on the domain structure of permalloy microstructures grown on thin membranes," *Physical Review B*, vol. 77, no. 17, p. 174427, 2008.

[131] M. Vaňatka, M. Urbánek, R. Jíra, L. Flajšman, M. Dhankhar, M.-Y. Im, J. Michalička, V. Uhlíř, and T. Šikola, "Magnetic vortex nucleation modes in static magnetic fields," *AIP Advances*, vol. 7, no. 10, p. 105103, 2017.

[132] T. Uhlig, M. Rahm, C. Dietrich, R. Höllinger, M. Heumann, D. Weiss, and J. Zweck, "Shifting and Pinning of a Magnetic Vortex Core in a Permalloy Dot by a Magnetic Field," *Physical Review Letters*, vol. 95, no. 23, p. 237205, 2005.

[133] R. L. Compton and P. A. Crowell, "Dynamics of a Pinned Magnetic Vortex," *Physical Review Letters*, vol. 97, no. 13, p. 137202, 2006.

[134] M. Möller, J. H. Gaida, and C. Ropers, "Pinning and gyration dynamics of magnetic vortices revealed by correlative Lorentz and bright-field imaging," *Physical Review Research*, vol. 4, no. 1, p. 013027, 2022.

[135] T. Y. Chen, M. J. Erickson, P. A. Crowell, and C. Leighton, "Surface Roughness Dominated Pinning Mechanism of Magnetic Vortices in Soft Ferromagnetic Films," *Physical Review Letters*, vol. 109, no. 9, p. 097202, 2012.

[136] A. Vansteenkiste, J. Leliaert, M. Dvornik, M. Helsen, F. Garcia-Sanchez, and B. Van Waeyenberge, "The design and verification of MuMax3," *AIP Advances*, vol. 4, no. 10, p. 107133, 2014.

[137] L. Exl, S. Bance, F. Reichel, T. Schrefl, H. Peter Stimming, and N. J. Mauser, "LaBonte's method revisited: An effective steepest descent method for micromagnetic energy minimization," *Journal of Applied Physics*, vol. 115, no. 17, p. 17D118, 2014.

[138] R. Hertel, "Thickness dependence of magnetization structures in thin Permalloy rectangles: Dedicated to Professor Dr. Helmut Kronmüller on the occasion of his 70th birthday," *Zeitschrift für Metallkunde*, vol. 93, no. 10, pp. 957–962, 2002.

[139] A. Götz, E. Taurel, J. L. Pons, P. Verdier, J. M. Chaize, J. Meyer, F. Poncet, G. Heunen, and E. Götz, "TANGO a CORBA Based Control System," in *Proceedings of ICALEPS 2003*, 2003, p. 3.

[140] D. M. Pozar, *Microwave Engineering*, 4th ed. John Wiley & Sons, 2012.

[141] F. J. T. Goncalves, G. W. Paterson, D. McGrouther, T. Drysdale, Y. Togawa, D. S. Schmool, and R. L. Stamps, "Probing microwave fields and enabling in-situ experiments in a transmission electron microscope," *Scientific Reports*, vol. 7, no. 1, p. 11064, 2017.

[142] R. N. Simons, *Coplanar Waveguide Circuits, Components, and Systems*, ser. Wiley Series in Microwave and Optical Engineering, K. Chang, Ed. New York, USA: John Wiley & Sons, Inc., 2001.

[143] Ernst Ruska-Centre for Microscopy and Spectroscopy with Electrons, "FEI Titan 80-300 TEM," *Journal of large-scale research facilities*, vol. 2, no. 0, p. 41, 2016.

[144] ——, "FEI Titan G2 60-300 HOLO," *Journal of large-scale research facilities*, vol. 2, p. A44, 2016.

[145] X. Zhang, Y. Lao, J. Sklenar, N. S. Bingham, J. T. Batley, J. D. Watts, C. Nisoli, C. Leighton, and P. Schiffer, "Understanding thermal annealing of artificial spin ice," *APL Materials*, vol. 7, no. 11, p. 111112, 2019.

[146] F. Schulz, R. Lawitzki, H. Głowiński, F. Lisiecki, N. Träger, P. Kuświk, E. Goering, G. Schütz, and J. Gräfe, "Increase of Gilbert damping in Permalloy thin films due to heat-induced structural changes," *Journal of Applied Physics*, vol. 129, no. 15, p. 153903, 2021.

[147] A. Neudert, J. McCord, R. Schäfer, and L. Schultz, "Subnanosecond vortex transformation in ferromagnetic film elements observed by stroboscopic wide-field Kerr microscopy," *Journal of Applied Physics*, vol. 97, no. 10, p. 10E701, 2005.

[148] A. Vansteenkiste, "X-ray imaging of the dynamic magnetic vortex core deformation," *NATURE PHYSICS*, vol. 5, p. 3, 2009.

[149] J. C. Williamson, J. Cao, H. Ihee, H. Frey, and A. H. Zewail, "Clocking transient chemical changes by ultrafast electron diffraction," *Nature*, vol. 386, no. 6621, pp. 159–162, 1997.

[150] X. Fu, E. Wang, Y. Zhao, A. Liu, E. Montgomery, V. J. Gokhale, J. J. Gorman, C. Jing, J. W. Lau, and Y. Zhu, "Direct visualization of electromagnetic wave dynamics by laser-free ultrafast electron microscopy," *Science Advances*, vol. 6, no. 40, p. eabc3456, 2020.

[151] J. W. Lau, K. B. Schliep, M. B. Katz, V. J. Gokhale, J. J. Gorman, C. Jing, A. Liu, Y. Zhao, E. Montgomery, H. Choe, W. Rush, A. Kanareykin, X. Fu, and Y. Zhu, "Laser-free GHz stroboscopic transmission electron microscope: Components, system integration, and practical considerations for pump–probe measurements," *Review of Scientific Instruments*, vol. 91, no. 2, p. 021301, 2020.

[152] L. Zhang, M. W. H. Garming, J. P. Hoogenboom, and P. Kruit, "Beam displacement and blur caused by fast electron beam deflection," *Ultramicroscopy*, vol. 211, p. 112925, 2020.

[153] M. Campbell, J. Alozy, R. Ballabriga, E. Frojdh, E. Heijne, X. Llopart, T. Poikela, L. Tlustos, P. Valerio, and W. Wong, "Towards a new generation of pixel detector readout chips," *Journal of Instrumentation*, vol. 11, no. 01, pp. C01 007–C01 007, 2016.

[154] H. J. Richter, "The transition from longitudinal to perpendicular recording," *Journal of Physics D: Applied Physics*, vol. 40, no. 9, pp. R149–R177, 2007.

[155] S.-K. Kim, "Micromagnetic computer simulations of spin waves in nanometre-scale patterned magnetic elements," *Journal of Physics D: Applied Physics*, vol. 43, no. 26, p. 264004, 2010.

[156] M. Duerrschnabel, M. Yi, K. Uestuener, M. Liesegang, M. Katter, H.-J. Kleebe, B. Xu, O. Gutfleisch, and L. Molina-Luna, "Atomic structure and

domain wall pinning in samarium-cobalt-based permanent magnets," *Nature Communications*, vol. 8, no. 1, p. 54, 2017.

[157] M. Nord, A. Semisalova, A. Kákay, G. Hlawacek, I. MacLaren, V. Liersch, O. M. Volkov, D. Makarov, G. W. Paterson, K. Potzger, J. Lindner, J. Fassbender, D. McGrouther, and R. Bali, "Strain Anisotropy and Magnetic Domains in Embedded Nanomagnets," *Small*, vol. 15, no. 52, p. 1904738, 2019.

[158] A. Fert, V. Cros, and J. Sampaio, "Skyrmions on the track," *Nature Nanotechnology*, vol. 8, no. 3, pp. 152–156, 2013.

[159] N. Rubiano da Silva, M. Möller, A. Feist, H. Ulrichs, C. Ropers, and S. Schäfer, "Nanoscale Mapping of Ultrafast Magnetization Dynamics with Femtosecond Lorentz Microscopy," *Physical Review X*, vol. 8, no. 3, p. 031052, 2018.

[160] N. Leo, M. Pancaldi, S. Koraltan, P. V. González, C. Abert, C. Vogler, F. Slanovc, F. Bruckner, P. Heistracher, K. Hofhuis, M. Menniti, D. Suess, and P. Vavassori, "Chiral switching and dynamic barrier reductions in artificial square ice," *New Journal of Physics*, vol. 23, no. 3, p. 033024, 2021.

[161] P. Gypens, N. Leo, M. Menniti, P. Vavassori, and J. Leliaert, "Thermoplasmonic Nanomagnetic Logic Gates," *arXiv:2110.14212 [physics]*, 2021.

[162] A. S. Garanina, V. A. Naumenko, A. A. Nikitin, E. Myrovali, A. Y. Petukhova, S. V. Klimyuk, Y. A. Nalench, A. R. Ilyasov, S. S. Vodopyanov, A. S. Erofeev, P. V. Gorelkin, M. Angelakeris, A. G. Savchenko, U. Wiedwald, A. G. Majouga Dr, and M. A. Abakumov, "Temperature-controlled magnetic nanoparticles hyperthermia inhibits primary tumor growth and metastases dissemination," *Nanomedicine: Nanotechnology, Biology and Medicine*, vol. 25, p. 102171, 2020.

[163] S. V. Mohd Sagheer and S. N. George, "A review on medical image denoising algorithms," *Biomedical Signal Processing and Control*, vol. 61, p. 102036, 2020.

[164] L. Gondara, "Medical Image Denoising Using Convolutional Denoising Autoencoders," in *2016 IEEE 16th International Conference on Data Mining Workshops (ICDMW)*, 2016, pp. 241–246.

[165] D. Jannis, C. Hofer, C. Gao, X. Xie, A. Béché, T. J. Pennycook, and J. Verbeeck, "Event driven 4D STEM acquisition with a Timepix3 detector: Microsecond dwell time and faster scans for high precision and low dose applications," *Ultramicroscopy*, vol. 233, p. 113423, 2022.

[166] D. Jannis, K. Müller-Caspary, A. Béché, A. Oelsner, and J. Verbeeck, "Spectroscopic coincidence experiments in transmission electron microscopy," *Applied Physics Letters*, vol. 114, no. 14, p. 143101, 2019.

[167] P. C. Hansen, "Analysis of Discrete Ill-Posed Problems by Means of the L-Curve," *SIAM Review*, vol. 34, no. 4, pp. 561–580, 1992.

List of own publications

Publications that are included in this thesis in a modified version are marked with an asterisk (*).

[P1] T. Weßels, S. Däster, Y. Murooka, B. Zingsem, V. Migunov, M. Kruth, S. Finizio, P.H. Lu, A. Kovács, A. Oelsner, K. Müller-Caspary, Y. Acreman, R.E. Dunin-Borkowski. Continuus illumination picosecond imaging using a delay line detector in transmission electron microscopy. *Ultramicroscopy*, 233:113392, 2022.*

[P2] T. Weßels, A. Kovács, S. Gliga, S. Finizio, J. Caron, R.E. Dunin-Borkowski. Quantitative imaging of the magnetic field distribution in an artificial spin ice studied by off-axis electron holography. *J. Magn. Magn. Mater.*, 543:168535, 2022.*

[P3] F. Zheng, A. Kovács, T. Denneulin, J. Caron, T. Weßels, R.E. Dunin-Borkowski, Magnetic Field Mapping using Off-Axis Electron Holography in the Transmission Electron Mikrosope. *J. Vis. Exp.*, 166:e51907, 2020.

[P4] S. Finizio, K. Zeissler, S. Wintz, S. Mayr, T. Weßels, A.J. Huxable, G. Burnell, C.H. Marrows, J. Raabe. Deterministic Field-Free Skyrmion Nucleation at a Nanoengineered Injector Device. *Nano Lett.*, 19:7246-7255, 2019.

[P5] S. Finizio, S. Wintz, D. Bracher, E. Krik, A.S. Semisalova, J. Förster, K. Zeissler, T. Weßels, M. Weigand, K. Lenz, A. Kleibert, J. Raabe. Thick permalloy films for the imaging of spin texture dynamics in perpendicularly magnetized systems. *Phys. Rev. B*, 98:104415, 2018.

Band / Volume 253
Topological magnonic properties of two-dimensional magnetic materials
L. Zhang (2022), xx, 154 pp
ISBN: 978-3-95806-621-2

Band / Volume 254
Role of secondary metabolites in antiphage defense in *Streptomyces*
Aël Hardy (2022), IV, 193 pp
ISBN: 978-3-95806-633-5

Band / Volume 255
Neutron Scattering
Lectures of the JCNS Laboratory Course held at Forschungszentrum Jülich and at the Heinz-Maier-Leibnitz Zentrum Garching
edited by T. Brückel, S. Förster, M. Kruteva**,** M. Zobel, and R. Zorn (2022), ca. 300 pp
ISBN: 978-3-95806-634-2

Band / Volume 256
Magnetoelectric Interactions in Multiferroic Thin-film Heterosystems and Nanostructures
H. Gökdemir (2022), x, 140 pp
ISBN: 978-3-95806-635-9

Band / Volume 257
High-Performance Computing Approach to Hybrid Functionals in the All-Electron DFT Code FLEUR
M. Redies (2022), xi, 109 pp
ISBN: 978-3-95806-639-7

Band / Volume 258
Establishing regulatable expression systems in the acetic acid bacterium *Gluconobacter oxydans* 621H
P. M. Fricke (2022), VIII, 187 pp
ISBN: 978-3-95806-642-7

Band / Volume 259
Density-Functional Perturbation Theory within the All-Electron Full-Potential Linearized Augmented Plane-Wave Method: Application to Phonons
C.-R. Gerhorst (2022), xvi, 317 pp
ISBN: 978-3-95806-649-6

Band / Volume 260
Crystal and Magnetic Structure of CrAs under Extreme Conditions
A. Eich (2022), viii, 235 pp
ISBN: 978-3-95806-655-7

Band / Volume 261
Applications of transcription factor-based biosensors for strain development and evolutionary engineering
R. G. Stella (2022), x, 128 pp
ISBN: 978-3-95806-657-1

Band / Volume 262
Strömungsmechanische Simulation und experimentelle Validierung des kryogenen Wasserstoff-Moderators für die Europäische Spallationsneutronenquelle ESS
Y. Beßler (2022), XXIV, 154, xxxiii pp
ISBN: 978-3-95806-660-1

Band / Volume 263
9th Georgian-German School and Workshop in Basic Science September 12 – 16, 2022 | Kutaisi, Tbilisi | Georgia
A. Kacharava, E. Portius, N. J. Shah, H. Ströher (2022)
ISBN: 978-3-95806-664-9

Band / Volume 264
Self-assembly of Au-Fe_3O_4 dumbbell nanoparticles
N. Nandakumaran (2022), xiv, 234 pp
ISBN: 978-3-95806-666-3

Band / Volume 265
Time-resolved and three-dimensional characterisation of magnetic states in nanoscale materials in the transmission electron microscope
T. Weßels (2023), xx, 211 pp
ISBN: 978-3-95806-685-4

Schlüsseltechnologien / Key Technologies
Band / Volume 265
ISBN 978-3-95806-685-4

Mitglied der Helmholtz-Gemeinschaft

JÜLICH
Forschungszentrum